An Investigation of the Structure, Stability and Transport of Hydrogen in Uranium Oxides

Flitcroft, Joseph

Award date:
2018

Awarding institution:
University of Bath

An Investigation of the Structure, Stability and Transport of Hydrogen in Uranium Oxides

Joseph Malcolm Flitcroft

A thesis presented for the degree of
Doctor of Philosophy

Department of Chemistry
University of Bath
September 2017

Contents

Abstract **iv**

Acknowledgements **v**

Publications and Presentations **vii**

1 Introduction **1**
1.1 Nuclear Power . . . 1
1.2 Nuclear Reactors . . . 2
1.2.1 Reactor Operation . . . 3
1.2.2 Thermal Reactors . . . 4
1.2.3 Fast Reactors . . . 5
1.2.4 Future Nuclear Reactors . . . 5
1.3 Nuclear Fuels . . . 6
1.4 The Nuclear Fuel Cycle . . . 6
1.5 The Uranium-Oxygen System . . . 8
1.5.1 Fluorite Based Uranium Oxides . . . 9
1.5.2 Layered Based Uranium Oxides . . . 9
1.6 Hydrogen in Oxides . . . 13
1.6.1 The Interaction of Water and MO_2 (M = Ce, U, Pu) . . . 15
1.7 Aims of the Thesis . . . 17

2 Computational Methodology **18**
2.1 Computational Theory . . . 19
2.1.1 Quantum Mechanics . . . 19
2.2 Energy Minimisation . . . 28
2.2.1 Steepest Descent . . . 29
2.2.2 Conjugate Gradients . . . 30
2.2.3 Newton-Raphson . . . 30
2.2.4 Quasi-Newton . . . 31
2.3 Periodicity . . . 32
2.3.1 Periodic Boundary Conditions . . . 32
2.3.2 The Reciprocal Lattice . . . 32
2.3.3 Bloch Theorem and Plane Waves . . . 34
2.3.4 Pseudopotentials . . . 35
2.4 Calculation of Crystal Properties . . . 37
2.4.1 Density of States . . . 37
2.4.2 Bulk Modulus . . . 38
2.4.3 Vibrational Properties . . . 39

2.4.4 Reference Energies 40

3 Uranium Dioxide (UO_2) 44
3.1 UO_2 Literature Review 44
3.1.1 Structure 44
3.1.2 Elastic Properties 46
3.1.3 Magnetic Properties 48
3.1.4 Electronic Properties 49
3.1.5 Vibrational Properties 50
3.1.6 Intrinsic Point Defects 51
3.2 Calculated Properties 54
3.2.1 Convergence Tests 54
3.2.2 Structure 57
3.2.3 Elastic Properties 59
3.2.4 Magnetic Properties 59
3.2.5 Electronic Properties 62
3.2.6 Vibrational Properties 67
3.2.7 Point Defects 68
3.3 Conclusions 69

4 Hydrogen in UO_2: Functional Dependence 70
4.1 Hydrogen Defects 71
4.1.1 Monatomic Hydrogen Behaviour in UO_2 72
4.1.2 Molecular Hydrogen Behaviour in UO_2 74
4.1.3 Dependence on Functional 75
4.1.4 Effect of Concentration 75
4.1.5 Electronic Properties 78
4.2 Conclusions 83

5 Hydrogen in $UO_{2\pm x}$ 85
5.0.1 Hydrogen in UO_2 85
5.0.2 Hypostoichiometric UO_2 ($UO_{1.97}$) 87
5.0.3 Hydrogen Defects in $UO_{1.97}$ 88
5.0.4 Hyperstoichiometric UO_2 ($UO_{2.03}$) 92
5.0.5 Hydrogen Defects in $UO_{2.03}$ 93
5.1 Conclusions 96

6 Hydrogen Transport in UO_2 98
6.1 Intra-cell Hydrogen Behaviour 98
6.1.1 Hydrogen behaviour in the <100> Direction 101
6.1.2 Hydrogen behaviour in the <110> Direction 102
6.1.3 Hydrogen behaviour in the <111> Direction 103
6.1.4 Hydrogen Species in UO_2 104
6.2 Inter-cell Hydrogen Behaviour 105
6.2.1 Monatomic Hydrogen 106
6.2.2 Molecular Hydrogen 107
6.3 Conclusions 112

7 The Interaction of Hydrogen with Oxygen Defect Clusters in UO_{2+x} 114
7.1 Literature Review . . . 114
7.2 Structural Models for UO_{2+x} and $UO_{2+x}H_n$ . . . 117
7.2.1 UO_{2+x} Structural Models . . . 117
7.2.2 $UO_{2+x}H_n$ Structural Models . . . 117
7.2.3 Energetics of Hydrogen in UO_{2+x} . . . 118
7.3 Effect of Hydrogen on Oxygen Defect Clusters . . . 119
7.3.1 H-O clusters at 117 μgH / gUO_2 . . . 120
7.3.2 H-O clusters at 234 μgH / gUO_2 . . . 122
7.3.3 H-O clusters at 351 μgH / gUO_2 . . . 124
7.3.4 H-O clusters at 467 μgH / gUO_2 . . . 126
7.3.5 Thermodynamic Distribution of Defect Clusters . . . 130
7.4 Conclusions . . . 131

8 Uranium Hydride (UH_3) 133
8.1 UH_3 Literature Review . . . 133
8.2 Convergence Tests . . . 137
8.3 Methodology Assessment . . . 138
8.4 Oxidation of Uranium Hydride . . . 145
8.4.1 Electronic Properties . . . 147
8.5 Conclusions . . . 151

9 Representation of Thermodynamic Stability 152
9.1 Methodology . . . 152
9.1.1 Calculating the Free Energy at Equilibrium ($\delta G_{T,p}$) . . . 152
9.1.2 Calculating the Free Energy (ΔG^0) . . . 154
9.2 Thermodynamically Stable Structures . . . 154
9.2.1 Full Thermodynamic Model . . . 156
9.2.2 Inhibiting Higher Uranium Oxides . . . 158
9.2.3 Complete Inhibition of Higher Uranium Oxides . . . 160
9.3 Conclusions . . . 161

10 Conclusions and Future Work 163
10.1 DFT Model of Hydrogen in UO_2 . . . 163
10.2 Hydrogen Defects in $UO_{2\pm x}$ . . . 164
10.3 Hydrogen Transport in UO_2 . . . 164
10.4 Uranium Hydride . . . 165
10.5 Thermodynamic Model . . . 166

References 167

Appendix A pDOS of Hydrogen Defects in UO_2 198

Appendix B Hydrogen Defects in Larger Oxygen Defect Clusters 211

Appendix C Complete UH_3 Oxygen Defects Data 213

Abstract

The aim of this thesis is to develop an understanding of how hydrogen defects behave in uranium dioxide. As a major concern is the formation of pyrophoric UH_3 at the uranium metal/uranium oxide interface. There is currently very little data, experimental or theoretical, available for hydrogen in UO_2. However, due to uranium dioxide's prominence as a nuclear fuel, there is a vast repository of data for UO_2 available in the literature. This has shown that UO_2 is also highly susceptible to oxidation, this further complicates the problem of determining how hydrogen behaves as this is highly dependent on the oxygen stoichiometry.

This thesis begins by outlining the background to nuclear power, the nuclear fuel cycle and the uranium-oxygen system (Chapter 1). This is followed by an explanation of the quantum mechanical methodology used (Chapter 2). A range of different GGA+U functionals (PBE+U, PBEsol+U, PW91+U and rPBE+U) are investigated to determine the most suitable for simulation of UO_2 (Chapter 3). This is followed by an assessment of the functional dependence on the predicted behaviour of hydrogen in UO_2 (Chapter 4). From the results of Chapters 3 and 4 the PBE+U functional was determined to be the most suitable for the simulation of UO_2 and predicting hydrogen behaviour in UO_2. The PBE+U functional was then used to investigate the behaviour of hydrogen as a function of oxygen content in $UO_{2\pm x}$ (Chapter 5), where hypostoichiometric UO_2 was found to favour hydride formation and hyperstoichiometric UO_2 favoured protonic defects (as part of a hydroxyl group). Having determined the preferred hydrogen species in UO_2 the energy barriers to transport are the assessed (Chapter 6), with the lowest energy pathway predicted to involve the conversion of hydride defects to hydroxyl defects, with a corresponding U^{5+} to U^{3+} conversion. UO_2 is particularly susceptible to oxidation, leading to a large range of proposed oxygen defect clusters in the literature. The effect of hydrogen on the stability on the smallest of these clusters (split di-interstitial and 2:2:2 Willis) is investigated (Chapter 7), where a single hydrogen atom is enough to stabilise the 2:2:2 Willis cluster. One of the motivations for investigating hydrogen behaviour in UO_2 is the formation of UH_3 at the metal oxide interface. The chosen methodology for hydrogen defects in UO_2 is assessed for its suitability to simulate UH_3 (Chapter 8) and the oxidation of the hydride is investigated. In the final results chapter (Chapter 9) a model is developed to assess the thermodynamic stability of all the different defects as a function of varying oxygen and hydrogen chemical potentials. Finally, the conclusions and possible directions for building on the work in this thesis are presented (Chapter 10).

Acknowledgements

First and foremost I would like to thank my supervisor Professor Steve Parker, who has been a constant source of enthusiasm, support, knowledge and advise throughout my PhD, without which this project would have not been possible. A second big thank you goes to Dr Marco Molinari for his technical support, ideas and aid in the completion of this thesis. I would also like to acknowledge and thank Dr Mark Storr, my industrial supervisor and AWE for funding.

I would also like to thank the past and present members of Parker group. In particular, Dr Nick Williams, Dr Nick Brincat and Adam Symington for their insightful discussions on uranium oxides. In addition, I would like to thank Dr Stephen Yeandle and Joshua Tse for their technical assistance.

I would also like to acknowledge the University of Bath for funding and use of the Aquila and Balena HPC facilities. I also wish to than the Materials Chemistry Consortium (MCC) for time on the HECToR and ARCHER HPC facilities, funded through EPSRC (EP/F067496 and EP/L000202) provided by UoE HPCx Ltd, Cary Inc and NAG Ltd at the University of Edinburgh.

Finally, I would like to thank my friends and family for all their support throughout my PhD and of course not forgetting athletics for providing a means of escaping the stress of a PhD.

Publications and Presentations

Publications

Flitcroft, J.M.; Brincat, N.A.; Molinari, M.; Parker, S. C.; Storr, M.T.; Hydride Ion Formation in Stoichiometric UO_2, Chemical Communications, **51**, 16209, 2015.

Presentations

Talks:

Hydrogen Defects in Hyperstoichiometric Uranium Dioxide
HPC Symposium, University of Bath, June 2017.

Modelling Hydrogen Defects in Uranium Dioxide
Postgraduate Symposium, Internal, University of Bath, May 2016.

DFT Simulation of Hydrogen in UO_2 and UH_3
Actinide Thin Film Meeting, University of Bristol, June 2015.

Hydrogen Defects in Stoichiometric UO_2
HPC Symposium, University of Bath, June 2015.

Modelling of Hydrogen in UO_2 and UH_3
AWE EMR meeting, University of Bristol, April 2015.

The Structure and Transport of Hydrogen Defects in UO_2
Second Year PhD Talks, Internal, University of Bath, February 2015.

The Structure and Transport of Hydrogen Defects in UO_2
Computational Chemistry Seminar, Internal, University of Bath, January 2015.

Posters:

Using DFT to Explore Hydrogen Behaviour in $UO_{2\pm x}$
CCP5 AGM, Harper Adams University, September 2016.

Using HPC to Explore Hydrogen Behaviour in $UO_{2\pm x}$
HPC Symposium, University of Bath, June 2016.

Hydrogen Defects and Diffusion in UO_2
2^{nd} Materials Chemistry Consortium Conference, Cardiff University, April 2016.

Uranium Dioxide Containing Hydrogen Defects
RSC Solid State Chemistry Christmas Meeting, University of Kent, December 2015

Computer Simulation of Hydrogen in $UO_{2(+x)}$
Materials Showcase, AWE, Aldermaston, December 2015.

Hydrogen Defects in Uranium Matrixes
Defence and Doctoral Symposium, Cranfield University, November 2015.

Hydrogen Defects in Uranium Matrixes
Defence and Doctoral Symposium, Cranfield University, November 2015.

Modelling H defects in UO_2 and UH_3
Nuclear Analytical & Materials Science Exchange Convention, AWE, Aldermaston, January 2015.

Hydrogen Defects in UO_2
South West Computational Chemistry Group Meeting, University of Bath, October 2014.

The Structure and Transport of H Defects in UO_2
Plutonium Futures, Renaissance Hotel, Las Vegas, USA, September 2014.

An atomistic and experimental investigation of the U-O-H system
CCP5 AGM, Harper Adams University, September 2014.

Hydrogen Species in UO_2 - Defect Formation and Diffusion Paths
HPC Symposium, University of Bath, June 2014.

Hydrogen Species in UO_2 - Defect Formation and Diffusion Paths
Chemistry Postgraduate Symposium, Internal, University of Bath, May 2014.

Modelling the structural and defect properties of Uranium Oxides and Minerals
RSC Solid State Chemistry Christmas Meeting, University of Bath, December 2013

1 Introduction

There is an ever growing need to generate a large amount of energy, without causing the harmful environmental effect of CO_2 production. Nuclear power is a proven technology for the reliable generation of energy on demand without CO_2 production. However, nuclear power does present other challenges such as how to safely store nuclear waste. Not only does spent nuclear fuel need to be stored over a long period to reduce radioactivity but the material integrity needs to be maintained to ensure the harmful radionuclide species, stored in the fuel, are prevented from reaching the environment. Therefore, there is a need to engage in fundamental research to understand the materials chemistry, and hence be able to predict material behaviour under varying conditions and as a function of time. However, there is one element, that is ubiquitous in all components of nuclear fuel, but has received remarkably little attention; hydrogen. Thus investigating the effect of hydrogen on the materials chemistry is overdue and the subject of this thesis.

This chapter will summarise the background knowledge to explain the context for the research described in this thesis. First nuclear power will be introduced, followed by discussion of the different types of nuclear reactor and nuclear fuels. Then, the nuclear fuel cycle for uranium oxide will be described. This will be followed by a broad overview of the whole uranium oxygen system. An overview of the behaviour of hydrogen in other oxide materials will be given, before, finally the detailed objectives of this thesis are set out. A detailed discussion of the relevant literature for UO_2, hydrogen and the interaction of hydrogen with different defects in UO_2 can be found at the beginning of the appropriate chapters.

1.1 Nuclear Power

Nuclear power refers to the process of converting the heat of nuclear fission into electrical power. The fission process is where the nucleus of an atom splits into smaller fragments and a small amount of mass is converted into energy. The radioactive decay of a nucleus is a natural form of nuclear fission.

Nuclear fission was first demonstrated by Otto Hahn and Fritz Strassmann in 1938 [1]. This discovery coincided with the start of World War II, which led to a vast research effort to exploit and harness the power of nuclear fission. This was successfully done by the USA in the Manhattan project. After the Second World War the development of nuclear weapons continued, leading to an arms race between the USA and the Soviet Union, a key component of the Cold War.

As a result of developing nuclear weapons, a large number of the other technologies were acquired. This included the realisation that it would be possible to harness the power of the nuclear bomb to generate power. The 1950s and 1960s

saw the development of nuclear reactors. The first nuclear reactor to produce electricity was the Experimental Breeder reactor in December 1951, 18 miles southeast of Arco, Idaho. Commercial nuclear power would not become available for another nine years. The first commercial reactor, designed by Westinghouse, was operational for 32 years from 1960 until 1992 [2].

Towards the end of the 1970s nuclear power and research into nuclear materials had fallen into a decline [3]. This decline was, in part, due to growing public concern over the safety of nuclear technologies. Incidents such as the Three Mile Island accident in 1979 and the Chernobyl disaster in 1986 helped turn public opinion away from nuclear power.

More recently, there has been a nuclear renaissance. An increased awareness of issues, such as CO_2 emissions, diminishing fossil fuel supplies and ensuring a secure energy supply has led to renewed interest in nuclear power [4]. However, this renaissance has been set back by the Fukushima Daiichi nuclear disaster, which caused the public to once again question the safety of nuclear power. The public outcry was most evident in Germany, where there were large scale protests [5]. In response to these protests the German government announced a reversal of its policy to maintain its nuclear plants and instead promised to close them by 2022 [6]. Despite this, there are around 440 nuclear reactors operating in 31 countries, providing approximately 11% of global energy requirements [7].

1.2 Nuclear Reactors

The evolution of nuclear reactors can be divided into four generations (Figure 1.1). There are four main types of nuclear reactor in operation today, all of which come from generation II or III: the pressurised water reactor (PWR) (Figure 1.2a), the

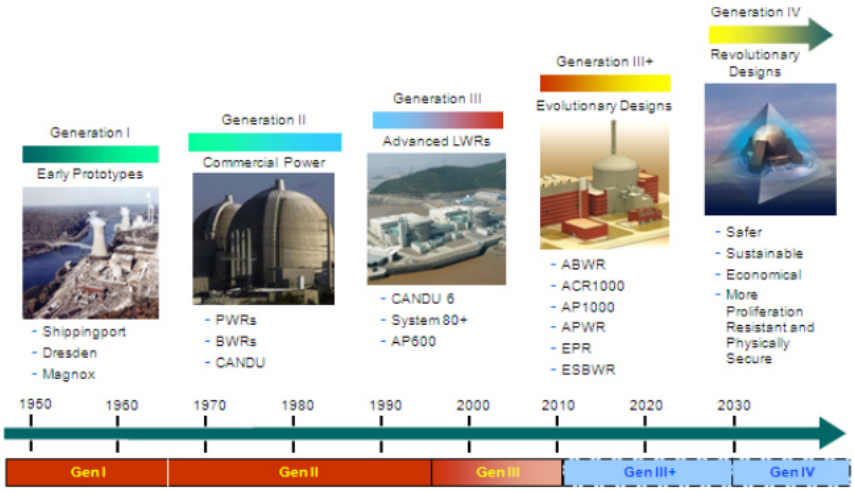

Figure 1.1: Evolution of nuclear power plants designs [8].

boiling water reactor (BWR) (Figure 1.2b), the pressured heavy water reactor (PHWR/Candu) (Figure 1.2c) and the advanced gas cooled reactor (AGR) (Figure 1.2d). Generation III+ are improvements to the current generation III reactors and generation IV are new reactor designs, possibly using different fuel materials, such UO_2 particles in a prism [9].

1.2.1 Reactor Operation

Nuclear reactors operate on the same principles as conventional fossil fuel power stations. Heat is used to convert water into steam and drive a turbine. All reactors have the same components: the fuel, a moderator, control rods, coolant, a pressure vessel, a steam generator and some form of containment [10]. The fuel is usually uranium based, either as UO_2 or U metal, though mixed oxide fuels of Pu and U are possible. The different types of nuclear fuel will be discussed more in Section 1.3.

In order to be able to harness the fission process to generate energy, the rate of fission needs to be increased in a controlled manner. This is achieved by using neutrons to split a nucleus, and for uranium this results in additional neutrons being released causing a chain reaction to occur. The chain reaction is moderated by the control rods, which are comprised of a neutron absorbing material. The control rods prevent the chain reaction from a nuclear reactor from becoming supercritical. The control rods can be inserted or removed from the reactor to regulate the power generation.

The purpose of the moderator is to reduce the speed of the neutrons released from the fission process. Neutrons released from a fission reaction are known as fast neutrons. Once they have been moderated, they are known as thermal neutrons. The moderator is typically water (either H_2O or D_2O) or graphite. The former ensures a there is a readily available source of hydrogen in close proximity to the fuel. There are reactors based on both types of neutrons, fast and thermal, with the vast majority of commercially active plants using thermal reactors.

The control rods determine the amount of heat produced from a reactor. They are typically made from cadmium, hafnium or boron as these materials are good neutron absorbers. To reduce the power output the control rods are inserted further into the reactor, this results in more neutrons being absorbed and less fission of the fuel occurring.

The coolant and reactor core are all contained in the pressure vessel which contains the extreme pressures present in the reactors. These can be up to 150 times atmospheric pressure [10]. Most nuclear reactor designs use two separate systems for the transfer of heat from the reactor to the steam generator. The exception is the BWR type which uses the cooling water to directly power the steam turbine. If there are two circuits to transfer heat, then the coolant will go to a heat exchanger where a second water circuit is used to generate steam. Regardless of the method used to generate steam, the steam produced drives a steam turbine and this is where the electricity is produced. Finally all reactors are contained within a meter thick concrete and steel structure. This is to protect the reactor from damage and reduce the effects of radiation on people who work at the power station.

1.2.2 Thermal Reactors

A thermal reactor is a reactor which has a moderator to slow the neutrons released from the fission process. The vast majority of commercial reactors in operation are thermal reactors [10]. Figure 1.2 shows the four main reactor designs. Both the PWR and PHWR reactor designs are very similar in how they function. The difference is that for the PWR reactor the core is completely surrounded by water and can only be accessed when the reactor is off-line and the coolant drained. For the PHWR the fuel elements are in individual pressure tubes, which allows for them to be isolated during reactor operation so that fuel can be replaced as the reactor is running. The BWR reactor is a simplified version of the PWR reactor, where the coolant is used to directly drive the steam turbine. This reduces construction costs, but does increase maintenance costs as radiological protection is needed during turbine maintenance. The AGR uses a different material for the moderator and coolant (Graphite and CO_2, respectively) but other than this it operates in the same manner as the PWR reactor.

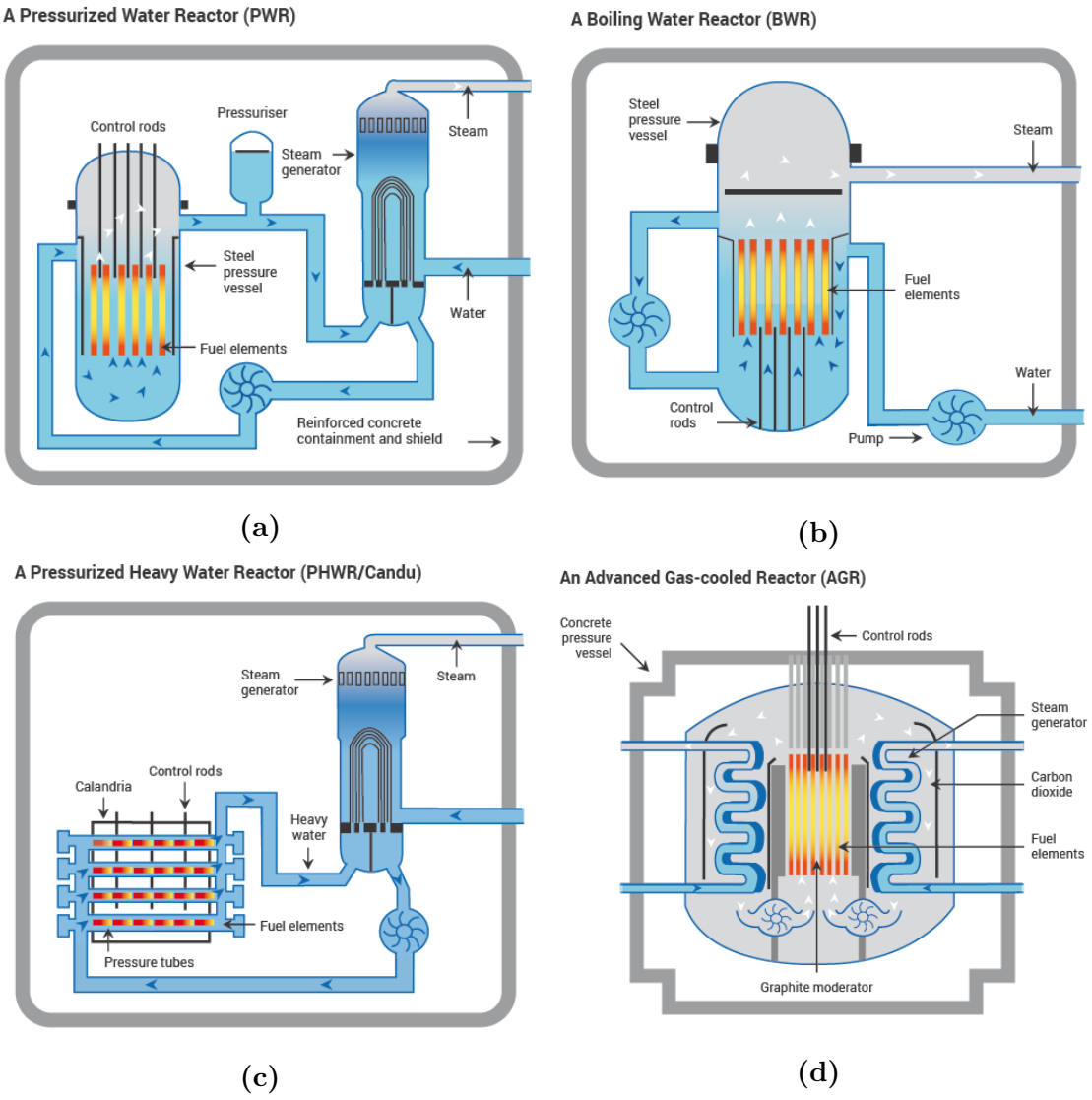

Figure 1.2: The four main types of nuclear reactor in operation today [10].

1.2.3 Fast Reactors

Fast neutron reactors are a reactor in which there is no moderator to slow the neutrons. The main fuel source is plutonium rather than uranium as fission using fast neutrons from uranium is inefficient, due to a low neutron cross section [11]. As plutonium does not occur naturally, reactors which use plutonium as the fuel source are initially filled with uranium and this is converted into plutonium. Fission of plutonium is sufficient using fast neutrons to maintain the chain reaction. As fission of plutonium also produces more neutrons than uranium per event, there are enough neutrons to convert more of the non-fissile U-238 isotope to Pu-239 and Pu-241. These isotopes of plutonium then undergo fission to produce neutrons in the same manner as U-235 in a thermal reactor. Fast neutron reactors can be divided into three different types; burners, breeders and iso-breeders. This is based on the amount of plutonium that the reactor produces. Burners consume more than produced, breeders produce more than consumed and iso-breeders produce the same amount of plutonium as consumed in operation. Burner reactors have been suggested as a means of disposal for ex-military plutonium. The future nuclear reactors are all likely to be fast reactors rather than thermal [12]. This is because a fast neutron reactor makes more efficient use of the fuel source than a thermal reactor by up to 60 times. Fast reactors have another advantage over thermal reactors which is their ability to fission actinides. This means that waste from a conventional reactor could be placed in a thermal reactor and the long-lived nuclides can be reduced to shorter lived nuclides. The latest generation of nuclear reactors, generation IV, are all likely to be based on fast neutrons for these reasons.

1.2.4 Future Nuclear Reactors

The latest generation of nuclear reactors, Generation IV, are being developed by the Generation IV International Forum (GIF) [9]. It is an international collective representing 13 countries; Argentina, Brazil, Canada, China, France, Japan, Russia, South Korea, South Africa, Switzerland, the UK, the USA and the EU. In 2002 GIF announced six reactor technologies that were to be developed as the future of nuclear power. These new reactors will be deployed between 2020 and 2030. The reactor designs were chosen based on being a clean, safe and cost-effective means of meeting increased energy demands sustainably. Also, the designs were chosen to be resistant to weapons proliferation and secure from terrorist attacks. The new reactor designs include gas-, lead- or sodium-cooled fast reactors, molten-salt reactors, super-critical water-cooled reactors and very high-temperature reactors.

1.3 Nuclear Fuels

The most commonly used nuclear fuel is uranium, normally in the oxide form UO_2 [10]. Uranium is composed of two different isotopes, U-235 and U-238. In a conventional thermal reactor it is the U-235 which is split to produce energy. The U-238 is non-fissile. Unfortunately natural uranium is only 0.7 % U-235 [13]. Therefore, less than 1 % of the uranium is available to produce energy. For the PWR and BWR reactor designs which use light water (H_2O) as the moderator, the percentage of U-235 needs to be increased. Nuclear fuel that has had the percentage of U-235 increased is known as enriched fuel. The reason for the enrichment is that light water absorbs some neutrons in addition to slowing them down. The percentage of U-235 is increased from 0.7 % to between 3 - 5 %.

If heavy water (D_2O) or graphite is used as the moderator, as is the case in the PHWR and AGR designs, then it is possible to use an unenriched uranium fuel source [10]. The four reactors discussed in Section 1.2 all use UO_2 as a fuel source. For all reactors, except the PHWR, this is enriched UO_2, even though the AGR uses a graphite moderator, so does not need an enriched fuel source. There is, however, a lesser degree of enrichment of 2.5 - 3.5 %, compared to the PWR and BWR at 3 - 5 % [10].

Some earlier nuclear reactors used uranium metal as a fuel source. The predecessor to the AGR reactor was the Magnox reactor, and this used unenriched uranium metal as the fuel source. The Magnox reactor was developed, in the UK, due to the USA having a virtual monopoly on uranium enrichment [2].

The future materials used as nuclear fuels are likely to be very different from the standard UO_2 currently used. The next generation of nuclear reactors will likely be fast rather than thermal reactors. Current fast reactors, which are more research orientated rather than commercial, use a variety of materials as fuels sources ranging from more conventional metal and oxide, to carbide and nitride. These are either purely uranium based or a mixture of uranium and plutonium, *e.g.* UC, UC_2, U_2C_3 and (U, Pu)C [14]. For the generation IV reactors being developed, some fuels are even more exotic, such as UF in salt [9].

1.4 The Nuclear Fuel Cycle

The nuclear fuel cycle refers to all the processes involved in the production of electricity from nuclear fuels, from mining to reprocessing and waste storage. The nuclear fuel cycle can be broken down into three separate phases: the front end, power generation and the back end. This is shown schematically in Figure 1.3.

The front end, or first phase, refers to the process involved in the production of nuclear fuel. This starts with the mining of uranium ore, which is then milled, converting it into U_3O_8, sometimes known as yellowcake. The waste ore from this process or tailings contains most of the radioactivity and waste material from the mining stage. Tailings need to be properly disposed of due to their high levels of radioactive material, though the quantity and lifetime of the radionuclides present is shorter than the original ore [15]. It is not possible to use U_3O_8 as a nuclear fuel, so it is refined into UO_2. At this stage, the uranium can be used in a reactor that does not require an enriched fuel source, such as the PHWR and AGR designs, or it

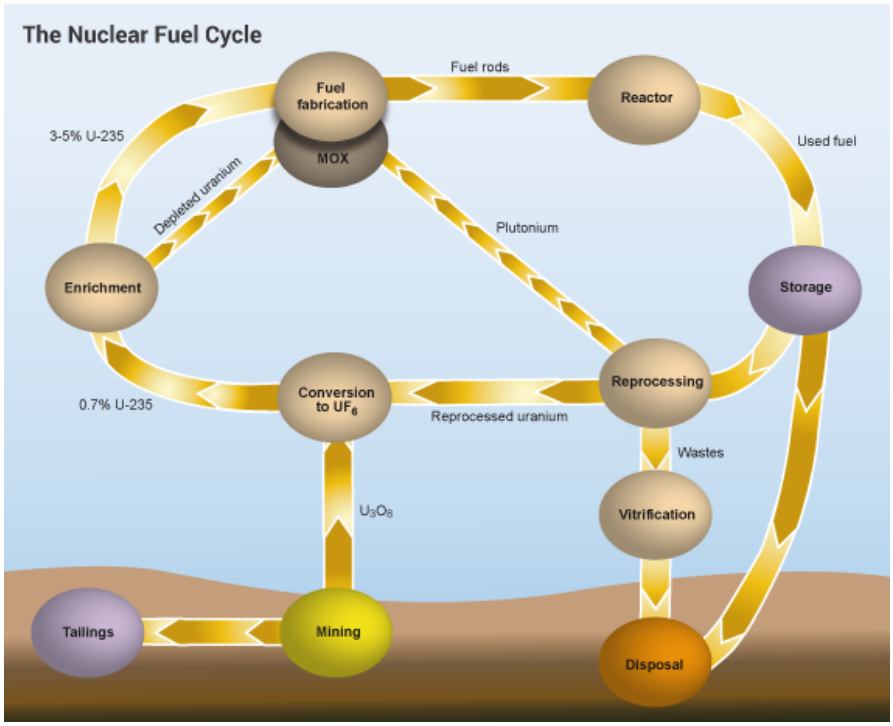

Figure 1.3: A schematic image of the complete nuclear fuel cycle [15].

can be converted into UF_6 and sent to an enrichment plant. Most uranium is sent to the enrichment plant, where the two different isotopes of uranium are separated in centrifuges. After the enrichment process, the UF_6 is then converted back into UO_2. The final stage of the front end is the fuel fabrication stage. Pressed pellets of UO_2 are sintered at high temperatures (1400 - 1750 °C), usually in an argon/hydrogen atmosphere [15, 16].

The second stage of the nuclear fuel cycle is power generation. This is when the fuel pellet is placed in the reactor and used to generate electricity.

The final stage of the nuclear fuel cycle is the back end. This, is where spent nuclear fuel is either reprocessed or prepared for disposal in long-term storage. Used nuclear fuel still contains the vast majority of the original uranium, approximately 96 %, though the U-235 content is less than 1 %. The rest of the fuel is comprised of plutonium (1 %) and high level radioactive waste (3 %) [15]. The spent fuel can either be reprocessed into enriched UO_2, or converted into a mixed oxide fuel (MOX). MOX fuels combine plutonium and uranium, using the plutonium to substitute for the U-235.

A future use for spent fuels would be as a fuel source for a fast neutron reactor. This has the advantage that there would be much less waste from a thermal reactor. Any spent fuel stored would be useful as a fuel source for future fast reactors.

The very last stage of the nuclear fuel cycle is disposal. This is where used fuel containing high-level radioactive waste is incorporated into borosilicate glass placed into a stainless steel container. These containers are currently placed into long term storage, rather than being disposed of completely. This is for two reasons: firstly, the total volume of waste produced is not large and secondly, the spent fuel represents a significant energy resource which could later be harnessed, *e.g.* in generation IV fast neutron reactors.

1.5 The Uranium-Oxygen System

UO_2 has the lowest oxygen content of the isolatable uranium oxides, the upper oxygen limit is represented by UO_3 [17–19]. Between these two limits exist a range of different oxides in which uranium is present in a variety of oxidation states, U^{4+}, U^{5+} and U^{6+}, as well as a number of polymorphs. This affinity for additional oxygen, coupled with the range of oxidation states which uranium can readily adopt (U^{4+} - U^{6+}), gives rise to a complex family of oxides, existing between the limits of UO_2 and UO_3 [19]. Shown in Figure 1.4a is the uranium oxide phase diagram [19] formed as a function of the oxygen/uranium ratio and temperature. Figure 1.4b shows how the uranium/oxygen phase diagram varies when pressure is included.

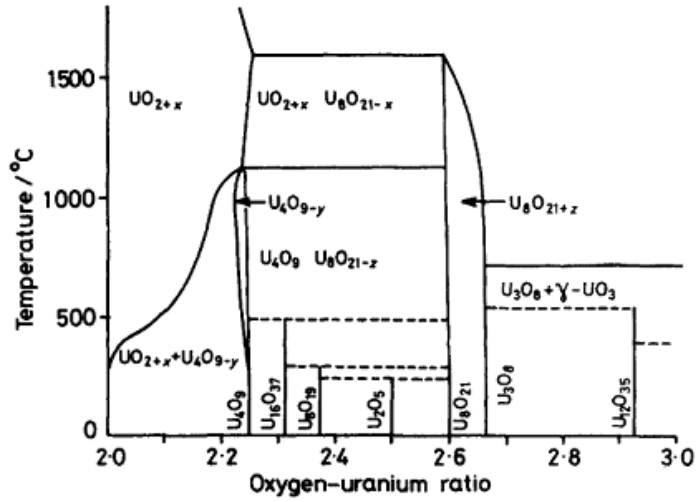

(a)

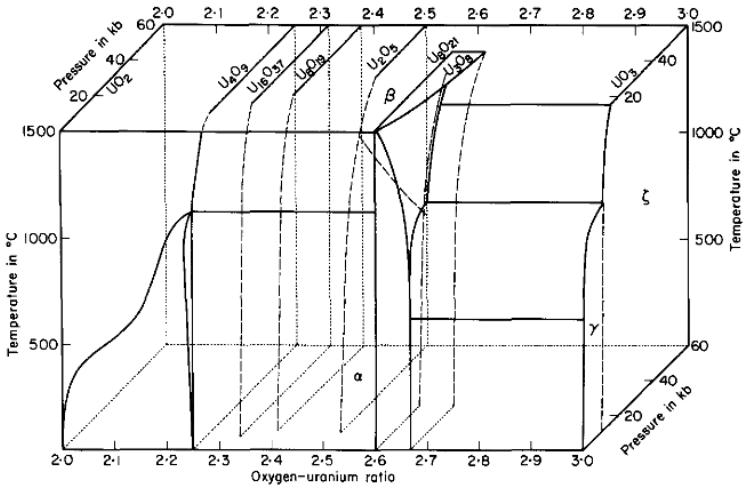

(b)

Figure 1.4: Phase diagram of the binary uranium/oxygen system, for compositions in the range UO_2 - UO_3. Figure 1.4a: oxygen/uranium ratio as a function of temperature; Figure 1.4b: oxygen/uranium ratio as a function of temperature and pressure [19].

There are two main classes of structures for uranium oxides: fluorite and layered. The type of structure is determined by the oxygen/uranium (O/U) ratio. When O/U ≤ 2.5, *e.g.* UO_2, U_4O_9 and U_3O_7, a fluorite-type structure is adopted. For higher oxides, where O/U ≥ 2.5, *e.g.* U_3O_8 and UO_3 a layered structure is preferred. The transformation between these two structural types occurs at an oxygen/uranium ratio of 2.5 (U_2O_5). U_2O_5 is reported to have a range of polymorphs with some fluorite based and others layered [20]. The most well-studied of all the uranium oxides is UO_2, which comes from the predominance of UO_2 as a commercial nuclear fuel [18, 20–37], as well as concerns over the formation of uranium hydride at UO_2/U metal interfaces [38–44].

1.5.1 Fluorite Based Uranium Oxides

For the fluorite-based oxides, the additional oxygen is initially incorporated as point defects and once a high enough defect concentration is reached defect clustering starts to occur. There have been a wide range of defect clusters proposed, both experimentally and theoretically, from the 2:2:2 Willis cluster [45–47], to a variety of split di-, tri- and quad- interstitial clusters and a range of cuboctahedral defects [26, 48]. There is still considerable debate in the literature over the nature of the defect-clustering scheme that occurs. This is possibly best characterised by the discrepancy between experiment and theory over the appearance of the Willis Cluster. The Willis cluster has been proposed experimentally, but subsequent theoretical studies found isolated Willis clusters to be energetically unstable with respect to a split di-interstitial [24, 49]. More recently, Brincat *et al.* [21] found edge-sharing 2:2:2 Willis clusters in UO_{2+x}, with composition $0.125 < x < 0.25$, to be stable. Below $x = 0.125$ the clusters were unstable and relaxed to split di-interstitial clusters, demonstrating that the oxygen stoichiometry has a significant impact on cluster structure. A more detailed discussion of the different types of oxygen defect clustering in UO_{2+x} can be found in Chapter 7.

1.5.2 Layered Based Uranium Oxides

For the higher uranium oxides, there is by contrast, much less fundamental research. However, in recent years there has been a growing body of research into the higher oxides [18, 20, 22, 50–52]. As noted above, once the uranium oxygen ratio reaches 2.5 the structure type transfers from being fluorite based to layered. The layered uranium oxide structures display a large range of polymorphism, with multiple different phases reported for each stoichiometry. The non-stoichiometric behaviour shown by the fluorite-based uranium oxides, (Figure 1.4), is also evident for the layered structures, especially for the trioxide. Cornman [53] reported difficulties in achieving stoichiometric samples, with the U/O ratio ranging from 3.03 - 3.07. Girgis [54] reported oxygen/uranium ratios of 2.97 - 3.00 for six different polymorphs of UO_3, suggesting the presence of uranium interstitials or oxygen vacancies. As the oxygen content increases, from 2.5 to 3, there is also an increase in the number of reported different polymorphs. Table 1.1 summarises the reported literature structures of uranium oxides, with a U/O ratio ≥ 2.5.

Table 1.1: Summary of reported uranium oxide phases with a stoichiometry of $UO_{2.5}$ or greater. † Fluorite based U_2O_5 phases. ‡ Proposed structural symmetry used by Johnson [55].

Stoichiometry	Phase	Symmetry	Space Group	Reference
U_2O_5	α-U_2O_5†	-	-	[19]
	β-U_2O_5†	Hexagonal	-	[19]
	γ-U_2O_5†	Monoclinic	-	[19]
	δ-U_2O_5	Orthorhombic	*Pnma*	[56]
U_3O_8	α-U_3O_8	Orthorhombic	*Amm2*	[57]
		Orthorhombic	*C222*	[58]
	β-U_3O_8	Orthorhombic	*CmCm*	[59]
		Orthorhombic	$P2_1/m$	[60]
	γ-U_3O_8	Hexagonal	*P-62m*	[36]
UO_3	α-	Hexagonal	*P-3m1*	[61]
		Orthorhombic	*C2mm*	[62]
		Orthorhombic	*C2*	[18]
		Orthorhombic	*C222*	[63]
	β-UO_3	Monoclinic	$P2_1$	[64]
	γ-UO_3	Tetragonal	$I4_1$	[65]
		Orthorhombic	*Fddd*	[65]
	δ-UO_3	Cubic	*Pm-3m*	[66]
	η-UO_3	Orthorhombic	$P2_12_12_1$	[67]
	ϵ-UO_3	Triclinic‡	-	[55, 68]
	ζ-UO_3	Amorphous	-	[53, 54]

1.5.2.1 U_2O_5

As U_2O_5 is the transitional stoichiometry between the fluorite and layered structural types, reported structures include both fluorite [19] (α-, β-, γ- U_2O_5) and layered [56] (δ-U_2O_5) structures. Since the work of Hoekstra [69] and Kovba [56] there have been no further experimental structural investigations of U_2O_5. For the fluorite-based structures, this means there is a lack of structural information available, which also hampers any theoretical research on the structural and electronic properties. For δ-U_2O_5 there is structural data available and there are a limited number of computational studies on its properties [22, 50]. There are two possible types of uranium charge compositions in U_2O_5. The first is where there is a mixture of U^{4+}/U^{6+} [70], although more recent work has suggested the presence of U^{5+} [52]. The presence of U^{5+} is also further supported by the computational study of Brincat *et al.*[22], which found only U^{5+} and no mixed U^{4+}/U^{6+}. One of the reasons for the lack of experimental data for U_2O_5 is that it is thermodynamically unstable with respect to U_3O_8 [50], and therefore difficult to synthesise experimentally.

1.5.2.2 U_3O_8

U_3O_8 represents the first isolatable layered uranium oxide. This is because U_3O_8 is the kinetic oxidation product, whilst UO_3 is the thermodynamic oxidation product [51, 65]. Depending upon conditions other uranium oxides will either oxidise or disproportionate to UO_2 [71] and U_3O_8 over time. It is also possible to form U_3O_8 by the reduction of UO_3 at high temperatures. U_3O_8 is the first uranium oxide found in the nuclear fuel cycle, as this is the form that uranium is mined, before conversion to UO_2. The formation of U_3O_8 is of concern both during reactor operation and long-term spent waste fuel storage, as the formation of U_3O_8 from UO_2 is accompanied by a volume increase of approximately 36 % [72]. Therefore, U_3O_8 has been the subject of a number of studies examining its electronic, structural and thermodynamic properties [19, 36, 57–59, 69, 73–85], in addition to a number of theoretical studies [22, 50, 71, 86–89], as a result of its kinetic stability and importance to the nuclear fuel cycle.

There are five different polymorphs found in the literature [36, 57–60] for U_3O_8, as detailed in Table 1.1. The phase formed is dependent on the synthesis conditions. α-U_3O_8 is the most common phase formed under standard conditions, whereas β-U_3O_8 is the high-temperature phase and γ-U_3O_8 is the high-pressure phase [22].

U_3O_8 is a mixed-valence oxide, with two possible uranium charge configurations: either $1U^{4+}/2U^{6+}$ or $2U^{5+}/1U^{6+}$. Earlier experimental work suggests that the $1U^{4+}/2U^{6+}$ is the correct configuration [70, 90], whilst more recent studies suggest $2U^{5+}/1U^{6+}$ [52, 84]. Computational studies suggest an average charge of $U^{5.33+}$ [88, 91]; however, more recent DFT calculations support the $2U^{5+}/1U^{6+}$ configuration [22, 71, 89].

Whilst U_3O_8 has been the subject of a number of studies examining its properties, there are limited experimental measurements of the band gap and no experimental reports of the bulk modulus of U_3O_8 in the literature. There is only one theoretical report of bulk moduli values for the polymorphs of U_3O_8, in the work of Brincat *et al.* [22]. The bulk modulus for all phases of U_3O_8 was predicted to be lower than that of UO_2, and there was an inverse relationship between the volume per uranium ion and the bulk modulus.

Only the band gap of α-U_3O_8 has been reported, and these are substantially different from each other. Scott *et al* [92] measured a value of 0.6±0.1 eV, whereas He *et al.* [85] found a much higher value of 1.81±0.03 eV. Table 1.2 lists the literature values of the band gap for *Amm2* α-U_3O_8. Similar to the large discrepancy in experimental values, there is also a wide range of theoretical values, depending on the DFT functional used. From these values, it is possible to see that the charge configurations of the uranium ions has a significant effect on the band gap. The work of Brincat *et al.* [22] suggests that samples of He and Scott were in different charge configurations, as this would explain the large difference between the two measurements. The reason for the different charge states observed could due to differences in synthesis methodologies.

What is clear is that this is an area of research which needs more work, in order to definitively determine the charge configuration, band gaps and other properties of interest (*e.g.* bulk modulus) of not just *Amm2* α-U_3O_8 but all phases of U_3O_8.

Table 1.2: Experimental and theoretical literature values for the band gap of *Amm2* α-U_3O_8.

Method	U Charge Configuration	Band Gap (eV)	Reference
Experiment	-	0.6±0.1	[92]
Experiment	-	1.81±0.03	[85]
LDA+U	$2U^{5+}/1U^{6+}$	2.43	[85]
PBE+U	$1U^{4+}/2U^{6+}$	0.71	[22]
PBE+U	$2U^{5+}/1U^{6+}$	2.05	[22]
PW91+U	$2U^{5+}/1U^{6+}$	0.63	[89]
PBE	$3U^{5.33+}$	2.20	[88]
HSE	$2U^{5+}/1U^{6+}$	0.80	[71]
PBE+U	$2U^{5+}/1U^{6+}$	1.20	[71]

1.5.2.3 UO_3

Uranium trioxide (UO_3), represents the upper limit of uranium oxidation. At this stoichiometry, all of the uranium ions have been oxidised from U^{4+} to U^{6+}, and therefore all of the valence electrons have been removed. As seen in Table 1.1, UO_3 displays the largest number of polymorphs of all the uranium oxides. Understanding the properties of UO_3 is important, as UO_3 is the thermodynamic oxidation product for the uranium-oxygen system [51, 65]. This means that, given enough time and the correct conditions, eventually all uranium oxides will convert to UO_3.

Understanding the properties of UO_3 is not just of importance for the nuclear fuel cycle, to ensure materials safety and reactor integrity, but also has potential applications in the field of "nuclear forensics", as the polymorph of UO_3 formed is indicative of the synthesis conditions used [93].

Whilst UO_3 is certainly a much simpler material to simulate computationally, compared to the lower uranium oxides, due to only having U^{6+} and no f-electrons, experimentally it very difficult to produce stoichiometric UO_3 samples. This is because, in addition to the previously-mentioned extensive non-stoichiometry, UO_3 compounds are well known to form hydrolysis and hydration products, even under ambient conditions [94–96]. To further compound the difficulty, it is difficult to produce some trioxide samples without also forming others [66, 93]. As a result, the majority of studies on the different phases of UO_3 have focused on structural determination. However, there are a few phases which have been studied to determine electronic [54, 85, 97, 98], optical [93] and thermodynamic [99] properties. As the most stable of all the trioxide phases, or of any uranium oxide [74], γ-UO_3 is the most extensively studied of the trioxide phases.

Brincat *et al.*[18] studied five phases of UO_3 (α-, β-, γ-, δ and η-) σ- and ζ-UO_3 were not considered due to insufficient structural data. In UO_3, the U^{6+} ion is found in a range of co-ordination environments. One of the unique environments found in some UO_3 phases (β-, γ- and η-) at this stoichiometry is the uranyl bond, due to the presence of shorter axial bonds similar to those found in the uranyl (UO_2^{2+}) cation. It was predicted that phases which contained uranyl bonds had a smaller band gap and lower bulk modulus (<100 GPa), compared to those without uranyl bonds.

As with U_3O_8, there is a need for more research into the different phases of UO_3 to build a greater understanding of the fundamental properties of these materials, which would aid in the development of improved methodologies for the processing and long term storage of spent nuclear material.

1.6 Hydrogen in Oxides

As there are only a limited number of studies in the literature concerning the nature of hydrogen in UO_2, this section will briefly review the wider literature available for hydrogen in oxide materials. In addition the available literature for the interaction of H_2O with MO_2 (M = Ce, U, Pu) oxide surfaces will also be discussed, as the adsorption and dissociation of water to the surfaces of oxides has been proposed as a route for hydrogen incorporation in the UO_2 lattice.

Oxide materials find use in a wide range of technological applications including: battery materials [100], catalysts [101], electrochemical water splitting [102], energy storage [103], gas sensors [104], hydrogen separation membranes [105], mixed proton-electron conductors [106], hydrogen (deuterium, tritium) permeation barriers [107], solid oxide fuel cells [108] and nuclear fuels [109]. For all these applications the defect properties are essential in determining the material behaviour. The presence of hydrogen in oxide materials is generally overlooked, but can play a dominant role in determining properties and ultimately of the device performance [110].

Hydrogen in oxide materials can be broadly classified into two categories: desirable or undesirable. In applications such as mixed proton-electron conductors and solid oxide fuel cells, the presence of hydrogen is essential for the device performance. However, there are many other applications where the presence of hydrogen is undesirable, as it leads to embrittlement [111], device degradation [112] or the formation of other phases, such as pyrophoric hydride materials [113, 114].

Regardless of whether the presence of hydrogen is desired or not, before hydrogen can dissolve into an oxide lattice it first must interact with the oxide surface. This can result in the dissociation of H_2 via either a heterolytic or homolytic pathway, based on the redox activity of the oxide [115]. For a nonreducible oxide such as MgO [116, 117] or γ-Al_2O_3 [118], a heterolytic pathway is proposed due to the presence of M-H and O-H bands in the infra-red (IR) spectra, whereas for redox active oxides, such as TiO_2 [119] or CeO_2 [120, 121], a homolytic pathway is inferred due to the presence of only O-H bands in the IR spectrum.

However, recent theoretical work on CeO_2, has shown that it is possible to achieve the homolytic dissociation product via a heterolytic pathway [115]. The initial dissociation is heterolytic, caused by polarisation of the H-H bond as the hydrogen approaches the surface, resulting in M-H and O-H bonds. The hydrogen (in the M-H bond) then transfers to another oxygen atom, and the two electrons on the hydride transfer to metal ions. This is in contrast to the theoretical calculations of Reimers *et al.* [122], which showed for both ZnO and CeO_2 that hydrogen did not dissociate when in contact with the surface. The reason for the difference could be ascribed to the, experimentally observed low reactivity of pure ceria surfaces towards hydrogen [123].

Despite this inherently low reactivity towards hydrogen, it is possible to increase the reactivity of ceria. This is achieved by forming a mixed oxide with a more reactive oxide. Ga_2O_3 is far more reactive towards hydrogen than CeO_2 [123]. When

formed as a mixed oxide with ceria (75:25, Ce:Ga), a significant increase in the intensity of Ce^{3+} is observed, with no change of the Ga^{3+} oxidation state detectable upon exposure to hydrogen. As with CeO_2 forming a mixed oxide phase the reactivity of oxide surfaces can also be modified using dopants. In the case of ZnO, Be and Cu doping was shown to improve the adsorption of hydrogen to the $(000\bar{1})$ and $(10\bar{1}0)$ surfaces [104, 124].

In addition to changing the reactivity of an oxide, dopants can also be used to alter the solubility of hydrogen in an oxide. Altering the ratio of TiO_x/SiO_2, in TiO_x-MnO-SiO_2 results in a varying hydrogen content [125]. This also has the effect of changing the dominant dissolution mechanism from an incorporated hydroxyl to a free hydroxyl.

Whilst the use of dopants can be used to enhance the reactivity between oxide surfaces and hydrogen, for applications such as hydrogen sensors, this is not always desirable. There are many applications where the absorption of hydrogen is undesirable, as it leads to embrittlement [126, 127] or the formation of hydride phases [39, 40], which can exhibit pyrophoric behaviour [113]. This is particularity important in the nuclear fusion industry, where there are concerns over the loss of tritium from plasma degrading reactor integrity. As such there is considerable interest into hydrogen permeation barriers [111].

Hydrogen permeation barrier materials tend to be an undoped oxides, such as Al_2O_3 [107, 128], Cr_2O_3 [129], Er_2O_3 [128, 130], Y_2O_3 [131] and ZrO_2 [132]. There have also been some investigations of composite materials *e.g.* Er_2O_3/Cr_2O_3 [133]. The effectiveness of a material as a hydrogen permeation barrier is not just derived from the bulk materials, but is also dependent on the surface microstructure [131, 134]. Additionally, the formation of OH bonds in the oxide layer has been shown to help increase resistance to hydrogen diffusion through a $ZrO_2/Zr_{1.88}$ layer on zirconium hydride. Though at elevated temperatures hydrogen is rapidly removed from the zirconium oxide layer [135].

The solubility of hydrogen has been measured in a range of oxide materials, for both single-crystal and polycrystalline samples. In these measurements the solubility of hydrogen was greater in the polycrystalline samples, by an order of magnitude, suggesting that grain boundaries are important structural features where hydrogen can more easily dissolve and build up high local concentrations [42–44, 130, 136, 137]. This is an issue as grain boundaries present a break in an oxide layer which allows for hydrogen to more easily corrode and degrade materials below the oxide layer [40].

Another of the challenges in exploring hydrogen diffusion is determining the nature of the diffusing species. It is possible that the transport of hydrogen through an oxide results not just in a proton moving but also an electron. This generates a class of materials known as mixed proton-electron conductors, where the diffusion of a proton is accompanied by transport of an electron on the metal sites. An example of a mixed proton-electron conductor is CeO_2 [138]. In bulk stoichiometric CeO_2 DFT calculations have shown the preferred defect is the formation of a hydroxyl group accompanied by reduction of a Ce^{4+} to Ce^{3+} [139]. More recent calculations have also shown that this also occurs in PuO_2 [140], whereas a H^-/U^{5+} pair is the preferred defect in UO_2 [140, 141]. An additional layer of complexity to hydrogen diffusion is the nature of the crystal structure, which has been shown to influence the preferred direction of hydrogen diffusion in Al_2O_3 and Er_2O_3 [128]. This is where

hydrogen is diffusing parallel (favourable) or perpendicular (unfavourable) to the planes of Er_2O_3 units.

Recently, the interaction of atomic hydrogen with the PuO_2 (110) surface has been studied using DFT (PBE+U) calculations. H_2 was found to only weakly absorb to the surface, whereas H atoms are strongly bound to surface oxygen [142]. The energy barrier to hydrogen dissociation was calculated to be 0.48 eV, but there is a significantly favourable absorption energy of 5.147 eV, making the process favourable. However, the (110) surface shows a significant barrier to hydrogen diffusing to subsurface layers of 2.15 eV [143]. This suggests that pristine (110) surfaces could act as a barrier to hydrogen diffusion into the bulk oxide.

Modelling or measuring the properties of hydrogen in oxides remains a challenging but fundamentally important research area, as there are a vast multitude of applications which require an improved understanding of the behaviour of dissolved hydrogen ranging from materials safety to energy materials.

1.6.1 The Interaction of Water and MO_2 (M = Ce, U, Pu)

Whilst the interaction of hydrogen with the surfaces of UO_2 and other actinide and lanthanide oxides has not been the focus of significant research effort, the interaction of water with actinide/lanthanide oxide surfaces has been the subject of many studies [101, 144–150]. Additionally, the interaction of water with UO_2 specifically has been the subject of extensive investigation [151–155], mainly due to concerns over water ingress into a failed, spent waste container in a long-term waste repository [156].

The interaction of water with the surfaces of actinide/lanthanide oxides is not just a concern for long-term waste storage, but has also been proposed as a method for the generation of H_2 and O_2 [157]. Heating water in the presence of UO_2 would result in the dissociation of H_2O and oxidation of UO_2 with the production of H_2.

This would be a heavily surface dependent process, and would require an understanding of how water interacts with the various surfaces of UO_2. For the low index surfaces of stoichiometric MO_2 oxides ((100), (110), (111)) there is a variation in the nature of the water absorption, *i.e.* whether it is dissociative or molecular in nature.

For the pristine (100) and (110) surfaces there is a clear preference for dissociative absorption regardless of metal cation (Ce, U, Pu) [101, 148], whereas the (111) surface shows no preference for either dissociative or molecular absorption [101, 147–149] and a mix of dissociative and molecular absorption occurs. The strength of the interaction between the water oxygen ion and surface cation and the value of the oxide lattice constant affects the strength and structure of the H-bonding network, as well as the electrostatic repulsion between charged dissociated moieties, which determine the degree of dissociation which occurs [149].

When the surfaces are defective, the dissociative absorption of water is favourable at all Miller indices reported, as this results in the regeneration of the stoichiometric surface [101, 147, 148, 152, 155]. The dissociative absorption which occurs on the defective surfaces also results in the generation of hydrogen [152, 153]. The presence of hydrogen has also been shown to reduce the degree of oxidation that occurs when UO_2 is exposed to steam [158]. Therefore, the generation of hydrogen by restoring defective surfaces may reduce the rate of oxidation and prevent further oxidation to higher oxides.

UO_2 Spent Fuel Storage

One of the proposed routes for dealing with, highly radioactive, spent nuclear fuel is a long-term waste repository. This is where the spent fuel containing the radioactive species is stored underground for a sufficient length of time that the radioactive material decays away to safe levels. The ingress of water could lead to the radiolytic dissolution of the fuel matrix and release of high level radioactive isotopes into the ground water. The radiolytic fission of the water in contact with the surface of UO_2 leads to the production of a large range of reactive reducing (e^-_{aq}, $H^\bullet$, H_2) and oxidising species ($OH^\bullet$, H_2O_2, $HO^\bullet_2$, $O^{\bullet-}_2$, $CO^{\bullet-}_3$, H^+) [159–164]. As illustrated in Figure 1.5, these reactive species result in the oxidation of surface U^{4+} to U^{6+} and the formation of the uranyl ion (UO^{2+}_2), which has significantly greater solubility in water than UO_2 [165]. The dissolution of UO_2 in this way would also result in the release of the stored radioactive nuclides in the fuel matrix into the groundwater.

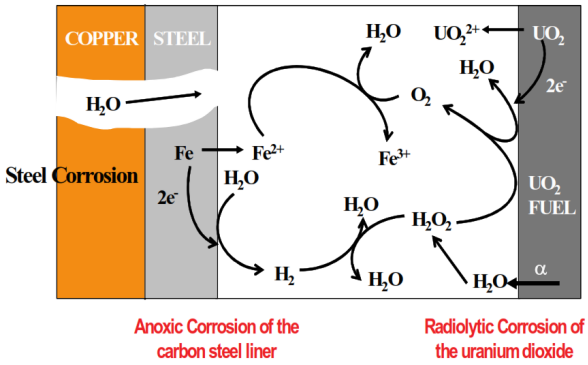

Figure 1.5: A schematic illustration of the key chemical reactions anticipated in a failed, ground water flooded waste container [166].

Whilst a large array of oxidising species are produced from the radiolysis of water, H_2O_2 has been shown to be the only oxidant of real significance [165]. The oxidation of UO_2 by H_2O_2 is catalysed by the inclusion of Pd [167]. Pd is used to simulate the composition of a spent nuclear fuel pellet, which will have other metal ions present in addition to uranium. Additionally, the oxidative dissolution of UO_2 is further enhanced by the presence of HCO^-_3 and CO^{2-}_3 [160, 162, 164, 168]. This enhancement to the dissolution occurs because the HCO^-_3 and CO^{2-}_3 ions prevent the build-up of U^{6+} on the surface of the fuel pellet.

One of the reducing species produced both from the corrosion of the steel container and the radiolysis of water is hydrogen. The presence of a hydrogen atmosphere has been shown to reduce or entirely inhibit the oxidation of the UO_2 pellet, depending on hydrogen pressure, the presence of noble metal particle inclusions and the concentration of other gas species [166, 169–172].

There is also some variation in the oxidative dissolution yield, the ratio between the amount of dissolved uranium and the amount of consumed H_2O_2, with the pellet composition [173]. These differences in oxidative yield have been shown to be due to the redox reactivity of the pellet used, and as the irradiation time increases this difference in oxidative dissolution yield decreases [174].

One further consideration that has not been extensively considered is the surface morphology and any cracks present in the pellet. However, a 2D model has been

proposed for how the redox conditions in cracks evolve over time [175]. The model shows that as time progresses the conditions in the cracks become more reducing than the surrounding environment, preventing corrosion from proceeding.

1.7 Aims of the Thesis

The radioactive nature of uranium oxides and the challenge in determining the behaviour of hydrogen experimentally make theoretical approaches attractive for studying hydrogen in uranium oxides. The aim of this thesis is to explore the behaviour of hydrogen in $UO_{2\pm x}$, in order to probe the structure, stability and transport of hydrogen in $UO_{2\pm x}$, making predictions of preferred defect structures and electronic properties.

The aims of this thesis are:

- Establish a single effective DFT approach for simulating:
  - Uranium dioxide.
  - Uranium dioxide containing hydrogen defects.
  - Uranium hydride.
- Use the chosen approach to evaluate how oxygen stoichiometry affects hydrogen incorporation.
- Calculate how hydrogen affects the structure and stability of oxygen defect clusters.
- Consider the size of the barriers to hydrogen transport through the oxide lattice.
- Develop a thermodynamic model to identify the most stable defects as a function of oxygen and hydrogen concentration.

The following chapter describes the DFT approach used and validation of the simulations used throughout the investigation. Results are then presented beginning with an assessment of different functionals for simulating UO_2 (Chapter 3), followed by an assessment of these functionals with hydrogen defects in UO_2 (Chapter 4) to determine the most appropriate functional for simulating hydrogen in UO_2. Having established the most suitable methodology this will then be used to explore how oxygen stoichiometry affects hydrogen behaviour (Chapter 5), the barriers to hydrogen transport in UO_2 (Chapter 6), how hydrogen affects the properties of oxygen defect clusters is explored in (Chapter 7), the suitability of the methodology to simulating UH_3 is also determined (Chapter 8), the data from the previous chapters is then used as the input for a thermodynamic model (Chapter 9). Each chapter will begin with a discussion of the relevant literature, followed by a presentation and discussion of results. Finally the thesis will conclude with a summary of the findings presented (Chapter 10), and will discuss the potential future directions for work building on this thesis.

2 Computational Methodology

In order to model a chemical system at the atomic level successfully, an accurate representation of the interactions between atoms is required. This can be achieved by using one of two theoretical approaches; classical or quantum mechanics. Each of these approaches makes approximations which balance the accuracy of the calculation with the time taken to get the result. For either of these two different theoretical approaches, there are range of different techniques which can be used depending on the nature of the problem being investigated. These include energy minimisation, which seeks to find the lowest energy configuration from a given starting configuration, molecular dynamics, where Newton's equations of motion are solved to determine the trajectories of ions in a system and Monte Carlo where random moves are generated and the result accepted based on how the energy of the system is affected.

In the classical mechanics approach, the interactions between atoms are described by a set of parametrised equations. The equations are derived by fitting to experimental or quantum mechanical data, for known properties such as lattice parameters or defect energies. However, as the ions are modelled as point charges, the electrons are not explicitly considered. This means that electronic redistribution is not possible, and electronic properties cannot be calculated. The advantage of being able to use classical mechanics to model a system is that a large system, numbering many hundreds of thousands of atoms, can be simulated with relative ease.

In contrast, quantum mechanical calculations calculate the properties of a system by explicitly considering the electrons (or electron density). This requires far less prior knowledge of the system being studied in comparison to classical mechanics. The drawback to this approach is that the calculation is far more computationally expensive and as a result the size of system that can be modelled is far smaller than with classical mechanics.

As an aim of this thesis is to explore the behaviour of hydrogen in UO_2, for which there is very little experimental data to derive potential models for classical simulations, it is sensible to start with a quantum mechanical approach for this problem.

This chapter is divided into three sections. The first covers the theoretical background, the second covers the different computational techniques and the final section covers the calculation of crystal properties.

2.1 Computational Theory

This section will describe the background theory and explain what needs to be considered to allow for calculation of materials properties.

2.1.1 Quantum Mechanics

The aim of quantum mechanics is to accurately describe the behaviour of a chemical system by solving the many-body Schrödinger equation. The time-independent form of the Schrödinger equation is shown in Equation 2.1,

$$\hat{H}\Psi = E\Psi \tag{2.1}$$

where $\hat{H}$ is the Hamiltonian operator, E is the total energy of the system and Ψ is the electronic wave function. The Hamiltonian operator is composed of the operators for the kinetic and potential energy of the nuclei and electrons, as described by Equation 2.2.

$$\hat{H} = \hat{T}_n + \hat{T}_e + \hat{V}_{nn} + \hat{V}_{ee} + \hat{V}_{ne} \tag{2.2}$$

where $\hat{T}_n$ and $\hat{V}_{nn}$ are the kinetic and potential nuclear operators, $\hat{T}_e$ and $\hat{V}_{ee}$ are the equivalent electronic operators and $\hat{V}_{ne}$ represents the nuclear-electron interaction.

One issue is that the $\hat{V}_{ne}$ term needs to be decoupled into a set of independent equations. This is addressed by the Born-Oppenheimer approximation [176], which allows the nuclear and electronic degrees of freedom to be decoupled. The Born-Oppenheimer approximation states that even though the forces acting on the nuclei and electrons are the same, due to the significant different in mass of the nuclei compared to the electron, the nuclei are effectively stationary compared to the electrons. The result of this approximation is that the nuclei can be considered to be fixed charges and therefore form part of the external potential. The Hamiltonian can then be redefined as shown by Equation 2.3.

$$\hat{H} = \hat{T}_e + \hat{V}_{ee} + \nu_{\text{ext}}\{(\mathbf{R}_i)\} \tag{2.3}$$

The Hamiltonian now considers an N electron system in an external potential, ν_{ext}, which is imposed by the configuration of the nuclear positions $\mathbf{R}_i$.

2.1.1.1 Density Functional Theory

Density functional theory (DFT) is one of the various electronic structure methods that currently exist, another example being the Hartree-Fock (HF) approach. In the HF approach, the multi-electron wave function is expressed as a Slater determinant of N single electron wave functions, and the full calculation of the N-electron wave function is performed [177]. Unlike HF, DFT uses single electron functions to calculate the electron density. The principle underpinning DFT is that there is a relationship between the total electronic energy and the electron density. The major advantage of using the electron density is that it reduces the dimensionality of the

problem from $4N$ degrees of freedom, of the electron spin-orbitals, to just three spatial coordinates. The reduction of dimensionality results in a solution being more computationally tractable.

The first attempts to use this approach were by Thomas and Fermi in 1927 [178, 179]. However, the exclusion of exchange and correlation effects made it too inaccurate to be of practical use for general calculations. Dirac modified this approach to include a local approximation for exchange in 1930 [180], though it would not be until the work of Hohenberg and Kohn in 1964 that a real breakthrough was made in the use of this approach to electronic structure calculations.

2.1.1.2 The Hohenberg-Kohn Theorems

The two theorems which form the basis of modern DFT were formulated by Hohenberg and Kohn in 1964 [181]. The first of these theorems state that the external potential (ν_{ext}) in the Hamiltonian (Equation 2.3) is a unique functional of the electron density (ρ(r)). This has the result that the full many-body ground state wave function (Ψ) is also a unique functional of ρ(r). Therefore, the ground and excited state properties of a given atomic system are uniquely determined by the electron density of that system. This allows for the total energy to be written as a function of the electron density:

$$E[\rho] = \int \rho(\mathbf{r})\nu_{\text{ext}}(\mathbf{r})d\mathbf{r} + F_{\text{HK}}[\rho] \tag{2.4}$$

The first term accounts for the interaction of the electron density with the external potential. The second of the Hohenberg-Kohn theorems states that the Hohenberg-Kohn functional, $\text{F}_{\text{HK}}[\rho]$, produces the lowest energy for a system when it is provided with the true ground state electron density. The Hohenberg-Kohn functional is composed of the kinetic energy ($\text{T}[\rho]$) and the total energy of the electron-electron interactions ($\text{E}_{\text{ee}}[\rho]$).

$$F_{\text{HK}}[\rho] = T[\rho] + E_{\text{ee}}[\rho] \tag{2.5}$$

The total electronic energy term ($\text{E}_{\text{ee}}[\rho]$) is defined as the sum of the electron-electron Coulomb repulsion ($\text{J}[\rho]$) and a non-classical contribution ($\text{E}_{\text{ncl}}[\rho]$), which accounts for the exchange and correlation contributions.

$$E_{\text{ee}}[\rho] = J[\rho] + E_{\text{ncl}}[\rho] \tag{2.6}$$

If all terms in the Hohenberg-Kohn functional are known exactly, it is possible to obtain the exact solution to the Schrödinger equation. However, whilst the classical contribution ($\text{J}[\rho]$) is well known, the kinetic energy, $\text{T}[\rho]$, and non-classical contribution, $\text{E}_{\text{ncl}}[\rho]$, are unknown contributions.

However, whilst the Hohenberg-Kohn theorems provide the foundation for DFT methods and show that in principle it is possible to solve the Schrödinger equation to obtain the ground state, they do not provide a method to locate a solution. The later work of Kohn and Sham built on the Hohenberg-Kohn theorems to provide a means to approximate the unknown functionals.

2.1.1.3 The Kohn-Sham Equations

The work of Kohn and Sham [182] provides a way of approximating the unknown quantities in the Hohenberg-Kohn functional. Previous attempts to calculate the electronic structure were too inaccurate because they tried to calculate the kinetic energy explicitly as a function of the position-space electron density. The difficulty of using this approach is that the kinetic energy is dependent on the electron velocities, and consequently has a complicated relationship with the position-space electron density, which only contains the spatial distribution of the electrons.

In the Kohn-Sham approach the interacting many-electron system is replaced by a system of non-interacting electrons in an effective potential (ν_{ref}), due to the other electrons, Equation 2.7.

$$\hat{H}_{\text{ref}} = \sum_{i=1}^{N}[-\frac{1}{2}\nabla_i^2 + \nu_{\text{ref}}(r_i)] \tag{2.7}$$

The non-interacting reference system is defined so that it has an identical electron density to the real system as defined in Equation 2.8. The advantage of using the non-interacting electron system, is this removes the electron-electron interactions in the reference system. The solution can then be exactly represented by a Slater determinant comprised of single electron functions (ϕ_i), known as Kohn-Sham orbitals, which give the electron density of the system (ρ_0).

$$\rho_0(\mathbf{r}) = \sum_{i}^{N}|\phi_i(\mathbf{r})|^2 \tag{2.8}$$

The advantage of the Kohn-Sham approach, to previous approaches, is that as much of the energy as possible is calculated explicitly and the rest is then approximated. The contribution from the non-interacting reference system is calculated exactly, Equation 2.9.

$$T_{\text{ref}} = -\frac{1}{2}\sum_{i}^{N}\int \phi_i^*\nabla^2\phi_i d\tau \tag{2.9}$$

The exactly known part of the kinetic energy can be incorporated into the Equation for the total energy for the real system of interacting electrons (Equation 2.11). The unknown part of the kinetic energy is then incorporated into the exchange-correlation functional, $\text{E}_{\text{XC}}[\rho]$, Equation 2.10.

$$E_{\text{XC}}[\rho] = (T[\rho] - T_{\text{ref}}[\rho]) + (E_{\text{ee}} - J[\rho]) = T_{\text{Corr}}[\rho] + E_{\text{ncl}}[\rho] \tag{2.10}$$

The exchange-correlation functional replaces the non-classical contribution in Equation 2.6. The $\text{E}_{\text{XC}}[\rho]$ term contains all the unknown components of the electronic energy: the exchange and correlation effects and the remaining part of the kinetic energy. This gives the Kohn-Sham energy system as defined in Equation 2.11.

$$E_{\text{KS}}[\rho] = \int \rho(\mathbf{r})\nu_{\text{ref}}(\mathbf{r})d\mathbf{r} + T_{\text{ref}}[\rho] + J[\rho] + E_{\text{XC}}[\rho] \tag{2.11}$$

As the Kohn-Sham system is composed of non-interacting electrons, the solutions can be found independently (Equation 2.12).

$$[-\frac{1}{2}\nabla_i^2 + \nu_{\text{ext}}(\mathbf{r}) + J[\rho] + V_{\text{XC}}(\mathbf{r})]\phi_i = \epsilon_i\phi_i \tag{2.12}$$

The first term is the kinetic energy operator, ν_{ext} is the external potential, the third term is the Coulomb interaction and, finally, $\text{V}_{\text{XC}}(\mathbf{r})$ is the exchange-correlation potential. The final component of the Kohn-Sham equation is to find a reference potential which will produce a non-interacting electron density which matches the electron density of the real system.

For any system, when a trial density ($\bar{\rho}$) is used the calculated energy will always be greater than or equal to the real ground state energy (E_0) (Equation 2.13). The only condition under which $\text{E}[\bar{\rho}]$ will equal E_0 is when the trail density matches the electron density of the real system.

$$E[\bar{\rho}] \geq E_0 \tag{2.13}$$

By comparing equation 2.12 with the one-electron Kohn-Sham operator (Equation 2.14).

$$\hat{f}_{\text{KS}} = -\frac{1}{2}\nabla^2 + \nu_{\text{ref}}(\mathbf{r}) \tag{2.14}$$

It is possible to write an expression for the reference potential in terms of the interacting system as shown in Equation 2.15

$$\nu_{\text{ref}}(\mathbf{r}) = \nu_{\text{ext}}(\mathbf{r}) + J[\rho] + V_{\text{XC}}(\mathbf{r}) \tag{2.15}$$

Where the exchange-correlation potential, which is defined as the functional derivative of E_{XC} with respect to the electron density, ρ, is given by

$$V_{\text{XC}}(\mathbf{r}) = \frac{\delta E_{\text{XC}}}{\delta\rho(\mathbf{r})} \tag{2.16}$$

In order to solve the Kohn-Sham equations, a self-consistent approach is used. An initial trial electron density in used (Equation 2.12) to generate a set of Kohn-Sham orbitals, which are then used to generate an improved representation of the electron density. The improved electron density is then compared to the input density, and the process is repeated until the input density matches the output density. The electronic energy of the system can then be calculated using Equation 2.11.

All of the uncertainty in the Kohn-Sham Equations is combined into the exchange-correlation functional. The final part of calculating the electronic structure is to choose an exchange correlation functional to approximate this contribution to the total electronic energy.

2.1.1.4 Exchange-Correlation Functionals

As all of the uncertainty with the Kohn-Sham approach has been collected into the exchange-correlation functional, all that is required is to determine a functional which best approximates the exchange and correlation interactions. However, exact functionals are only known for the free electron gas. There are two main different ways to build the exchange-correlation functional, either semi-empirical methods (*e.g.* BLYP [183]) or purely theoretically (*e.g.* PBE, PBEsol [184, 185]). The functionals used in this work are based on the theoretical approach. Most available functionals are based on either the local density approximation (LDA) or the extension of LDA known as the generalised gradient approximation (GGA).

DFT functionals are classified by what is known as Jacob's ladder [186], with each rung representing a higher level of theory. The lowest rung represents LDA functionals and the second GGA. There are several rungs beyond GGA functionals which include additional terms to increase the accuracy of the calculations, at the cost of greater computational expense. This work uses the GGA functional PBE, as current higher level functionals have been shown to be impractical to simulation of uranium oxides [187] due to simulation time and limits on system size, therefore a brief summary of other functionals will be given followed by a more detailed description of the functionals used in this thesis.

The LDA approach is the simplest and uses the uniform electron gas to obtain E_{XC}. The drawback of this is that in order to accurately predict properties the electron density needs to vary slowly through space. This is typically suitable for metals but not for insulating systems (*e.g.* UO_2). Beyond LDA is the GGA approach which includes the first derivative of the electron density this allows for an improvement over LDA by allowing variation in electron density to be considered.

The first of the functional types beyond GGAs are meta-GGAs which include the second derivative of the electron density ($\nabla^2\rho_\sigma$) [188, 189] or the kinetic energy density (τ_σ) [190–194]. There are even some meta-GGAs which incorporate both $\nabla^2\rho_\sigma$ and τ_σ [195, 196]. There are now a wide variety of meta-GGA functionals available in the literature [191, 193, 197–202], which obey a varying number of known exact constraints [203–206].

The next rung on the ladder above meta-GGAs are hybrid functionals, which are different to the previously mentioned functionals because they include an amount of exact exchange from Hartree-Fock (HF) theory. There are a variety of hybrid functionals available [207–211], which either add fixed amounts of HF exchange energy (PBE0 [209]) or allow for a tuning of the HF exchange which is added (HSE [210]).

The highest rung of the ladder is the random phase approximation (RPA), which, when using KS orbitals, is believed to treat long-range correlation exactly [186] and gives most of the van der Waals interactions [212–214]. However, the RPA struggles with short range correlation, though it is possible to incorporate it through a local field factor [215, 216] or an explicit density functional.

Finally, there are also a number of other functionals available which correct for van der Waals interactions that local and semi local functionals struggle to capture. These are either applied as an additive correction [217–219] or as a more general, van der Waals inclusive functional [220–223].

The Local Density Approximation

The simplest functional available for approximating the exchange-correlation energy is the LDA approach, which is based on the uniform electron gas model [181]. The exchange-correlation energy is calculated locally assuming a uniform electron gas. The form of the exact exchange functional for the uniform electron gas was determined by Dirac [180].

$$E_{\mathrm{X}}^{\mathrm{LDA}}[\rho] = -\frac{3}{4}\left(\frac{3}{\pi}\right)^{\frac{1}{3}} \int \rho^{\frac{4}{3}} d\mathbf{r} \tag{2.17}$$

The exchange-correlation energy, $\mathrm{E_{XC}}$, is assumed to depend solely on the local electron density where the functional is evaluated (Equation 2.18). Where ϵ_{XC} is the exchange-correlation energy for the uniform electron gas, with a density $\rho(\mathbf{r})$.

$$E_{\mathrm{XC}}^{\mathrm{LDA}}[\rho] = \int \rho(\mathbf{r})\epsilon_{\mathrm{XC}}[\rho] d\mathbf{r} \tag{2.18}$$

However, the correlation functional cannot be determined in the same manner as exchange functional, from first principles. Instead, the correlation functional is derived from Monte Carlo simulations of the uniform electron gas [224], which is fitted to an analytic form, examples of which include the Vosko, Wilk and Nusair (VWN) [225], Perdew and Zunger (PZ) [226] and Perdew and Wang (PW92) [227].

The extension of the LDA approximation for spin-polarised systems is called the local spin density approximation (LSDA). Calculation of the exchange energy is simple when the exact spin scaling is known. For the correlation energy, as with the LDA, further approximations are required to facilitate its calculation. The LSDA functional is described by Equation 2.19, where the total density is the sum of ρ_α and ρ_β, which represent the two different spin densities [228].

$$E_{\mathrm{XC}}^{\mathrm{LSDA}}[\rho_\alpha \rho_\beta] = \int \rho(\mathbf{r})\epsilon_{\mathrm{XC}}[\rho_\alpha \rho_\beta] d\mathbf{r} \tag{2.19}$$

The LDA is based on the assumption that the exchange-correlation energy depends only on the local electron density. The electron correlation is, however, inherently non-local, resulting in a number of errors in the predicted properties of materials. This occurs because the LDA requires that the electron density varies slowly through space, which is not the case for strongly correlated systems (*e.g.* semiconductors) [229]. The common errors associated with LDA calculations are predicting stronger binding energies, resulting in shorter bond lengths, smaller system volumes, underestimating band gaps and a failure to describe van der Waals interactions accurately. Despite this, the LDA does give good predictions of charge moments, equilibrium geometries and vibrational frequencies.

The Generalised Gradient Approximation

The generalised-gradient approximation (GGA) improves upon the LDA by including the gradient of the electron density in the exchange-correlation functional. This offers an improvement over LDA as it attempts to account for variation in density. GGAs can be written generally as shown in Equation 2.20, where the F_{XC} term is a correction chosen to satisfy exact constraints on E_{XC} [203].

$$E_{XC}^{GGA}[\rho] = \int \rho(\mathbf{r})\epsilon_{XC}[\rho]d\mathbf{r} + \int F_{XC}[\rho(\mathbf{r}), \nabla\rho(\mathbf{r})]d\mathbf{r} \tag{2.20}$$

For the GGA approach the gradient corrections are typically divided into exchange and correlation contributions. However, there is no clear method by which to choose the F_{XC} term. This has led to a variety of functionals being proposed in the literature.

The first approach is empirical fitting to experimental data. Becke (B88) [183] proposed a functional containing a single empirical parameter fitted to experimental data for rare gas atoms to correct the exchange portion of the energy. This is also the form used in the Perdew-Wang (PW91) functional [230], though it was modified to remove the dependence on empirical parameters.

The second approach is to determine the correction theoretically. This is the approach used in the Perdew-Burke-Ernzerhof (PBE) [184] and Becke86 (B86) [231] functionals. Typically, these GGA functionals display the opposite behaviour to the LDA in that they underbind, resulting in longer bond lengths and larger volumes. In order to overcome this issue, the PBE functional was modified for densely packed solids (PBEsol) [185]. This resulted in a functional which gave slightly compressed lattice parameters compared to PBE, though it is less accurate for the calculation of dissociation and cohesive energies [185]. As with LDA, GGA functionals also underestimate band gaps and fail to describe van der Waals interactions accurately.

Whilst they do not correct all the issues with LDA functionals, generally GGA functionals offered an improved description of materials compared to LDA. Though results can vary between different GGA functionals, for the same material, resulting in a need to compare against experimental data to ensure accuracy.

2.1.1.5 The Hubbard Correction

One of the major limitations of DFT is that it often fails to describe strongly correlated (localised) *d*- and *f*- electrons. This is common to both LDA and GGA functionals.

If a system that contains an isolated atom is connected to an external reservoir with which it can exchange charge (either to or from), then the change in the system energy when part of an electron is added or removed is linear in $\delta E/\delta n_{elec}$ and is discontinuous at integer occupation values [232]. The linear behaviour between integer occupation values (*i.e.* ± 1 electron) is because partial occupation is described quantum mechanically as a time average of states with an integer number of electrons. Both LDA and GGA functionals deviate from this behaviour as they have continuous derivatives with respect to n_{elec}, which artificially lowers the energy for partial occupancies (Figure 2.1) [233]. This gives the self-interaction error. This is exhibited as an electron repelling itself. The result is transition metal

and rare-earth oxide semiconductors and insulators can be predicted to have metallic electronic band structures with itinerant electrons, in contrast to their actual properties [234–236].

One commonly used method to overcome this limitation is the Hubbard model [237]. This treats the Coulomb interaction in a mean-field Hartree-Fock manner. When using the Hubbard model, the Hubbard correction is added to the Hamiltonian, so that the total energy of the system is the sum of the DFT functional and the Hubbard correction. The Hubbard correction itself depends on two parameters, the onsite Coulomb interaction (U) and the effective onsite exchange parameter (J). The effect of using the Hubbard correction is that it forces the orbital occupancy to an integer value for the number of electrons (*i.e.* making partial occupancy less energetically favourable).

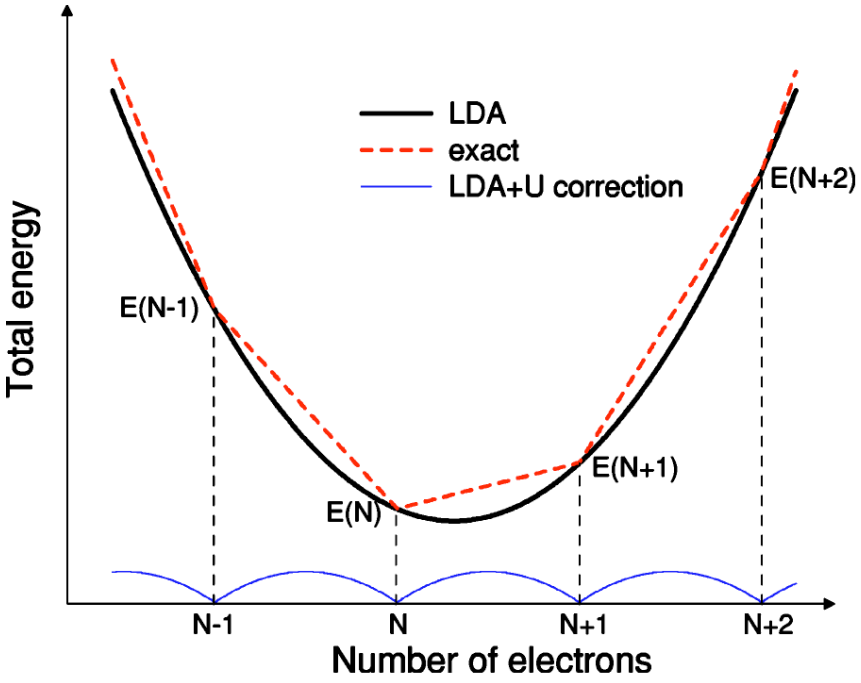

Figure 2.1: Graphical representation of the total energy profile as a function of the number of electrons in a general atomic system. This applies for both LDA and GGA. The correction is simply the difference between the exact energy and the LDA (or GGA) energy [233].

There are two common implementations of the Hubbard model; the Lichtenstein [238] and Dudarev [236, 239] approaches. In the Lichtenstein approach both U and J are considered and contribute to correct the self-interaction error, whereas in the Dudarev scheme (Equation 2.21) only the difference between U and J (U_{eff}) is important. The $n_{m\sigma}$ term gives the number of electrons occupying an orbital with the magnetic quantum number m and spin σ at a given atomic site.

$$E_{\text{DFT+U}} = E_{\text{DFT}} + \frac{U - J}{2} \sum_{m\sigma} (n_{n\sigma} - n_{m\sigma}^2) \tag{2.21}$$

Values for U and J can be determined from linear regression [240, 241], or by tuning to produce the correct band gap or structural parameters for the material

being investigated using experimental data. This work uses the Dudarev approach with $U_{\text{eff}} = 3.69$ eV ($U = 4.50$ eV and $J = 0.54$ eV), which is applied to the uranium f-electrons. The value of U_{eff} was derived from X-ray photoelectron experiments on UO_2 [242, 243].

Another consideration on the implementation of a Hubbard coefficient is not only to which electrons the correction is applied (*i.e.* d- or f-, depending on the element) but how the orbital occupancies are determined from the calculated electron density. VASP determines the orbital occupancies by projecting the orbitals onto spherical harmonics for the electron density within a cutoff distance from a given atom. The value of the cutoff distance can only be defined unambiguously for mono-atomic systems, where the volume of the spheres around each atom should give the total volume of the cell. For systems with more than one atomic species present there are several ways which the cutoff distance can be set; the first is to set the cutoff distance so that overlap between spheres is minimised, the second, and simpler implementation, is to set the radius of each sphere to the covalent radius of an atom. The overwhelming majority of DFT calculations use this second approach for determining than nature of the electron density around each atom, rather than explicitly varying the size of the cutoff, and this is the method employed in this thesis.

An alternative method to overcome the issue of the self-interaction error is hybrid DFT. A hybrid DFT functional includes a portion of exact exchange from Hartree-Fock theory combined with exchange and correction from either *ab initio* or empirical sources. In hybrid DFT the exact exchange energy functional is expressed in terms of Kohn-Sham orbitals, rather than electron density. As orbitals rather than the electron density are used as the basis for Hartree-Fock theory this means that the expression for the orbital energy contains a Coulomb interaction and an exchange interaction of opposite sign (Equation 2.22).

$$\epsilon_{a,\text{occupied}} = \langle\phi_a|\hat{h}|\phi_a\rangle + \sum_{b=1}^{N}\langle\phi_a\phi_b|\phi_a\phi_b\rangle - \langle\phi_a\phi_b|\phi_b\phi_a\rangle \tag{2.22}$$

As the sum over b is over all the occupied orbitals, self-interaction happens when $b = a$. When this occurs, the Coulomb interaction of an electron with itself is cancelled by an equivalent term in the exchange energy. Therefore the self-interaction energy is exactly cancelled. Whilst hybrid DFT provides a means to remove the self-interaction error, the functionals are currently too computationally expensive to be used for uranium oxides [187]. This additional expense comes from the calculation of the exchange energy using the Hartree-Fock approach, as a large basis set will be required to accurately describe the uranium ions. Additionally, Hartree-Fock uses the electron-spin orbitals rather than the density so the full N-electron wave-function is calculated.

2.1.1.6 Allocating Charge States

Related to the determination of the nature of electrons on an atomic site is the allocation of an atom's charge state. By default the charge assigned to an atom comes from using the projectors, described above, to divide the charge density in the system between the atoms. As before this is an arbitrary process, however, there

are schemes which attempt to apply a criterion to the allocation of charge density, one of these is Bader analysis. In the Bader approach atoms are divided by zero flux surfaces. A zero flux surface is a 2-D surface on which the charge density is at a minimum perpendicular to the surface, the charge density is assessed between pairs of atoms.

For this work both methods have been assessed and found that they do not provide a clear discrimination between atoms in different charge states. Therefore, an alternative method to discriminate between different charge states is required. Examining the magnetic moment calculated for each ion provides a means of clearly discriminating between ions in different charge states. For example a U^{4+} ion has a calculated magnetic moment of 2 μB, whereas a U^{5+} has a value of 1 μB.

2.2 Energy Minimisation

Energy minimisation (EM) is one of three main techniques used to find the lowest energy configurations from a given starting geometry. The work in this thesis uses METADISE [244] to setup the simulations cells and VASP [245–248] to perform the DFT calculations and EM. It is possible to perform *ab initio* molecular dynamics (AIMD) and quantum MC, but both of these approaches are too computationally intensive to be a practical approach.

Regardless of which EM algorithm is used, EM requires an initial configuration of the atoms. Typically, this will come from an experimentally determined crystal structure. An alternative approach is to trial a large number of initial configurations, to improve the chance of finding the global minimum. Though, this second approach can be computationally intensive and there is no absolute guarantee that the global minimum has been found, unless all possible configurations can be trialled.

There are, however, a number of limitations to the EM approach that need to be considered:

- An initial configuration is required, which can bias a simulation.
- EM will find the closest energy minimum to the initial configuration, which is not guaranteed to be the global energy minimum.
- The simulation neglects temperature. Therefore, the vibrational properties of the crystal are neglected. Strictly speaking this is not a 0 K simulation because the zero point energy contributions are also neglected.

Despite these limitations, EM is an effective tool for exploring the energy landscape of different materials. Additionally, because EM locates the closest minimum it is an effective tool for exploring the relative stability of different polymorphs [18].

EM is an iterative procedure which aims to decrease the lattice energy U_{L} to a minimum based on the atomic coordinates $\mathbf{r}$. This is achieved by trying to minimise the force on each atom to zero, *i.e.* a stationary point on the potential energy surface.

$$\frac{\delta U_L}{\delta r} = 0 \tag{2.23}$$

In order to use the iterative approach for EM, the energy is expressed as a Taylor expansion in terms of the basis strain ($\delta\mathbf{r}$). As the positions $\mathbf{r}$ are composed of three components, this generates a $3N$ array.

$$U_{\mathrm{L}}(\mathbf{r}+\delta\mathbf{r}) = U_{\mathrm{L}}(\mathbf{r}) + \frac{\partial U_{\mathrm{L}}(\mathbf{r})}{\partial \mathbf{r}}\delta\mathbf{r} + \frac{1}{2!}\frac{\partial^2 U_{\mathrm{L}}(\mathbf{r})}{\partial^2 \mathbf{r}}\delta\mathbf{r}^2 + \cdots + \frac{1}{n!}\frac{\partial^n U_{\mathrm{L}}(\mathbf{r})}{\partial^n \mathbf{r}}\delta\mathbf{r}^n \tag{2.24}$$

As the energy is expressed as a Taylor expansion the more terms that are included the longer the calculation will take to complete. The procedure of EM then becomes a balancing act between computing time and accuracy. Typically, in DFT simulations the highest derivative calculated analytically is the first.

Finally, there are two main different types of EM calculations, constant volume (CV) and constant pressure (CP). In a CV calculation, the atoms are allowed to relax but the cell parameters are kept fixed, whereas in a CP calculation the cell parameters are allowed to relax in addition the atomic coordinates. This is achieved by applying Hooke's law to alter the lattice vectors based on the bulk lattice strain.

2.2.1 Steepest Descent

The simplest EM algorithm is the steepest descent approach (Equation 2.25), where the initial positions ($\mathbf{r}_i$) are updated to a lower energy configuration, by moving in the direction defined by the gradient vector ($\mathbf{s}_i$).

$$\mathbf{r}_{n+1} = \mathbf{r}_i + \alpha_n \mathbf{s}_n \tag{2.25}$$

where the gradient vector is defined in Equation 2.26 and $\mathbf{g}_i$ is the gradient for iteration i. All that is left now is to determine α_i, which is the step size in the direction of the minimisation.

$$\mathbf{s}_i = \frac{-\mathbf{g}_i}{|\mathbf{g}_i|} \tag{2.26}$$

There are two methods for determining α_i. The first and most simple approach is an arbitrary step length. This is where an initial default value is used, and if the energy decreases the step length is increased, until the energy increases, at which point the method is deemed to have overshot the minimum so the direction is revered and the step length decreased.

The second approach is a one-dimensional line search. In this approach, three points are found along one direction such that the middle point is lower than the end two points. The energy minimum must therefore be between the two outer points. This process is then repeated by reducing the distance between the two outer points until the minimum has been located.

While the steepest-descent approach is not the most computationally intensive, it can result in oscillations back and forth across an energy well, particularly if well with is less than α, and this result in a large number of iterations being performed to reach the minimum. As such, the steepest descent method is rarely employed in modern computational studies.

2.2.2 Conjugate Gradients

The conjugate gradient approach is a progression of the steepest descent method. In a conjugate gradient minimisation the first step is the same as a steepest descent minimisation, but for all subsequent iterations information from the previous gradient is used in the calculation of the new gradient vector [249, 250]. The gradient vector is now defined as in Equation 2.27.

$$\mathbf{s}_i = \frac{-\mathbf{g}_i}{|\mathbf{g}_i|} + \gamma_i \mathbf{s}_{i-1}; \qquad \gamma_i = \frac{\mathbf{g}_i \cdot \mathbf{g}_i}{\mathbf{g}_{i-1} \cdot \mathbf{g}_{i-1}} \tag{2.27}$$

The addition of information from the previous step in the gradient vector results in an algorithm that will converge well regardless of the shape of the energy landscape. This also removes the oscillations in narrow energy minima that the can occur with the steepest descent approach. Consequently, the conjugate gradient approach is commonly used in computational studies, as it is an efficient method for finding energy minima. The conjugate gradient approach is used in the EM calculations presented in this work.

2.2.3 Newton-Raphson

Beyond the first derivative EM techniques are second derivative approaches. The simplest of these is the Newton-Raphson method, which uses the second derivative of the energy to increase the efficiency of the calculation. This reduces the required number of steps to reach the minimum, but the computational cost of each step is increased, as the second derivatives must be calculated [251].

The Newton-Raphson method takes the Taylor expansion of the energy (Equation 2.24) to the second derivative. The gradient of iteration i is then expressed in Equation 2.28.

$$\mathbf{g}_{i+1} = \mathbf{g}_i + \mathbf{W}_{i-1} \cdot \delta\mathbf{r} \tag{2.28}$$

where $\mathbf{W}_{i-1}$ is the Hessian matrix and $\delta\mathbf{r}$ is the displacement of ions between iterations i and i-1. When the gradient is equal to zero, the atomic displacements are given by Equation 2.29.

$$\delta\mathbf{r} = -\mathbf{g}_{i-1} \cdot \mathbf{W}_{i-1}^{-1} \tag{2.29}$$

$\mathbf{W}_{i-1}^{-1}$ is the inverse Hessian, which is used to determine the new atomic positions (Equation 2.30).

$$\mathbf{r}_{i+1} = \mathbf{r}_i - \mathbf{g}_i \cdot \mathbf{W}_i^{-1} \tag{2.30}$$

As with the first-order EM algorithms, the Newton-Raphson approach is implemented iteratively. For a purely harmonic system only one iteration would be needed. However, most energy surfaces are not perfectly harmonic, so convergence will take several iterations. One drawback, however, is that if the starting configuration is far from the energy minimum convergence will be inefficient. This means

ensuring a good starting configuration when using a Newton-Rahpson minimisation is necessary. Typically this would mean preforming a minimisation with a first-order approach, *e.g.* conjugate gradient, then use the Newton-Raphson method to find a more precise minimum.

The major drawback of Newton-Raphson is that for each step the Hessian and the inverts Hessian have to be calculated. Computationally this is very expensive, even though there is an efficiency gain from using the second derivatives so fewer iterations are required and typically for DFT codes, such as VASP, these are not routinely calculated. In order to try and retain the advantages of the Newton-Raphson approach but reduce the computational cost the Quasi-Newton methods have been developed.

2.2.4 Quasi-Newton

In order to increase the speed of the Newton-Raphson method whilst retaining its accuracy, the quasi-Newton methods approximate the inverse Hessian matrix, rather than explicitly calculate a new inverse Hessian. There are a number of different quasi-Newton algorithms proposed in the literature, including the Davidon-Fletcher-Powell (DFP) [249], Broyden-Fletcher-Goldfarb-Shanno (BFGS) [252–255] and the RMM-DIIS methods [256].

The quasi-Newton methods only use the change in forces, strain and the previous inverse Hessian matrix, which itself may be an estimate, in the calculation of the new inverse matrix. Equation 2.31 shows how the Hessian is approximated for the DFP approach. $\delta\mathbf{r}$ is the change in atomic co-ordinates and $\delta\mathbf{g}$ is the change in the gradient.

$$\mathbf{W}_i \approx \mathbf{W}_{i-1} + \frac{\delta\mathbf{r} \otimes \delta\mathbf{r}}{\delta\mathbf{r} \cdot \delta\mathbf{g}} - \frac{(\mathbf{W}_i \cdot \delta\mathbf{g}) \otimes (\mathbf{W}_i \cdot \delta\mathbf{g})}{(\delta\mathbf{g} \cdot \mathbf{W}_i \cdot \delta\mathbf{g})} \tag{2.31}$$

The BFGS approach is similar to the DFP method, but includes an additional term which results in greater efficiency.

$$\mathbf{W}_i \approx \mathbf{W}_i^{DFP} + (\delta\mathbf{g} \cdot \mathbf{W}_i \cdot \delta\mathbf{g})\mathbf{u} \otimes \mathbf{u} \tag{2.32}$$

The vector, $\mathbf{u}$ is defined by Equation 2.33.

$$\mathbf{u} = \frac{\delta\mathbf{r}}{\delta\mathbf{r} \cdot \delta\mathbf{g}} - \frac{\mathbf{W}_{i-1} \cdot \delta\mathbf{g}}{\delta\mathbf{g} \cdot \mathbf{W}_{i-1} \cdot \delta\mathbf{g}} \tag{2.33}$$

Using the assumption that the approximation of the inverse Hessian remains correct, with an increasing number of iterations the approximate inverse Hessian becomes closer to the true inverse Hessian. Once the quasi-Newton method approaches the minimum, it has a similar level of accuracy to the Newton-Raphson approach.

2.3 Periodicity

One of the issues of simulating a material is both quantum and classical methods are limited by the number of atoms that can be simulated ($\sim 10^2$ for DFT and $\sim 10^5$ for classical). This is many orders of magnitude less than the number of atoms that are present in a real system ($\sim 10^{23}$). This leaves the problem of how to simulate a near infinite system using a much smaller finite number of species.

2.3.1 Periodic Boundary Conditions

Periodic boundary conditions (PBC) provide the solution to this problem. PBCs work by surrounding the simulation cell with identical images of the cell. When an atom moves across the boundary of the simulation cell, the equivalent atom in the image on the opposite side moves into the simulation cell. Figure 2.2 shows an example of PBC in two dimensions.

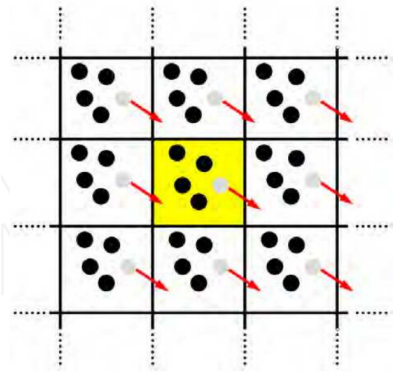

Figure 2.2: 2D representation of periodic boundary conditions. The simulation cell is highlighted in yellow [257].

There are a couple of drawbacks to using PBC to simulate a material. Firstly only periodic fluctuations which have a wavelength shorter than the simulation cell can be simulated. Secondly, if the simulation cell is not large enough, then the periodic interactions can impose an artificial long-range ordering that is not present in the real system. However, both of these issues can be overcome by using a sufficiently large simulation cell (albeit at greater computational expense).

Another feature of PBCs is that the electronic density will also be periodic, which allows for a more rapid calculation of the electronic properties. A key parameter of periodicity is the reciprocal lattice, discussed below.

2.3.2 The Reciprocal Lattice

The reciprocal lattice is a representation of a crystal lattice defined in reciprocal space (k space). This is commonly used by X-ray crystallographers, who define the three reciprocal lattice vectors $\mathbf{a}^*$, $\mathbf{b}^*$ and $\mathbf{c}^*$, such that $\mathbf{a}^*$ is perpendicular to $\mathbf{b}$ and $\mathbf{c}$ and scaled such that the product of $\mathbf{a}^*$ and $\mathbf{a}$ equals 1. $\mathbf{b}^*$ and $\mathbf{c}^*$ are similarly defined in Equation 2.34.

$$\mathbf{a}^* = \frac{\mathbf{b} \times \mathbf{c}}{\mathbf{a} \cdot \mathbf{b} \times \mathbf{c}}; \quad \mathbf{b}^* = \frac{\mathbf{a} \times \mathbf{c}}{\mathbf{b} \cdot \mathbf{a} \times \mathbf{c}}; \quad \mathbf{c}^* = \frac{\mathbf{a} \times \mathbf{b}}{\mathbf{c} \cdot \mathbf{a} \times \mathbf{b}} \tag{2.34}$$

For computational work it is convenient to work in an expanded reciprocal space. This is done by multiplying each of the reciprocal lattice vectors by 2π. This gives the reciprocal cell the same periodicity as the wave function.

$$\mathbf{a}^{\$} = 2\pi\mathbf{a}^{*}; \quad \mathbf{b}^{\$} = 2\pi\mathbf{b}^{*}; \quad \mathbf{c}^{\$} = 2\pi\mathbf{c}^{*} \tag{2.35}$$

As is the case with constructing real space from unit cells, the reciprocal lattice is constructed using primitive cells. The primitive cell associated with a particular lattice point has the property that any coordinate within the cell is closer to the lattice point than any other lattice point. The primitive cell is known as the first Brillouion zone (BZ). The reciprocal lattice vectors ($\mathbf{G}$) are defined such that:

$$\mathbf{G} = n\mathbf{a}^{\$} + m\mathbf{b}^{\$} + o\mathbf{c}^{\$} = 2\pi n\mathbf{a}^{*} + 2\pi m\mathbf{b}^{*} + 2\pi o\mathbf{c}^{*} \tag{2.36}$$

We can now consider the complex exponential function $\exp(i\mathbf{G}\cdot\mathbf{r})$, which can be expanded as the sum of cosine and sine functions (Equation 2.37), where α, β and γ are coefficients between 0 and 1.

$$\exp(i\mathbf{G}\cdot\mathbf{r}) = \cos(2\pi n\alpha + 2\pi m\beta + 2\pi o\gamma) + i\sin(2\pi n\alpha + 2\pi m\beta + 2\pi o\gamma) \tag{2.37}$$

As n, m and o are integral the function $\exp(i\mathbf{G}\cdot\mathbf{r})$ varies with the same periodicity as the real space lattice. This is of crucial importance to electronic structure calculations as the electronic wave function can be completely characterised in the first BZ.

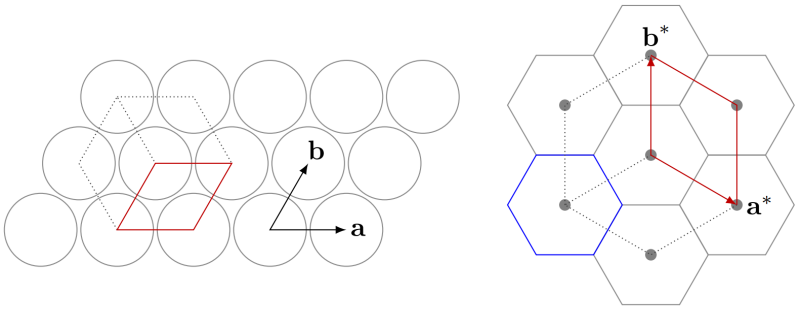

Figure 2.3: A 2D hexagonal lattice showing the relationship between the real space and reciprocal space lattice. (a) shows the real space hexagonal lattice atoms (grey circles), with the unit cell in red. (b) shows the corresponding reciprocal lattice. The reciprocal lattice points shown in grey, reciprocal unit cell in red and the first BZ in blue. [258].

2.3.3 Bloch Theorem and Plane Waves

Whilst PBCs allow for simulation of an infinite material with a finite number of species, there are a further two problems to solving the Schrödinger equation that PBCs do not directly solve. The first of these is that because the crystal is infinite there are an infinite number of electrons to be simulated. In addition, the wave function for each of these electrons is spread over the entire crystal, resulting in the need for an infinite basis set [259]. These limitations can be overcome by using Bloch's Theorem.

Bloch's theorem states that an electron's wave function in a periodic potential can be expressed as the product of a wave-like term and a term which has the same periodicity as the unit cell, known as a Bloch wave (Equation 2.38).

$$\psi_n(\mathbf{r}) = e^{i\mathbf{k}\cdot\mathbf{r}} f_n(\mathbf{r}) \tag{2.38}$$

$\psi_n(\mathbf{r})$ is the wave function of an electron (n) in a periodic potential, $\mathbf{k}$ is the wave vector representing the direction and frequency of the Bloch wave in the first BZ. The cell dependent part of the wave function ($\mathrm{f}_n(\mathbf{r})$) is comprised of a discrete set of plane waves (Equation 2.37), where $\mathbf{G}$ represents the wave vectors for all possible reciprocal lattice vectors.

$$f_n(\mathbf{r}) = \sum_{\mathbf{G}} c_{n,\mathbf{G}} \exp(i\mathbf{G}\cdot\mathbf{r}) \tag{2.39}$$

The wave function for each electron is now the sum of all plane waves defined by the coefficients c_n, $\mathbf{k}+\mathbf{G}$.

$$\psi_n(\mathbf{r}) = \sum_{\mathbf{G}} c_{n,\mathbf{k}+\mathbf{G}} \exp\{i(\mathbf{k}+\mathbf{G})\cdot\mathbf{r}\} \tag{2.40}$$

Truncating the series allows for the basis set to be limited to a finite size because plane waves with higher $|\mathbf{G}|$ have a higher kinetic energy and contribute an ever decreasing amount to the wave function. In practice this requires that a cut-off energy is set and the plane wave basis set is then truncated to only include the plane waves with a kinetic lower energy than this value. For DFT calculations this means testing a system to determine when convergence has been achieved, *i.e.* increasing the cut off energy has no further effect on the calculated energy or properties of the system.

As the wave function (ψ) is a continuous function of $\mathbf{k}$, then two points in k-space that are close to each will have similar wave functions. Therefore, ψ over an appropriate volume of k-space can be represented using a single k-point. This means the system can be sampled with a finite number of discrete k-points, which removes the requirement of an infinite number of electrons.

As with the cut off energy, it is important to select an appropriate set of k-points for the system in question to achieve an accurate representation of band structures and density of states. This work uses the Monkhorst-Pack scheme [260], which distributes the k-points evenly throughout the first BZ, centred on the Γ-point. The Γ-point is the origin of the reciprocal lattice. The advantage of this method is that many k-points are then related by symmetry, resulting in a reduction of the number

of k-points that need to be evaluated. This homogeneous distribution of k-points is described in Equation 2.41.

$$k = x_1 a^* + x_2 b^* + x_3 c^* \tag{2.41}$$

The coefficient x_i is determined by the folding parameter n_i (Equation 2.42), and dictates the density of the k-point grid in direction i.

$$x_i = \frac{l}{n_i} \quad \text{with} \quad l = 1, \ldots, n_i \tag{2.42}$$

The density of the k-point mesh is determined by the type of material being simulated. Conducting materials (*e.g.* metals and small band gap semiconductors) require dense k-point meshes, so consequently have large folding parameters. Conversely, for insulating materials or large band gap semiconductors, a less dense k-point mesh is required and therefore a smaller folding parameter is used. Additionally, the larger the real-space simulation cell that is used the smaller the folding parameter needs to be, as the reciprocal cell is smaller and the k-points are closer together. For this work the folding parameters are varied for each material to have a consistent k-point density in all simulations.

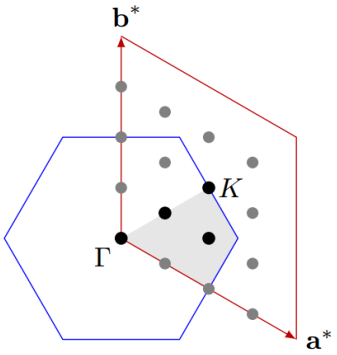

Figure 2.4: The Monkhorst-Pack k-point grid for a hexagonal reciprocal lattice. The Γ and K points are high symmetry points which represent the centre and edge of the BZ. k-points shown as dark grey points, with the irreducible k-points shown in black and the irreducible BZ shaded in light grey. [258].

2.3.4 Pseudopotentials

Plane waves are usually an inappropriate representation of the electronic wave functions of tightly-bound core electrons. This is because a large number of plane waves is needed to represent the spatial oscillations close to the nucleus. The problem is worse for elements with high masses, as the number of core electrons increases.

The basis of the pseudopotential approximation is that the physical properties of the system are determined by the valence electrons [261] and therefore the core electrons will have minimal impact on the physical properties. This means that the core electrons can be considered as part of a combined potential including the nucleus.

Practically, pseudopotentials work by replacing the core electrons and strong ionic potential of the nucleus with a weaker potential. The valence wavefunctions are modelled as pseudo-wave functions rather than true valence wavefunctions. The pseudo-wavefunction (ψ_{pseudo}) is the same as the all electron wave function (ψ) above a cut off distance and as a result is valid beyond the cut off distance. However, the advantage of pseudopotentials compared to all-electron calculations is that fewer plane waves are required to describe the wavefuncation. Figure 2.5 shows a schematic representation of a pseudopotential.

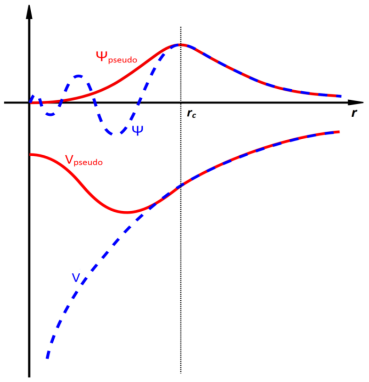

Figure 2.5: A schematic representation of the all electron (blue) and pseudo (red) potentials (V) and corresponding wavefunction (Ψ). The cut off ($\mathbf{r}_c$) represents the radius beyond which V_{pseudo} and Ψ_{pseudo} match V and Ψ respectively [259].

There are range of different types of pseudopotentials available [177, 229, 262]. The majority of pseudopotentials are derived from all-electron *ab initio* calculations. However, they can also be defined empirically. Pseudopotentials are categorised by "softness", which is a measure of the smoothness of the core and cut off distance. The softer a pseudopotential is, the fewer planes waves are needed. This comes at the cost of accuracy and reduced transferability due to the larger cut off distances.

The two earliest types of pseudopotential used are norm-conserving and ultrasoft. Norm-conserving pseudopotentials maintain the same valence electron density in the core region and consequently are more transferable than ultrasoft pseudopotentials. The ultrasoft pseudopotentials are smoother and require fewer plane waves to describe them, which reduces the calculation time. However, they are not norm-conserving, and make use of auxiliary functions close to the ion core to represent rapid variations in core electron density.

This work uses the projector augmented wave (PAW) method [263]. PAW potentials are similar to ultrasoft pseudopotentials, making use of localised auxiliary functions. Where the method differs is that it still captures the full all-electron wave function, by using mathematical operations to convert the smooth pseudopotential back to the real wave function. The result is a pseudopotential that requires fewer plane waves to describe but retains the accuracy of the full wave function.

2.4 Calculation of Crystal Properties

The final section of this chapter discusses how properties of a material are calculated after the structural minimisation has been performed. This is split into two parts: the first deals with material properties, such as the bulk modulus and the second details the calculated properties of reference materials, which are required to determine defect energies.

2.4.1 Density of States

The occupancy of the electronic states in a crystalline solid is given by the density of states (DOS). The DOS is defined as the number of electronic states per unit volume as a function of energy. In addition to being able to calculate the total DOS, it is also possible to determine the contributions from individual atoms, which gives the partial density of states (pDOS). The pDOS can be used to determine which states make up the conduction and valence bands. This provides information on which orbitals are occupied or are involved in bonding. Additionally, the Fermi level can be determined from DOS calculations. The Fermi level at 0 K and in thermodynamic equilibrium is defined as the energy level with a 50 % probability of occupation.

Where the Fermi level is located within the DOS determines the type of electrical behaviour a material exhibits. Semiconductors and insulators show a band gap between the valence and conduction bands. The band gap is a forbidden energy region where the DOS is equal to zero. For a metallic or semi-metallic system the Fermi level lies in a delocalised band and these materials do not possess a band gap. The lack of a band gap results in the high electrical conductivity as there is a large number of partially filled states that allow for high electron mobility. In comparison, for insulators the Fermi level lies in a large band gap which is far from any accessible states. The nature of the states on either side of the band gap determine the type of insulating behaviour. The most common behaviour observed is that of charge-transfer insulator, where the valence band are composed of anion states and the condition band is composed of cation states, *e.g.* in NiO [264]. The less common type of insulating behaviour is that of Mott-Hubbard insulating materials, where the states at the top of the valence band and bottom of the conduction band are composed predominately of the same orbitals, *e.g.* U5f states in UO_2 [265].

There are three types of semiconducting materials: p-type, n-type and intrinsic. For p-type semiconductors the Fermi level sits at the top of the valence band. Conversely for n-type semiconductors the Fermi level is at the bottom of the conduction band. Finally, for intrinsic semiconductors, the Fermi level sits between the conduction and valence bands.

A DOS is determined as part of the energy minimisation calculation, as the total energy is an integration over the occupied bands. The calculation of the DOS in this manner is not of high accuracy, however, due to the low k-point density typically used. In order to calculate an accurate DOS, there are two possible approaches. The first is to perform a minimisation with a very fine k-point mesh. This is a computationally intensive approach. The alternative is to perform a standard structural energy minimisation and then perform a non-self-consistent calculation, which keeps a fixed charge density, with a denser k-point mesh. For the calculation of DOS in this work the second of these two approaches is used, as it is significantly

less expensive and the results are comparable to a self-consistent approach.

2.4.2 Bulk Modulus

The bulk modulus represents the compressibility of a material. It can be calculated using one of two methods: fitting an energy/volume curve to the Birch-Murnaghan equation of state or through the effect of finite displacement on the stress matrix.

The first of these methods, the Birch-Murnaghan equation of state [266, 267], calculates the bulk modulus expanding and contracting the lattice from the predicted equilibrium geometry. For each expansion or contraction the structure is minimised at constant volume. The data for these points is then fit to the Birch-Murnaghan equation of state which yields the bulk modulus, as a fitting parameter. The advantage of this approach is that it is computationally inexpensive. However, it only calculates the bulk modulus, and provides no information on the individual derivatives of the elastic constant tensor. The Birch-Murnaghan equation of state is shown in Equation 2.43 [267].

$$E(\eta) = E_0 + \frac{9B_0V_0}{16}(\eta^2 - 1)^2(6 + B_0^{'}(\eta^2 - 1) - 4\eta^2) \tag{2.43}$$

The second method, which is computationally more intensive, uses the finite displacement method. The finite displacement method is based on Hooke's Law [268], that for small deformations the strain is directly proportional to the stress. In this approach, small finite displacements are made to the lattice parameters and atomic positions. The expense of the calculation can be reduced by only considering symmetry inequivalent sites [269]. The response of the stress matrix is then determined (Equation 2.44), where **W** is the second derivative matrix with respect to the strain (ϵ) and the co-ordinate displacement (r).

$$\mathbf{C} = \frac{1}{V_C}(\mathbf{W}_{\epsilon\epsilon} - \mathbf{W}_{\epsilon r}\mathbf{W}_{rr}^{-1}\mathbf{W}_{r\epsilon}) \tag{2.44}$$

This then produces the full elastic stiffness constant matrix (C_{11}:C_{66}), from which the bulk modulus can be determined by averaging the first nine (C_{11}:C_{33}) individual elastic constants. Alternatively, it is possible for the higher symmetry crystal types (Cubic [270], Hexagonal [271], Orthorhombic [272]) to use symmetry adjusted equations to calculate the bulk modulus (Equation 2.45 - 2.50). There are no symmetry adjusted equations for the lower symmetry crystal systems.

For cubic systems, which only have three unique elastic constants (C_{11}, C_{12}, C_{44}) the bulk modulus can also be calculated as shown in Equation 2.45 [270].

$$B = \frac{1}{3}(C_{11} + 2C_{12}) \tag{2.45}$$

Hexagonal crystals have five unique elastic constants (C_{11}, C_{12}, C_{13}, C_{33}, C_{55}) from which the bulk modulus can be calculated (Equation 2.46) [271].

$$B = \frac{2}{9}(C_{11} + C_{12} + C_{13} + \frac{C_{33}}{2}) \tag{2.46}$$

Finally, orthorhombic crystals have the most complex equation, due to lower crystal symmetry (Equation 2.47) [272].

$$B = \frac{\Lambda}{(1+\alpha+\beta)^2} \tag{2.47}$$

with Λ, α and β defined in Equations 2.48, 2.49 and 2.50 respectively.

$$\Lambda = C_{11} + 2C_{12}\alpha + C_{22}\alpha^2 + 2C_{13}\beta + C_{33}\beta^2 + 2C_{23}\alpha\beta \tag{2.48}$$

$$\alpha = \frac{(C_{11}-C_{12})(C_{33}-C_{13}) - (C_{23}-C_{13})(C_{11}-C_{13})}{(C_{33}-C_{13})(C_{22}-C_{12}) - (C_{13}-C_{23})(C_{12}-C_{23})} \tag{2.49}$$

$$\beta = \frac{(C_{22}-C_{12})(C_{11}-C_{13}) - (C_{11}-C_{12})(C_{23}-C_{12})}{(C_{22}-C_{12})(C_{33}-C_{13}) - (C_{12}-C_{23})(C_{13}-C_{23})} \tag{2.50}$$

2.4.3 Vibrational Properties

The calculation of vibrational properties has two main uses in computational chemistry: it allows for prediction of IR and Raman spectra and the stability of a structure can be assessed from the vibrational frequencies. The presence of imaginary modes indicates that the system is dynamically unstable, and that the calculated structure is thus not an energy minimum. However, by adjusting the atom coordinates in the direction of the associated eigenvector(s) a lower energy solution can usually be found by further minimisation. The presence of a single imaginary mode indicates the structure is a transition state between two energy minima (*i.e.* an energy maximum in one direction).

There are two approaches to calculating the vibrational frequencies. The first is the finite displacement method, this is the same method as was described for the calculation of the bulk modulus in Section 2.4.2. The second approach is to use Density Functional Perturbation Theory (DFPT) [273, 274]. The difference in the DFPT approach is that the force constants are found analytically rather than numerically. This work uses the finite displacement approach, as the bulk modulus can conveniently be determined at the same time.

2.4.4 Reference Energies

In order to calculate defect formation energies in this investigation, it is necessary to calculate a series of reference energies, for elemental hydrogen, oxygen and uranium. This section details the results of these calculations and compares calculated properties to experimental data, to validate the models.

2.4.4.1 Hydrogen Gas

A H_2 molecule was placed in the centre of a 20 x 20 x 20 Å box. The H_2 molecule was minimised using the PBE functional, with a plane wave cut off of 500 eV and a single Γ-centred k-point. Table 2.1 compares the calculated properties of H_2 with experimental values.

Table 2.1: Calculated and experimental properties of H_2. The reference energy is calculated directly from DFT for a hydrogen atom in a H_2 molecule. The dissociation energy is the energy of an isolated hydrogen atom minus the energy of a single hydrogen atom in a hydrogen molecule.

Property	**Experiment**	**Calculated**	**Δ%**
Bond Length (Å)	0.74 [275]	0.75	1.35
Vibrational Frequency (cm^{-1})	4401.23 [275]	4330	-1.62
Dissociation Energy, E_D (eV)	4.48 [275]	4.53	1.78
Reference Energy, E_H (eV)	-	-3.39	-

There is very good agreement between the calculated and observed properties of H_2. The dissociation energy (E_D) was calculated by comparing the difference in energy between an isolated atom (E_H) and half the energy of the hydrogen molecule (E_{H2}), as shown in Equation 2.51.

$$E_D = E_H - \frac{1}{2}E_{H_2} \tag{2.51}$$

While the calculated dissociation energy shows very good agreement, with the experimental values it was decided for consistency of approach the reference energy will be set to the value directly calculated from DFT.

2.4.4.2 Oxygen Gas

An O_2 molecule was placed in the centre of a 20 x 20 x 20 Å box. The O_2 molecule was minimised using the PBE functional, a plane wave cut off of 500 eV, a single Γ-centred k-point and the triplet electronic state. O_2 is multiconfigurational, possessing both a triplet, which is the electronic ground state and, a singlet excited state. The result this is that there are large differences in the reported calculated energies [187]. Table 2.2 compares the calculated properties of O_2 with experimental values.

Table 2.2: Calculated and experimental properties of O_2. The reference energy is calculated directly from DFT. The dissociation energy is the energy of an isolated oxygen atom minus the energy of a single oxygen atom in an oxygen molecule.

Property	Experiment	Calculated	Δ%
Bond Length (Å)	1.21 [276]	1.23	1.65
Vibrational Frequency (cm^{-1})	1580.2 [275]	1567	-0.84
Dissociation Energy, E_D (eV)	5.11 [277]	6.67	30.53
Reference Energy, E_O (eV)	-	-4.94	-

Good agreement between the calculated and experimental properties of O_2 is found, except for the calculated dissociation energy. The dissociation energy was calculated by comparing the energy of O in a 20 $Å^3$ box with the energy of O_2 in an equivalently sized box. While the calculated dissociation energy is significantly more than the experimental value, the reference energy calculated from DFT shows good agreement with the experimental dissociation energy. Therefore, in order to maintain consistent approach the reference energy will be set to the value directly calculated from DFT.

2.4.4.3 Uranium Metal

Uranium metal has three different phases (α [278], β [279], γ [280]) depending on the temperature. The α-U phase exists up to 945 K and is therefore the 0 K phase, as such, it was chosen as the reference uranium state. Figure 2.6 shows the four atom *Cmcm* unit cell of α-U.

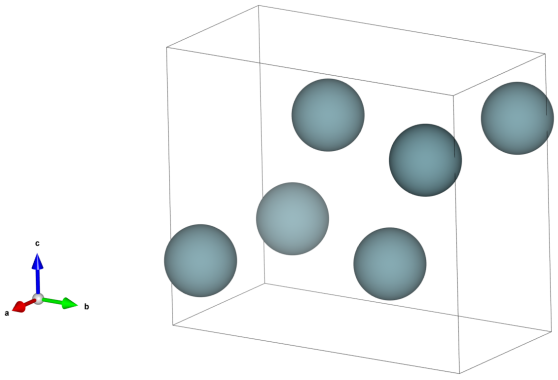

Figure 2.6: Orthorhombic *Cmcm* unit cell of α-uranium.

As one of the requirements to calculate the properties of the oxide is inclusion of a Hubbard parameter, the reference calculations also require the same parameter. Therefore calculations on uranium metal have also been performed with the Hubbard coefficient. This is despite typically the inclusion of a Hubbard coefficient is not required for the simulations of metals as it localises the electrons. However, ultimately the goal is to simulate an oxide supported on a metal surface and therefore having a consistent methodology that can be applied across the whole system regardless of if the uranium ion is in the metal or oxide layer is important. The

effective Hubbard coefficient used was that determined from Kotani *el al.*'s [243] experimental measurements on UO_2 ($U_{\text{eff}} = 3.96$ eV).

Simulation of metals requires a higher k-point density than for insulators. Figure 2.7 shows the k-point convergence test performed for α-U. The calculations were performed with a 500 eV cut off energy, using PBE and PBE+U. Convergence is achieved with a k-point density of 2 k-points/Å^3, for both PBE and PBE+U.

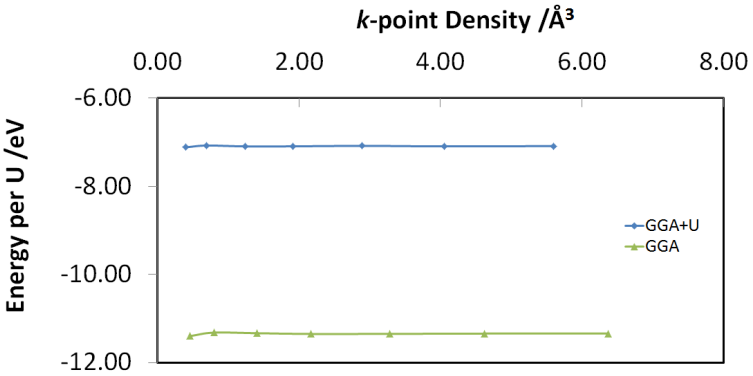

Figure 2.7: k-point convergence test for α-uranium with a 500 eV cut off energy using the PBE and PBE+U functionals.

Having determined the convergence criteria for α-U, the best magnetic configuration for α-U can be assessed. Table 2.3 compares the calculated properties for α-U metal to experiment and literature DFT simulations. The trialled magnetic configurations considered in this work were PBE and PBE+U using a non-magnetic (NM), ferromagnetic (FM) and an antiferromagnetic (AFM) ordering.

Table 2.3: Comparison of calculated properties of α-U metal with experiment and calculated literature values. For PBE+U three different magnetic orderings were trialled. The reference energy is calculated directly from DFT. The heat of deposition is the reference energy minus the energy of an isolated uranium atom. The percentage difference from experiment is given in brackets.

Method	a (Å)	b (Å)	c (Å)	Volume (Å^3)	Magnetic Moment / U (μ_B)	Heat of Deposition (eV)	Reference Energy, E_U (eV)
Experiment [278]	2.85	5.87	4.95	83.01	-	-5.52 [99]	-
PBE	2.77 (-2.8)	5.85 (-0.4)	4.87 (-1.6)	79.09 (-4.7)	0.00	-6.28 (13.77)	-11.34
PBE+U (NM)	2.97 (4.1)	5.97 (1.7)	5.08 (2.5)	90.04 (8.5)	0.00	-2.48 (-55.1)	-7.09
PBE+U (FM)	3.66 (28.2)	6.32 (7.8)	5.92 (19.5)	136.95 (65.0)	3.12	-3.95 (-37.1)	-8.56
PBE+U (AFM)	3.36 (17.8)	5.98 (1.8)	5.72 (15.5)	132.38 (38.4)	2.27	-3.94 (-37.3)	-8.54
PW91 [281]	2.75 (-3.5)	5.86 (-0.2)	4.92 (-0.6)	79.28 (-4.3)	-	-	-
PW91 [282]	2.83 (-0.8)	5.83 (-0.7)	4.91 (-2.2)	80.96 (-2.2)	-	-	-
PW91 [283]	2.80 (-1.8)	5.89 (0.4)	4.89 (-1.2)	80.77 (-2.5)	-	-	-
FP-LMTO [284]	2.84 (-0.2)	5.82 (-0.9)	4.99 (0.9)	82.69 (-0.1)	-	-	-
LDA [285]	2.85 (0.0)	5.88 (0.1)	4.93 (-0.2)	82.61 (-0.2)	-	-	-

The PBE configuration used here is in excellent agreement with experiment and the other literature calculations of α-U, with only a small percentage variation in the calculated lattice parameters. The NM PBE+U configuration has slightly larger predicted lattice parameters, this is to be expected from the inclusion of the Hubbard

coefficient. However, the heat of formation, for the NM PBE+U configuration, is significantly underestimated. For the FM and AFM magnetic configurations the structural parameters are overestimated compared to experiment. This is reduced using an AFM configuration where the attraction between the ions helps counter the expansion. The calculated heat of formation is still underestimated compared to experiment, but is a significant improvement upon the NM configuration. While the properties of α-U are not as well reproduced as either H_2 or O_2, in order to apply a consistent, fully *ab initio*, methodological approach the AFM PBE+U configuration was chosen as a reference state, due to reduced lattice expansion and an improved energetic description.

The inclusion of the Hubbard coefficient results in the localisation of the electrons. Therefore, there is a need to check the metallic nature of uranium metal is predicted. This can be examined by inspecting the DOS to ensure that there are states at the Fermi level. Figure 2.8 shows the calculated DOS of α-U using the AFM PBE+U configuration. At the Fermi level there are states indicating metallic behaviour and these are comprised of uranium f and d states. The predicted DOS here agrees well with the partial DOS predicted by Chantis *et al.*[286], who used a higher level of theory (QSGW) to predict the DOS of α-U.

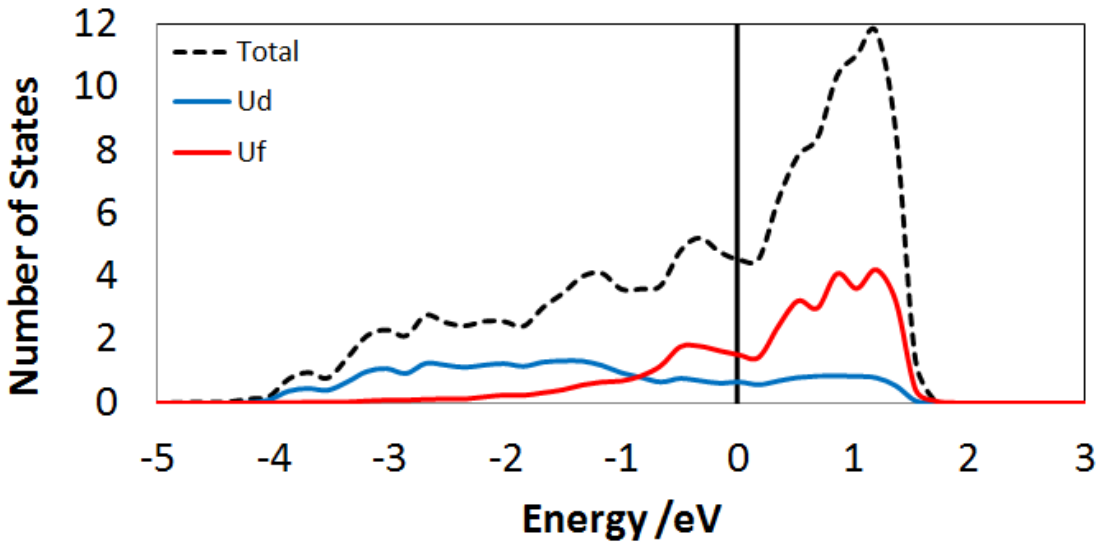

Figure 2.8: Calculated pDOS of α-U using AFM PBE+U. Only the spin up channel shown as the spin down is identical. Uranium f-states shown in red and d-states shown in blue, the total DOS is represented by the dashed line. The Fermi energy has been set to 0 eV.

Overall, the most appropriate model for α-U to use in this thesis is the AFM PBE+U configuration, as it has the best representation of the experimental energies, though this comes at the expense of the structural properties. Additionally, as the Hubbard coefficient is required for UO_2, the reference uranium calculation also require a Hubbard coefficient. Finally, whilst the inclusion of the Hubbard parameter reduces the number of states at the Fermi level, crucially, it still retains its metallic nature.

3 Uranium Dioxide (UO_2)

UO_2 has been extensively studied with many experimental and computational studies. Before considering hydrogen in UO_2, there is a need to assess the suitability of DFT for simulating stoichiometric UO_2. This chapter will describe the structure and relevant properties of UO_2 and give the details of the convergence tests and how well calculated properties compare to experimental values. Before the results are discussed and compared to experiment there is a short review of previous studies of UO_2.

3.1 UO_2 Literature Review

3.1.1 Structure

UO_2 has the fluorite structure, space group $Fm\bar{3}m$ (225), with a cubic unit cell, shown in Figure 3.1. Each unit cell contains four UO_2 formula units, with the uranium occupying face centred cubic positions and the oxygen in tetrahedral sites. Desgranges used neutron diffraction to determined a_0 as 5.468 Å [36] with a melting temperature of 3120 ± 30 K [287] and a density of 10.97 g cm^{-3} [287].

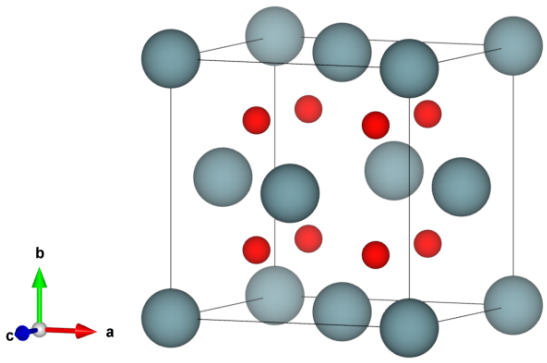

Figure 3.1: UO_2 unit cell. Uranium shown in blue and oxygen shown in red.

Is it commonly accepted that the fluorite structure of UO_2 is maintained until its melting point. However, the most recent work by Desgranges *et al.* [37] shows that UO_2 has local regions within the crystal structure which have lower local symmetry, $Pa\bar{3}$, this is used to explain some of the properties of UO_2 particularly the increase in heat capacity at approximately 1000 K, as well as the interesting thermoelectric properties displayed by UO_2.

At high pressure, Benedict *et al.* [32] report that, UO_2 undergoes a phase transition to an orthorhombic cotunnite structure, Figure 3.2, in a pressure range of

29 - 38 GPa. The structural fitting was unable to give an ambiguous structural assignment. It was able to determine the high pressure structure as one of two structures either; *Pnma* (a = 5.93, b = 3.51. c = 6.56 Å) or *Cmcm* (a = 3.41, b = 6.70. c = 6.07 Å). Later work by Idiri *et al.* [288] found a higher pressure phase transition at approximately 42 GPa and only the *Pnma* structure previously proposed corresponds to the phase observed, although the transition was not complete even at the highest pressure, 69 GPa.

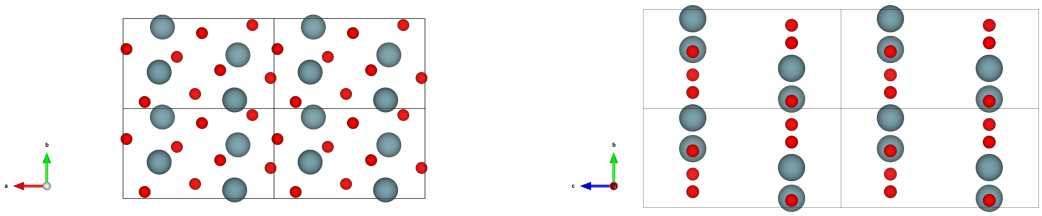

(a) **(b)**

Figure 3.2: High pressure cotunnite structure of UO_2. Uranium shown in blue and oxygen shown in red. [32]

Theoretical calculations on UO_2 and $UO_{2.03}$ found transition pressures of 18 GPa and 27 GPa, respectively, between cubic and orthorhombic phases [289]. This suggests that a reason for the large difference in reported phase transition pressures could be the stoichiometry of the samples.

Crowhurst *et al.* [290] have more recently measured a transition pressure of 35 GPa, but this transition was not complete until approximately 50 GPa. As the UO_2 samples were obtained from a single crystal which was grown approximately 30 years ago in 1985 it is likely that there is some degree of hyperstoichiometry. Therefore the different values for the transition pressure of fluorite UO_2 to cotunnite UO_2 is dependent on the O/U ratio and that the pressure to achieve complete conversion is higher with a larger O/U ratio.

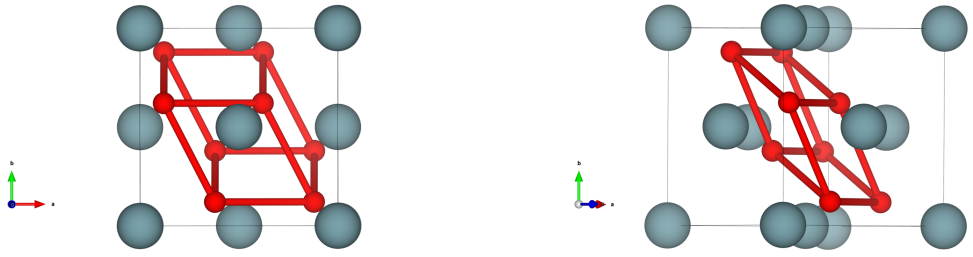

(a) **(b)**

Figure 3.3: High pressure and high temperature modified fluorite phase of UO_2. Uranium shown in blue and oxygen shown in red. [291]

When the structure of UO_2 was measured under both high temperature and high pressure by Gréaux *et al.* [291], the cotunnite phase reportedly previously [32, 288] was not observed. Instead a modified fluorite phase, Figure 3.3, $Pa\bar{3}$ (a = 5.329 Å) was observed at 18 GPa and an orthorhombic *Pbca* (a = 9.688 Å, b= = 5.332 Å, c = 5.350 Å) phase from 33 - 82 GPa, Figure 3.4.

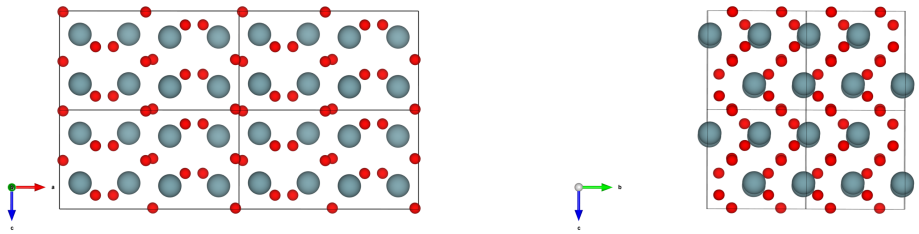

(a) (b)

Figure 3.4: High pressure and high temperature orthorhombic phase of UO_2. Uranium shown in blue and oxygen shown in red. [291]

These studies show that under high pressure and/or high temperatures the structure of UO_2 changes, this will have an effect on the bulk properties such as the bulk modulus, band gap and defect energies. However, as under normal nuclear fuel cycle conditions the high pressure phases are not observed, and the focus of this research is on how hydrogen behaves in the unmodified fluorite phase, they has not been considered, but represent an interesting class of materials worthy of study.

3.1.2 Elastic Properties

The bulk modulus of a material is defined as a material's resistance to uniform compression. A material's bulk modulus is determined by measuring the material's elastic constants. The bulk modulus can then be calculated by averaging the first nine elastic constants. However, it is also possible to derive equations to calculate the bulk modulus. These are a symmetry adapted simplification of averaging the first nine elastic constants. A cubic crystal has three unique elastic constants; C_{11}, C_{12} and C_{44}. The relationship between the elastic constants and the bulk modulus, for a cubic crystal, is given in equation 3.1 [270].

$$B = \frac{1}{3}(C_{11} + 2\ C_{12}) \tag{3.1}$$

Table 3.1 shows literature values for the bulk modulus of UO_2 from both experiment and theory. The experimental values are consistent with each other. There is a temperature dependence to the elastic constants, where C_{11} and C_{12} both increase with decreasing temperature to a maximum at approximately 80 K [35, 292].

There is then a rapid decrease in the values of C_{11} and C_{12} at the Néel temperature, before at increase below the Néel temperature. At temperatures below the Néel temperature the values of C_{11} and C_{12} are larger than at room temperature, therefore the theoretical methods may slightly overestimate the value of the bulk modulus. However, most of the theoretical calculations underestimate the values of the bulk modulus, some quite significantly. This usually comes from an underestimation of the C_{11} elastic constant, although in the case of rPBE there is also a significant underestimation of the C_{12} elastic constant.

The best theoretical value for the bulk modulus would appear to come from using the PBEsol+U functional [187], as this has the smallest difference from experiment at 0.37%. This occurs from a favourable cancellation of errors, the C_{11} elastic constant is underestimated and the C_{12} elastic constant is overestimated. Therefore

Table 3.1: Experimental and theoretical values for the unique elastic constants and bulk modulus of UO_2. Δ % is the percentage difference between the theoretical values and the experimental value [293] of the bulk modulus.

Method	**Temperature** (K)	$\mathbf{C_{11}}$ (GPa)	$\mathbf{C_{12}}$ (GPa)	$\mathbf{C_{44}}$ (GPa)	**BM** (GPa)	Δ %	**Ref**
Velocity of sound	298.15	395	121	64.1	212.3	-	[293]
Ultrasonic attenuation	20	400	125	58	216.6	-	[35]
Ultrasonic attenuation	80	403	125	55	217.6	-	[292]
Ultrasonic attenuation	200	399	123	63	215.0	-	[35]
Ultrasonic attenuation	200	396	123	64	213.0	-	[292]
Ultrasonic pulse superposition	296.15	389	118	59	209.0	-	[294]
PBE+U	-	382	130	54	214	0.8	[27]
PW91+U	-	361.2	114.7	63.9	197	-7.2	[270]
PBE+U	-	345.7	115.4	63.4	192.2	-9.5	[295]
PBE+U	-	343.1	121.3	62.7	209	-1.6	[296]
rPBE	-	370	86	69	180.7	-14.9	[297]
PBEsol+U	-	340.8	149.3	103.5	213.1	0.4	[187]
PBE+U	-	409.1	118.1	62.0	215.1	1.3	[187]

to understand fully if accurate elastic properties have been calculated the unique individual elastic constants also need to be examined.

This leaves the PBE+U functional, used by Dorado [27] and Brincat [187], with the best values for the bulk modulus and elastic constants when compared to experiment. However, as can be seen it is not just the functional which determines how well the bulk modulus is reproduced, as Sanati *et al.* [295] also used PBE+U but the value of the bulk modulus was lower than experiment by 9.5 %. This is likely due to a variation in the chosen input parameters.

3.1.3 Magnetic Properties

UO_2 is paramagnetic but undergoes a transition to an antiferromagnetic (AFM) ordering at 30.8 K [298]. A $1k$ collinear (CL) AFM was proposed by Allen [299], Figure 3.5a (Top). This was accompanied by a one dimensional Jahn-Teller distortion of the oxygen sub-lattice, Figure 3.5a (Bottom). Subsequent experimental work [300] revised this to a non-collinear (NCL) $2k$ AFM ordering, Figure 3.5b (Top), again with an oxygen sub-lattice distortion. The magnetic moment of the uranium ions in UO_2 has been determined as $1.74 \pm 0.02\ \mu_B$ [301].

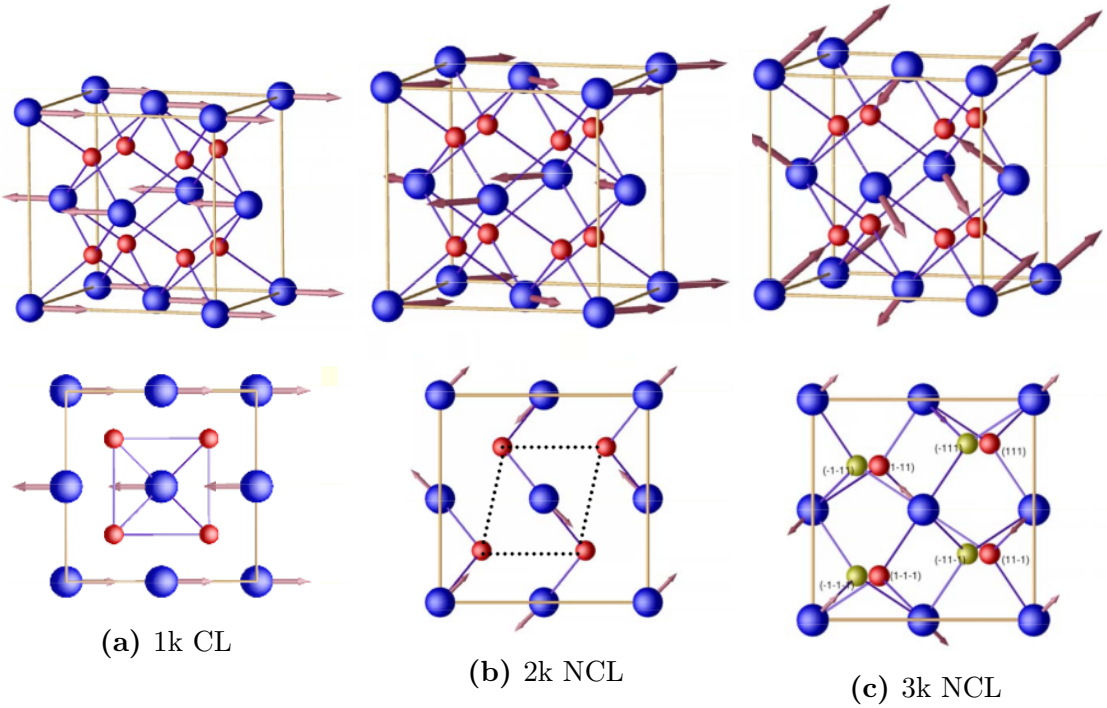

(a) 1k CL **(b)** 2k NCL **(c)** 3k NCL

Figure 3.5: (Top) 1k, 2k and 3k magnetic configurations. (Bottom) 1, 2 and 3 dimensional oxygen sub-lattice distortions. Uranium ions shown in blue and oxygen shown in red [302].

More recent experimental work has shown that the magnetic structure, which best matches the observed properties, is a $3k$ NCL ordering [303, 304], with a three dimensional oxygen sub-lattice distortion, Figure 3.5c.

Theoretical calculations of the magnetic structure UO_2 have found that the $3k$, with a three dimensional oxygen sub-lattice distortion, to have the lowest energy [187, 305–307]. Additionally, the calculated electric field gradient of the uranium ions only agreed with the experimental uranium electric field gradient for the $3k$ structure [305]. Experimental and theoretical evidence now points towards the magnetic structure of UO_2 below 30.8 K to be $3k$ NCL AFM, with a three dimensional oxygen sub-lattice distortion.

Since DFT calculations are at 0 K, the AFM ordering is of importance as this is the ground state. There is the potential that this is not relevant for to real systems at ambient or elevated temperatures which will have a different magnetic ordering. Recently, DFT calculations using a paramagnetic ordering in UO_2 have been reported [30] to assess the effect of a $1k$ AFM ordering on the properties compared to a paramagnetic (PM) ground state. This used the disordered local

moments approach, where the spins are randomly orientated. The study showed that, providing defect energies are not dependent on the magnetic ordering, the $1k$ AFM ordering used by the majority of studies on UO_2 is an excellent approximation for the PM ordering at ambient temperature. As the difference in energy between the AFM and PM states is a few meV/atom compared to the several eV energies of point defects.

3.1.4 Electronic Properties

A range of experimental techniques have been used to determine the electronic properties of UO_2, including X-ray Photoemission Spectroscopy (XPS) and Bremsstrahlung Isochromat Spectroscopy (BIS). UO_2 has been determined to be an insulator with a band gap of 2.1 eV [308–310]. Additionally, UO_2 is known to be a Mott-Hubbard insulator [310], this is where the top of the valence band and the bottom of the condition band are both composed of uranium states. For UO_2 this has been confirmed as a f-f transition, by a combination of X-ray absorption and first principle calculations [310].

Table 3.2 shows the range of values reported in the literature, for a variety of different theoretical approaches, to calculating the band gap of UO_2. The calculated value for the band gap of UO_2 is heavily dependent on the parameters and functional selected. The same functional can also produce very different values for the band gap depending on the parameters selected. All the LDA and GGA calculations include a Hubbard U parameter, this prevents the self-interaction error of LDA and GGA calculations which predict a metallic ground state. The value of the Hubbard U has a significant effect on the value of the calculated band gap. This is because it acts on the f-states and these form the top of the conduction and bottom of the valence band. Therefore by varying the U parameter the size of the band gap can be controlled. Both the LSDA+U underestimate the value for the band gap. The LDA calculations get closer, though for one of these it is a ferromagnetic (FM) configuration and the ground state of UO_2, at 0 K is AFM. While the LDA calculations are an improvement on the value of the band gap, over the LSDA+U calculations, these did involve imposing symmetry constraints on the system [311].

At higher levels of theory, it is possible to include a percentage of Hartree-Fock (HF) exchange and spin orbit coupling (SOC), where the amount of HF exchange needs to be considered as this greatly affects the values of the band gap. A value of 40 % HF exchange appears to be the best value for reproducing the experimental band gap, as this also agrees with the calculations of Brincat [187] who used the HSE functional with 40 % HF exchange. However, these levels of calculations are very computationally expensive, illustrated by the HSE calculation of Brincat which was performed on a three atom UO_2 unit cell.

Table 3.2: Theoretical and experimental literature values for the band gap of UO_2.

Method	Magnetic Ordering	Band Gap (eV)	Ref
XPS	-	2.1±0.1	[308]
XPS/BIS	-	2	[309]
XPS/BIS	-	2.1	[310]
LDA+*U* SOC	AFM	2.0	[312]
LDA+*U*	FM	2.1	[311]
LSDA+*U*	AFM	1.3	[239]
LSDA+*U*	AFM	1.75	[313]
PBE+*U*	AFM	1.94	[187]
PBE+*U*	AFM	2.8	[28]
PBE1PBE	FM	2.6	[314]
PBE 25% HF SOC	AFM	1.401	[315]
PBE 40% HF SOC	AFM	2.025	[315]
HSE 40% HF	FM	2.20	[187]
rTPSS	AFM	2.17	[187]

3.1.5 Vibrational Properties

The vibrational properties of UO_2 are also well characterised, having been subject to numerous investigations, using both Infra-Red [316, 317] and Raman spectroscopy [80, 318–321]. The IR spectrum of UO_2 shows one peak at 340 cm^{-1} (transverse optical), with a shoulder at 470 cm^{-1} (longitudinal optical) [316]. There is a single peak in the Raman spectrum of UO_2 which occurs at 445 cm^{-1}, corresponding to a triply degenerate T_{2g} vibration [80], this has been assigned as a U-O stretching vibration [318].

The reason for extensive number of studies of the IR and Raman spectrum of UO_2 is that it can provided detailed information about the oxidation of UO_2. This is because excess oxygen concentration causes the IR and Raman spectra to change with new peaks appearing [318, 319], characteristic of higher oxide phases. Thus, it is also possible to use this information to determine which uranium oxide phases are present [80].

Raman spectroscopy has been combined with X-ray diffraction (XRD) [321] to explain the structural evolution that occurs as the oxygen increases from UO_2 to $UO_{2.24}$. Four different structural transitions were determined. Below $UO_{2.05}$ excess oxygen is incorporated as isolated interstitials. Between $UO_{2.05}$ and $UO_{2.11}$ the excess oxygen rearrange to ordered defect clusters. As the excess oxygen approaches $UO_{2.11}$ the clusters reorganise to cuboctahedral clusters. This reorganisation is complete by $UO_{2.20}$, which leads to a new ordered superstructure containing oxygen vacancies (U_4O_{9-y}). These oxygen vacancies are then filled, at least until $UO_{2.24}$.

3.1.6 Intrinsic Point Defects

UO_2 rarely exists in a pure stoichiometric form, most is hyperstoichiometric as oxygen is readily absorbed from the atmosphere [31]. This oxidation initially results in the formation of intrinsic point defects, in the form of oxygen interstitials. Overall, there are four different possible intrinsic point defects in UO_2; oxygen interstitials (O_i), oxygen vacancies (V_O), uranium interstitials (U_i) and uranium vacancies (V_U). Equations 3.2-3.5 describe the expected formation mechanism for these defects.

$$\frac{1}{2}O_{2(g)} + 2U_U^x \xrightarrow{UO_2} O_i'' + 2U_U^{\cdot} \tag{3.2}$$

$$2U_U^x + O_O^x \xrightarrow{UO_2} V_O^{\cdot\cdot} + 2U_U' + \frac{1}{2}O_{2(g)} \tag{3.3}$$

$$U_{(s)} + 4U_U^x \xrightarrow{UO_2} U_i^{\cdot\cdot\cdot\cdot} + 4U_U' \tag{3.4}$$

$$5U_U^x \xrightarrow{UO_2} V_U'''' + 4U_U^{\cdot} + U_{(s)} \tag{3.5}$$

By far the most common of these defects is the O_i, as UO_2 will readily absorb oxygen from the atmosphere. Conversely, V_O and uranium point defects are particularly unfavourable, with large positive formation energies (Table 3.3). This results in the limit of hypostoichiometry in UO_2 being $UO_{1.98}$ [17]. Stoichiometries with a O/U ratio less than 1.98 are unstable and will separate to form uranium metal and hypostoichiometric UO_2.

The reason for isolated V_O defects being unfavourable is that they should lead to the formation of U^{3+} defects, however, there is no report of the formation of a uranium sesquioxide (U_2O_3), while there are reports of other actinide oxides forming sesquioxide phases (Pu_2O_3 [322, 323], Cm_2O_3 [324], Am_2O_3 [325]). This suggests that the formation of a U^{3+} state is particularly unfavourable in uranium oxides.

This is supported by DFT calculations of V_O in UO_2, where a single V_O should result in the formation of two U^{3+} ions. However, delocalised charges are reported in the literature [187, 326]. In contrast to these results Dorado *et al.* [29, 327] calculated the defect energies where there were localised U^{3+} defects. The localisation of the U^{3+} does not alter the result of the calculation significantly, giving similar formation energies to other literature values which did not use occupational matrix control (OMC) [29]. The localisation of the U^{3+} was achieved by using OMC, this sets the $5f$ occupancies and the energy calculated with the given electronic configuration.

Schottky and Frenkel defects are formed of a number of individual point defects, Equations 3.6 - 3.8 describe the formation of an O Frenkel pair, U Frenkel pair and Schottky defect, respectively.

$$O_O^x \xrightarrow{UO_2} V_O^{\cdot\cdot} + O_i'' \tag{3.6}$$

$$U_U^x \xrightarrow{UO_2} V_U^{\cdot\cdot\cdot\cdot} + U_i'''' \tag{3.7}$$

$$\emptyset \xrightarrow{UO_2} 2V_O^{\cdot\cdot} + V_U^{\cdot\cdot\cdot\cdot} \tag{3.8}$$

A Frenkel pair represents when an ion becomes displaced form its lattice site forming a vacancy-interstitial pair. The Schottky defect is the removal of a formula unit from the bulk generating a set of vacancy sites. There are two ways to calculate the energies of Frenkel and Schottky defects either explicitly or by summing the values for the appropriate individual point defect calculations.

All the DFT calculations in Table 3.3 were performed in a 2 x 2 x 2 expansion of the cubic unit cell, except for three earlier reports which were in a 2 x 1 x 1 [285, 328, 329]. All the defects considered were neutral isolated point defects, except for the work of Crocombette *et al.* [330, 331] where charged defects were considered. All the potential model calculations considered the defects at infinite dilution.

When calculating Frenkel and Schottky defect energies by summing the appropriate equations from Equations 3.2 - 3.5 this results in there also being oxidation and reduction of the lattice which is not present when these defects form. For example calculating the energy of an O-Frenkel pair by summing Equations 3.2 and 3.3 would results in $2U^{3+}$ and $2U^{5+}$ which would cancel out in a crystal. It is possible to account for this using one of two approaches; the first is to place both defects within the same super-cell [332], the second is to explicitly alter the charge of the cell containing isolated defects [333]. The first approach resulted in a lowering for the Frenkel formation energies to 10.2 and 2.8 eV, for U and O respectively, compared with 14.2 and 4.0 eV, calculated from isolated charge neutral defects [332]. In the second approach by considering charged defects it was found that energy of the Frenkel and Schottky defects was lower for the charge defects compared with the charge neutral defects [333]. However, it was also reported that the charge neutral defect energies gave a better agreement with experiment than the charged defect calculations.

The calculations of Frenkel and Schottky defects in this thesis uses the isolated charge neutral defects approach and is therefore directly comparable to the majority of the DFT literature data presented in Table 3.3, with the exception of the previously mentioned calculations which use charged defects. Although, whilst the energies are not directly comparable the effect of altering the charge appears to be a shift to the energies and not a change in the energetic ordering of the defects. Therefore, it is possible to compare the predicted ordering of the defects.

Table 3.3: Literature values for isolated point defects, Frenkel pairs and Schottky trio defects in UO_2.

Method	Defect Energy (eV)						
	O_i	V_O	U_i	V_U	O Frenkel	U Frenkel	Schottky
Exp[334, 335]	-	-	-	-	4.6 ± 0.5	-	-
Exp[336]	-	-	-	-	3.0-4.6	8.5-9.6	6.0-7.0
Exp[337]	-	-	-	-	1.55-2.7	4.75-6.3	2.00-2.3
LDA[285]	-	-	-	-	3.9	10.7	5.8
LDA[328]	-3.3	10.0	11.5	19.1	5.9	22.1	14.5
GGA[329]	-2.5	6.1	7.0	4.8	3.6	11.8	5.6
LSDA+*U*[326]	-2.2	7.5	8.2	9.1	5.4	17.2	10.6
LSDA+*U*[338]	-	-	-	-	5.38	14.34	10.53
GGA+*U*[332]	-1.6	5.6	11.5	19.1	4.0	14.2	17.1
GGA+*U*[339]	-2.44	5.06	13.48	-6.50	2.61	6.974	3.62
GGA+*U*[333]	-1.34	5.29	8.04	7.04	3.95	15.08	7.6
PBE+*U*[340]	-0.44	4.46	4.70	8.45	-	-	-
PBE+*U*[29]	0.1	5.67	-	-	5.77	-	-
PBE+*U*[327]	-0.05	5.30	-	-	5.25	-	-
PBE+*U*[331]	-1.4	5.6	-	-4.7	4.2	-	6.4
PBE+*U*[187]	-1.76	5.77	4.13	7.75	2.00	5.94	6.43
PBE0[330]	-0.75	5.0	-	-4.25	6.4	-	9.9
PM[341]	-11.05	17.17	-60.06	81.57	5.31	18.54	10.32
PM[342]	-11.35	16.44	-61.63	79.98	5.09	18.35	9.78
PM[343]	-12.15	16.91	-60.82	80.22	4.76	19.40	11.33
PM[344]	-	-	-	-	3.5	12.1	4.5
PM[345]	-	-	-	-	1.6	6.3	2.2
PM[346]	-	-	-	-	3.6-3.8	10.4	2.5-3.0
PM[337]	-11.52	16.14	-60.91	78.12	2.19	8.15	2.62
PM[347]	-	-	-	-	4.4	6.1	9.4
PM[348]	-	-	-	-	3.4	10.3	5.2

3.2 Calculated Properties

Before modelling hydrogen in UO_2 it is important to test whether the property calculated is specific to the functional that has been chosen or is consistent across a variety of functionals. Therefore in the following section a number of calculated properties of UO_2 will be compared for a range of cell sizes and functionals. There will also be calculations which include the effects of SOC. There are a range of functionals available in the VASP code. These include, but are not limited to, PBE [184], revised PBE [349] (rPBE), the modification to PBE for solids PBEsol [185], Perdew-Wang 91 [230] (PW91) and the functional developed by Mattsson and Armiento (AM05) [350, 351]. The AM05 functional is not used as this was unable to successfully minimise H_2 as a reference state to determine the formation energies of hydrogen defects.

3.2.1 Convergence Tests

In this thesis four different sized simulation cells of bulk UO_2 are used; a single unit cell (12 atom) shown previously in Figure 3.1, a 2 x 2 x 2 expansion of the 12 atom unit cell (96 atoms) Figure 3.6c, a reorientation of the cubic cell along a <111> axis which was then expanded 2x1x1 (36 atoms) Figure 3.6a, and a reorientation of the cubic cell along a <110> axis which was then expanded 2 x 1 x 2 (48 atoms) Figure 3.6b.

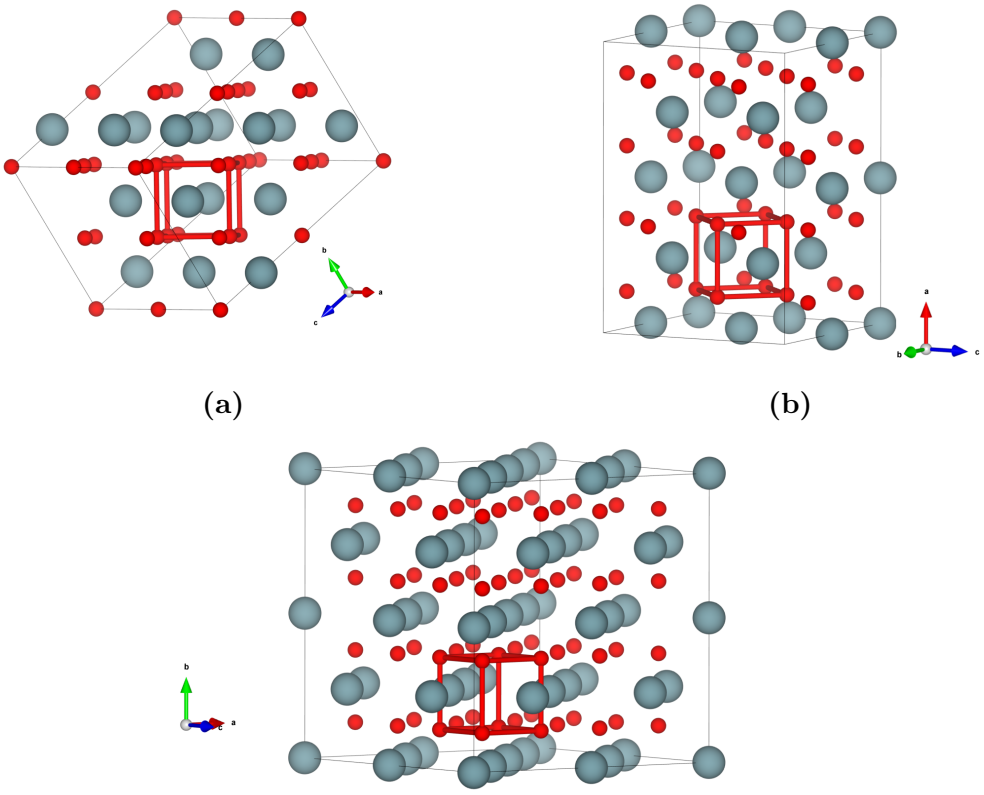

(a) **(b)**

(c)

Figure 3.6: 36 atom (3.6a), 48 atom (3.6b) and 96 atom (3.6c) UO_2 cells. Uranium shown in blue and oxygen shown in red. Bonds shown for clarity.

As a test to verify that the selected parameters provide an accurate representation of the system being studied it is important to ensure that convergence of the parameters has been achieved. These parameters include the cut-off energy and k-point sampling meshes. This ensures that a model with sufficient accuracy is computed within a reasonable amount of CPU time. Table 3.4 shows the cut-off energy ranges and k-point meshes used for the four different bulk UO_2 simulations cells. The results of the convergences tests are displayed in Figure 3.7, as k-point density verses the calculated energy per UO_2 formula unit, in the simulation cell.

Table 3.4: Energy cut-off ranges and k-point mesh tests for bulk UO_2 models used in this thesis. The energy cut-off was varied in 100 eV steps and the k-point mesh was varied uniformly, in 1x1x1 steps, between the smallest and largest meshes.

System		**12 atom**	**36 atom**	**48 atom**	**96 atom**
Energy Cut-off Range (eV)		400 - 600	300 - 600	300 - 600	300 - 500
***k*-point meshes**	**Smallest**	3x3x3	1x1x1	1x1x1	1x1x1
	Largest	6x6x6	6x6x6	5x5x5	4x4x4

From the convergence tests it is clear that for a 12 atom unit cell that an energy cut-off of 400 eV is too low. However, when the energy cut off is increased to 500 eV the energy converges with a k-point density of 0.1 k-points/Å^3. For the 36 atom bulk system, Figure 3.7b, as with the 12 atom system a cut-off energy of 400 eV is not enough to reach convergence. Again, when a 500 eV cut off energy is used convergence is reached at a k-point density of 0.07 k-points/Å^3. Figure 3.7c, shows the convergence tests for the 48 atom bulk UO_2 simulation cell. From the 400 eV cut off upwards good convergence is observed, with the energy reaching a convergence at 0.02 k-points/Å^3. In order to maintain a similar k-point density to the previous simulation cells the k-point density was increased to 0.05 k-points/Å^3.

Finally, for the 96 atom super cell as this is a simple 2 x 2 x 2 expansion of the 12 atom unit cell the reciprocal lattice vectors will be half the magnitude and as such the k-point mesh of the single unit cell can be halved. The final consideration with the 96 atom cell is that a 500 eV cutoff energy requires a large amount of computationally very expensive. In order to reduce this expense a lower cut off energy of 400 eV has been chosen as this still provides accurate results at a reduced computational expense. Employing the lower energy cut-off results in an energy difference of 0.02 eV per UO_2 formula unit between the 12 atom and 96 atom simulation cells. Employing this lower cut off energy criteria is consistent with the literature on simulation of UO_2 in a 2 x 2 x 2 expansion of the unit cell [21, 25, 187]. This gives an energy of -29.34 eV/UO_2 for the 96 atom cell, compared to -29.32 eV/UO_2 for the 12 atom system and -29.35 eV/UO_2 for both the 36 and 48 atom systems.

Table 3.5, summarises the selected energy cut values and k-point meshes chosen for this work. The rest of this chapter will now asses how well these parameters reproduce experimental properties of UO_2 as a validation of the chosen parameters

Table 3.5: Selected energy cut off and k-point meshes for bulk UO_2 systems used in this work.

System	12 atom	36 atom	48 atom	96 atom
Energy Cut-off (eV)	500	500	500	400
***k*-point Mesh**	4x4x4	4x4x4	4x4x4	2x2x2

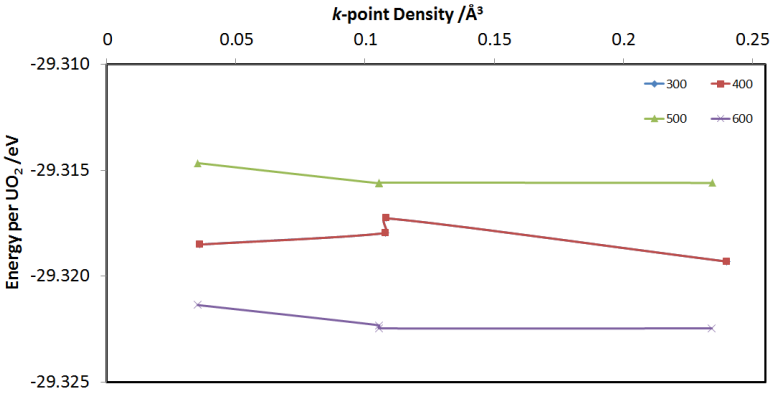

(a) 12 atom UO_2 simulation cell.

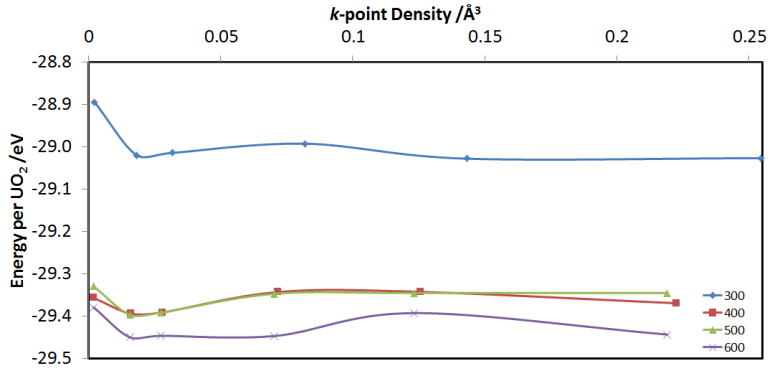

(b) 36 atom UO_2 simulation cell.

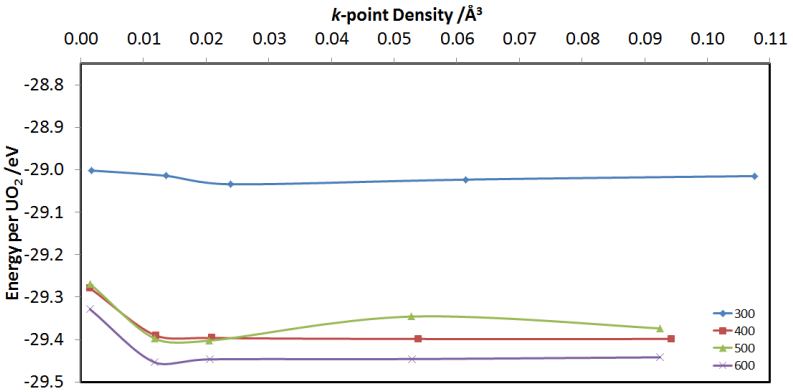

(c) 48 atom UO_2 simulation cell.

Figure 3.7: Convergence tests of the 12, 36 and 48 atom UO_2 simulation cells.

3.2.2 Structure

Table 3.6 compares the calculated lattice parameters for a 12 atom unit cell of UO_2 using a range of different functionals. All the different functionals perform in a comparable manner, there is a marginal expansion of the lattice in all directions and there is a tetragonal distortion present in all. Though the rPBE+U comes the closest to reproducing a cubic lattice, however, it has the largest volume expansion compared to experiment.

Table 3.6: Lattice Constants of UO_2 for a range of functionals.

Method	***a*** **(Å)**	***b*** **(Å)**	***c*** **(Å)**	**Volume (Å^3)**	**Volume per U (Å^3)**
Exp [36]	5.468	5.468	5.468	163.49	40.81
PBE+*U*	5.57	5.50	5.57	170.60	42.65
PBEsol+*U*	5.50	5.44	5.50	164.56	41.14
PW91+*U*	5.57	5.49	5.57	170.32	42.58
rPBE+*U*	5.57	5.56	5.57	172.49	43.12

Table 3.7 shows the calculated lattice parameters, volume and volume per UO_2 unit for the 12, 36 and 96 atom cells compared with experiment. In all cases the calculated lattice parameters are a small overestimation of the experimental lattice parameters. This is a known effect of the GGA+U methodology which tends to overestimate the lattice parameter and has been reported previously using the DFT+U methodology [27, 295, 313].

In addition to the small overestimation of the lattice parameter there is also a hexagonal distortion of the lattice present, this results in the b lattice parameter being shorter than the a and c lattice parameters. The distortion is caused by the simplified magnetic ordering which is used in the calculation (1k collinear configuration), Figure 3.5a. The distortion occurs because there is an overestimation of the attraction between the layers of opposite magnetic spins. This distortion however is another known effect of the methodology used and has been reported in the literature [187, 306, 313].

It possible to remove the distortion caused by the $1k$ AFM ordering, this involves including SOC which allows for three dimensional rotation of the magnetic vector. As can be seen for the 12 atom unit cell the inclusion of SOC results in a consistent expansion to all three lattice vectors. Additionally, the use of hybrid functionals, such as PBE0 or HSE, can prevent the occurrence of the tetragonal distortion [187, 352]. Though these methods are computationally more expensive and the small improvement to the lattice parameter itself does not warrant the extra cost.

Table 3.7: Comparison of calculated and experimental lattice parameters, volume and volume per UO_2 unit for 12, 36, 48 and 96 atom cells. Calculated using PBE+U functional. † Experimental unit cell parameters, for the 36 atom and 48 atom (<111> and <110> orientations, respectively), were calculated by reorientation of a cubic unit cell using METADISE [244]. ‡ Experimental parameters for the 96 atom cell calculated by doubling experimental cubic unit cell. Numbers in parenthesis are the percentage difference to experimental values.

	12 atom		
	Exp	**CL**	**SOC**
***a* (Å)**	5.468	5.47 (1.9)	5.55 (1.5)
***b* (Å)**	5.468	5.50 (0.6)	5.55 (1.5)
***c* (Å)**	5.468	5.47 (1.9)	5.55 (1.5)
Volume (Å^3)	163.49	170.60 (4.4)	170.95 (4.6)
Volume /U (Å^3)	40.87	42.65 (4.4)	42.74 (4.6)
	36 atom		
	Exp†	**CL**	**SOC**
***a* (Å)**	7.72	7.87 (1.9)	7.83 (1.4)
***b* (Å)**	6.69	6.76 (1.1)	6.80 (1.6)
***c* (Å)**	9.46	9.60 (1.5)	9.60 (1.5)
Volume (Å^3)	488.58	510.73 (4.5)	511.14 (4.6)
Volume /U (Å^3)	40.71	42.56 (4.5)	42.60 (4.6)
	48 atom		
	Exp†	**CL**	**SOC**
***a* (Å)**	11.14	11.00 (-1.6)	11.10 (-0.4)
***b* (Å)**	7.83	7.87 (0.5)	7.82 (-0.1)
***c* (Å)**	7.83	7.87 (0.5)	7.87 (0.5)
Volume (Å^3)	682.98	681.31 (-0.3)	683.13 (0.1)
Volume /U (Å^3)	42.69	42.58 (-0.3)	42.70 (0.1)
	96 atom		
	Exp‡	**CL**	**SOC**
***a* (Å)**	10.94	11.05 (1.0)	-
***b* (Å)**	10.94	10.93 (-0.1)	-
***c* (Å)**	10.94	11.05 (1.0)	-
Volume (Å^3)	1309.34	1334.58 (1.9)	-
Volume /U (Å^3)	40.92	41.71 (1.9)	-

3.2.3 Elastic Properties

Table 3.8 shows the predicted independent elastic constants and bulk modulus for UO_2, using a range of functionals. The PBE+U functional gives very good agreement with experimental values of the bulk modulus and performs better than when SOC is included. However, this largely comes down to PBE+U SOC significantly underestimating the C_{11} elastic constant. For the overall bulk modulus the best value is the PBEsol+U functional, however, there is a significant overestimation of the C_{44} constant. The PBEsol+U functional also had the smallest predicted lattice constants, as would be expected from this functional, as it was designed to reduce the lattice expansion of the PBE functional. Correspondingly, the smallest predicted bulk modulus is for rPBE+U, this functional had the largest predicted lattice constants and hence volume, of all the functionals.

Table 3.8: Experimental and predicted independent elastic constants and bulk modulus for UO_2. A 12 atom UO_2 unit cell was used with a range of functionals, the effects of SOC were included for the PBE+U functional.

Method	**Independent Elastic Constants (GPa)**						**Bulk Modulus (GPa)**	
	$\mathbf{C_{11}}$	$\Delta\%$	$\mathbf{C_{12}}$	$\Delta\%$	$\mathbf{C_{44}}$	$\Delta\%$		$\Delta\%$
Experiment [35]	399	-	123	-	63	-	215.0	-
PBE+U	378.2	-5.2	114.1	-7.2	61.3	-2.7	200.2	-6.9
PBE+U SOC	359.0	-10.0	113.5	-7.7	59.6	-5.4	195.4	-9.1
PBEsol+U	390.1	-2.2	131.0	6.5	79.4	21.6	214.2	-0.4
PW91+U	369.6	-7.4	116.0	-5.7	71.7	13.8	195.5	-9.1
rPBE+U	353.5	-11.4	109.0	-11.4	60.5	-4.0	190.0	-11.6

3.2.4 Magnetic Properties

The experimental value of the magnetic moment of the uranium ions, below the Néel temperature, is 1.74 μB [305]. This is the sum of the orbital and spin components. As previously mentioned this work uses a simplified $1k$ AFM ordering, which only accounts for the spin component. For all the bulk UO_2 systems used, with the $1k$ AFM ordering, the calculated value of the magnetic moment is 2.00 μB, as shown in Table 3.9. This is a slight over estimation, however, agrees well with experiment. As with the Hubbard correction the calculated magnetic moment is affected by the choice of projector scheme used, this is discussed in Section 2.1.1.5. By comparing the calculated and experimental values for the magnetic moment it is possible to have confidence that the choice of projector used is a good representation of the system, as the predicted magnetic moments match well with experimental values.

If SOC is included the number of possible magnetic configurations increases, Figure 3.8 shows the calculated energy difference for all the possible magnetic configurations and oxygen sub-lattice distortions. As can be seen the $3k3k$ magnetic ordering is significantly more stable than the other orderings. Using the $3k3k$ magnetic ordering the predicted values (spin 1.54 μB, orbital -3.25 μB and total 1.71 μB) compares very well to previously reported calculations using the all electron code

WIEN2k [305] (spin 1.80 μB, orbital -3.55 μB and total 1.75 μB). As the cell simulation cell size is increased the calculated total magnetic moment improves to become the reported experimental value, of 1.74 μB.

Table 3.9: Experimental and calculated total magnetic moment and the magnitude of the spin and orbital contributions, for the uranium ions in a 12, 36, 48 and 96 atom cells. Calculated using PBE+U functional. The magnetic ordering and oxygen sub-lattice distortion is given by nknk; where the first nk refers to the alignment of the magnetic moment and the second denotes along how many lattice vectors the oxygen sub-lattice has been distorted. For a diagram of the different magnetic orderings see Section 3.1.3.

UO_2 Cell	**Magnetic Ordering**	**Spin Only (μB)**	**Orbital (μB)**	**Total Magnetic Moment (μB)**
Exp [305]	-	-	-	1.74
12 atom	**1*k*0*k***	1.99	-	1.99
	3*k*3*k*	1.54	-3.21	1.67
36 atom	**1*k*0*k***	2.00	-	2.00
	3*k*3*k*	1.54	-3.25	1.71
48 atom	**1*k*0*k***	2.00	-	2.00
	3*k*3*k*	1.53	-3.27	1.74
96 atom	**1*k*0*k***	1.99	-	1.99

An additional advantage of including SOC is that the tetragonal distortion caused by the 1k magnetic ordering is removed, however inclusion of SOC results in approximately a 2400% increase in calculation time. Thus, as the improvement in the description of UO_2 with the inclusion of SOC, is small compared to the increased computational cost, SOC will be used to confirm important results found using the 1k co-linear magnetic configuration are consistent with the inclusion of SOC. In addition previously reported work has shown the effect of SOC to be negligible on the structure, relative stability and electronic properties of UO_2 [353].

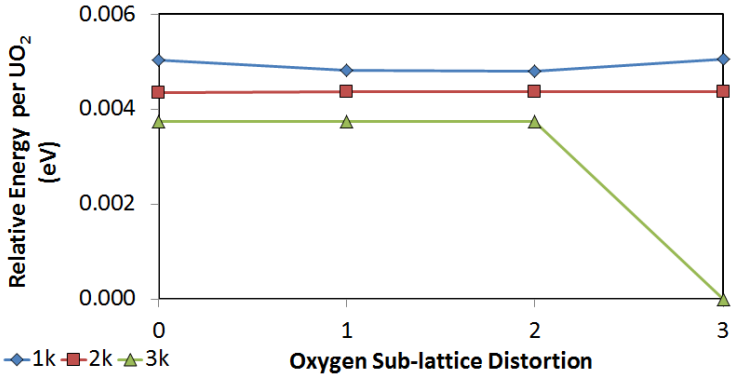

Figure 3.8: Calculated energy different for $1k$, $2k$ and $3k$ magnetic configurations and $1k$, $2k$ and $3k$ oxygen sub-lattice distortions, in a 12 atom UO_2 atom cell. The magnetic ordering is given by each line and the oxygen sub-lattice distortion by the position along the x-axis. The lowest energy configuration ($3k3k$) has been set to zero. Lines have been added to highlight the points.

Finally, Table 3.10 compares the calculated spin only magnetic moments for a range of different functionals. All the functionals reproduce a magnetic moment of 2 μB per uranium ion in both the 12 and 96 atom simulation cells.

Table 3.10: Spin only contribution to the magnetic moment in a 12 and 96 atom UO_2 for a range of functionals.

Functional	**Magnetic Moment μB**	
	12 atom	**96 atom**
PBE+U	1.99	1.99
PBEsol+U	1.99	1.99
PW91+U	2.00	1.98
rPBE+U	2.00	1.99

3.2.5 Electronic Properties

UO_2 is a Mott-Hubbard insulator, where the top of the valence band and bottom of the conduction band are composed of $5f$ uranium states [310], with a band gap of 2.1 eV [308]. Figure 3.9 shows the partial density of states (pDOS) for the spin only UO_2 simulation cells, with the calculated values for the band gap listed in Table 3.11. All pDOS calculations reproduce the Mott-Hubbard insulating nature of UO_2, however, the 12 atom unit cell significantly underestimates the band gap. This is due to a large tail in the conduction band, compared to the large systems predicted conduction bands. Predicting the shape of the conduction band is more difficult for DFT techniques, as these states are empty and therefore do not contain any electron density. There is also the appearance of a large gap between -2 and -3 eV for the 12 atom system, this is made to look much larger than it is on the graph due to the scaling, the actual gap distance is $\approx$0.25 eV.

There is variation in the shape of the DOS especially between the cubic (12 and 96 atom) and orthorhombic (36 and 48 atom) systems, this is most prevalent for the O p-states between -2 - -7 eV. This is likely due to a magnetic superstructure effect, which in the orthorhombic cells does not fit within the re-orientated unit cell, but is captured by the cubic systems. When SOC is included the DOS (Figure 3.10) shows a better agreement between the cubic and orthorhombic cells. This can be attributed to the distortion caused by alternating planes of opposing magnetic spins being removed, which is most prevalent for the 12 atom system as the distortion is the most significant in this system. Overall, the variation in DOS between the cubic and orthorhombic systems is a combination of the tetragonal distortion and a magnetic superstructure which is not fully captured by using the orthorhombic simulation cells. Importantly, this difference in the pDOS does not have a significant effect on the predicted band gap. For the larger simulation cells there is a small over estimation of the band gap. This decreases as the system size increases until the 96 atom UO_2 cell reproduces the experimental band gap.

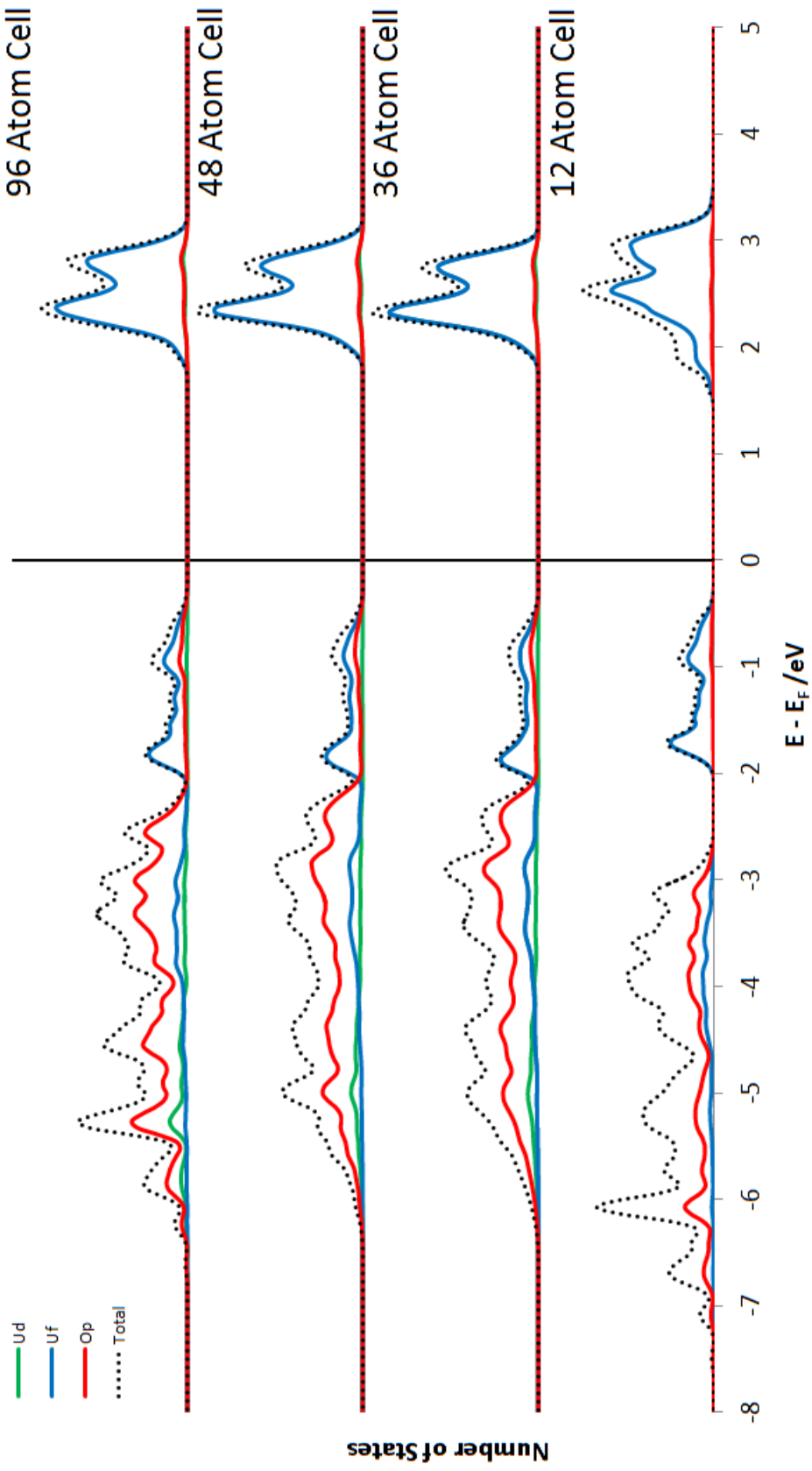

Figure 3.9: Partial DOS for $1k$ AFM 12, 36, 48, and 96 atom UO_2 systems calculated without SOC. Only the spin up channel shown as the spin down is identical. The Fermi energy has been set to 0 eV. Calculated using PBE+U functional.

Table 3.11: Calculated values of the band gap in UO_2 for the 12, 36, 48 and 96 atom systems using the spin only and SOC formalisms. SOC was not included for the 96 atom system due to computational cost. Calculated using PBE+U functional.

UO_2 System	**Band Gap (eV)**	
	Spin Only	**SOC**
12 atom	1.68	2.17
36 atom	2.25	2.18
48 atom	2.19	2.18
96 atom	2.12	-
Exp [308]	2.1	

The pDOS for the 12, 36 and 48 atom simulation cells including SOC is shown in Figure 3.10. As with the spin only pDOS all the systems reproduce the Mott-Hubbard insulating nature. The inclusion of SOC has the largest effect on the 12 atom unit cell where the tail in the conduction band is removed. The other effect of including SOC is that now for all systems virtually the same band gap is predicted (2.18 eV), which is in very good agreement with experiment.

The calculated pDOS for a range of functionals is shown in Figure 3.11, all functionals reproduce the Mott-Hubbard insulating nature. The calculated band gap values are shown in Table 3.12. The PBE+U functional reproduces the band gap as would be expected, due to the Hubbard parameter being determined to reproduce the band gap. Both PW91+U and rPBE+U both underestimate the band gap by 0.2 eV. The PBEsol+U functional significantly underestimates the band gap by 0.4 eV. As with the 12 atom PBE+U unit cell this appears to come from a tail in the conducting states.

Table 3.12: Calculated band gap of a 96 atom UO_2 cell for a range of functionals.

Functional	**Band Gap (eV)**
PBE+U	2.12
PBEsol+U	1.67
PW91+U	1.91
rPBE+U	1.99

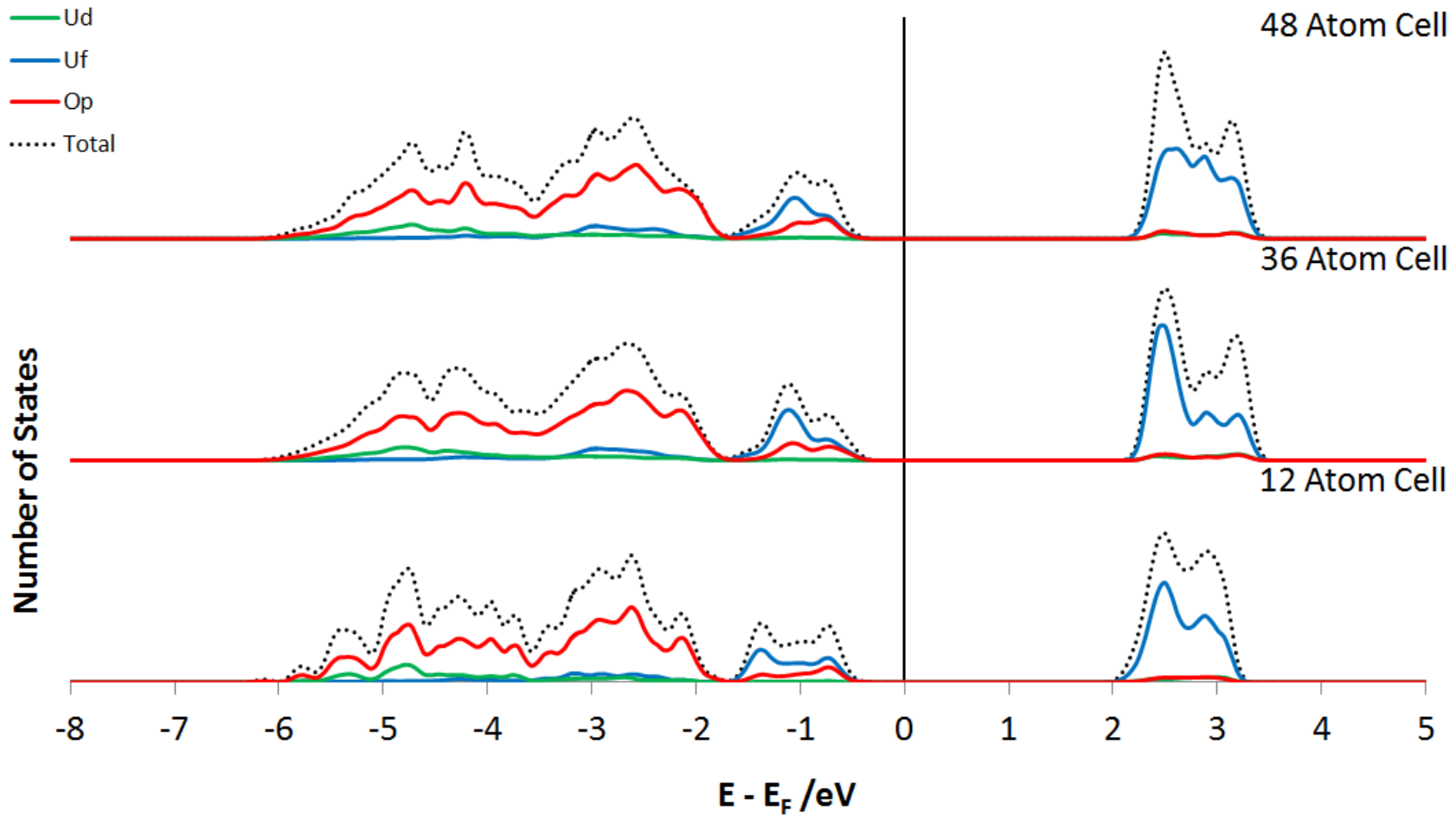

Figure 3.10: Partial DOS for AFM 12, 36 and 48 atom UO_2 systems calculated with SOC. The Fermi energy has been set to 0 eV. Calculated using PBE+U functional.

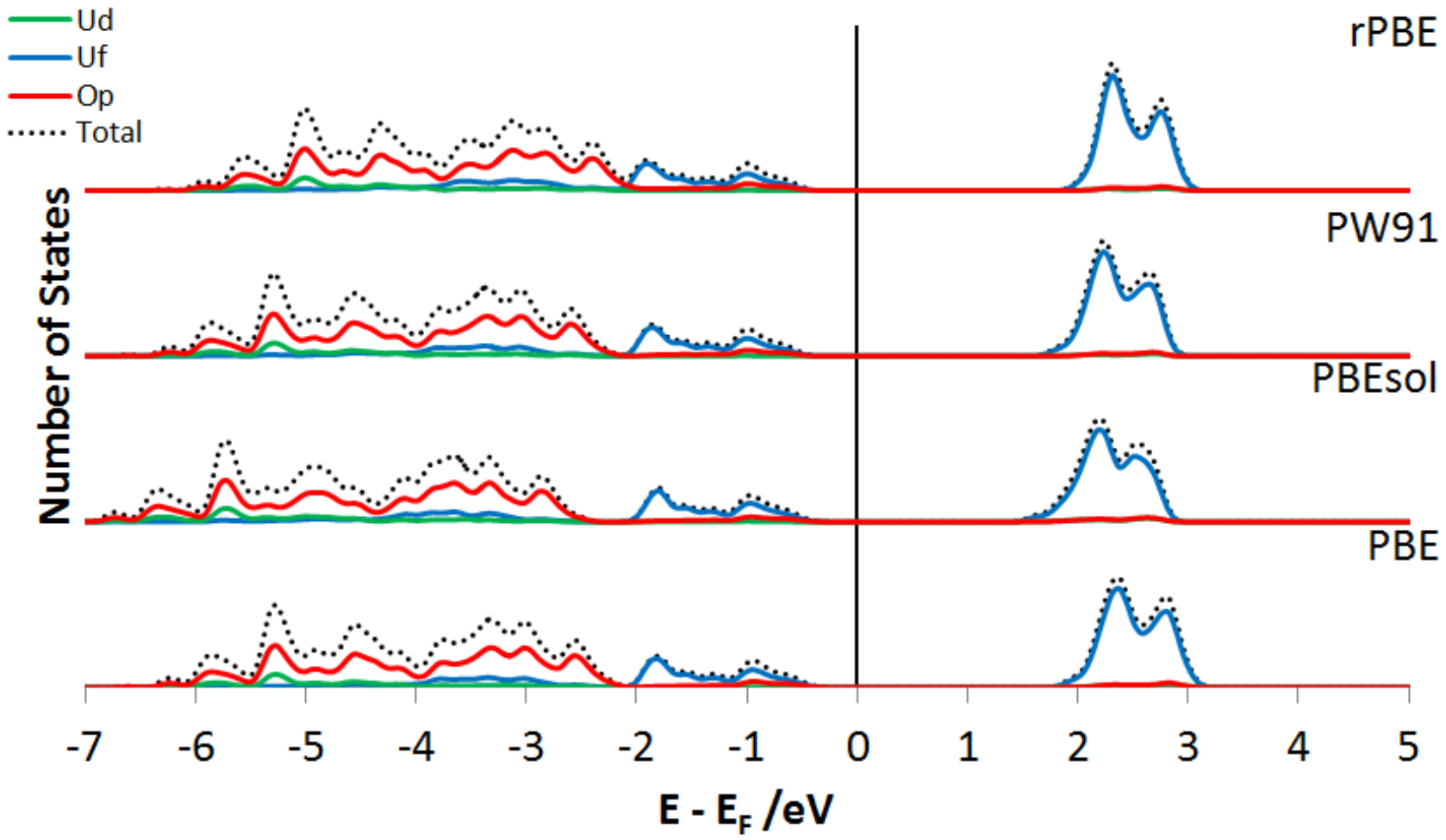

Figure 3.11: Partial DOS for 96 atom UO_2 systems calculated with a range of functionals. Only the spin up channel shown as the spin down is identical. The Fermi energy has been set to 0 eV.

3.2.6 Vibrational Properties

The infra-red spectrum for UO_2 has been calculated using a range of functionals and the spectrum is displayed in Figure 3.12. The values of the peaks are listed in Table 3.13. Experimentally, UO_2 has a single IR peak in the region of 280 cm^{-1} [308]. All the functionals predict a peak that is shifted to a lower wave number, except for PBEsol+U. The PBEsol+U spectrum predicts two separate peaks, the reason for this split is the tetragonal distortion that occurs due to the 1k AFM magnetic ordering, as the PBE+U SOC calculation has a single peak. The PW91+U and PBE+U functionals both show slight shoulders but do not have a clear separation of peaks, again due to the tetragonal distortion. The rPBE+U shows a single peak with no shoulder and again this can be related to the lack of a tetragonal distortion in the calculated lattice parameter. The shift to a lower wave number appears to be related to the calculated lattice parameter. The greater the expansion of the lattice predicted, by a functional, the lower the wave number at which the peak is predicted to occur.

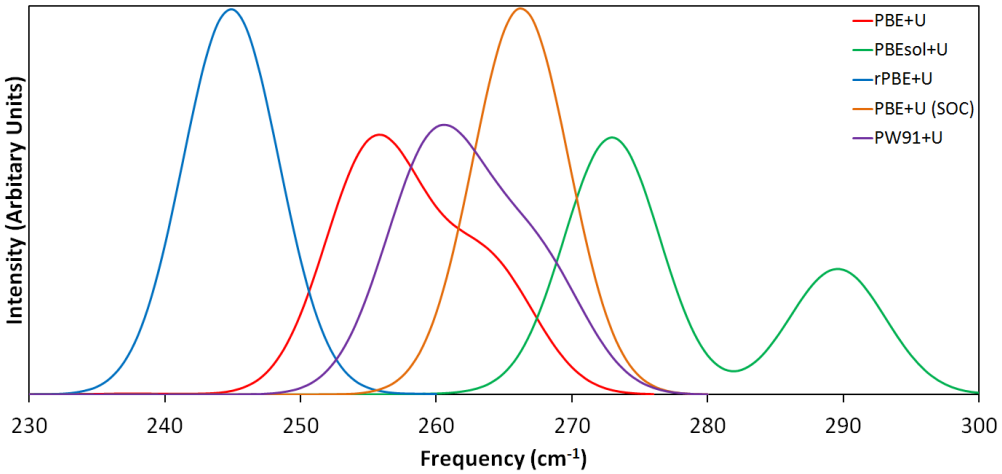

Figure 3.12: Calculated infra-red spectrum for UO_2 with a range of functionals and 1k AFM ordering.

Table 3.13: Experimental and calculated infra-red peaks.

		IR peak (cm^{-1})
Experimental	Axe and Petit [354]	278 ± 2
	Schoenes [355]	280 ± 2
Theoretical	PBE+U	261, 269
	PBE+U (SOC)	266
	PBEsol+U	273, 290
	PW91+U	263, 270
	rPBE+U	250

3.2.7 Point Defects

Table 3.14 summarises the calculated isolated point defect, Frenkel and Schottky defects for UO_2, using a range of functionals. All defects were calculated using the 96 atom UO_2 simulation cell. All of the defects calculated here are charge neutral. The addition or removal of a uranium or oxygen atom causes a significant change to the stoichiometry of the unit simulation cell; $UO_{2.03}O_i$, $UO_{1.97}V_O$, $UO_{1.94}U_i$ and $UO_{2.06}V_U$. All functionals predicted the same ordering of defect energies, except for rPBE+U where the uranium interstitial (U_i) is higher in energy than the oxygen vacancy (V_O). However, the same ordering of Frenkel and Schottky energies (O-Frenkel < Schottky < U-Frenkel) as experiment is achieved for all functionals.

All the functionals predict that the more favourable defect is an oxygen interstitial (O_i), this is accompanied by the oxidation of two U^{4+} to U^{5+}. This is consistent with the oxidation of UO_2 which occurs under atmospheric conditions. The V_O defect was accompanied by the delocalisation of the charge over four uranium ions rather than localisation to form two U^{3+} defects, which is consistent with the literature on the formation of U^{3+} being unfavourable. For the U_i defect as with the V_O there is a delocalisation of the charge across the uranium ions, though one uranium ion is fully reduced to U^{3+}. In the case of a uranium vacancy (V_U) four uranium ions were oxidised to U^{5+}. This further supports the ease of uranium oxidation in UO_2 compared with the reduction of uranium to U^{3+}.

Table 3.14: Calculated formation energy of isolated point defects, oxygen and uranium Frenkel defects and Schottky defects in a 96 atom UO_2 cell for a range of functionals. Frenkel defect energies refer to the entire defect and the Schottky defect energies are given per individual defect (total energy divided by three), as is the literature convention. Selected theoretical literature references are also included for comparison. A full table of literature values is presented in Table 3.3.

	Defect Formation Energy (eV)						
	O_i	**V_O**	**U_i**	**V_U**	**O-Frenkel**	**U-Frenkel**	**Schottky**
Exp [336]	-	-	-	-	3.0-4.6	8.5-9.6	6.0-7.0
GGA+U [332]	-1.6	5.6	11.5	19.1	4.0	14.2	17.1
GGA+U [339]	-2.44	5.06	13.48	-6.50	2.61	6.974	3.62
GGA+U [333]	-1.34	5.29	8.04	7.04	3.95	15.08	7.6
PBE+U [340]	-0.44	4.46	4.70	8.45	-	-	-
PBE+U [187]	-1.76	5.77	4.13	7.75	2.00	5.94	6.43
PBE+U	-1.23	5.77	3.00	8.19	4.54	11.19	6.58
PBEsol+U	-1.03	4.00	3.32	8.26	2.98	11.58	5.42
PW91+U	-0.98	5.38	3.78	8.88	4.40	12.66	6.55
rPBE+U	-1.02	4.34	4.86	8.45	3.32	13.31	5.71

The study of point defects experimentally is extremely difficult and the only experimental study which provides values for both Frenkel pairs and the Schottky defect comes from Matzke [336]. The calculated defect energies for the oxygen

Frenkel all fall in the range provided by Matzke. The PBE+U and PW91+U also agree very well with the value provided by Hutchings [335] of 4.6 ± 0.5 eV.

The uranium Frenkel energy is overestimated, regardless of the functional. The closest agreement to experiment is achieved using the PBE+U functional. For the Schottky defect PBEsol+U and rPBE+U both underestimate, whereas PBE+U and PW91+U both fall within the experimental range. Comparing the calculated values to literature theoretical values sees good agreement, the O_i is the most favourable and only values with a negative value with the exception of the V_U in the calculation of Yu *et al.* [339].

3.3 Conclusions

The fluorite UO_2 system is an excellent benchmark, against which to test the suitability of a range of different GGA+U functionals and the inclusion of SOC, to determine the best modelling approach as there is an abundance of experimental data with which to compare.

The selected parameters for the cut off energy and k-points (Table 3.5) reproduce the experimentally observed properties of UO_2 to a high degree of accuracy, validating the choice of cut off energy and k-point mesh.

Overall, all the functionals used to predict the properties of UO_2 perform well. Whilst the best functional varies depending on the property being evaluated, the functional which performs consistently across all properties is PBE+U. The PBE+U functional reproduces the bulk modulus (Δ14.8 GPa, -6.9 %), the best band gap value (Δ0.02 eV, 0.9 %), vibrational spectrum (Δ17 cm^{-1}, -6.1 %), point defect energies (no experimental data but good agreement with other theoretical literature) and has the best agreement with experiment for the O-Frenkel (within experimental range), U-Frenkel (Δ1.59 eV, 16.6 %) and Schottky defect energies (within experimental range).

The inclusion of SOC was found to improve the predicted properties in all cases where it was included in the calculation. Particularly, in the calculation of the magnetic moment and removal of the tetragonal distortion caused by the *1*k AFM approximation. The inclusion of SOC also improved the consistency for the different cell sizes with which the calculation of the band gap. However, the significant increase in computational expense means that it is unsuitable for the largest system. Therefore, SOC is going to be used on key results to confirm the energies and properties calculated using the PBE+U functional. Potentially, with the advancement of computing power it will be possible to include the effect of SOC for all systems, including the 96 atom simulation cell.

Whilst the functional chosen is reliable for reproducing the known properties of UO_2, it is unknown if the predicted properties will depend on the functional when hydrogen is present. Therefore, the next chapter will evaluate the defect energies and properties of hydrogen in UO_2 using the range of functionals assessed in this chapter.

4 Hydrogen in UO_2: Functional Dependence

There are a very limited number of experimental studies of hydrogen in bulk UO_2. The first of these was by Wheeler [42] in the early 1970s, who examined the diffusion of hydrogen in single crystals of UO_2. Subsequent to this study Sherman and Olander [43, 44, 356] performed several experiments which investigated hydrogen dissolution in polycrystalline UO_2 samples.

The solubility of hydrogen in UO_2 is found to increase by an order of magnitude when going from single crystals (0.04 μg H / g UO_2 [42]) to polycrystalline samples (3.3 μg H / g UO_2 [43, 44]). Additionally, there is little difference in the solubility of hydrogen in stoichiometric and hyperstoichiometric UO_2. However, there is an increase by an order of magnitude when using hypostoichiometric UO_2 [44].

The nature of the hydrogen charge state in UO_2 has not been definitively determined. There is a debate whether hydrogen is present as a monatomic or molecular species [42, 44]. Wheeler suggests that hydrogen may be present as H_2, additionally the presence of hydrogen as hydroxyl species is suggested [42]. In contrast Sherman and Olander present data which suggest that hydrogen dissolves as a monatomic species, as Sievert's law is obeyed [44]. Theoretical studies of hydrogen in UO_2 are even more limited than the available experimental literature. There has been a single study which examined hydrogen in both UO_2 and PuO_2 computationally [140], this agreed with the published work [141] from this chapter concerning the nature of hydrogen in UO_2. It was predicted that in UO_2 that the preferred defect state for hydrogen was as a hydride in the octahedral interstitial site, compensated by the formation of a U^{5+}. Conversely, in PuO_2 the opposite was observed where the hydroxyl defect was more favourable with the formation of a Pu^{3+} [140].

As there is a lack of a consensus on the nature of hydrogen defects in UO_2 this chapter aims to evaluate the preferred defect nature of hydrogen in UO_2. This will be achieved by examining different defects and the effect of the functional on the predicted hydrogen behaviour.

A paper concerning the behaviour of monatomic hydrogen defects in UO_2 has been published in *Chemical Communications* entitled "*Hydride Ion Formation in Stoichiometric UO_2*"[141].

4.1 Hydrogen Defects

Three types of hydrogen defect have be considered. The first is a single H atom in the octahedral interstitial site, (Figure 4.1a), the second is displacement of the H atom in a [111] direction towards a lattice oxygen, Figure 4.1b. The distance displaced is ≈1.5 Å, this generates a hydroxyl starting configuration. The final configuration is H_2 placed in the octahedral interstitial site, Figures 4.1c.

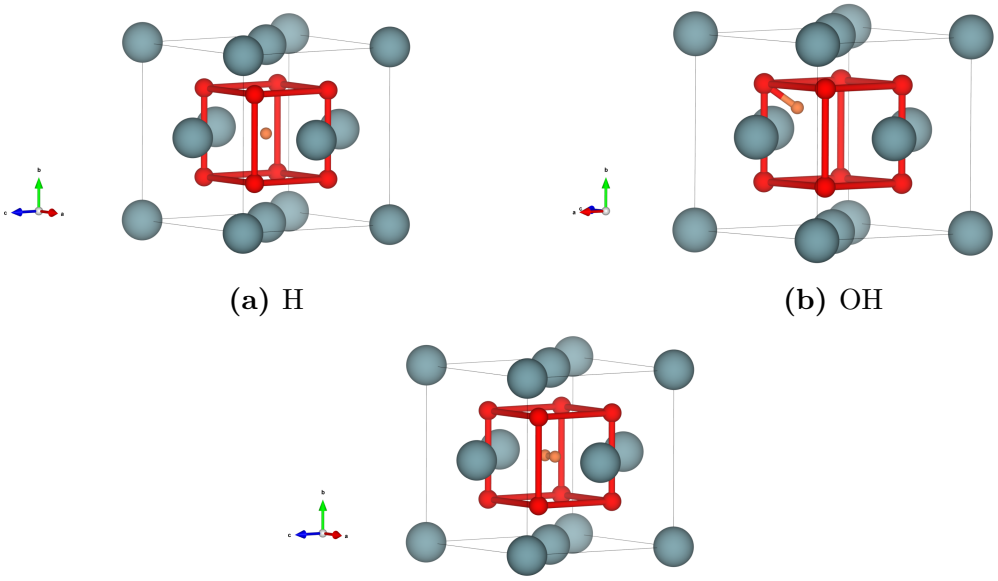

(a) H **(b)** OH

(c) H_2

Figure 4.1: Hydrogen defect locations in UO_2. 4.1a atomic hydrogen in the octahedral interstitial site, 4.1b single hydrogen atom displaced from the octahedral interstitial site towards a lattice oxygen and 4.1c molecular hydrogen in the octahedral interstitial site. Only a single unit cell and oxygen bonds shown for clarity. Uranium shown in blue, oxygen shown in red and hydrogen in orange.

As discussed in the previous chapter, the inclusion of SOC significantly increases the cost of the calculation and thus it is not possible to use SOC for the 96 atom cell. Therefore, in order to assess the significance of SOC the different hydrogen defects have been modelled in the smaller 36 atom cell. The solution energies for all of the different hydrogen defects was calculated according to Equation 4.1.

$$E_{\mathrm{Sol}} = E_{\mathrm{UO_2H_m}} - (E_{\mathrm{UO_2}} + \frac{n}{2}E_{\mathrm{H_2}}) \tag{4.1}$$

As molecular hydrogen represents double the hydrogen concentration compared with the monatomic defects these two cases will be analysed separately. First, the predicted behaviour of monatomic defects with the PBE+U functional will be presented, as this functional gave the best representation of UO_2. This will then be followed by the results for the other functionals that were tested for UO_2 for comparison. Then the results of the predicted behaviour for how molecular hydrogen behaves will be presented. For both monatomic and molecular species a comparison between the spin only formalism and SOC will also be made.

4.1.1 Monatomic Hydrogen Behaviour in UO_2

Table 4.1 shows the predicted results for monatomic hydrogen defects in a 36 atom simulation cell, with and without SOC. The predicted lattice parameters and final defect states are in excellent agreement, between the spin only formalism and the SOC calculation. The inclusion of SOC does result in an increase to the predicted solution energy compared to the spin only calculation. However, the relative energy of the hydride and hydroxyl defects are very similar, with only 0.03 eV difference between the spin only and SOC calculation.

If hydrogen is placed in the octahedral interstitial site a hydride defect compensated by a U^{5+} is predicted to form, this defect is more stable than the hydroxyl defect which forms when the hydrogen is displaced towards a lattice oxygen. The lower energy of the hydride defect can be attributed to the formation of a U^{5+} defect compared with a U^{3+} for the hydroxyl. U^{5+} formation is favourable for the UO_2 lattice whereas U^{3+} is known to be a particularity unfavourable oxidation state for uranium to adopt in UO_2.

Table 4.1: Predicted solution energy (E_{Sol}) and relative solution energy (ΔE_{Sol}) to the most stable defect. Defect states, lattice parameters and change in volume (ΔV) compared to pure UO_2 for hydrogen defects in a 36 atom UO_2 cell, calculated using the PBE+U functional with and without the inclusion of SOC.

	Spin Only		**SOC**	
Defect Location	H	OH	H	OH
$\boldsymbol{E_{\mathrm{Sol}}}$ **/H (eV)**	1.31	1.56	2.08	2.30
$\boldsymbol{\Delta E_{\mathrm{Sol}}}$ **/H (eV)**	0.00	0.25	0.00	0.22
H Defect	H^-	OH^-	H^-	OH^-
U Defect	U^{5+}	U^{3+}	U^{5+}	U^{3+}
a **(Å)**	7.82	7.93	7.82	7.89
b **(Å)**	6.80	6.88	6.80	6.86
c **(Å)**	9.55	9.53	9.56	9.59
ΔV /H (Å^3)	-3.29	8.18	-2.61	7.93

As with stoichiometric UO_2 it is important to understand if the behaviour shown is specific to the functional that has been chosen or is consistent across a variety of functionals. As seen in the previous chapter there is some variation between the functionals in the representation of the properties of UO_2. Overall the PBE+U functional gave the best representation across the properties considered, when compared to experiment. Table 4.2 summarises the results for the predicted hydrogen behaviour for the PBEsol+U, PW91+U and rPBE+U functionals, with and without including the effects of SOC.

Table 4.2: Predicted solution energy (E_{Sol}) and relative solution energy (ΔE_{Sol}) to the most stable defect. Defect states, lattice parameters and change in volume (ΔV) compared to pure UO_2 for hydrogen defects in a 36 atom UO_2 cell, calculated using the PBEsol+U, PW91+U and rPBE+U functionals with and without the inclusion of SOC.

	PBEsol+U				**PW91+U**				**rPBE+U**			
	Spin Only		**SOC**		**Spin Only**		**SOC**		**Spin Only**		**SOC**	
Defect Location	H	OH	H	OH	H	OH	H	OH	H	OH	H	OH
$\boldsymbol{E_{\mathrm{Sol}}}$ **/H (eV)**	1.53	2.22	2.00	2.61	4.41	4.55	2.28	5.11	1.70	1.33	2.42	2.38
$\boldsymbol{\Delta E_{\mathrm{Sol}}}$ **/H (eV)**	0.00	0.69	0.00	0.61	0.00	0.14	0.00	2.83	0.37	0.00	0.04	0.00
H Defect	H^-	OH^-	H^-	OH^-	H^-	OH^-	H^-	OH^-	$H^{\cdot}$	OH^-	$H^{\cdot}$	OH^-
U Defect	U^{5+}	U^{3+}	U^{5+}	U^{3+}	U^{5+}	U^{3+}	U^{5+}	U^{3+}	-	U^{3+}	-	U^{3+}
a **(Å)**	7.74	7.83	7.75	7.78	7.83	7.94	7.83	7.89	7.89	8.03	7.88	7.93
b **(Å)**	6.70	6.84	6.71	6.76	6.78	6.84	6.79	6.86	6.86	6.87	6.84	6.91
c **(Å)**	9.48	9.49	9.51	9.48	9.57	9.56	9.62	9.60	9.64	9.62	9.68	9.68
$\boldsymbol{\Delta}$**V /H (Å^3)**	-2.91	6.37	-0.45	4.17	-16.10	-5.32	-0.26	7.80	0.03	8.51	0.10	8.92

In all cases there is agreement between the spin only and SOC calculations, for each functional, as to the nature of the hydrogen defect, compensating uranium defect and predicted lattice parameters. For the PBEsol+U and PW91+U this is the same as for the PBE+U functional. Both a hydride compensated by a U^{5+} and a hydroxyl compensated for by a U^{3+} are predicted, with the hydride being the more favourable defect. In the case of the rPBE+U functional a hydride defect could not be stabilised in the octahedral interstitial site, for this defect concentration of hydrogen. A hydroxyl defect was predicted when the hydrogen was displaced towards the oxygen of the lattice, the hydroxyl defect is predicted to be most stable defect with the rPBE+U functional. This can be ascribed to the larger volume that the rPBE+U functional predicts for pure UO_2, resulting in the hydroxyl defect being favoured.

Comparing between the spin only formalism and SOC calculation for each functional as with the PBE+U functional the inclusion of SOC results in a shift to the predicted solution energies. Only for the PBEsol+U does the relative energy difference stay comparable at 0.08 eV. For the PW91+U and rPBE+U there is a large increase and decrease in the relative energy respectively, upon inclusion of SOC. This does not change the order of stability for the defects. All the calculations predict that E_{Sol} is positive which agrees with the observations of Wheeler and Sherman and Olander who report endothermic adsorption for hydrogen in UO_2 [42, 44].

Typically the inclusion of SOC results in an increase to the predicted solution energies for the defects. However for the hydride defect using the PW91+U functional a significant decrease in the solution energy occurs. This can likely be attributed to the significant volume change that is predicted for the spin only calculation compared with the SOC calculation, where even the formation of a U^{3+} defect is predicted to have a volume decrease, despite the formation of a larger ion.

4.1.2 Molecular Hydrogen Behaviour in UO_2

The predicted results for molecular hydrogen defects in UO_2 are shown in Table 4.3. As with the monatomic hydrogen defects there is very good agreement between the spin only formalism and SOC calculations for the lattice parameters, defect states and change in volume except for the PW91+U functional where there is a large discrepancy between the predicted volume change between the only formalisms and SOC calculation. The predicted lattice parameters show excellent agreement between the SOC and spin only calculations. As before, with the monatomic hydrogen, there is a large discrepancy between the predicted volume change for the PW91+U functional, which is due to the spin only calculation for the pure UO_2 over estimating the volume. All the calculations predict that a molecular hydrogen defect will remain as H_2 and not dissociate. The likely reason for this is that by remaining as H_2 there is no change in the any of the uranium's oxidation states.

Table 4.3: Predicted solution energy (E_{Sol}), defect states, lattice parameters and change in volume (ΔV) compared to pure UO_2 for molecular hydrogen defects in a 36 atom UO_2 cell, calculated using the PBE+U, PBEsol+U, PW91+U and rPBE+U functionals with and without the inclusion of SOC.

	PBE+U		**PBEsol+U**		**PW91+U**		**rPBE+U**	
	Spin	**SOC**	**Spin**	**SOC**	**Spin**	**SOC**	**Spin**	**SOC**
E_{Sol} **/H (eV)**	0.29	2.03	0.45	0.48	3.72	1.20	0.37	0.76
H Defect	H_2	H_2	H_2	H_2	H_2	H_2	H_2	H_2
U Defect	-	-	-	-	-	-	-	-
a **(Å)**	7.85	7.83	7.76	7.74	7.86	7.83	7.89	7.90
b **(Å)**	6.80	6.80	6.70	6.73	6.78	6.80	6.85	6.86
c **(Å)**	9.63	9.66	9.56	9.55	9.66	9.66	9.70	9.70
Δ**V /H (Å^3)**	1.26	1.68	1.34	1.54	-5.08	3.15	1.49	3.58

4.1.3 Dependence on Functional

For both monatomic and molecular hydrogen defects there is very good agreement between the spin only and SOC calculations for all the functionals as to the nature of the hydrogen defect, any compensating uranium defect, predicted lattice parameters and the change in volume. There are only a couple of exceptions to this, first is for the PW91+U functional where there are significant differences in the predicted volume change between the spin only and SOC calculations. The second is for the rPBE+U functional where a hydride defect could not be stabilised at the octahedral interstitial site. Instead a radical defect was predicted, this occurred for both the spin only and SOC calculations. The other three functionals tested all predicted a hydride species to form. The exact reason for the hydrogen radical being predicted, is uncertain, however the rPBE+U functional was the least suitable for the simulation of pure UO_2 and had the largest expansion of the lattice. Therefore, it is possible that this carries over and the interactions which result in the formation of a hydride are not adequately described, using the rPBE+U functional.

Upon inclusion of SOC there is a shift in the solution energies, typically an increase, though for the PW91+U hydride and H_2 calculation there is a decrease. This occurs from the SOC predicting a more accurate volume for the pure UO_2. For both the PW91+U and rPBE+U there is a large difference in the predicted relative energies between the two monatomic hydrogen defects between the spin only and SOC calculations. The PBE+U and PBEsol+U show very good agreement in the relative energies between the hydride and hydroxyl defects for the spin only and SOC calculations.

4.1.4 Effect of Concentration

The previous section considered hydrogen defects in a 36 atom cell and how these results were affected by the inclusion of SOC. However, this represents a very high hydrogen defect concentration 311 μg H / g UO_2 (622 μg H / g UO_2 for H_2). This is far in excess of the experientially reported concentration for both single

(0.04 μg H / g UO_2 [42]) and polycrystalline samples (3.3 μg H / g UO_2 [43, 44]). Therefore, this section will evaluate hydrogen defects in the largest UO_2 simulation cell used in this thesis (96 atoms), with the same range of functionals that were used previously. The defect concentration for a monatomic hydrogen defect in a 96 atom simulation cell is still large at 117 μg H / g UO_2 and 234 μg H / g UO_2 for H_2. The only difference here is due to the size of these calculations there is no comparison with calculations including the effect of SOC.

This will be set out as with the previous sections; first monatomic hydrogen defects will be discussed followed by the molecular hydrogen defects results.

4.1.4.1 Monatomic Hydrogen

The results of monatomic hydrogen defects placed at the octahedral interstitial site in the 96 atom cell and displaced towards a lattice oxygen are shown in Table 4.4. The results are very similar to the 36 atom system calculations. The PBE+U, PBEsol+U and PW91+U functionals all predict a hydride and hydroxyl defect as before, with the hydride being the more stable of the two defects. Interestingly, the PBEsol+U predicts a favourable solution energy for the hydride defect, this would suggest at these concentrations that hydrogen will favourable dissolve into UO_2. This would run counter to the endothermic absorption reported experimentally [42, 44].

The decrease in concentration has also resulted in the rPBE+U functional predicting a hydride and hydroxyl defect combination. The difference here is that the hydroxyl is predicted to be marginally more stable than the hydride defect (0.07 eV).

The agreement between the different functionals for the predicted defect states and change of volume are in very good agreement with each other. The relative energies between the different defects varies more than the other properties.

Table 4.4: Predicted solution energy (E_{Sol}), defect states, lattice parameters and change in volume (ΔV) compared to pure UO_2 for monatomic hydrogen defects in a 96 atom UO_2 cell, calculated using the PBE+U, PBEsol+U, PW91+U and rPBE+U functionals.

	PBE+U		**PBEsol+U**		**PW91+U**		**rPBE+U**	
Defect Location	H	OH	H	OH	H	OH	H	OH
$\boldsymbol{E_{\mathrm{Sol}}}$ **/H (eV)**	0.19	0.41	-0.22	0.66	0.59	0.77	0.51	0.44
$\boldsymbol{\Delta E_{\mathrm{Sol}}}$ **/H (eV)**	0.00	0.22	0.00	0.88	0.00	0.18	0.07	0.00
H Defect	H^-	OH^-	H^-	OH^-	H^-	OH^-	H^-	OH^-
U Defect	U^{5+}	U^{3+}	U^{5+}	U^{3+}	U^{5+}	U^{3+}	U^{5+}	U^{3+}
a **(Å)**	11.01	11.02	10.89	10.91	11.00	11.02	11.08	11.10
b **(Å)**	11.02	11.05	10.89	10.92	11.02	11.04	11.09	11.12
c **(Å)**	11.01	11.05	10.89	10.93	11.00	11.05	11.08	11.12
Δ**V /H (Å^3)**	-2.52	7.24	-3.01	7.64	-2.95	7.76	-2.79	7.87

4.1.4.2 Molecular Hydrogen

The predicted properties of molecular H_2 at the octahedral interstitial site are shown in Table 4.5. All of the functionals show reasonable agreement with each other. All predict that H_2 will remain as H_2 and that there is a small volume increase compared with pure UO_2. They also all predict a favourable solution energy, as with the favourable energy predicted for the hydride defect using the PBEsol+U functional, this would seem to be in contradiction to experiment [42, 44], where endothermic adsorption of hydrogen is reported.

A potential explanation is that at low concentrations the adsorption of hydrogen is favourable and as the concentration increases it becomes unfavourable, as seen be the difference in solution energies for H_2 in the 26 and 96 atom simulation cells. Alternatively, it is possible that H_2 has to dissociate to dissolve into UO_2 and is predominantly a monatomic species in the lattice, as suggested by Sherman and Olander [44]. However, if hydrogen recombines to form H_2, as this is energetically favourable, then hydrogen molecule may represents an irreversible trap in UO_2.

Table 4.5: Predicted solution energy (E_{Sol}), defect states, lattice parameters and change in volume (ΔV) compared to pure UO_2 for hydrogen defects in a 96 atom UO_2 cell, calculated using the PBE+U, PBEsol+U, PW91+U and rPBE+U functionals.

	PBE+U	**PBEsol+U**	**PW91+U**	**rPBE+U**
E_{Sol} /H (eV)	-0.28	-0.42	-0.14	-0.11
H Defect	H_2	H_2	H_2	H_2
U Defect	-	-	-	-
***a* (Å)**	11.02	10.91	11.02	11.11
***b* (Å)**	11.03	10.90	11.03	11.11
***c* (Å)**	11.02	10.90	11.02	11.11
ΔV /H (Å^3)	1.32	1.37	1.48	1.58

The overall effect of hydrogen defects on the structure of UO_2, as represented by the volume change per hydrogen, shows no dependence on concentration for molecular hydrogen defects, but some effect for monatomic defects, where a change of uranium oxidation state occurs. In the 36 atom simulation cell the predicted volume change was -3.29 Å^3 for the hydride, 8.18 Å^3 for the hydroxyl and 1.26 Å^3 for molecular hydrogen compared to -2.52 Å^3 for the hydride, 7.24 Å^3 for the hydroxyl and 1.32 Å^3 for molecular hydrogen in the 96 atom simulation cell. There is a smaller contraction and expansion predicted for the hydride and hydroxyl defects at lower concentrations respectively, whereas for molecular hydrogen no significant volume change is predicted between the two concentrations (0.06 Å^3).

The concentration has a far more significant effect on the solution energies for both monatomic and molecular hydrogen defects, with the higher concentration of hydrogen resulting in much larger solution energies.

The predicted defect states and compensating uranium defects do not change with a change of hydrogen concentration for all of the functionals with the exception of rPBE+U functional and monatomic hydrogen occupying the octahedral

interstitial site. Here a change from a hydride at lower concentrations to a radical at high concentrations occurred.

The next stage is assessing the effect of hydrogen defects on the electronic proprieties of the UO_2 lattice.

4.1.5 Electronic Properties

Table 4.6 contains the calculated bad gap for the three different hydrogen defects in UO_2 for both the 96 and 36 atom cells, with and without the inclusion of SOC (36 atom simulation cell). While, Figures 4.2, 4.3 4.4 show the pDOS for the H_2, hydroxyl and hydride defects, in a 96 atom cell, respectively. Figure 4.5 shows a zoomed in section of the hydride pDOS graphs to clearly show the hydride defect states exist. Due to the similarity of all the pDOS graphs for the different systems only the 96 atom graphs are shown, the full series of pDOS graphs can be found in Appendix A.

Table 4.6: Calculated values of the band gaps, in eV, for hydrogen defects in a 36 atom UO_2 cell with and without including the effects of SOC and hydrogen defects in a 96 atom cell, using a range of functionals. A - represents where there are states at the Fermi level.

Defect	**Hydride**			**Hydroxyl**			**H_2**		
System	**36 SOC**	**36 Spin**	**96 atom**	**36 SOC**	**36 Spin**	**96 atom**	**36 SOC**	**36 Spin**	**96 atom**
PBE+U	0.78	0.88	1.18	0.52	0.58	0.65	2.05	2.06	2.06
PBEsol+U	-	1.22	1.25	-	0.51	0.45	2.05	2.06	2.00
PW91+U	1.53	1.36	1.05	0.68	0.51	0.58	2.03	2.04	2.19
rPBE+U	-	-	1.18	0.52	0.86	0.71		2.23	2.11

For all the different functionals, in a 96 atom cell, the pDOS spectrum of all the different defects are very similar. The predicted value of the band gaps are all very similar as are the location of the defect states. For the H_2 defect the band gap remains nearly unchanged from that of non-defective UO_2. This is because the H_2 states appear between 8-9 eV below the Fermi level. This would also equate with the H_2 being a very stable defect in UO_2.

For the hydroxyl defect the U^{3+} occupies what was the band gap of pure UO_2. As the hydrogen has become protonic there are no states associated with the hydrogen and this does not appear in the pDOS spectrum. The location of the U^{3+} states results in a much smaller band gap than pure UO_2. In the case of the hydride defect the hydride states exist at the top of the valence band (Figure 4.5), while the U^{5+} defect states occur at the bottom of the conduction band. The result of these features is that the hydride gives a smaller band gap than stoichiometric UO_2, but a much larger band gap than the hydroxyl defect.

Similar behaviour is observed for the 36 atom system with and without the inclusion of SOC. The only exceptions to this are for the rPBE+U H defect for both spin and SOC calculations, along with the PBEsol+U SOC monatomic hydrogen calculations. In these cases there are states at the Fermi level which suggest a metallic behaviour. Again the results shown by the rPBE+U functional can be explained by the presence of a hydrogen radical rather than a hydride ion.

As for the PBEsol+U SOC calculations metallic behaviour is predicted for both the hydride and hydroxyl defects. Whilst the exhibited behaviour is of a hydride defect (Table 4.2), closer examination of the hydrogen species shows that the hydrogen defect is not completely converted into a hydride defect and therefore retains some hydrogen radical nature. For the hydride defect this is caused by defect states at the top of the valence band, occupying the bottom of what was the stoichiometric band gap (Figure A.11). As seen with the rPBE+U functional, when the hydrogen defect is a radical species states are predicted to exist at the Fermi level (Figure A.12). Potentially, this could be due to the PBEsol+U predicting a smaller band gap for the stoichiometric oxide (Table 3.12) compared with the other functionals. This is not seen in the PBEsol+U spin only calculations as there is complete conversion of the hydrogen into a hydride defect. Whereas in the hydroxyl defect case it is caused by the U^{3+} defect states occupying what was the top of the stoichiometric band gap and merging into the conduction band (Figure A.10).

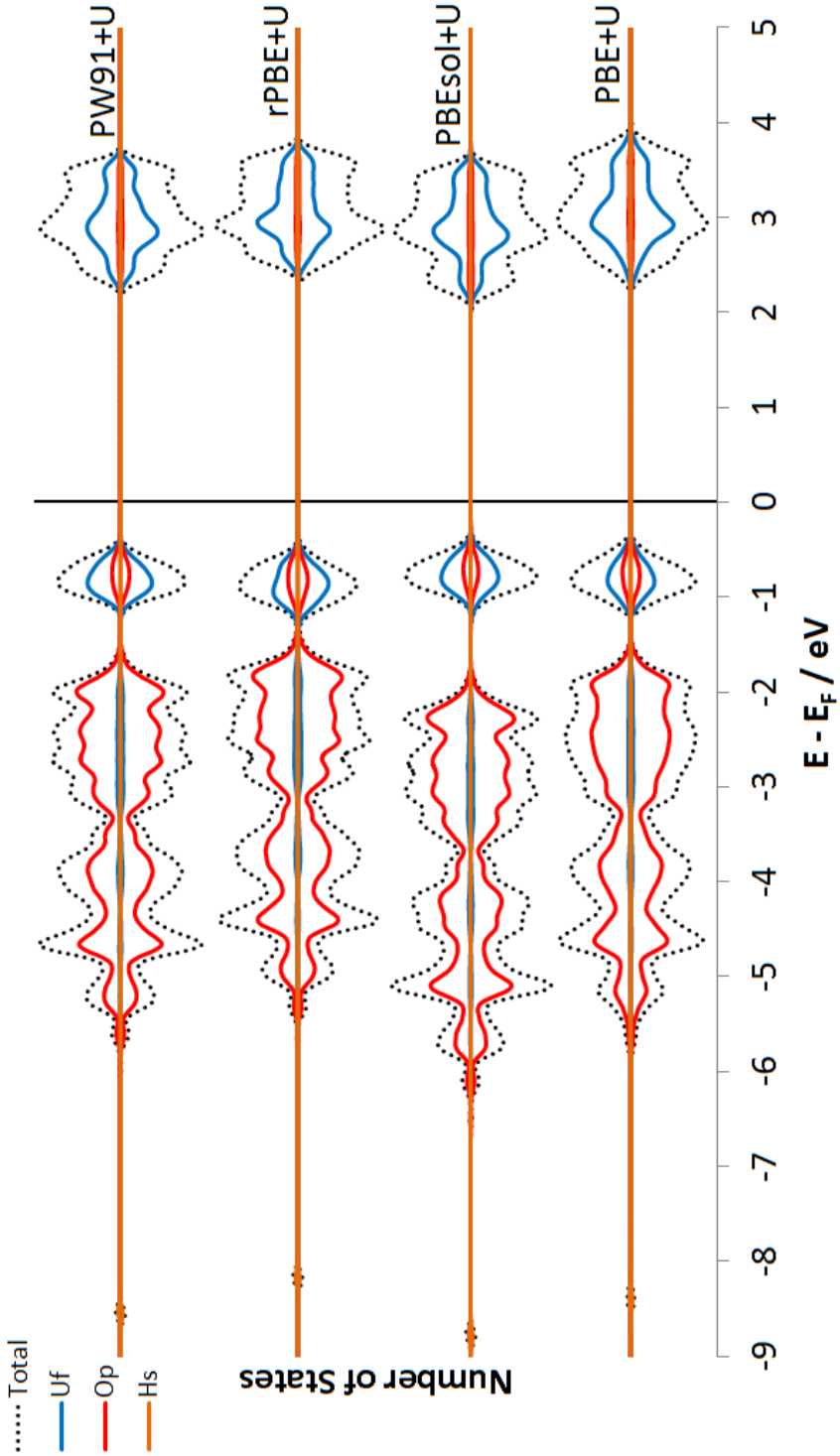

Figure 4.2: Partial DOS for a molecular hydrogen defect in a 96 atom UO_2 cell calculated with a range of functionals. The Fermi energy has been set to 0 eV.

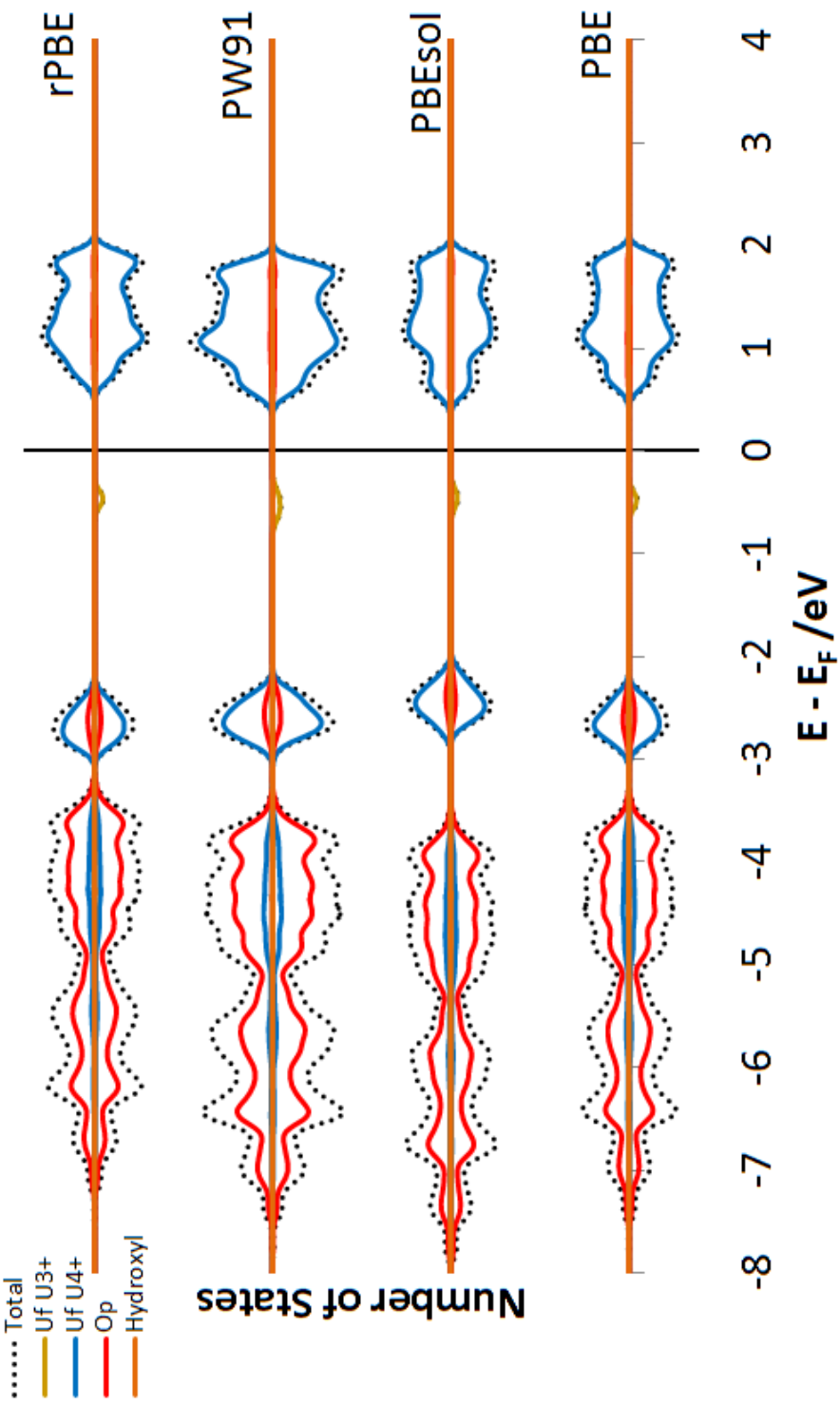

Figure 4.3: Partial DOS for a hydroxyl defect in a 96 atom UO_2 cell calculated with a range of functionals. The Fermi energy has been set to 0 eV.

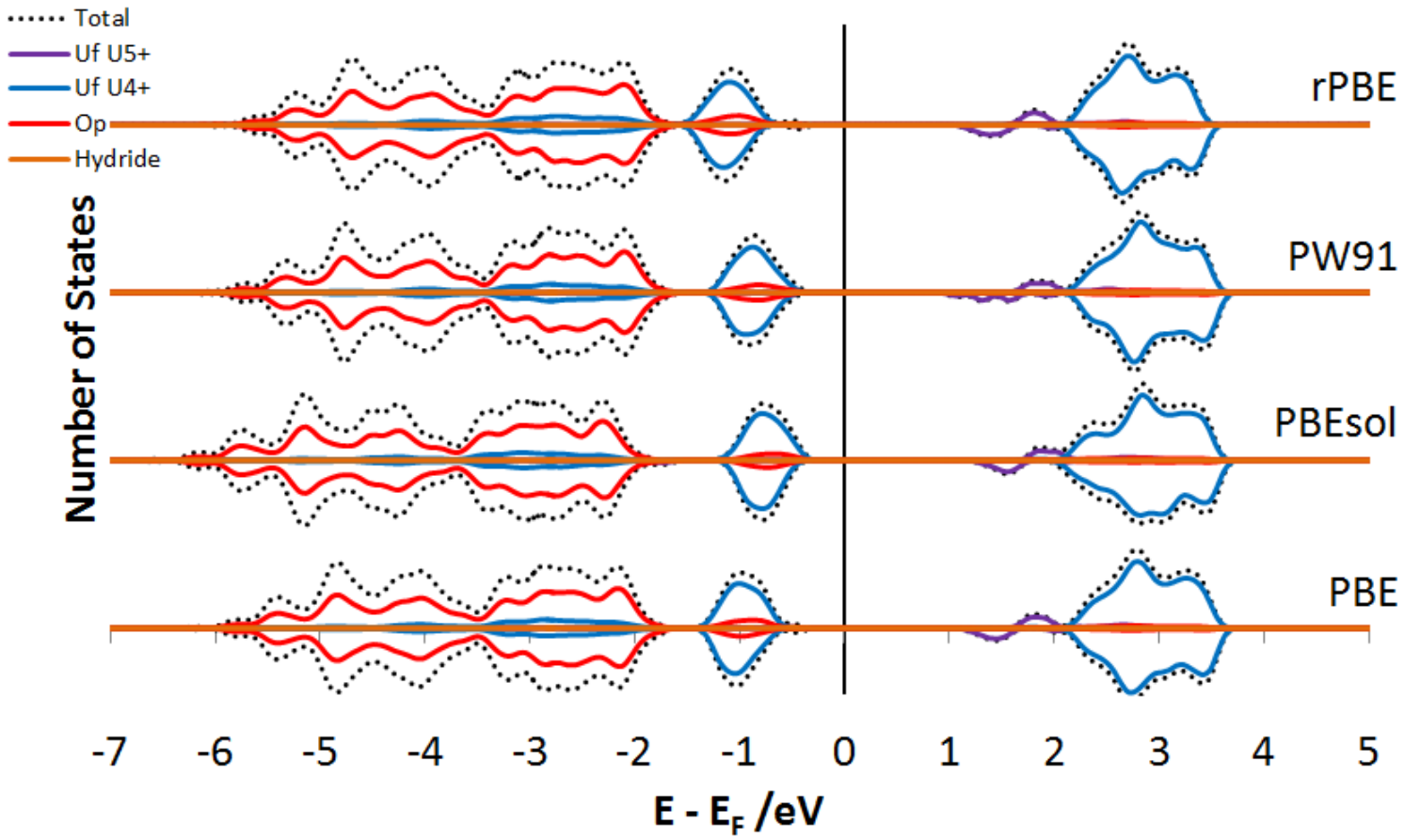

Figure 4.4: Partial DOS for a hydride defect in a 96 atom UO_2 cell calculated with a range of functionals. The Fermi energy has been set to 0 eV.

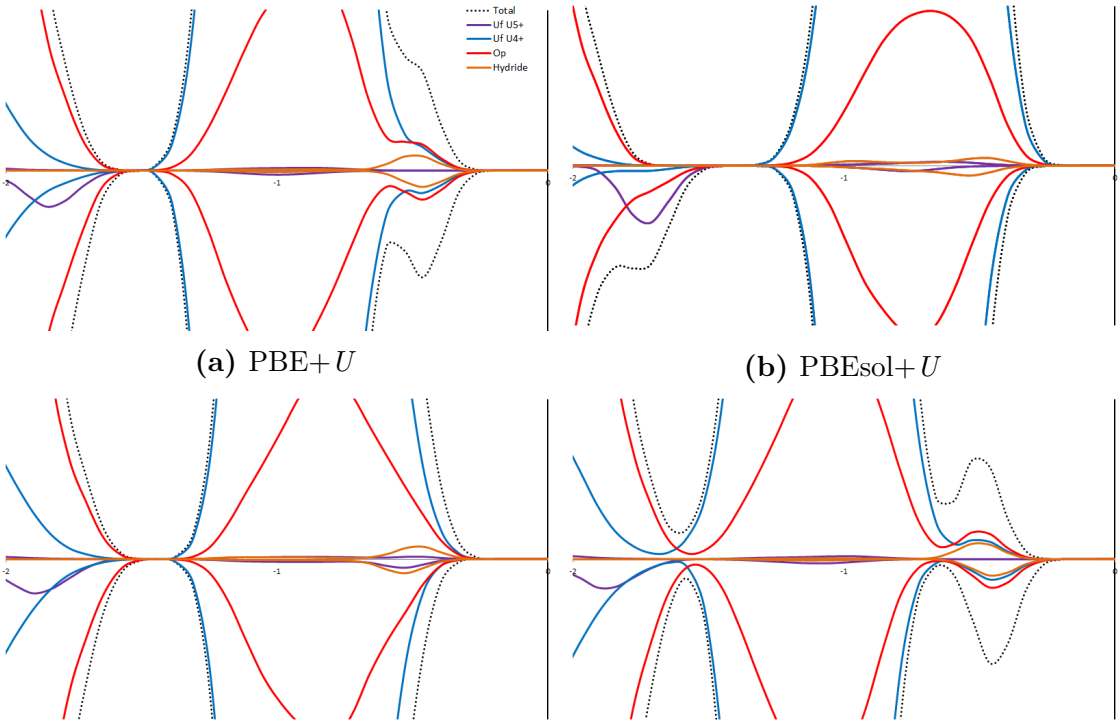

(a) PBE+U **(b)** PBEsol+U

(c) PW91+U **(d)** rPBE+U

Figure 4.5: Partial DOS for a Hydride defect in a 96 atom UO_2 cell calculated with a range of functionals. The Fermi energy has been set to 0 eV. The graph has been scaled to show the Hydride states at the top of the valence band.

4.2 Conclusions

The results of incorporating hydrogen at the two concentrations shows that the concentration of hydrogen in the cell has a marked effect on the predicted solution energies, with a higher concentration having a higher solution energy. Consequently the solubility is significantly dependent on the hydrogen concentration, particularly for the molecular hydrogen defects which were predicted to have a favourable solution energy at the lowest concentration. All of the functionals agree structurally in terms of the hydrogen speciation (with minor exceptions) and geometry. There is a minimal effect of the volume change as a function of hydrogen concentration for monatomic defects and no effect for molecular hydrogen defects. The predicted electronic properties show very consistent behaviour across all the functionals, with similar band gaps predicted for all the different defects. The only calculations where this differed is where a metallic nature was predicted.

The major constraint, in assessing hydrogen behaviour as a function of concentration was the CPU resource available, but in future it would be useful to test larger cells and lower hydrogen concentrations to determine the convergence of hydrogen defect properties.

Overall the behaviour of hydrogen in UO_2 as predicted by the different functionals tested in this chapter suggest that there is not a large properties dependence of the functionals. There are some small difference as would be expected from using a range of functionals.

On balance the rPBE+U and PW91+U functionals appear to be less well suited to the modelling of hydrogen defects in UO_2 when compared to the PBE+U and PBEsol+U functionals. Lastly, from this exploration of the dependence of hydrogen behaviour of the functional the best and most consistent functional is PBE+U. There were no cases in which the PBE+U functional exhibited different behaviour form the majority of the functionals. Additionally, where it was possible to compare with SOC calculations the relative energy of the hydrogen defects agreed with the SOC calculations. From the previous chapter the PBE+U functional was also the most appropriate for the simulation of UO_2. Therefore, going forward in this work on the PBE+U functional will be used, as it gives the best representation of UO_2 and the behaviour of hydrogen defects in UO_2.

Having now shown that the behaviour of hydrogen is largely independent of the selected functional the next chapter will now use the PBE+U functional to explore how hydrogen behaves in $UO_{2\pm x}$.

5 Hydrogen in $UO_{2\pm x}$

The aim of this chapter is to explore how a wider range of hydrogen defects (concentrations and compositions) behave in UO_2. In addition to exploring how hypo- and hyper- stoichiometry affects the hydrogen defects. As hyperstoichiometric UO_2 is the most commonly found form of uranium dioxide. It is also known that uranium hydride (UH_3) forms at uranium metal/oxide interfaces [39, 40], therefore hydrogen is going to be present in a region where the uranium oxide is likely to be hyposto-ichiometric. This will be achieved by using a 96 atom simulation cell with either a single V_O or single O_i. The reason for only considering a single defect is that the removal of one oxygen from a 96 atom cell is already at the limit of hypostoichiometry of UO_2, generating a cell that has stoichiometry of $UO_{1.97}$ [17]. In both cases in order to determine the preference for hydrogen to interact with the defect site (V_o/O_i) or to be separate from the defect, hydrogen was added to the system in two separate approaches. The first is where the hydrogen is interacting with the defect location (*i.e.* hydrogen is in the same unit cell as the defect). The second is where the hydrogen was added in a unit cell which did not contain the oxygen defect.

5.0.1 Hydrogen in UO_2

To explore the behaviour of hydrogen in UO_2 a range of different hydrogen defect concentrations and configurations have been considered. For single hydrogen defects two different configurations were trialled, the octahedral site and displacement in a [111] direction as described in the previous chapter. Doubling the defect concentration, four different configurations were assessed. These were H_2 and three 2H configurations. Figure 5.1 shows the different 2H defect configurations, where 2H were placed on separate octahedral sites, 2H were displaced from separate octahedral sites and finally one hydrogen was placed on an octahedral site and the other was displaced from the octahedral site. The final defect configuration considered was where there were $2H_2$ defects on separate octahedral sites. The solution energy was calculated according to either Equation 5.1 (Stoichiometric), Equation 5.2 (Hypostoichiometric) or Equation 5.3 (Hyperstoichiometric), depending on the stoichiometry of the UO_2.

$$UO_2 + \frac{n}{2}H_2 \rightarrow UO_2H_m \tag{5.1}$$

$$UO_2 + \frac{n}{2}H_2 \rightarrow UO_{1.97}H_m + 0.03O_2 \tag{5.2}$$

$$UO_2 + 0.03O_2 + \frac{n}{2}H_2 \rightarrow UO_{2.03}H_m \tag{5.3}$$

The initial configurations of the H, OH and H_2 defects is the same as in the previous chapter (Figure 4.1). The new configurations for the 2H defect configurations are shown in Figure 5.1. For the H OH configuration this was trialled with both hydrogen in the same cell (Figure 5.1c) and separate cells (Figure 5.1).

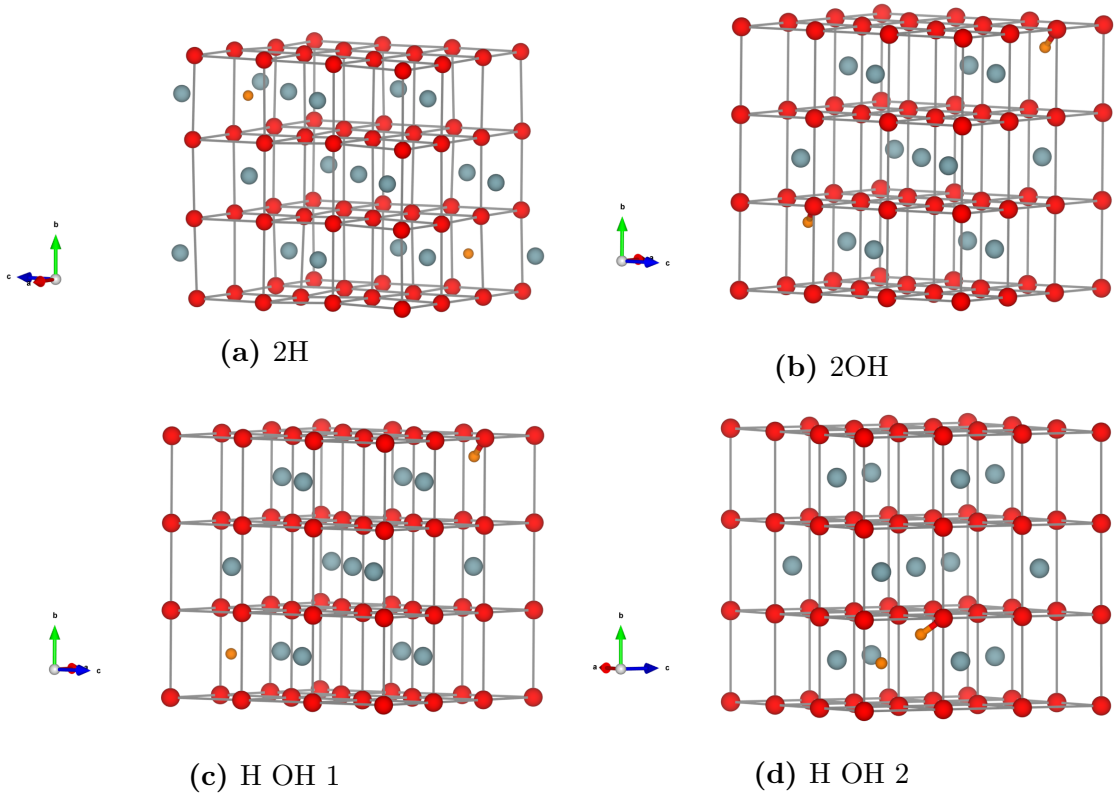

(a) 2H **(b)** 2OH **(c)** H OH 1 **(d)** H OH 2

Figure 5.1: 2 Hydrogen defect locations in UO_2. Uranium shown in blue, oxygen shown in red and hydrogen in orange. Bonds have been drawn between oxygen atoms for clarity.

The H, OH and H_2 defects behave as described before in the previous chapter. However, a significant change in behaviour is observed on addition of a second hydrogen defect. If this is added to another octahedral interstitial site (Figure 5.1a), rather than two hydrides forming only one hydrogen converts to a hydride, the other remains as a radical. This is further supported by the presence of a single U^{5+} defect. The reason for this could be that due to the fact the hydrogen atoms were placed as far apart as possible that the formation of $2U^{5+}$ defects over this distance is unfavourable. In contrast when an oxygen is added as an interstitial both of the U^{5+} localise next to the oxygen defect, suggesting a preference for defects to be clustered together.

More interesting is, when the 2 hydrogen defects are either set up as two OH defects or a H OH configuration in separate cells (Figure 5.1c), then no oxidation of the uranium ions occurs. Instead one of the hydrogen remains as a proton and the other adopts the position of a hydride defect in the octahedral interstitial site. This behaviour changes if the H and OH occupy the same cell, in this case the hydrogen defects form molecular H_2. This is consistent with the previous two defect configurations which suggest that the most favourable hydrogen defects are those which result in there being no oxidation of the uranium ions. Both the defect

configurations where there is a single H_2 present have favourable solution energies. The favourable solution energy only occurs for the lowest concentrations of hydrogen defects as the addition of a second H_2 molecule results in an unfavourable solution energy. However this is not very endothermic.

Table 5.1: Predicted solution energy (E_{Sol}), defect concentration, defect states, lattice parameters and volume change for hydrogen defects in a 96 atom UO_2 cell. ΔV is calculated relative to the predicted volume of UO_2.

Initial Defect	**H**	**OH**	**2H**	**2OH**	**H OH (1)**	**H OH (2)**	**H_2**	**$2H_2$**
[H] μg/gUO_2	117	117	233	233	233	233	233	467
E_{Sol}/H (eV)	0.19	0.41	1.36	0.42	0.50	-0.22	-0.28	0.20
Hydrogen Defect	H^-	OH^-	H^- / $H^{\cdot}$	H^- / OH^-	H^- / OH^-	H_2	H_2	$2H_2$
Uranium Defect	U^{5+}	U^{3+}	U^{5+}	-	-	-	-	-
***a* (Å)**	11.01	11.02	11.01	11.03	11.03	11.02	11.02	11.03
***a* (Å)**	11.02	11.05	11.01	11.03	11.03	11.03	11.03	11.02
***a* (Å)**	11.01	11.05	11.00	11.03	11.03	11.03	11.02	11.05
Volume (Å^3)	1334.68	1344.44	1344.10	1342.21	1341.33	1340.59	1339.84	1342.96
ΔV/H (Å^3)	-2.52	7.24	-3.11	5.01	4.12	3.38	2.64	5.76

Overall for hydrogen defects in UO_2, it is possible to say that hydride defects are more favourable than hydroxyl defects. Hydrogen defects configurations that do not result in a change of uranium oxidation are also particularly stable configurations. The predicted volume change could be potentially be used as an indicator of the hydrogen defect state in UO_2, as hydrides are predicted to cause a volume contraction and H_2 is predicted to cause a volume expansion.

Having gained insight into the behaviour of hydrogen in UO_2 the next two sections will examine how hydrogen behaves when the stoichiometry changes, as the majority of UO_2 is likely to be hyperstoichiometric.

5.0.2 Hypostoichiometric UO_2 ($UO_{1.97}$)

In order to generate hypostoichiometric UO_2 an oxygen atom was removed from a 96 atom UO_2 cell. This generated a stoichiometry of $UO_{1.97}$, as shown in Equation 5.4. This had a formation energy of 5.77 eV. Formally a V_O should generate two U^{3+}, however, the excess charge delocalised over four uranium ions, which surrounded the V_O, Figure 5.2. This is consistent with the literature on the formation of $2U^{3+}$ being unfavourable and requiring the use of methods such as occupational matrix control to achieve. There was also a small volume expansion (0.55 Å^3) predicted.

$$UO_2 \rightarrow UO_{1.97} + \frac{1}{2}O_2 \tag{5.4}$$

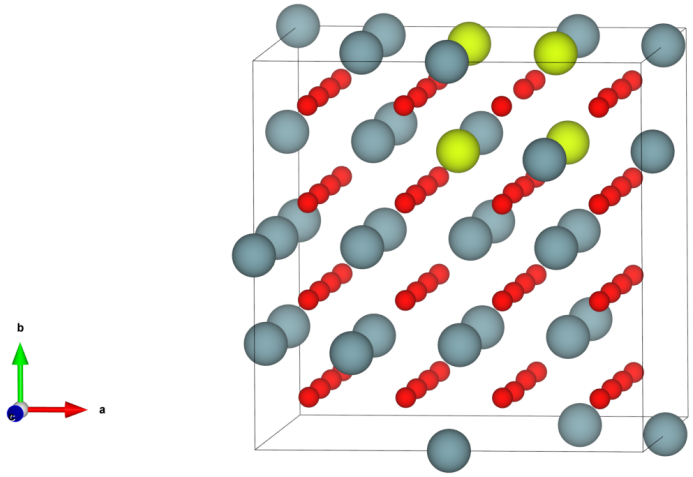

Figure 5.2: Minimised configuration of a single oxygen vacancy in UO_2. U^{4+} shown in blue, reduced uranium ions shown in yellow and oxygen shown in red.

5.0.3 Hydrogen Defects in $UO_{1.97}$

The introduction of an oxygen defect (either V_O of O_i) results in another variable to be considered when adding hydrogen defects. Namely, does the hydrogen prefer to interact with the defect site or be isolated from the defect location? As such, for both the V_O and O_i defects hydrogen has been added where it is directly interacting with the oxygen defect, this is defined as being in the same unit cell as the defect. Hydrogen was also added where it was not interacting with the oxygen defect, by being placed as far as possible from the location of the oxygen defect.

There were six different initial hydrogen defect configurations for hydrogen interacting with the V_O (Figure 5.3). The first of these is one hydrogen placed on the V_O (Figure 5.3a), the second is where a single hydrogen is on the octahedral site in the unit cell containing the vacancy (Figure 5.3b) and the third is a H_2 molecule on the V_O (Figure 5.3c). The next three defects are all initially configured as hydroxyl defects, where the direction of the hydroxyl is in either a [100], [110] or [111] from the V_O site (Figure 5.3d - 5.3f).

The predicted properties of hydrogen defects are shown in Table 5.2, where the energy of solution has been calculated as according to Equation 5.5. All of the defects show a large positive solution energy.

$$UO_2 + \frac{n}{2}H_2 \rightarrow UO_{1.97}H_n + \frac{1}{2}O_2 \tag{5.5}$$

The most favourable location was for monatomic hydrogen to be on the V_O site, since when the hydrogen is present on the V_O site it forms a hydride defect. The formation of the hydride defect accounts, for one of the excess electrons present and additionally stabilises the formation of a single U^{3+}. This hints at how the hydride phase might begin to nucleate at metal oxide interfaces. Hydride defects form on V_O sites and this helps stabilise U^{3+} which can then potential act as a nucleation site for the formation of the hydride. However, the most stable defect by far is when H_2 is on a V_O site, as the H_2 dissociates into two hydride ions, which bridge the V_O

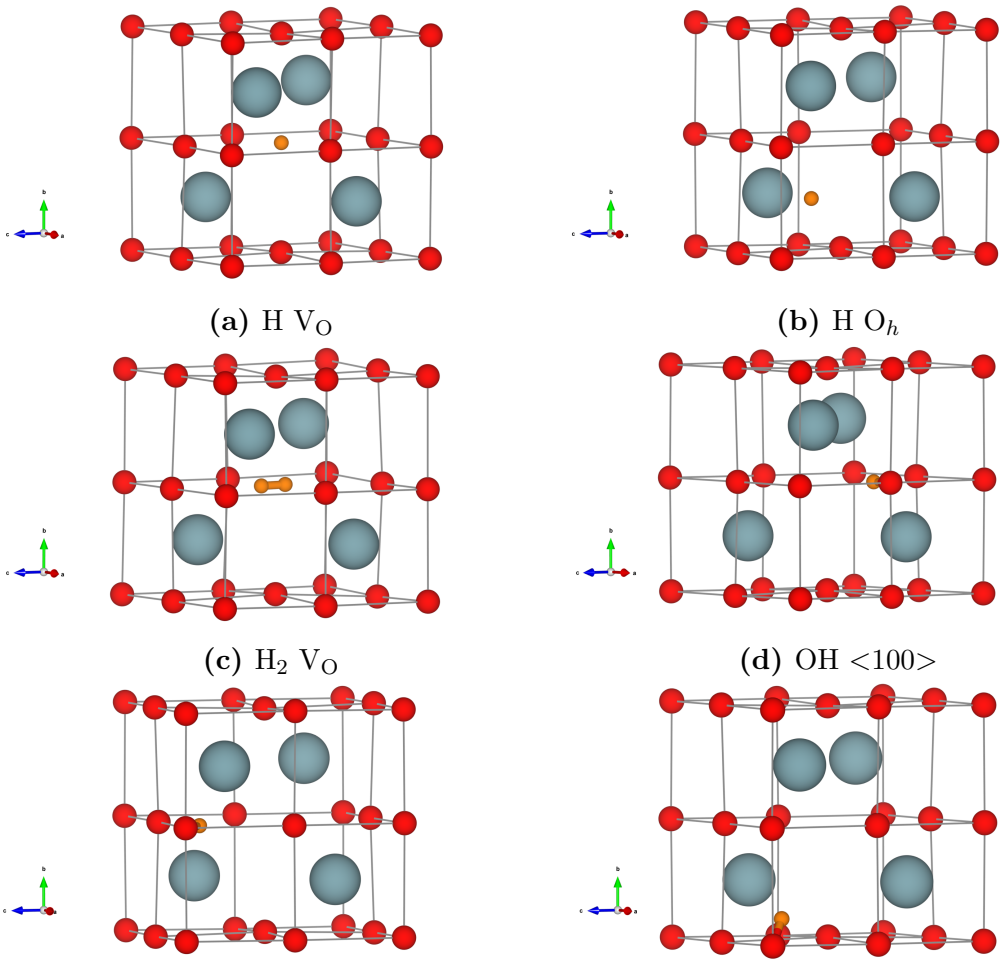

(a) H V_O **(b)** H O_h

(c) H_2 V_O **(d)** OH <100>

(e) OH <110> **(f)** OH <111>

Figure 5.3: Initial hydrogen defect configurations in UO_2. Uranium shown in blue, oxygen shown in red and hydrogen in orange. Bonds have been drawn between oxygen atoms for clarity.

site (Figure 5.4). This further illustrates the unfavourable nature of U^{3+} formation in UO_2. This also may suggests why the nucleation of UH_3 occurs at the metal oxide interface rather than in the oxide layer itself. As in bulk UO_2 the presence of hydrogen acts to absorb excess electrons, via the formation of hydride ions, whereas at the metal oxide interface the presence of hydride ion helps promote the formation of U^{3+}, hence the formation of UH_3.

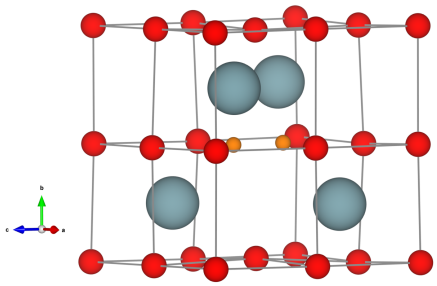

Figure 5.4: Final H_2 defect configurations in $UO_{1.97}$. Uranium shown in blue, oxygen shown in red and hydrogen in orange. Bonds have been drawn between oxygen atoms for clarity.

Where the hydrogen was initially placed at the octahedral site, the predicted structure appears to have converged to a local minima, as it lies partway from transitioning from the octahedral site to the V_O location (Figure 5.5). The solution energy is also over 1 eV higher than hydrogen which was placed on the V_O site.

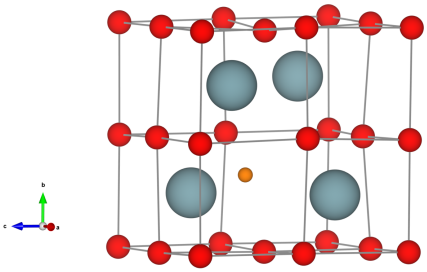

Figure 5.5: Final H defect configurations in $UO_{1.97}$. Uranium shown in blue, oxygen shown in red and hydrogen in orange. Bonds have been drawn between oxygen atoms for clarity. The H-H distance is 1.35 Å, compared to 0.74 Å for H_2.

The formation of hydroxyl defects is particularly unfavourable, even more so than in stoichiometric UO_2. This is due the formation of additional U^{3+} ions. The hydride defect being the most favourable defect is also evidenced by the initial hydroxyl defects, where in the <100> configuration the hydrogen transitions from the oxygen to the V_O site. In the initial <110> and <111> this did not occur and the solution energy is more than double compared to the <100> configuration.

Where the hydrogen defects are not interacting with the V_O site a total of six different configurations were considered. These are divided into two single hydrogen defects, one at the octahedral interstitial location and the other is a hydroxyl. These are configured the same way as in stoichiometric UO_2 (Figure 4.1). The remaining four hydrogen defects are where there are two hydrogen present in the simulation cell (Figure 5.1). The first of these is H_2 at the octahedral interstitial site. The other three two hydrogen configurations are where there are two single hydrogen defects present in the simulation cell. These are two hydride, two hydroxyl and a hydride hydroxyl configuration, as shown in Figure 5.1.

Table 5.2: Predicted solution energy (E_{Sol}), defect states, lattice parameters and volume change for hydrogen defects in a 96 atom UO_2 cell containing a single oxygen vacancy. Where the hydrogen was added to the same cell as the V_O. ΔV is calculated relative to the predicted volume of $UO_{1.97}$. $U^{3.5+}$ represents a partially reduced uranium and $U^{4.5+}$ represents a partially oxidised uranium.

Hydrogen Location	**Defect Cell**					
	H V_O	**H O_h**	**OH <100>**	**OH <110>**	**OH <111>**	**H_2 V_O**
***E_{Sol}*/H (eV)**	2.88	3.95	3.10	6.39	6.51	2.16
Final Hydrogen Defect	H^-	H^-	H^-	OH^-	OH^-	$2H^-$
Uranium Defect	U^{3+}	$2U^{3.5+}/2U^{4.5+}$	U^{3+}	$2U^{3+}/2U^{3.5+}$	$U^{3+}/3U^{3.5+}$	-
***a* (Å)**	11.03	11.01	11.03	11.03	11.04	11.00
***b* (Å)**	11.02	11.02	11.02	11.06	11.03	11.00
***c* (Å)**	11.02	11.01	11.02	11.04	11.03	11.08
Volume (Å^3)	1339.18	1336.97	1339.70	1346.21	1343.84	1340.22
ΔV/H (Å^3)	1.42	-0.79	1.95	8.46	6.09	1.24

The results of the calculations where hydrogen was in a separate cell to the V_O are given in Table 5.3. Similar behaviour is observed as for the hydrogen interacting with the V_O. These calculations further support the hydride defect being the most favourable defect in hypostoichiometric UO_2. In all cases where a single hydrogen atom occupied the octahedral interstitial site became a hydride defect. The only case that hydrogen at the octahedral interstitial did not become a hydride was the case of H_2, which remained as H_2. As before the case where two hydride defects could be formed (2H O_h) was the most favourable defect. This is due to the hydrogen preventing the formation of U^{3+} defects, but as these defects are not close to positive V_O site the energy is significantly higher, 0.40 eV/H. The significant energy difference between two hydride defects on the V_O with two hydrides occupying two separate octahedral interstitials suggests that V_O have the potential to be trap sites for hydrogen in UO_2. As the metal/oxide interface is likely to be hypostoichiometric in nature, resulting in a significant quantity of V_O sites, this could act as a trapping region for hydrogen. Which would allow for a significant concentration of hydride to accumulate at the interface region. The build up of hydride at the interface in this way could also be another way the nucleation of UH_3 at interface regions occurs.

Wheeler [42] suggests that H_2 could diffuse through the UO_2 lattice via an interstitial vacancy mechanism, without changing the uranium valency. The calculations presented here suggest that presences of H_2 does not result in a change to the uranium valency. However, this is because the H_2 dissociates into two hydride ions. Additionally, the calculations suggest that the V_O site is most energetically favourable site for the hydrides to occupy. Therefore the hydride may not diffuse through the lattice but become trapped on V_O sites.

Table 5.3: Predicted solution energy (E_{Sol}), defect states, lattice parameters and volume change for hydrogen defects in a 96 atom UO_2 cell containing a single oxygen vacancy. Where the hydrogen was added to a cell not containing the V_O. ΔV is calculated relative to the predicted volume of $UO_{1.97}$. $U^{3.5+}$ represents a partially reduced uranium and $U^{4.5+}$ represents a partially oxidised uranium.

Hydrogen Location	**Non-Defect Cell**					
	H O_h	**OH**	**H_2 O_h**	**2H O_h**	**2OH**	**H O_h / OH**
E_{Sol}**/H (eV)**	4.64	6.63	2.64	2.56	4.29	3.46
Final Hydrogen Defect	H^-	OH^-	H_2	$2H^-$	$2OH^-$	H^- / OH^-
Uranium Defect	$2U^{3.5+}/2U^{4.5+}$	$U^{3+}/3U^{3.5+}$	$3U^{3.5+}$	-	$2U^{3+}/4U^{3.5+}$	$4U^{3.5+}$
a **(Å)**	11.02	11.04	11.00	11.02	11.06	11.02
b **(Å)**	11.01	11.04	11.01	11.01	11.05	11.02
c **(Å)**	11.02	11.03	11.06	11.05	11.07	11.04
Volume (Å^3)	1334.07	1344.50	1340.39	1339.46	1351.58	1341.08
ΔV/H (Å^3)	-0.69	6.75	1.32	0.85	6.91	1.66

Unlike stoichiometric UO_2, where the preferred defect is hydride or H_2 depending on the hydrogen concentration. The preferred defect in $UO_{1.97}$ is a hydride which is on the V_O, this preference is further increased when H_2 is on the V_O site as it can dissociate into two hydrides which bridge the vacancy. Additionally, it was found to be more favourable for hydrogen defects to be interacting with the V_O defect site. The reason for the formation of the hydride being so preferable is that it prevents the formation of a U^{3+} defect, which allows for the second U^{3+} to be stabilised and form, rather than being delocalised. If it possible for two hydride defects to form then this is even more favourable as it prevents the formation of any U^{3+} defects. This is similar to what was seen for UO_2 where hydrogen defects that did not change the uranium oxidation state where particularity favourable.

5.0.4 Hyperstoichiometric UO_2 ($UO_{2.03}$)

$UO_{2.03}$ was generated by adding a single O atom to an octahedral interstitial site, with the defect energy calculated according to Equation 5.6. This has a favourable formation energy of -1.23 eV, which agrees well with literature values and matches the observation that UO_2 will oxidise under atmospheric conditions. The addition of an O atom resulted in the oxidation of two U^{4+} to U^{5+}, this is accompanied by a predicted decrease in the volume of 4.96 Å^3.

$$UO_2 + \frac{1}{2}O_2 \rightarrow UO_{2.03} \tag{5.6}$$

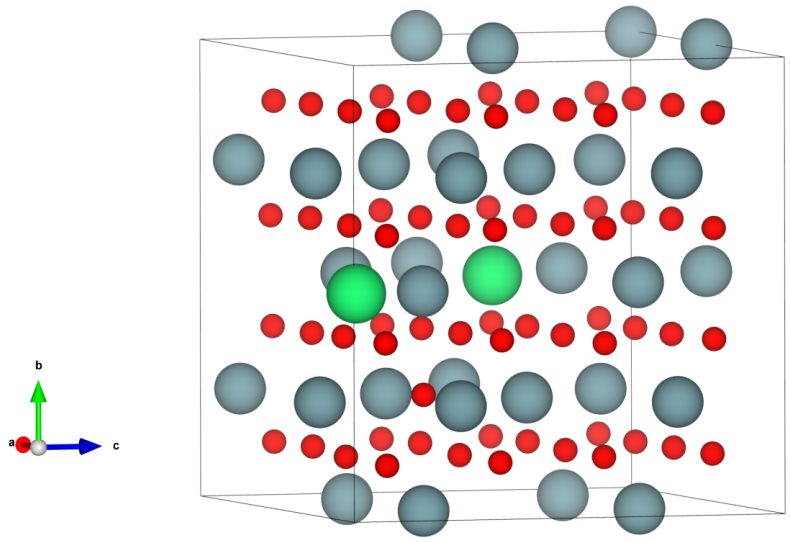

Figure 5.6: Minimised configuration of a single oxygen interstitial in UO_2. U^{4+} shown in blue, U^{5+} ions shown in green and oxygen shown in red.

5.0.5 Hydrogen Defects in $UO_{2.03}$

As with $UO_{1.97}$ the hydrogen defects were considered where there was a direct interaction with the O_i and when the hydrogen was added to a unit cell that did not contain the O_i. In all cases the solution energy of the hydrogen defects was calculated following Equation 5.7.

$$UO_2 + \frac{1}{2}O_2 + \frac{n}{2}H_2 \rightarrow UO_{2.03}H_n \tag{5.7}$$

Where hydrogen was added to the cell containing the O_i five different configurations were considered. There were two single hydrogen defects, these were hydrogen placed a bond length from the O_i in either a <100> or <111> direction, Figure 5.7a - 5.7b. The remaining defects were three different orientations of H_2 in relation to the O_i. These were hydrogen placed end on to the O_i (Figure 5.7c), H_2 placed side on to the O_i (Figure 5.7d) and H_2 placed in a <111> direction between the O_i and a lattice oxygen (Figure 5.7e).

The results of adding hydrogen defects to the O_i defect are shown in Table 5.4. In all cases the calculated solution energy was significantly favourable, suggesting that partial oxidation of UO_2 may enhance the solubility of hydrogen in UO_2. When an O_i is added there is a predicted reduction in the volume due to the formation of U^{5+}, addition of hydrogen results in a predicted volume expansion as the hydrogen become protonic in nature, reducing the U^{5+} to U^{4+}. For the single hydrogen defects one U^{5+} was reduced and in the case of H_2 both U^{5+}, introduced by the O_i were reduced. Similar to the case of H_2 on the V_O site in $UO_{1.97}$, addition of H_2 to the O_i resulted in dissociation of the H_2, into either two hydroxyl groups (Figure 5.8b) or the formation of a water molecule (Figure 5.8a). There is no significant energetic preference found between the interstitial water of two hydroxyl defects.

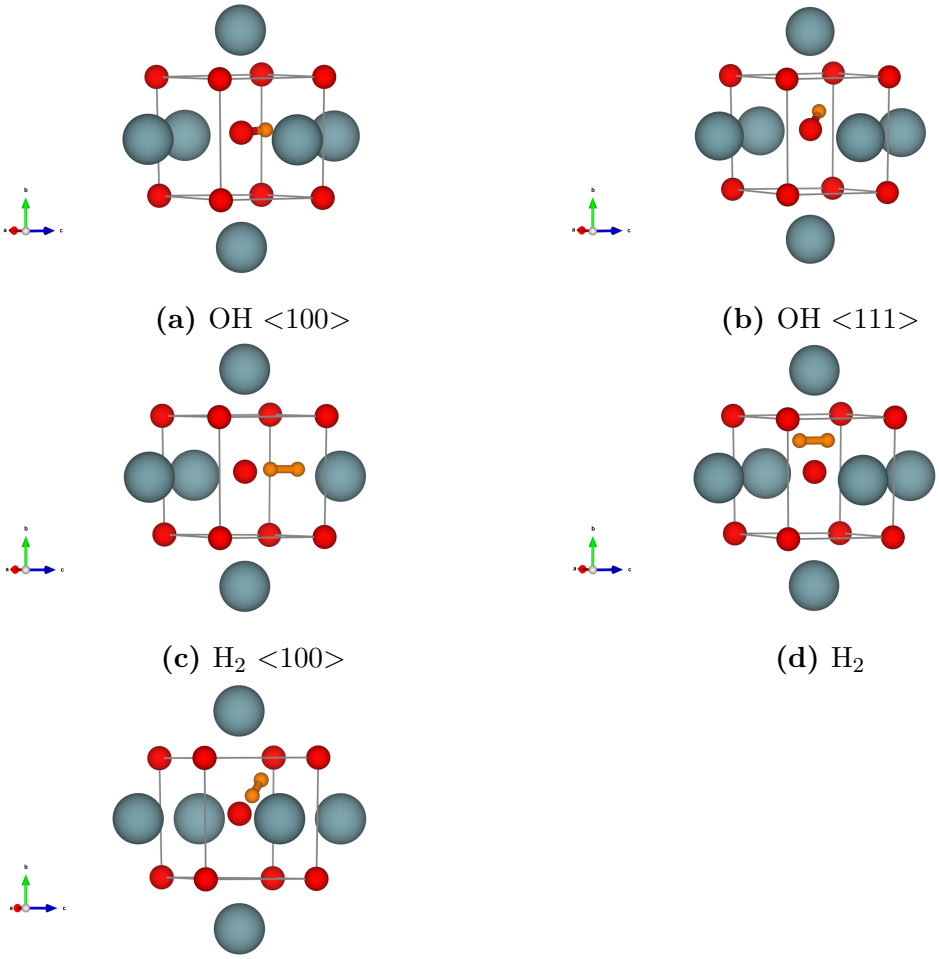

(a) OH <100>

(b) OH <111>

(c) H_2 <100>

(d) H_2

(e) H_2 <111>

Figure 5.7: Initial hydrogen defect configurations in UO_2. Uranium shown in blue, oxygen shown in red and hydrogen in orange. Bonds have been drawn between oxygen atoms for clarity.

Table 5.4: Predicted solution energy (E_{Sol}), defect states, lattice parameters and volume change for hydrogen defects in a 96 atom UO_2 cell containing a single oxygen vacancy. Where the hydrogen was added to the same cell as the O_i. ΔV is calculated relative to the predicted volume of $UO_{2.03}$.

Hydrogen Location	**Defect Cell**				
	OH <100>	**OH <111>**	**H_2O_i <100>**	**H_2O_i**	**H_2O_i <111>**
E_{Sol}/H (eV)	-1.92	-1.99	-0.81	-0.83	-0.52
Final Hydrogen Defect	OH^-	OH^-	$2OH^-$	H_2O	$2OH^-$
Uranium Defect	U^{5+}	U^{5+}	-	-	-
***a* (Å)**	11.01	11.03	11.04	11.02	11.05
***b* (Å)**	11.02	11.02	11.03	11.04	11.04
***c* (Å)**	11.04	11.02	11.06	11.06	11.06
Volume (Å^3)	1339.00	1339.17	1346.25	1345.87	1349.23
ΔV/H (Å^3)	6.76	6.93	7.00	6.81	8.49

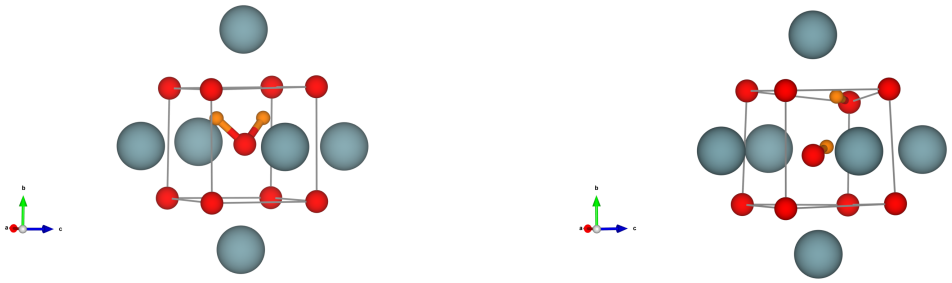

(a) H_2 **(b)** H_2 <111>

Figure 5.8: Final hydrogen defect configurations in $UO_{2.03}$. Uranium shown in blue, oxygen shown in red and hydrogen in orange. Bonds have been drawn between oxygen atoms for clarity.

The calculated properties of hydrogen defects not directly interacting with the O_i are shown in Table 5.5. The hydrogen defect configurations are the same as in the case of $UO_{1.97}$, except they are in relation to an O_i rather than a V_O.

As with $UO_{1.97}$ it is far less favourable for hydrogen to be in a separate cell from the oxygen defect. The only case with a significantly favourable solution energy is the OH defect configuration, however, this is 1.44 eV less favourable than a single hydrogen on the O_i. The formation of additional U^{5+} defects, as seen when single hydrogen atoms were placed on the octahedral site, is particularly unfavourable. An interesting result is the two initial hydroxyl defects converted to form a hydroxyl and hydride defect, without changing the oxidation of the uranium ions. The previous defect configurations have shown that if hydrogen can be added and this prevents the oxidation or reduction caused by an oxygen defect then this is usually quite a favourable configuration.

Table 5.5: Predicted solution energy (E_{Sol}), defect states, lattice parameters and volume change for hydrogen defects in a 96 atom UO_2 cell containing a single oxygen vacancy. Where the hydrogen was added to a cell not containing the O_i. ΔV is calculated relative to the predicted volume of $UO_{1.97}$. $U^{3.5+}$ represents a partially reduced uranium and $U^{4.5+}$ represents a partially oxidised uranium.

Hydrogen Location	**Non-Defect Cell**					
	H O_h	**OH**	**H_2 O_h**	**2H O_h**	**2OH**	**H O_h / OH**
$\boldsymbol{E_{Sol}}$**/H (eV)**	0.80	-0.55	-0.08	1.65	0.85	0.75
Final Hydrogen Defect	H^-	OH^-	H_2	H^- / $H^\cdot$	H^- / OH^-	H^- / OH^-
Uranium Defect	$3U^{5+}$	U^{5+}	$2U^{5+}$	$3U^{5+}$ / $U^{4.5+}$	$2U^{5+}$	$2U^{5+}$
a **(Å)**	10.99	11.03	11.00	10.98	11.08	11.01
b **(Å)**	11.00	11.03	11.01	10.99	11.01	11.02
c **(Å)**	11.00	11.02	11.03	11.01	11.04	11.02
Volume (Å^3)	1329.86	1340.25	1335.14	1329.97	1339.28	1337.16
ΔV/H (Å^3)	-2.39	8.01	1.45	-1.14	3.52	2.46

Similar behaviour is observed for hydrogen in $UO_{2.03}$, compared with $UO_{1.97}$. In both cases placing the hydrogen defect, interacting or not with the O_i, the preferred defect species for hydrogen is as a proton, in either a hydroxyl or part of a H_2O molecule. As with $UO_{1.97}$, there is a clear preference for hydrogen to be interacting with the defect oxygen.

The formation of the protonic defects (OH^-) resulted in a reduction of the number of U^{5+} present equal to the concentration of hydrogen defects added to the system. The ability of hydrogen to reduce U^{5+}/U^{6+} defects has been observed in experimental fuel pellet dissolution studies [166, 169–172], where a pressure of hydrogen was able to reduce or completely prevent the oxidative dissolution of UO_2 fuel pellets.

5.1 Conclusions

As uranium dioxide goes from hypostoichiometric to stoichiometric and finally hyperstoichiometric the nature of the preferred hydrogen defect species changes. In hypostoichiometric UO_2 hydride is the preferred hydrogen species. For stoichiometric UO_2 for monatomic hydrogen species the hydride is more stable than the hydroxyl defect, however, there is a preference for configurations which do not result in oxidation of the uranium ions. Finally, in hyperstoichiometric UO_2 the preferred hydrogen defect is protonic, as this results in reduction of the U^{5+} introduced by the additional oxygen.

It is possible that measuring the changes in the lattice parameters could be used as an indicator of the hydrogen charge state. This will however require the stoichiometry of the oxide to be known, as the volume change predicted depends not only on the hydrogen charge state but also the stoichiometry of the UO_2. Given that unless it is tightly controlled, UO_2 is likely to be hyperstoichiometric, it can be said that protonic defects cause an expansion of the lattice parameters, whereas hydride defects result in a reduction.

In stoichiometric UO_2 it is predicted that the hydride defect is more favourable than the hydroxyl defect, though there is not a significant energy difference between the two defects. For H_2 a favourable solution energy is predicted, however on increasing the defect concentration this becomes unfavourable. Which agrees with the experimentally observed low solubility of hydrogen in UO_2. The most favourable defect configurations are those that do not result in any oxidation of the uranium ions.

In hypostoichiometric UO_2 it is predicted that the most favourable defect is a hydride species which occupies the oxygen vacancy. This results in the localisation of the remaining excess charge in a single U^{3+} ion. If it is possible to form hydride defects for each V_O then no U^{3+} formation is observed. The favourable nature of hydride defects on V_O sites indicates that they may be trap sites which prevent the diffusion of hydrogen through the oxide lattice. This may also lead to an explanation of why hydriding occurs at the metal oxide interface. The presence of V_O in the oxide allows for the build up of hydride species at the metal/oxide interface, which stabilises the formation of U^{3+} ions, which could potentially act as nucleation site for the formation of the hydride.

For hyperstoichiometric UO_2 the hydrogen defects show a preference to interact with the oxygen defect as was the case in $UO_{1.97}$. However, the preferred charge

state of hydrogen is now a proton, either as part of a hydroxyl (or water) group. The formation of the protonic defects also resulted in the reduction of the U^{5+} defects introduced by the addition of oxygen to the lattice. The ability of hydrogen to reduce U^{5+}/U^{6+} has been observed in experimental fuel pellet dissolution studies. Therefore, the presence of hydrogen in hyperstoichiometric UO_2 may help slow the rate of oxidation of UO_2. Given the low solubility it may be that the quantity of hydrogen that can be dissolved is inconsequential to the oxidation rate.

Whilst this chapter has built an understanding of the different hydrogen defects present in UO_2, what has not been considered is how these hydrogen species diffuse through the lattice. Thus the next chapter aims to begin to explore how hydrogen defects diffuse through the UO_2 lattice.

6 Hydrogen Transport in UO_2

The previous chapter explored the structure and relative stability of a range of hydrogen defects in UO_2. However, this ignores an important consideration which is how does hydrogen diffuse through the oxide lattice. Experimentally, it has been shown that monatomic dissolution occurs [44]. The implication of this is that the diffusing species is, at least initially, monatomic hydrogen. The previous chapters have shown that the nature of the hydrogen defects can vary significantly based on the location and stoichiometry of the UO_2. This presents a complex landscape of defect states through which hydrogen could transform as it moves through the oxide lattice.

This chapter will focus on exploring how hydrogen defects change as they move through the oxide lattice, to build the foundations of exploring hydrogen transport in UO_2. This chapter will be further divided into two sections; the first will consider the conversion of the hydride defect to the hydroxyl as these two defects have a similar formation energy ($\Delta E \approx 0.2$ eV), therefore it is necessary to understand how easily the conversion between these two defect states can occur. Additionally, the hydride and hydroxyl defect positions are only separated by a very small distance of ≈1.5 Å. The second will consider how hydrogen (H^- and H_2) move between octahedral interstitial locations. This can be thought of as intra- and inter- cell behaviour, respectively.

A paper concerning the conversion of hydride to hydroxyl defects in UO_2 has been published in *Chemical Communications* entitled "*Hydride Ion Formation in Stoichiometric UO_2*"[141].

6.1 Intra-cell Hydrogen Behaviour

As seen in the Chapter 4 the hydride and hydroxyl defects in UO_2 have a similar formation energy ($\Delta E \approx 0.2$ eV) and the optimised locations are only separated by a distance of ≈1.5 Å. Therefore, it is likely that conversion between these two different defect species could occur on a rapid basis. This may result in similar defect populations of hydride and hydroxyl species in UO_2, particularly at higher temperatures. Additionally, if there are hydroxyl defects present they may rotate and the hydrogen could dissociate in one of the remaining two crystallographic directions (<100> and <110>).

In order to assess the barrier between these two defect species, along the three directions (<100>, <110> and <111>), re-orientated unit cells were used to allow for the use of selective dynamics methodology. For the <100> and <110> a 48 atom system was used and for the <111> a 36 atom system was generated. This is where the hydrogen was only allowed to minimise in two of the three crystallographic

directions and held fixed in the third. This means that the hydrogen will explore the energy landscape at a fixed distance from the lattice oxygen atom.

The combinations of all these calculations will then give a fuller view of how hydrogen behaves in the pure UO_2 lattice as a function of O-H distance. The use of different sized simulation systems will result in solution energies which vary from each other. This can be seen in the solution energies for the hydride and hydroxyl defects in the 36 atom cell (1.31 eV (H^-) and 1.56 eV (OH^-)) and 96 atom cell (0.19 eV (H^-) and 0.41 eV (OH^-)), in Chapter 4. Whilst the absolute value of the solution energy does change, the relative energy for the two systems remained similar (0.25 eV for the 36 atom and 0.22 eV for the 96 atom). This allows for a comparison of the behaviour of hydrogen at different defect concentrations and relative energies but not the absolute values of the energies.

Figure 6.1 shows the hydrogen defects along the three different crystallographic directions. The full simulation cell is shown along with a single oxygen sub-lattice highlighting the individual pathway being explored. The orientation of the oxygen sub-lattice is identical to that displayed in the full simulation cell. Only the two end points of each direction are displayed. The range of distances considered, for each direction, is from an O-H bond length from the oxygen atom to the mid-point between the two oxygen atoms at the end of each direction.

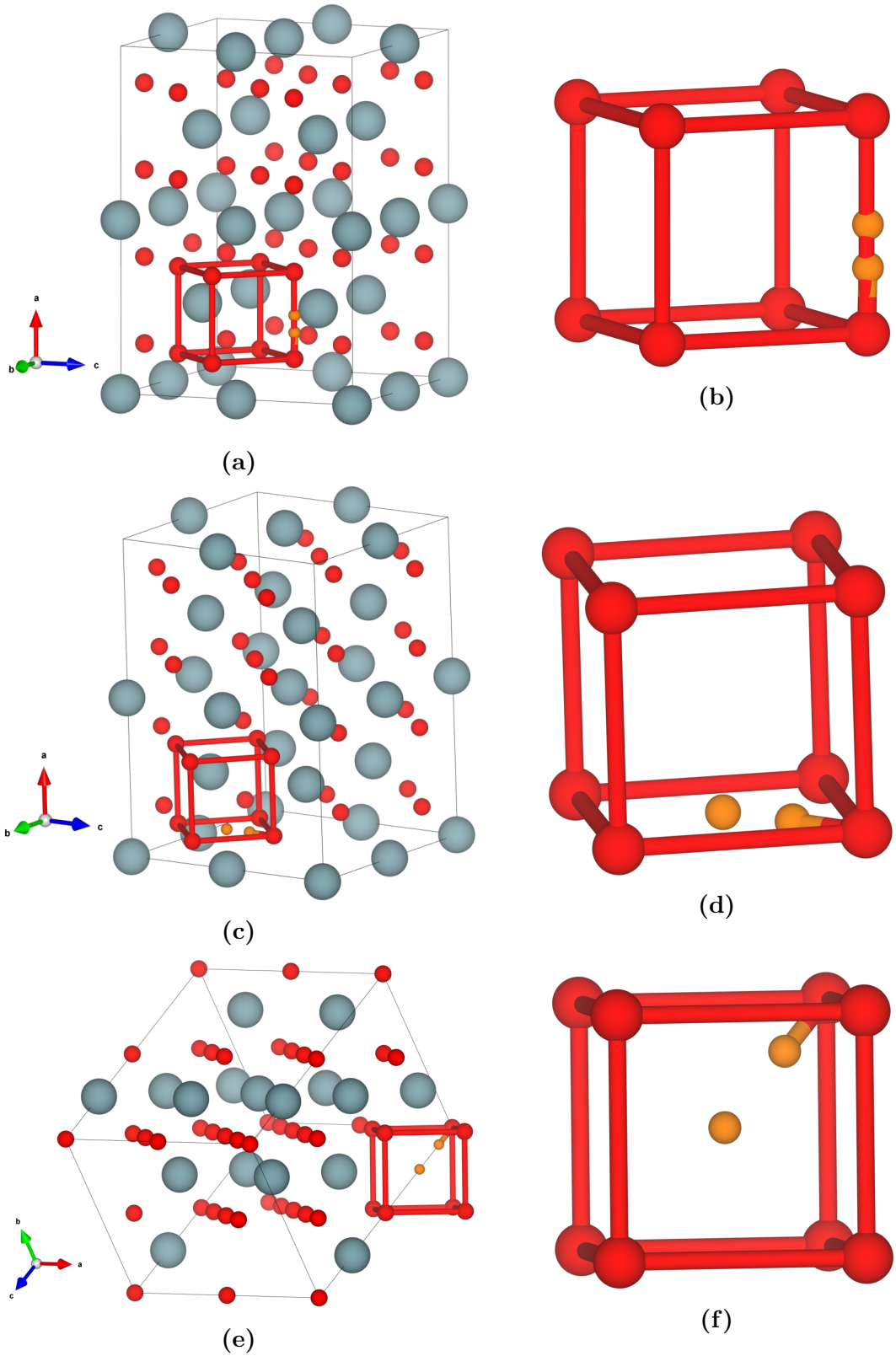

Figure 6.1: End points of hydrogen exploration along the <100> (6.1a and 6.1b), <110> (6.1c and 6.1d) and <111> (6.1e and 6.1f) crystallographic directions. Red atoms are oxygen, blue are uranium and orange are hydrogen. Bonds have been drawn on the oxygen sub-lattice for clarity. The orientation of the oxygen sub-lattice is the identical to that displayed in the full simulation cell.

6.1.1 Hydrogen behaviour in the <100> Direction

The <100> direction is the shortest of the three directions considered, with the O-O distance of 2.73 Å. As the O-H distance is never very large the final hydrogen species is protonic, in all except two cases, as seen in Figure 6.2. The two cases where protonic defects where not formed hydride species were predicted. These two defects are significantly higher in energy (0.5 eV and 0.85 eV) than the most stable hydroxyl defects. The energy of the hydroxyl defects predominately showed only a small variation as a function of O-H distance, with all except four defects within 0.26 eV of the most stable. The volume showed a consistent change ($\approx 7 Å^3$) for the hydroxyl defects regardless of the O-H distance, due to the formation of a U^{3+} ion. There is slight decrease in the volume expansion with larger O-H distances but his is marginal. Interestingly, the two hydride defects also predict a volume expansion, despite the formation of a smaller U^{5+} ion. This can be ascribed to the repulsion caused by the formation of a negative charge (hydride defect) between the two oxide ions.

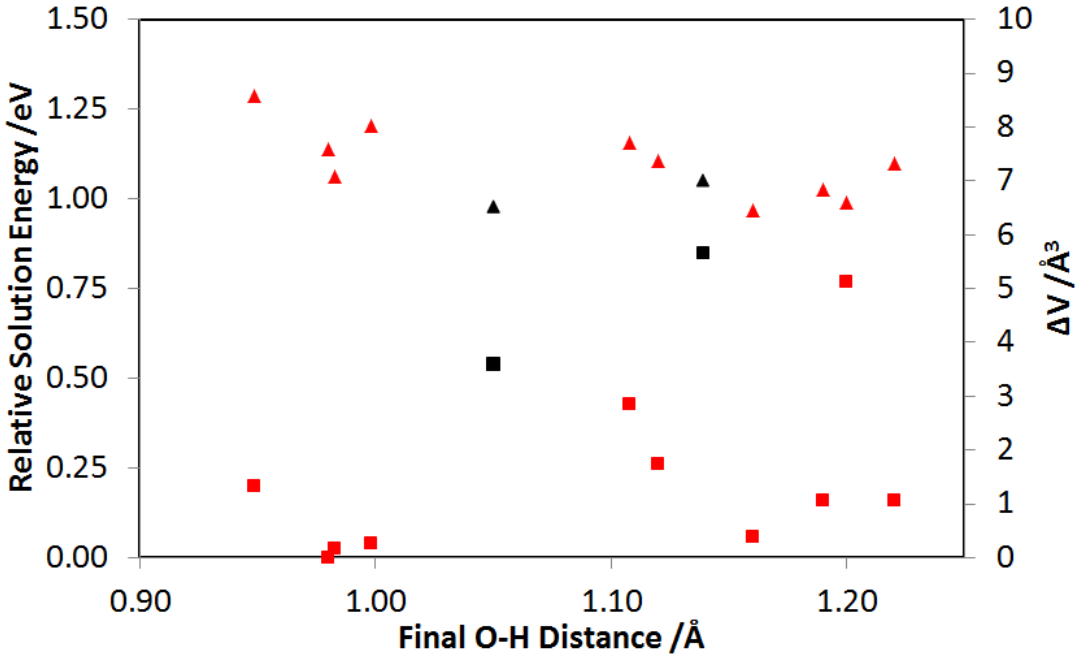

Figure 6.2: The relative solution energy (Squares) and change in cell volume (Triangles) for the hydrogen in a <100> path in UO_2. Final hydrogen species represented by colour; red proton and black hydride. The energies are set relative to the lowest energy configuration (OH^- and U^{3+}).

6.1.2 Hydrogen behaviour in the <110> Direction

The profile of hydrogen as it transitions across the face of the oxygen sub-lattice, in the <110> direction, is shown in Figure 6.3. Similar behaviour is observed to the <100> direction, up to ≈1.2 Å, where protonic defects (OH^-) compensated by U^{3+} and corresponding volume expansion is predicted. The most stable defect is again predicted to be a hydroxyl group. This protonic region is then followed by a region for which there was no final O-H distance between ≈ 1.2 - 1.5 Å, suggesting that it is a particularity unfavourable distance. Above 1.5 Å the hydrogen is predicted to exist as a radical species, these decrease in energy as the O-H distance increases. As there are no species, that have an O-H distance, in the region where the transition between the protonic and radical species occurs trends have been extrapolated from the protonic and radical results to predict an energy barrier. This suggests that the barrier to in this direction is between 0.45 - 0.55 eV.

The volume shows a linear decrease as the O-H distance increases, where if a U^{3+} species is formed then there is a large increase in volume. Whereas when a radical species is formed there is no significant volume change and as the radical species become lower in energy there is a gradual decrease in the volume predicted. The most stable radical species also have a slight volume decrease predicted and upon examining the uranium magnetisation this is due to partial oxidation occurring, where some of the U^{4+} is being partially converted to a U^{5+}.

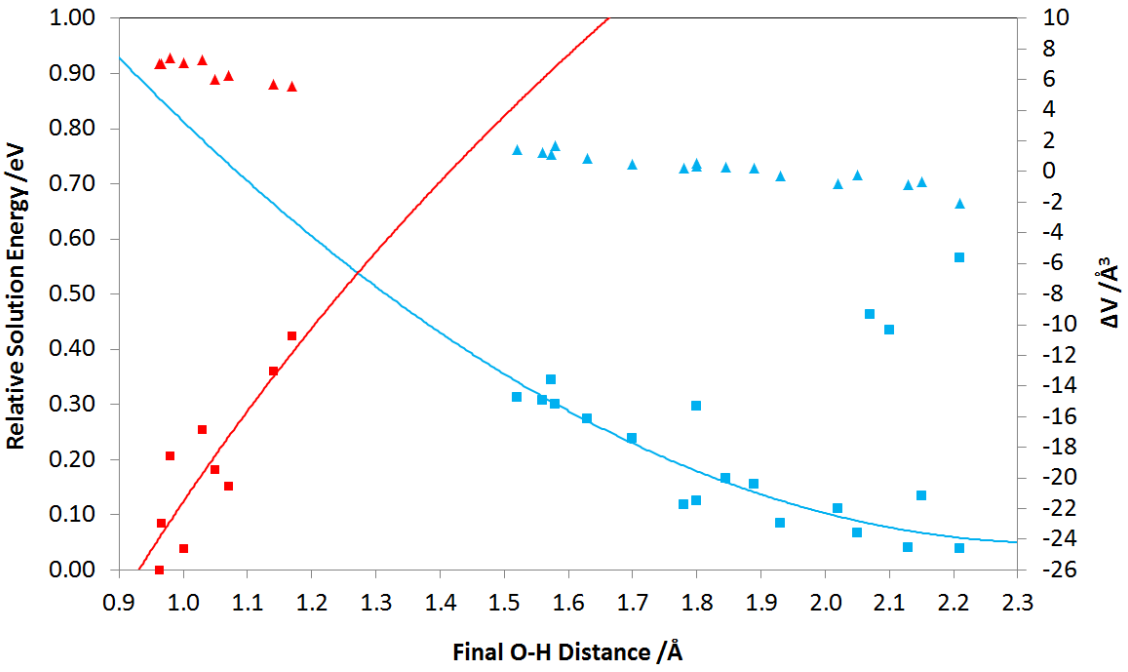

Figure 6.3: The relative solution energy (Squares) and change in cell volume (Triangles) for the hydrogen diffusion path in UO_2. Final hydrogen species represented by colour; red proton and blue radical. The energies are set relative to the lowest energy configuration (OH^- and U^{3+}). Trend lines added to predict the intersection of the two species.

6.1.3 Hydrogen behaviour in the <111> Direction

The profile analysis of hydrogen moving along in a <111> between a hydride and hydroxyl defect as a function of hydrogen oxygen distance is shown is Figure 6.4.

As the hydrogen moves from the octahedral site towards the lattice oxygen it converts from a hydride to a radical hydrogen species before becoming part of a hydroxyl defect. There are three distinct regions shown in Figure 6.4. The first occurs close to the oxygen atom, up to 1.13Å, where the hydrogen becomes a proton, as part of a hydroxyl group, and there is a corresponding U^{3+} defect formed. This has a large increase (1.40%) in volume of the unit cell due to the formation of the U^{3+}. The second region, at 1.13Å - 2.00Å from the oxygen atom, is where there is no change in oxidation state of the hydrogen or uranium. In this region the hydrogen is a radical and could be seen as an intermediate state between the hydride and proton species. This region is higher in and shows a small volume expansion (0.06% - 0.50%) compared to the stoichiometric unit cell. The final region, when the oxygen hydrogen distance is greater than 2.00Å, the final hydrogen species is a hydride and this is the most stable hydrogen defect. The formation of the hydride is accompanied by the formation of a U^{5+} and results in a decrease (-0.30% - -0.66%) in volume of the unit cell.

For all of the protonic defects formed the corresponding U^{3+} defect was formed as a nearest neighbour defect (2.38Å – 3.56Å). For the hydride defects, the U^{5+} formed as a next nearest neighbour defect (4.27Å - 5.85Å).

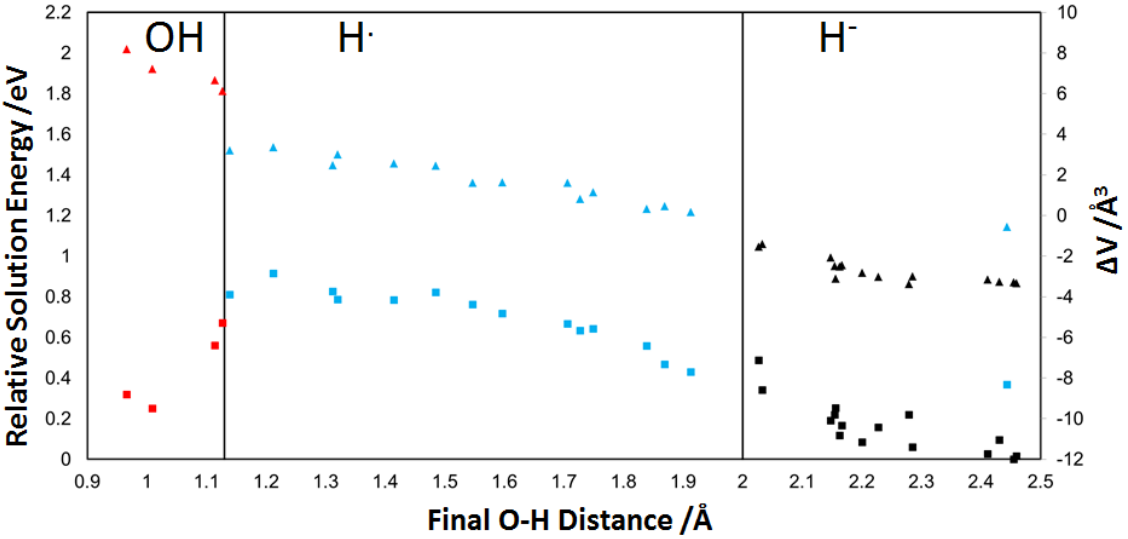

Figure 6.4: The relative solution energy (Squares) and change in cell volume (Triangles) for the hydrogen diffusion path in UO_2. Final hydrogen species represented by colour; red proton, blue radical and black hydride. The energies are set relative to the lowest energy configuration (H^- and U^{5+}).

The only two exceptions, where the U^{5+} defect formed as a nearest neighbour defect (2.36Å, 2.64Å), were both higher in energy than the positions to either side of them, however the energy difference was only ≈0.1 eV. Thus whilst forming a U^{5+} as a nearest neighbour defect is less favourable, it is not accompanied by significant increase in energy. This suggests that there are multiple local minima which may have implications for electron transport.

As there are three distinct regions, shown in Figure 6.4, where the hydrogen is a proton, then a radical and finally a hydride this shows that the transition between the proton and hydride could occur as two one step processes, where the proton becomes a radical and then a hydride, rather than a single two step electron process where the proton becomes a hydride. From Figure 6.4 it is also possible to estimate the activation energy barrier for the formation a hydroxyl group from a hydride species; the barrier is 0.94 eV.

The presence of the two different defects, hydride and hydroxyl, relatively close to each other in location and with similar energies will have an influence on the diffusion of hydrogen in stoichiometric UO_2. It is possible that the diffusion of hydrogen could be a concerted mechanism involving both species, compared to the diffusion of hydrogen in CeO_2 where the hydrogen remains as a proton and moves as a proton from one lattice oxygen to the next. It is therefore clear that the fluorite structure might trigger hydrogen dissolution but as the hydrogen solubility in CeO_2 was reported to be lower than in UO_2, this implies that the nature of the actinide cation has a significant impact [44, 353]. Ce^{4+} does not oxidise to higher oxidation states while U^{4+} does [84], but readily reduces to Ce^{3+} while U^{4+} does not. Thus, CeO_2, contrary to UO_2 is a mixed proton electron conductor as hydrogen dissolves as a proton forming hydroxyl groups [101, 357]. On the other hand, it is difficult to define the hydrogen species diffusing and the mechanisms due to the uncertainties of the quantum nature of the hydrogen, which might require *ab initio* path integral molecular dynamics [358, 359]

The DOS spectrum is the same as was seen in the Chapter 4 (Figure 4.3 and Figure 4.4) where the hydride occupies states just below the top of the valence band and the U^{5+} is at the bottom of the conduction band. For the hydroxyl defect the U^{3+} has become the top of the valence band.

6.1.4 Hydrogen Species in UO_2

The exploration of hydrogen behaviour along the three different directions has allowed for a picture of the energetic landscape to be established. In addition the preferred defect state shows a strong dependence on the O-H distance, with this influencing the hydrogen species that forms which in turn determines how the uranium sub-lattice responds, either oxidation or reduction. As a result of this it is possible to make a prediction of the hydrogen charge state based on the O-H distance, though at the interface region between two defects states is not clearly defined as a hard change. There is instead a small region where the charge states are in between two different defect states, however these regions are particularly unstable so the hydrogen will not spend a significant amount of time in these regions. Figure 6.5 shows a visual representation of the hydrogen behaviour in UO_2 based on the O-H distance as has been determined from the results above.

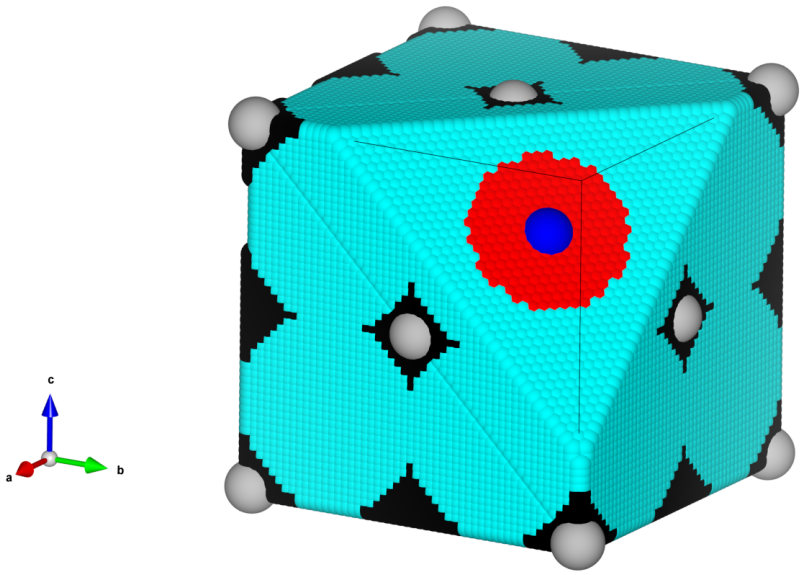

Figure 6.5: Visual representation of the behaviour of hydrogen based on O-H distance in UO_2. Where hydrogen is protonic in nature shown in red, as a radical in light blue and as a hydride in black. Uranium shown in light grey and oxygen shown in dark blue. The top corner has been cut away to show the environment around the oxygen atoms.

6.2 Inter-cell Hydrogen Behaviour

The previous section has examined how a monatomic hydrogen defect behaves within a UO_2 unit cell, this can be used as the base for building an understanding of how hydrogen transitions between unit cells. The ideal method to examine diffusion behaviour is *ab initio* molecular dynamics, however this is too computationally expensive to be applied to UO_2. Therefore, two alternative methods to examine hydrogen transport have been applied. The first uses a series of isolated minimisations, in a 96 atom simulation cell, on different hydrogen configurations in order to generate a series of energy levels which will scope out the energy landscape. This will not provide the barrier to hydrogen diffusion but can help reduce the search space to find the likely pathway of hydrogen diffusion. Additionally, using the largest cell possible will give a more realistic hydrogen concentration.

The second approach is the climbing nudged elastic band method (cNEB), unfortunately, the 96 atom cell is too large to use the cNEB approach at a reasonable computational cost. Therefore, the smaller 48 atom simulation cell will be used with the cNEB method to fully scope out the pathway and determine the barriers to diffusion, in addition to investigating how the nature of the hydrogen species evolves as it moves between interstitial sites.

6.2.1 Monatomic Hydrogen

The structure of the fluorite lattice is such that diffusion can only easily occur by passing through the edge of the cube of the oxygen sub-lattice, as any other direction is blocked by a U^{4+} ion. In the <111> direction this means passing through the edge of the cube of the oxygen sub-lattice. Including the data about hydrogen behaviour within a unit cell from the previous section there are three possible pathways for hydrogen diffusion in UO_2. Hydride moving between adjacent octahedral sites as a hydride species (Pathway 1, Figure 6.6a), hydride moving between octahedral sites via a hydroxyl intermediary (Pathway 2, Figure 6.6b) and finally, there is the proton hopping between lattice oxygen, without changing to a hydride defect (Pathway 3, Figure 6.6c). In order to initially assess these different potential pathways the key individual positions where constructed and minimised in a 96 atom simulation cell.

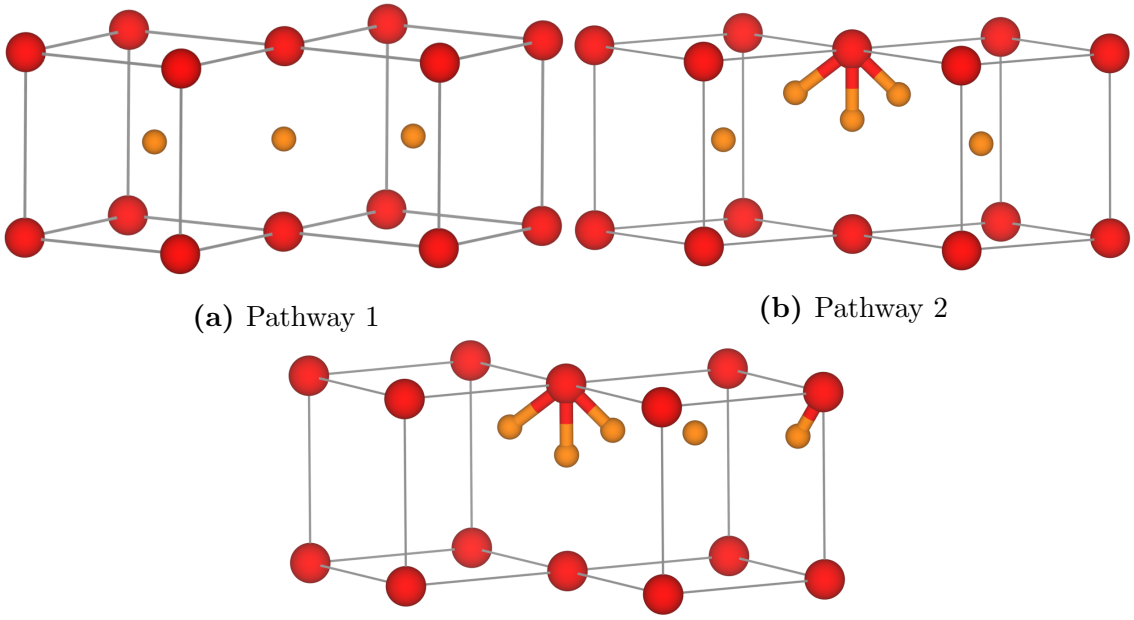

(a) Pathway 1 **(b)** Pathway 2

(c) Pathway 3

Figure 6.6: Initial configurations of H used to explore the energy landscape towards monatomic hydrogen diffusion in UO_2. Figure 6.6a shows the configurations where the diffusing species is hydride. Figure 6.6c shows where the diffusing species is a proton. Figure 6.6b shows where the hydride converts to a hydroxyl and back for the diffusing species. Oxygen shown in red and hydrogen in orange. Uranium not shown and bonds have be drawn between oxygen for clarity.

Figure 6.7 shows the relative energies of these positions representing key positions on the pathway between unit cells for a hydrogen atom, as it diffuses between unit cells. The energies have been set relative to the lowest energy defect, which is hydride at the octahedral interstitial site. Each of the individual levels for the three pathways corresponds to the position of a hydrogen atom in the pathway illustrated by Figure 6.6. The black line corresponds to Pathway 1, blue to Pathway 2 and red to Pathway 3.

As can clearly be seen while the initial transition within the unit cell is similar for all pathways, when the main transition occurs both the hydride to hydride and hydroxyl to hydroxyl pathways have a significantly larger energy barrier than the

hydride converting to a hydroxyl defect. Based on these results as hydrogen diffuses through the lattice it is not as a static species but involve a more complicated diffusion mechanism, involving both hydride and hydroxyl defects. This, has the additional complication that as the hydrogen changes from hydride to hydroxyl a uranium ion changes from the 5+ oxidation state to the 3+ oxidation state.

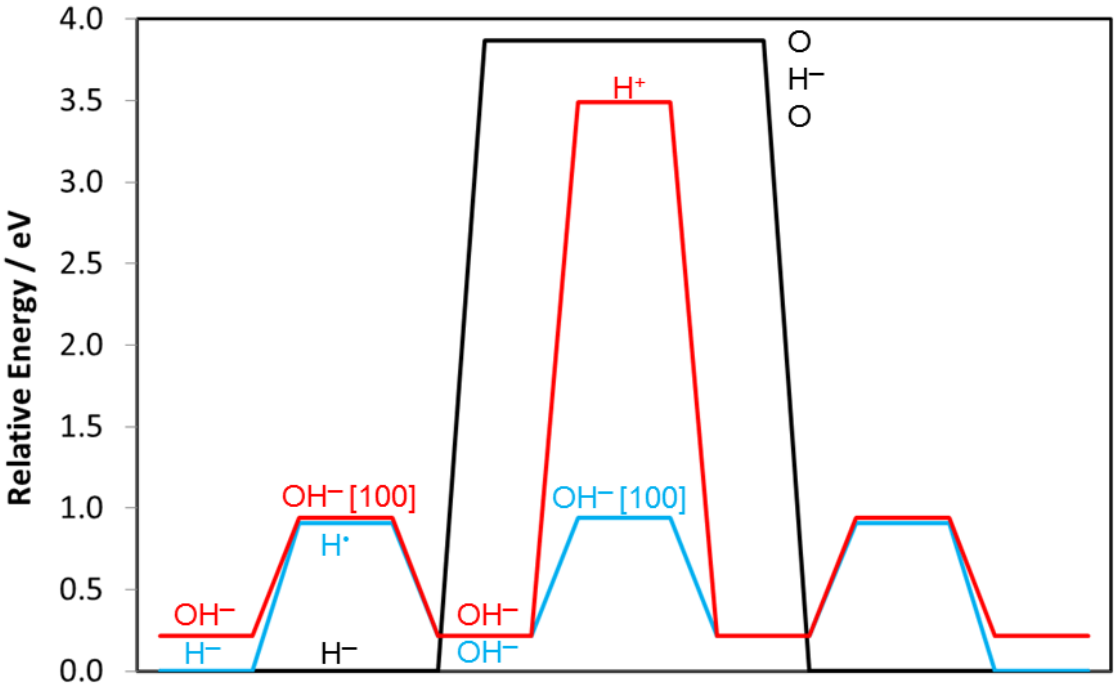

Figure 6.7: Relative energies of different diffusing pathways for monatomic hydrogen defect, moving between octahedral interstitial sites in UO_2. Energies have been set relative to the lowest energy defect. Pathway 1 (Hydride to Hydride) shown in black, Pathway 2 (Hydride to Hydride via Hydroxyl) shown in blue and Pathway 3 (Hydroxyl to Hydroxyl) shown in red.

6.2.2 Molecular Hydrogen

From Chapter 4 when molecular hydrogen's properties were calculated using range of functionals all predicted a favourable solution energy. This suggests that if H_2 forms in UO_2 then it has the potential to be trapped and in order to move through the lattice may require dissociation to occur.

To explore this and simulate how H_2 moves between octahedral interstitial sites a series of isolated H_2 configurations representing different stages of a H_2 transition were created. These are shown in Figure 6.8, the first three positions represent the transition from the octahedral interstitial site to the O-O edge. Positions 4-6 represent the different potential transitions H_2 could have at the O-O edge. Position 4 (Figure 6.8d) is where the H_2 carries on along a linear trajectory and passes through the centre of the O-O edge. Position 5 (Figure 6.8e) is similar to position 4 except that the H_2 passes through the O-O edge closer to one of the lattice oxygen that the other. This was set such the both hydrogen atoms of the H_2 were approximately an O-H bond length from the lattice oxygen. Finally, position 6 (Figure 6.8f) is where the H_2 passes through the O-O parallel rather than perpendicular. This puts the

hydrogen atoms at an O-H distance away from the lattice oxygen.

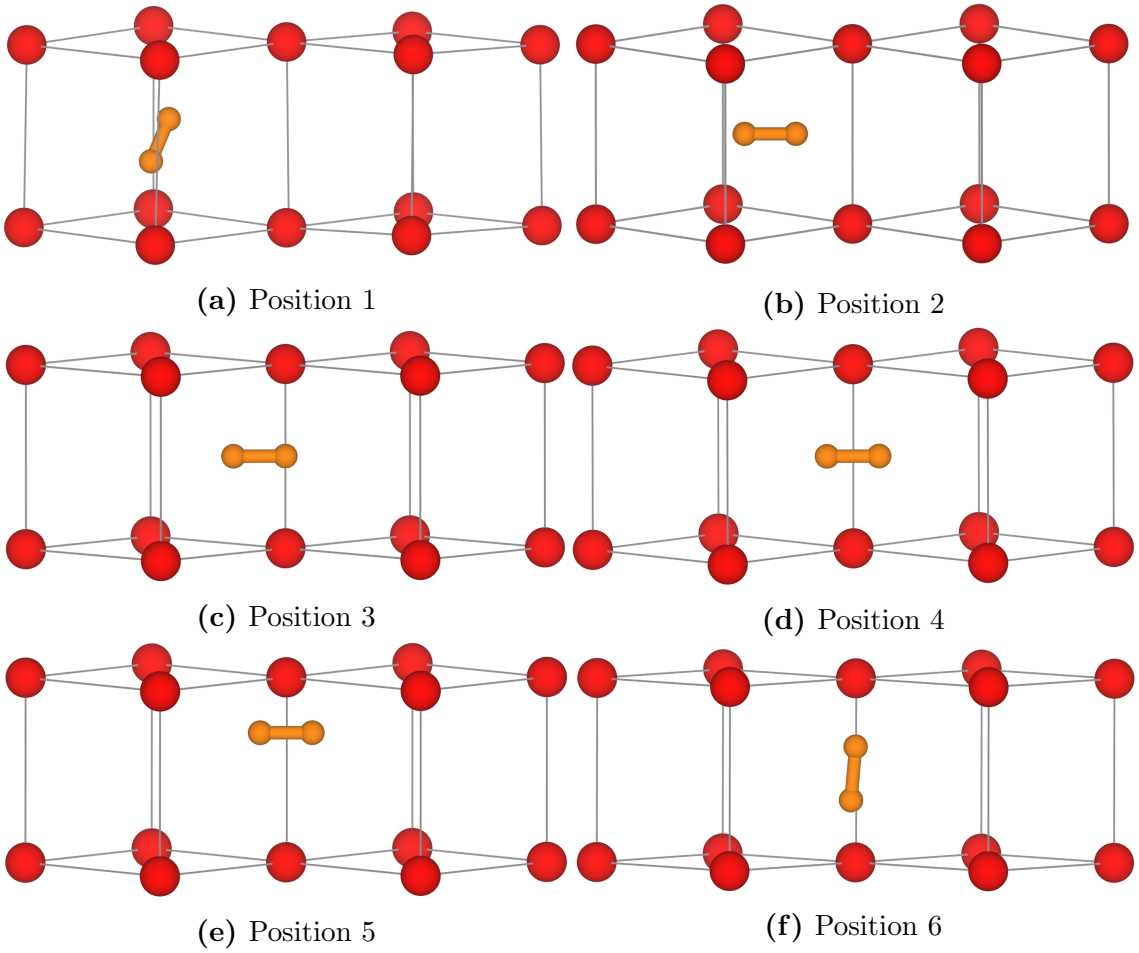

(a) Position 1 **(b)** Position 2

(c) Position 3 **(d)** Position 4

(e) Position 5 **(f)** Position 6

Figure 6.8: Initial configurations of H_2 used to explore the energy landscape towards hydrogen diffusion in UO_2. Oxygen shown in red and hydrogen shown in orange. Uranium removed and bonds shown between oxygen for clarity.

The resulting relative energies for these calculation are given in Table 6.1, where the energy of H_2 at the octahedral interstitial site (Figure 6.8a) has been set to zero. There is a small energy barrier for hydrogen to move towards the O-O edge, ≈0.5 eV. However, once the hydrogen occupies the space between the two oxygen atoms the energy barrier rapidly increases to ≈2.3 eV. In all cases the H_2 remained as H_2 and did not dissociate. Instead either one or both of the oxygen atoms on the corners of the cube moved away from their lattice sites, moving towards forming interstitial oxygen species (Figure 6.9).

Table 6.1: Relative energy of different H_2 positions (H_2 in the O_h site set to zero) and the change in volume compared to stoichiometric UO_2.

Position	1	2	3	4	5	6
Relative Energy (eV)	0.00	0.54	2.32	2.59	2.54	2.27
ΔV (Å^3)	2.80	4.06	7.92	12.96	7.93	13.07

The lowest energy configuration is for position 6, where the H_2 is parallel to the O-O edge, this configuration is lower in energy by ≈0.3 eV. This appears to be due to two medium strength hydrogen bonds which are present at position 6 between the H_2 and the two oxygen atoms which are displaced. This is compared to the two configurations (Positions 4 and 5) where the hydrogen is perpendicular to the O-O edge and the presence of only very weak hydrogen bonding interactions.

The size of the energy barrier also raises the question of how readily H_2 diffuse through the lattice, given the barrier is ≈2.3 eV. It is possible that if H_2 forms within the oxide lattice that it is effectively trapped within a unit cell and only if it dissociates is it able to diffuse. As the barrier to monatomic hydrogen diffusion is lower at ≈1 eV.

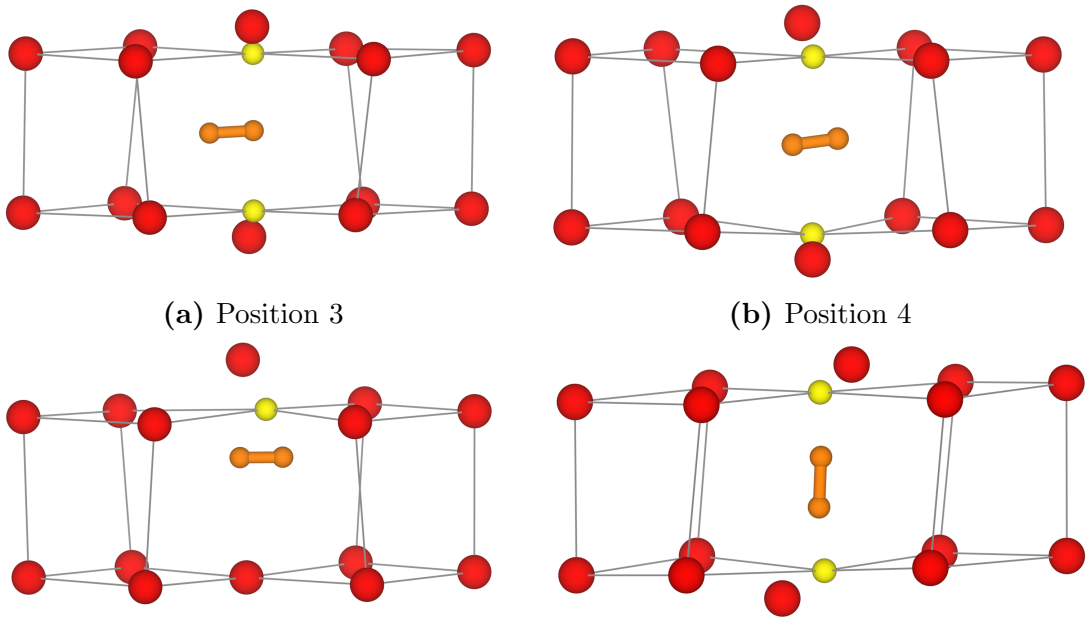

(a) Position 3 **(b)** Position 4

(c) Position 5 **(d)** Position 6

Figure 6.9: Final configurations for positions 3-6. Lattice sites where oxygen has moved away from its lattice site indicated by yellow atom. Oxygen shown in red and hydrogen shown in orange. Uranium removed and bonds shown between oxygen for clarity.

Whilst the rotated H_2 molecule, which is parallel to the O-O edge, is the lowest in energy (from these calculations) the likelihood of rotation occurring is unknown from these calculations. In order to explore this there are two possible methods; *ab inito* molecular dynamics, which is too computationally expensive, or the climbing nudged elastic band method. The second of these two methods have been employed here and the results are discussed in the next section.

cNEB Approach

In the climbing nudged elastic method there are two minimised end configurations which are then linked by a series of images representing the pathway between the two end points. In effect a reverse minimisation is preformed such that the middle image becomes the highest energy point between the two minima. For the exploration of the behaviour of H_2 in these calculations one and three images have been used.

Table 6.2 summaries the energies, final defect states and change in volume for the 5 image cNEB calculations. The final configurations are shown in Figure 6.10. As the H_2 moves from one interstitial site to the next there is only small increase in the energy, until the O-O edge is crossed. At this point the energy barrier becomes very large and this is seen visually in Figure 6.11. Equally there is a large change in volume as the H_2 moves across the O-O edge, this arises from the two oxygen atoms on the corner of the oxygen sub-lattice being moved off their lattice sites (Figure 6.10c), as was seen in the static calculations.

Table 6.2: Relative energy, final defect state and the change in volume compared to stoichiometric UO_2 for the 5 image H_2 cNEB calculation.

Image	1	2	3	4	5
Relative Energy (eV)	0.00	0.46	2.38	0.64	0.11
Hydrogen Defect	H_2	H_2	H_2	H_2	H_2
H_2 Bond Length (Å)	0.75	0.76	0.87	0.75	0.75
ΔV (Å^3)	2.60	4.38	12.73	7.18	2.36

Whilst the H_2 remains as H_2 and does not dissociate, there is a significant lengthening of the H-H bond distance as the molecule crosses the O-O edge. This occurs because whilst the two oxygen atoms have been displaced from their lattice potions there are still very strong O-H interactions. The O-H distances are 1.39 Å and 1.71 Åand these O-H interactions are strong to high medium strength H-bond interactions [360]. This offers an explanation as to why the barrier to diffusion is predicted to be so large, and as to why it increases very rapidly as hydrogen approaches the O-O edge. In order for H_2 to move from one unit cell to the next it needs to displace two oxygen atoms from their lattice positions and overcome two strong O-H interactions. The O-H interactions cause the lengthening of the H_2 bond from its equilibrium distance, without causing full dissociation to occur and this is energetically unfavourable for the H_2 molecule.

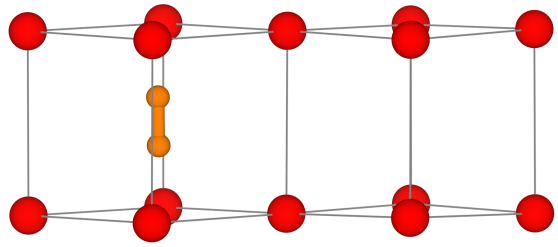

(a) Image 1

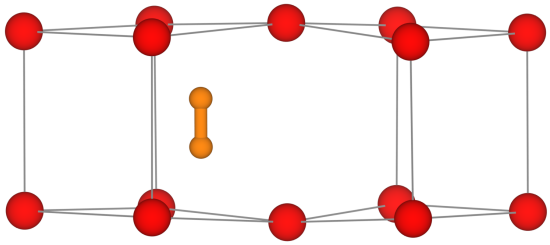

(b) Image 2

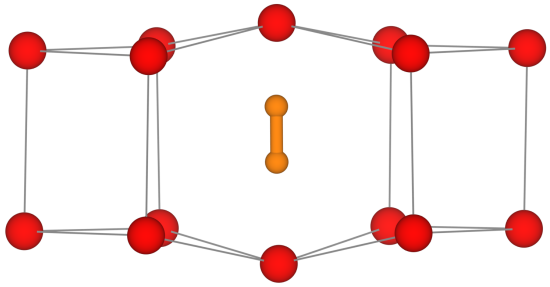

(c) Image 3

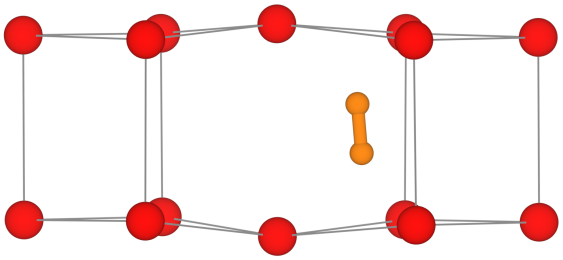

(d) Image 4

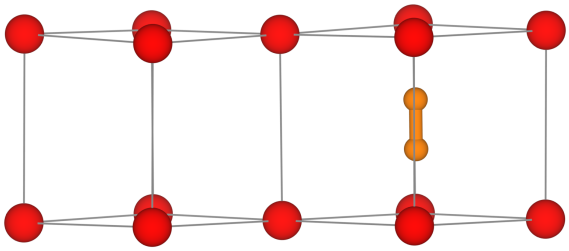

(e) Image 5

Figure 6.10: Final configurations for of H_2 in the 5 image cNEB calculation. Oxygen shown in red and hydrogen shown in orange. Uranium removed and bonds shown between oxygen for clarity.

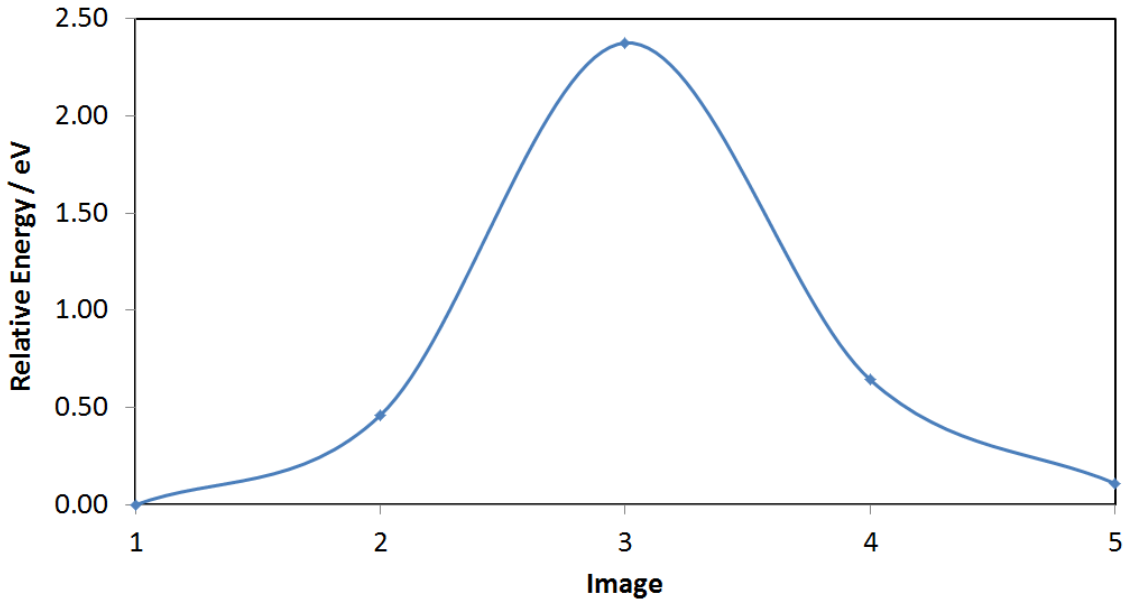

Figure 6.11: Relative energies of H_2 5 image cNEB calculation. Energies have been set relative to the lowest energy defect.

6.3 Conclusions

In this chapter we have begun to evaluate the energy surface for hydrogen migration in UO_2, although clearly there is still much more work required to explore fully hydrogen diffusion in UO_2. The preferred hydrogen defect state is governed by the oxygen hydrogen distance. At short OH distances ($<\approx$1.20 Å) protonic defects are formed, compensated for by the formation of a U^{3+}. When the OH distance is large ($>\approx$2.0 Å) hydride defects form, with the oxidation of a U^{4+} to U^{5+}, this is the most stable monatomic hydrogen defect found in UO_2. In between these two limits no oxidation or reduction of the uranium ions occurs and the hydrogen remains as a radical species, this is typically the most energetically unfavourable species formed.

In addition to mapping the energy landscape of hydrogen in UO_2, the barriers to both monatomic and molecular hydrogen species diffusing have been assessed. For monatomic hydrogen three different pathways were considered, the most energetically favourable pathway involved conversion of the hydride defect to a hydroxyl defect, with a corresponding conversion of U^{5+} to U^{3+}. The barrier to a monatomic hydrogen defect diffusion is $\approx$ 1 eV.

For molecular hydrogen the barrier to diffusion was calculated to be $\approx$ 2.4 eV. The energy landscape of H_2 is relatively flat, until the H_2 approached the edge of the oxygen sub-lattice where the energy rises rapidly. Interestingly, the most favourable geometry for the H_2 to pass through the edge for the oxygen sub-lattice cube was parallel, where two strong O-H interactions occur. This seems to be the major contribution to the large barrier to diffusion. This is more favourable than a perpendicular crossing of the O-O edge as in this case four, individually less strong, O-H interactions occur. However, overall these interactions sum to be greater than the parallel transition geometry. One way to more fully assess the barriers and states that form on hydrogen diffusion would be to use *ab initio* molecular dynamics but currently this is too computationally expensive to be employed for these systems.

Further work could also include the calculation of the H_2 dissociation mechanism with UO_2, a further exploration of the energy landscape and consideration of how the energy landscape is modified in the presence of non-stoichiometry (both hypo and hyper) and the subsequent effects this has on hydrogen diffusion.

DFT is an excellent method to explore the electronic structure of materials and make an assessment of the size of energy barriers that exist for atoms to diffuse. One limitation is that under the Born-Oppenheimer approximation the nuclei are treated as classical partials, the larger the mass of the nucleus the more applicable the approximation. Hydrogen represents the case where the Born-Oppenheimer approximation is the least applicable, as of all nuclei the mas of hydrogen is closest to that of an electron. This leads to the likelihood that when using DFT to assess energy barriers to hydrogen diffusion that the barrier will be overestimated and the rate underestimated because hydrogen is able to tunnel through energy barriers. One method by which this could be assessed is *ab initio* path integral molecular dynamics, this would allow for the hydrogen to be treated as a quantum rather than classical particle. This would allow for an assessment of the importance of tunnelling for hydrogen diffusing in UO_2.

This chapter has considered how hydrogen defect diffuse through a non-defective UO_2 lattice, as this is the simplest case of UO_2. The majority of UO_2 is likely to be hyperstoichiometric due to the natural affinity for excess oxygen which UO_2 displays. Therefore, in order to assess the behaviour of hydrogen in more realistic systems the next chapter will determine the effect which hydrogen has on oxygen defect clusters.

7 The Interaction of Hydrogen with Oxygen Defect Clusters in UO_{2+x}

As previously mentioned UO_2 does not exist purely as a stoichiometric oxide phase but commonly as UO_{2+x} hyperstoichiometric phases and the fluorite lattice can adopt significant amounts of excess oxygen whilst retaining its structure (up to x = 0.5). This has given rise to a large number of different defect cluster models for UO_2 representing a variety of excess oxygen concentrations. Therefore it is useful to consider how hydrogen interacts with these clusters in order to investigate if there are any significant effects to the local crystal and electronic structure of UO_2. Additionally, the trapping of hydrogen at oxygen defect clusters must also be considered, as it may affect the solubility of both types of defects. Hydrogen trapping in functional materials is also a nanoscopic phenomenon with macroscopic effects on the materials properties.

This chapter will first cover the literature of oxygen defect clusters in UO_2, before detailing the models used to simulate hydrogen in UO_{2+x} and a method for distinguishing between reversible and irreversible traps in UO_{2+x}.

As the introduction of excess oxygen greatly increases the number of potential configurations of hydrogen and defect oxygen it is not feasible to simulate every possible configuration. Therefore, as the interest is in obtaining the effect of hydrogen on the defect clusters only hydrogen interacting with the defect clusters has been considered.

A paper concerning the behaviour of hydrogen defects in UO_{2+x} is in preparation and is entitled "*The Critical Role of Hydrogen on the Stability of Oxygen Defect Clusters in Uranium Oxide*".

7.1 Literature Review

As the predominant nuclear fuel, substantial research has been directed towards UO_2, revealing that it is highly susceptible to oxidation during the nuclear fuel cycle [73]. Despite many studies having shown that the defect chemistry of UO_2 is highly sensitive to the oxygen partial pressure, there are not many that focus on the interaction of hydrogen with the UO_2 matrix. This is despite hydrogen being present throughout the fuel's lifetime from fabrication [361] to long term repository storage of spent fuel [166]. A major concern is during the corrosion of uranium metal as hydrogen diffuses through the UO_2 layer which coats U metal [41, 362] generating pyrophoric uranium hydride [113, 363]. A comprehensive mathematical model for the initiation of hydriding of U metal, thus predicting hydrogen diffusivity in the coating layer of UO_2 was proposed by Glascott [39, 40], accounting for hydrogen

permeation through the surface oxide film due to intrinsic variations in the oxide thickness. However, this macroscopic modelling does not provide information on structural features that interact directly with hydrogen species.

The presence of structural features such as defect clusters, grain boundaries and dislocations has been shown to increase oxygen diffusivity [24, 364, 365]. Conversely, dislocations in doped ceria have been shown to decrease the oxygen diffusion [201]. Thus, it is sensible to assume that these features may have a strong interaction with hydrogen. In this chapter the focus is on the relationship of hydrogen with oxygen defect clusters, not least as, the oxygen stoichiometry and clustering are highly likely to affect the hydrogen diffusion and solubility [43, 44].

Experimentally, it was found that stoichiometric and hyperstoichiometric UO_2 have comparable hydrogen solubility, while hypostoichiometric UO_2 displays an order of magnitude increase in hydrogen solubility. It was also proposed that hydrogen dissolves as an atomic species rather than as molecular hydrogen [44]. The effect of atomic hydrogen was studied in stoichiometric UO_2 using *ab initio* techniques [140, 141]. It was found that both hydride and hydroxyl defects may form, although the hydride was the most favourable and was accompanied by the oxidation of U^{4+} to U^{5+}. However, most of the theoretical work focusses on the adsorption and dissociation of water on the surfaces of lanthanides and actinides[145, 146, 148], which is only one of the routes by which hydrogen can be incorporated into the UO_2 lattice.

UO_2 is capable of incorporating significant amounts of excess oxygen whilst still (nominally) retaining the fluorite structure, giving rise to the structurally-complex, defective UO_{2+x} region of the U-O phase diagram. A large number of stable, non-stoichiometric, fluorite-based uranium oxides are known to exist in the region (most notably U_4O_9 and U_3O_7) and all are associated with periodic arrangements of defect clusters within the lattice. At low oxygen concentrations, excess oxygen is incorporated as isolated oxygen interstitials (O_i), and as the concentration increases, oxygen defect clusters form [21, 22, 24–26, 37, 50, 72, 321]. The complex redox chemistry of UO_2, including the oxidation state of uranium and oxygen clustering has led to the proposition of a range of different defect clusters [21, 26, 33, 34, 37, 45, 321, 366]. Figure 7.1 shows the different proposed oxygen defect clusters found in the literature.

The first cluster proposed was the 2:2:2 Willis cluster (W_{222}) [45–47] (Figure 7.1b). Theoretical calculations indicated that an isolated W_{222} is unstable and relaxes into a split di-interstitial (I_2^x) (Figure 7.1a). Recently, Brincat *et al.* [21] demonstrated that the oxygen stoichiometry has a significant impact on the defect cluster structure, as edge-sharing W_{222} clusters were found to be stable in UO_{2+x} with composition $0.125 < x < 0.25$, but not below $x = 0.125$.

Both the I_2^x and the W_{222} represent the smallest oxygen cluster proposed in the literature. As the excess oxygen concentration increases the oxygen cluster become larger, the next defect cluster proposed is the split tri-interstitial ((I_3^x)) (Figure 7.1c). This is composed of a single V_O surrounded by a tetrahedron of O_i.

Increasing the excess oxygen concentration further results in formation of the split quad interstitial cluster ((I_4^x)) (Figure 7.1d). In this cluster there two V_O and six O_i. This cluster can also be thought of being two adjacent I_2^x clusters.

The final and largest defect cluster model reported is the cuboctahedron (COT) (Figure 7.1e and 7.1f). In this cluster eight lattice oxide ions have become interstitial and there are an additional four interstitial oxygen atom which form the cuboctahedron cluster (Figure 7.1e). The centre of this defect can then be vacant or occupied

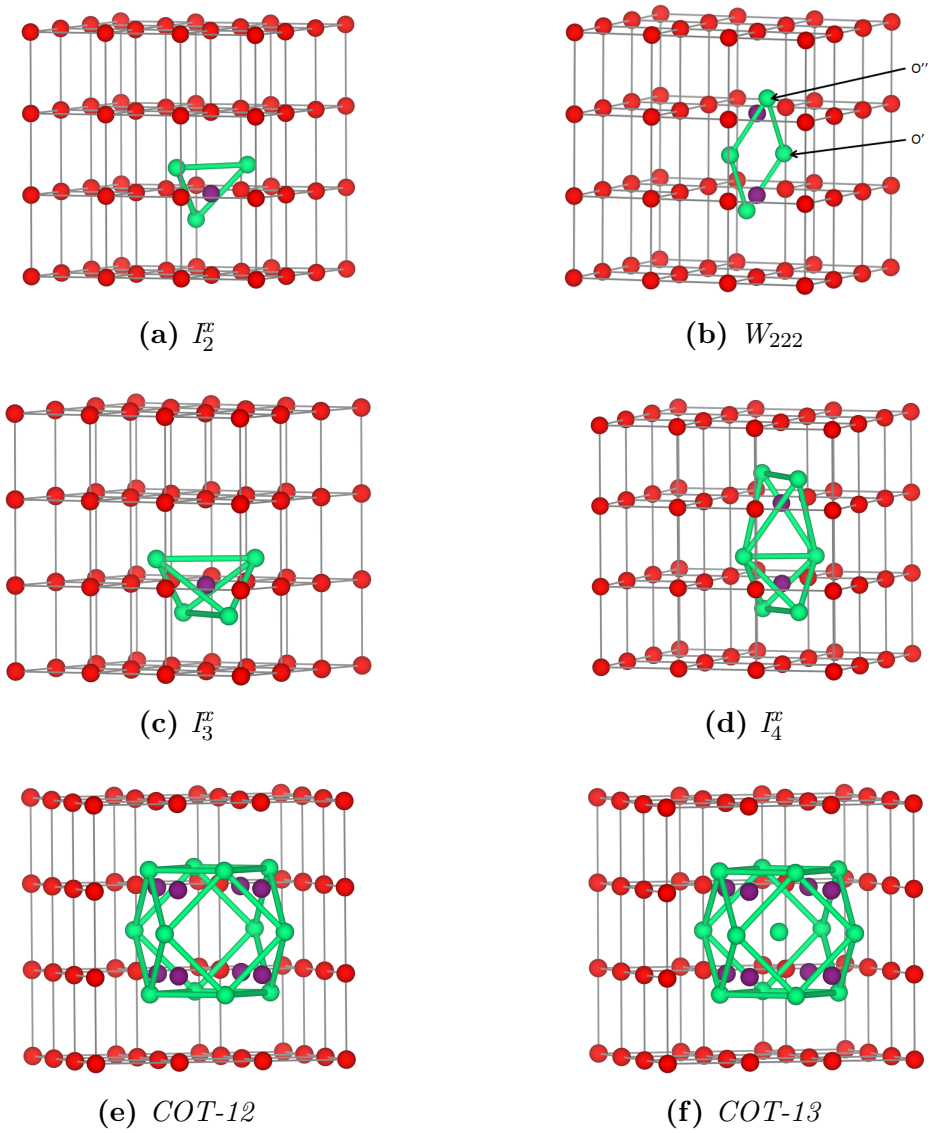

(a) I_2^x **(b)** W_{222}

(c) I_3^x **(d)** I_4^x

(e) *COT-12* **(f)** *COT-13*

Figure 7.1: Proposed oxygen defect clusters. U^{4+}/U^{5+} not shown for clarity, lattice oxygen shown in red, O_i in green and V_O shown in purple. Bonds have been drawn to highlight defect cluster geometries.

by an interstitial uranium ion or an additional oxygen atom. The COT cluster which has an oxygen occupying the centre of the defect has been found to be the most stable configuration of this defect cluster [49, 187, 367].

Whilst the evolution of oxygen defect clusters is a well-studied phenomenon in UO_2, although still debated, the interaction of hydrogen with defect cluster is not well explored. However, oxide materials find uses in a wide range of materials applications, from energy storage [100, 103] and generation [368–370], catalysts [101, 371, 372], mixed proton-electron conductors [106], electrochemical water splitting [102] to nuclear fuels [109]. In all of these materials, defects play an essential role in determining the materials properties. Although extensive research has been undertaken towards extrinsic substitutions and intrinsic oxygen defects in oxide materials, the presence of hydrogen is somewhat overlooked despite drastically affecting materials properties and device performance [110].

The nature of defects in oxide materials plays a key part in determining the

hydrogen behaviour. α-Al_2O_3 is used as a hydrogen permeation barrier material, where grain boundaries have increased hydrogen diffusion compared to the bulk. However, grain boundaries are also regions where radiation induced oxygen vacancies will cluster. Where clustering of oxygen vacancies occurs in the grain boundary plain. When the grain boundary possesses these oxygen vacancies then the grain boundary acts as a hydrogen trap, as opposed to enhancing hydrogen diffusion [373]. Additionally, oxygen vacancy clusters have been shown to act as strong trap sites for hydrogen in other materials (*e.g.* oxide dispersion-strengthened steels [374]).

7.2 Structural Models for UO_{2+x} and $UO_{2+x}H_n$

Before discussing the behaviour of hydrogen in UO_{2+x}, the structural models used and the corresponding energetics are explained.

7.2.1 UO_{2+x} Structural Models

The two smallest oxygen clusters proposed in UO_2 are the split di-interstitial (I_2^x) and the 2:2:2 Willis cluster (W_{222}), shown in Figure 1. A I_2^x cluster (Figure 7.2a) has a central oxygen vacancy (V_O) and three oxygen interstitials (O_i) displaced in the $< 111 >$ directions by approximately 1.6 Å. This causes the displacement of three lattice oxygen by approximately 0.3 Å from their lattice sites. In our models the excess oxygen changes the stoichiometry from $UO_{2.00}$ to $UO_{2.06}$. This results in oxidation of the four nearest neighbouring uranium ions to the V_O from U^{4+} to U^{5+}. A I_2^x cluster is found to have a formation energy of -1.27 eV in agreement with previous literature values [25, 49].

A W_{222} (Fig. 7.2b) consists of two V_O and four O_i each displaced approximately 1 Å from an octahedral interstitial site; two O_i displaced in <110> directions (O_i') and two in <111> directions (O_i''). The W_{222} cluster was the first cluster proposed for UO_2 [45, 46], and it was initially predicted to be stable by interatomic potential model calculations [341]. However, these calculations have since been rejected by *ab initio* calculations, which predict that W_{222} clusters relax to I_2^x clusters [24, 49, 326]. Only recently, *ab initio* calculations found edge-sharing W_{222} clusters are stable in UO_{2+x} ($0.125 < x < 0.25$) [21], but are unstable by $x = 0.33$ [23], emphasising how sensitive UO_2 defect chemistry is to oxygen partial pressure.

7.2.2 $UO_{2+x}H_n$ Structural Models

Hydrogen was added to our $UO_{2.06}$ models and the concentration was varied from 117 to 467 μgH / gUO_2 (equivalent to 1 to 4 interstitial hydrogen atoms). There are up to 35 million unique configurations of 1 - 4 hydrogen atoms in our chosen simulation cell, however as the aim of our research is to determine whether oxygen defect clusters act as hydrogen trapping sites, we have limited the number of configurations studied to those where hydrogen is interacting solely with oxygen atoms belonging to defect clusters forming hydroxyl groups and where the position of the hydrogen serves to maximise the hydrogen bonding network. This generates 16 different configurations for hydrogen interacting with the W_{222} cluster and 8 for hydrogen interacting with the I_2^x cluster.

The hydrogen can interact with the oxygen cluster in different ways: the newly formed hydroxyl group can hydrogen bond to lattice oxygen ions (superscript L) or other interstitial oxygen ions (*i.e.* those belonging to the defect cluster - superscript D). There are only two different configurations for each hydrogen concentration for the I_2^x system ($^LI_2^x$ and $^DI_2^x$), as it is composed of three equivalent O_i (Fig. 7.2a). The lower symmetry of the Willis cluster (arising from the two symmetrically inequivalent O_i) is responsible for the greater number of distinct configurations (*e.g.* $^DW_{222}^{O',2O''}$ denotes three hydrogen atoms, one at a O_i' interstitial site and one at each of the two O_i'' sites and all three hydrogen species are pointing towards O_i of the defect cluster).

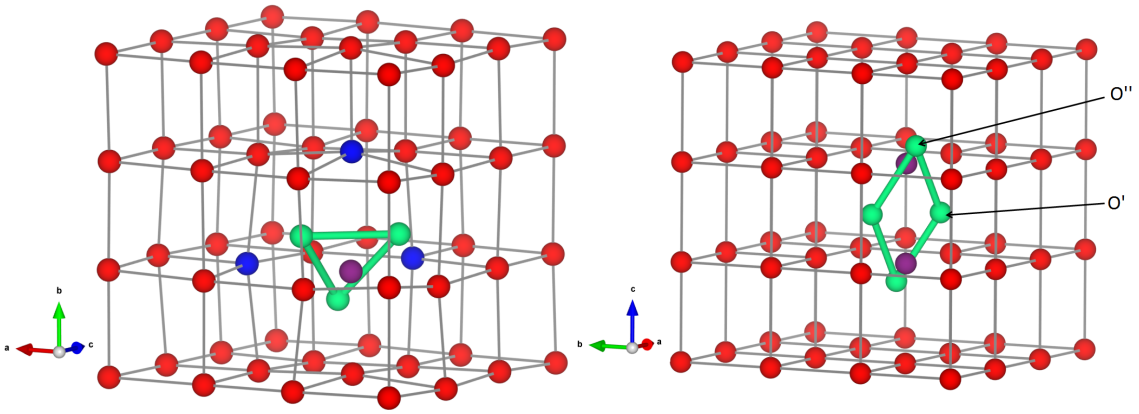

(a) I_2^x **(b)** W_{222}

Figure 7.2: Split di-interstitial (7.2a) and 2:2:2 Willis defect (7.2b) structures. Lattice oxygen shown in red, O_i in green, displaced lattice oxygen shown in dark blue and V_O shown in purple. Uranium ions not shown for clarity and bonds have been drawn to highlight defect cluster geometries.

7.2.3 Energetics of Hydrogen in UO_{2+x}

To study the thermodynamic stability of the clusters, the solution energies of a hydrogen defect is expressed as:

$$E_{Sol} = \frac{E_{UO_{2.06}H_n} - (E_{UO_{2.00}} + \frac{n}{2}E_{H_2} + E_{O_2})}{n} \tag{7.1}$$

where $E_{UO_{2.00}}$, $E_{UO_{2.06}}$ and $E_{UO_{2.06}H_x}$ are the energies of stoichiometric and hyperstoichiometric uranium dioxide and hydrogen doped uranium dioxide, while E_{H_2} and E_{O_2} are the energies of molecular H_2 and O_2, respectively. The hydrogen defect concentration is denoted by n.

To examine the preference for formation of hydrogen-oxygen defect clusters or isolated point defects (*i.e.* oxygen interstitial O_i and hydride), we have expressed the binding energy (E_{Bind}) of an oxygen defect cluster containing hydrogen as:

$$E_{Bind} = \frac{(nE_{H^-} + 2E_{O_i})}{n} - E_{Sol} \tag{7.2}$$

where $E_{UO_{2.06}H_x}$ is the energy of hyperstoichiometric, hydrogen doped uranium dioxide. The references for the isolated components of the defect cluster are the energies of an isolated hydrogen (E_{H^-}) in the form of the most stable hydride (0.2 eV) species found in UO_2 [141], and an O_i in the UO_2 structure (E_{O_i}) calculated to be -1.23 eV in agreement with previous literature [326, 331, 332, 340, 375]. A positive value of binding energy indicates a preference for the cluster with hydrogen over the isolated point defects.

7.3 Effect of Hydrogen on Oxygen Defect Clusters

Tables 1-4 summarises the structure of the hydrogen-oxygen defect clusters and their corresponding solution and binding energies at hydrogen concentrations of 117 - 467 μgH / gUO_2.

The introduction of an O_i in the UO_2 matrix is accompanied by the oxidation of two U^{4+} to U^{5+}. Thus, when considering I_2^x and W_{222} clusters, each contain two excess oxygen atoms, the compensating defect charges are localised on four U^{5+}. These are defined as nearest neighbour (NN) U^{5+} defects when the U^{5+} belongs to the first coordination sphere, and next nearest neighbour (NNN) when the U^{5+} is located in the second coordination sphere taking the centre of the defect as the origin. The addition of hydrogen to oxygen clusters is accompanied by the formation of hydroxyl groups and reduction of U^{5+} to U^{4+}. For every hydrogen added to a cluster of oxygen atoms a U^{5+} is reduced to U^{4+}. The location of the compensating U^{5+} defect (NN or NNN) do not greatly impact on the geometry and energetics of the defect clusters.

We have also calculated the number and strength of hydrogen bonds present in each defect cluster. We consider a hydrogen bond to be between the hydrogen and the acceptor oxygen (the oxygen not bonded directly to the hydrogen atom). The strength of a hydrogen bond is based on the oxygen-hydrogen distance; with a strong H-bond between 1.2-1.5 Å, a medium between 1.5-2.2 Å and a weak H-bond 2.2-3.0 Å[360].

7.3.1 H-O clusters at 117 μgH / gUO$_2$

The presence of hydrogen in I_2^x clusters does not significantly alter their structures (Figure 7.3). The results in table 7.1 there is an energetic preference of approximately 1 eV for the hydrogen species to point towards a lattice oxygen rather than towards an interstitial oxygen defects. The position of the compensating U^{5+} defects does not greatly impact the structure and energetics of I_2^x clusters.

The presence of hydrogen in W_{222} has a significant effect on the structure. In $^{D}W_{222}$ configurations where the hydrogen is pointing towards a defect cluster oxygen, the O" is prevented from relaxing onto the V_O site (Figure 7.2b). This has the remarkable effect of stabilising an isolated W_{222} cluster. In contrast, $^{L}W_{222}$ configurations with the hydrogen pointing towards a lattice oxygen were not stabilised by the presence of hydrogen and relaxed to I_2^x clusters, similarly to an isolated W_{222} in the absence of hydrogen. This is directly attributed to the absence of a hydrogen bond to the O" that prevents the oxygen from relaxing onto the vacant oxygen site.

Despite the increased stability of W_{222} clusters, the most stable clusters at 117 µgH / gUO$_2$ remain I_2^x clusters. All W_{222} clusters are less stable than $^{L}I_2^x$ clusters. Furthermore, whilst all the clusters at 117 µgH / gUO$_2$ have favourable solution energies, the binding energies suggest that it is still preferable for the cluster defect's components (*i.e.* individual O_i and H) to remain isolated rather than cluster together.

Table 7.1: Final hydrogen oxygen defect cluster configurations, an arrow denotes where a change in the initial oxygen cluster geometry has occurred. ΔV is the change in calculated volume compared to stoichiometric UO$_2$, U^{5+} defect concentration, solution and binding energies per hydrogen and number of strong, medium and weak hydrogen bonds at 117 μgH / gUO$_2$.

Cluster	Configuration	ΔV /H (Å^3)	[U^{5+}] (mgU^{5+} / gUO$_2$)		Energy / H (eV)		Hydrogen Bonds		
			NN	NNN	Solution	Binding	Strong	Medium	Weak
1	$^{L}W_{222}^{O'} \rightarrow {}^{L}I_2^x$	3.74	55	28	-1.52	-0.72	0	0	4
2	$^{L}I_2^x$	2.13	0	83	-1.44	-0.80	0	1	3
3	$^{L}W_{222}^{O''} \rightarrow {}^{L}I_2^x$	3.57	55	28	-1.27	-0.97	0	2	2
4	$^{D}I_2^x$	2.92	83	0	-0.58	-1.65	0	2	1
5	$^{D}W_{222}^{O'}$	4.35	55	28	-0.91	-1.33	1	0	2
6	$^{D}W_{222}^{O''}$	5.51	55	28	-0.58	-1.66	0	2	2

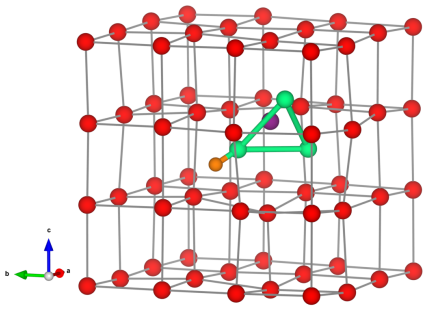

(a) ${}^{L}\mathrm{W}^{O'}_{222} \rightarrow {}^{L}I^{x}_{2}$

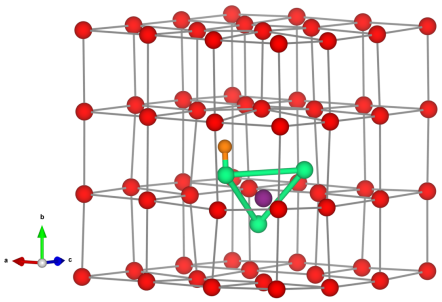

(b) ${}^{L}I^{x}_{2}$

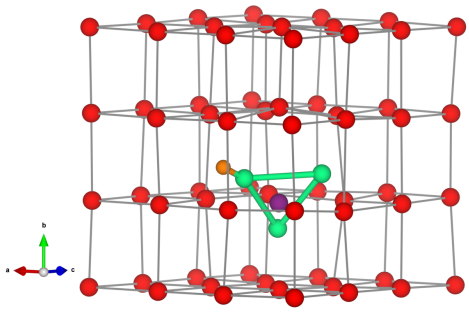

(c) ${}^{L}\mathrm{W}^{O''}_{222} \rightarrow {}^{L}I^{x}_{2}$

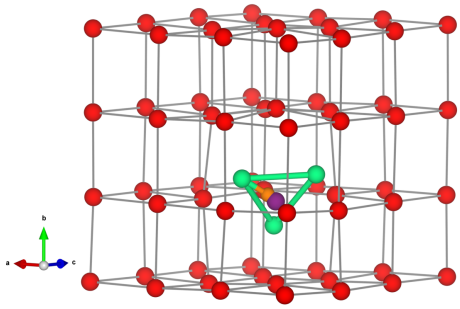

(d) ${}^{D}I^{x}_{2}$

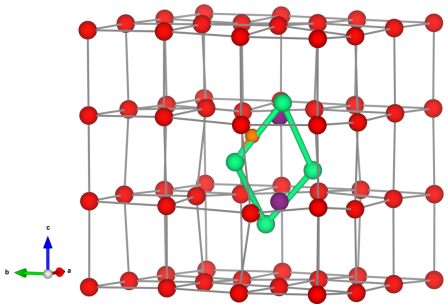

(e) ${}^{D}\mathrm{W}^{O'}_{222}$

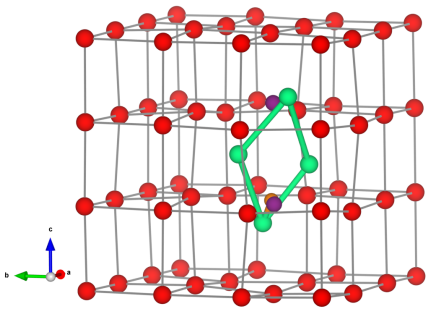

(f) ${}^{D}\mathrm{W}^{O''}_{222}$

Figure 7.3: Final configurations of clusters at 117 μgH / gUO_2. U^{4+}/U^{5+} not shown for clarity, lattice oxygen shown in red, O_i in green, V_O shown in purple and hydrogen shown in orange. Bonds have been drawn to highlight defect cluster geometries.

7.3.2 H-O clusters at 234 μgH / gUO$_2$

The most stable cluster at 234 μgH / gUO$_2$ is based on a Willis cluster ($^{L}\mathrm{W}_{222}^{2O''}$) rather than on a I_2^x cluster. This demonstrates further that hydrogen can significantly affect the stability of oxygen clusters. Once again, W_{222} clusters retain their structure if there is a hydrogen bonding network that prevents O" relaxation onto the vacant oxygen site (clusters 7, 8, 9 and 10) and relax into I_2^x clusters in the absence of such a network (clusters 12 and 13).

All clusters have favourable solution energies. Some of the defect clusters also have favourable (*i.e.* positive) binding energies (clusters 7 and 11). This may provide a viable route for irreversible hydrogen trapping, as hydrogen would prefer to cluster with O_i instead of remaining isolated. This also suggests that it is possible to have local regions (*i.e.* oxygen defect clusters) that can sustain and trap high hydrogen concentrations even if the overall hydrogen concentration in the sample remains low.

Table 7.2: Final hydrogen oxygen defect cluster configurations, an arrow denotes where a change in the initial oxygen cluster geometry has occurred. ΔV is the change in calculated volume compared to stoichiometric UO$_2$, U^{5+} defect concentration, solution and binding energies per hydrogen and number of strong, medium and weak hydrogen bonds at 234 μgH / gUO$_2$.

Cluster	**Configuration**	**ΔV / H (Å^3)**	**[U^{5+}] (mgU^{5+} / gUO$_2$)**		**Energy / H (eV)**		**Hydrogen Bonds**		
			NN	**NNN**	**Solution**	**Binding**	**Strong**	**Medium**	**Weak**
7	$^{L}\mathrm{W}_{222}^{2O''}$	5.19	28	28	-1.23	0.21	0	3	3
8	$^{L}\mathrm{W}_{222}^{2O'}$	4.91	0	55	-0.64	-0.37	0	2	7
9	$^{D}\mathrm{W}_{222}^{2O'}$	5.97	55	0	-0.79	-0.23	1	2	1
10	$^{D}\mathrm{W}_{222}^{2O''}$	7.43	55	0	-0.27	-0.74	0	4	4
11	$^{L}I_2^x$	4.36	0	55	-1.07	0.05	0	2	5
12	$^{L}\mathrm{W}_{222}^{O',O''} \rightarrow {}^{L}I_2^x$	4.71	0	55	-1.01	-0.01	0	2	6
13	$^{D}\mathrm{W}_{222}^{O',O''} \rightarrow {}^{D}I_2^x$	5.07	0	55	-0.61	-0.40	1	2	3
14	$^{D}I_2^x$	5.45	0	55	-0.59	-0.42	2	0	3

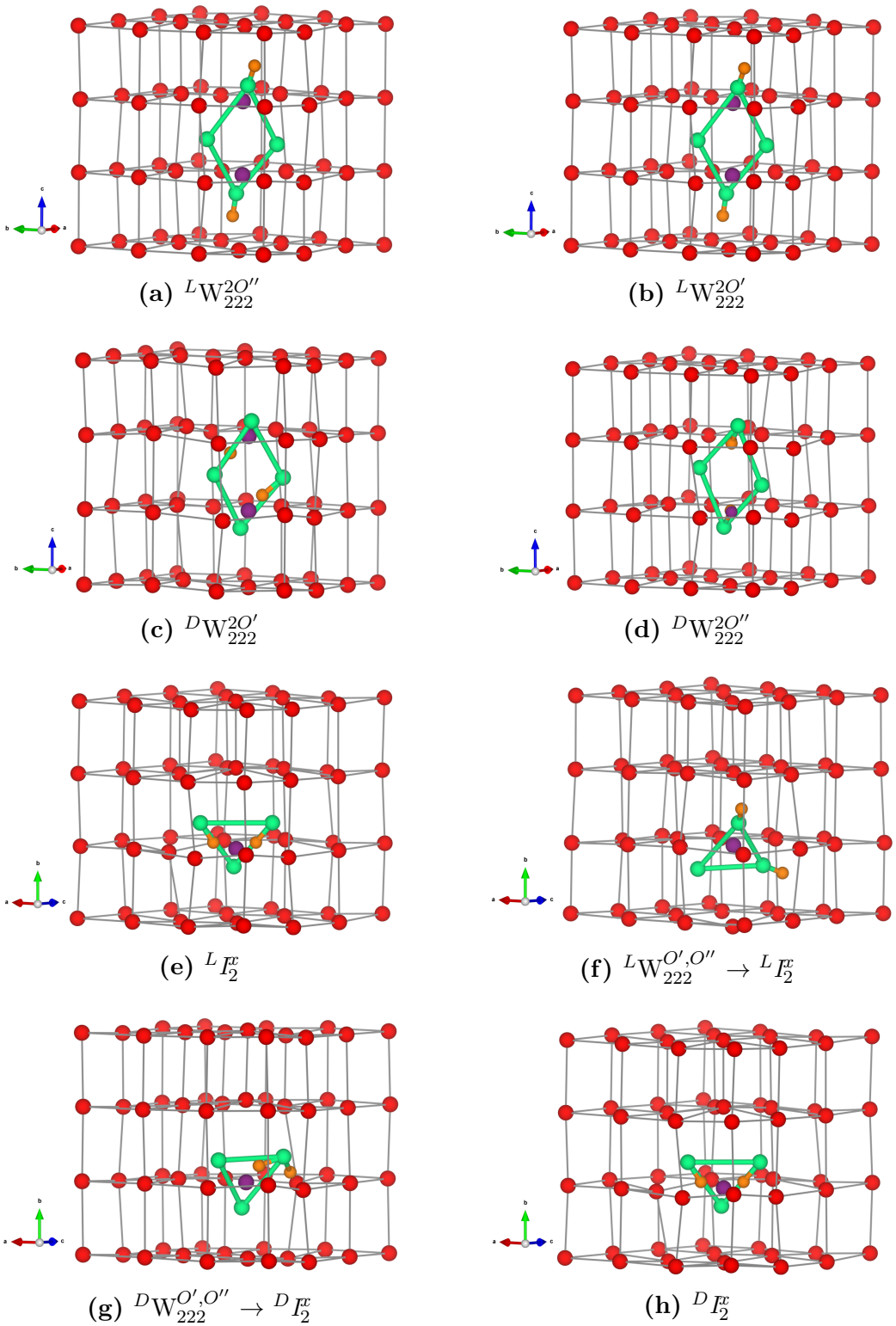

(a) ${}^{L}\mathrm{W}_{222}^{2O''}$ **(b)** ${}^{L}\mathrm{W}_{222}^{2O'}$

(c) ${}^{D}\mathrm{W}_{222}^{2O'}$ **(d)** ${}^{D}\mathrm{W}_{222}^{2O''}$

(e) ${}^{L}I_2^x$ **(f)** ${}^{L}\mathrm{W}_{222}^{O',O''} \rightarrow {}^{L}I_2^x$

(g) ${}^{D}\mathrm{W}_{222}^{O',O''} \rightarrow {}^{D}I_2^x$ **(h)** ${}^{D}I_2^x$

Figure 7.4: Final configurations of clusters at 234 μgH / gUO_2. U^{4+}/U^{5+} not shown for clarity, lattice oxygen shown in red, O_i in green, V_O shown in purple and hydrogen shown in orange. Bonds have been drawn to highlight defect cluster geometries.

7.3.3 H-O clusters at 351 μgH / gUO$_2$

At a hydrogen concentration of 351 μgH / gUO$_2$, all clusters retained their initial geometry after upon relaxation with the exception of ${}^{L}\mathrm{W}_{222}^{2O'O''}$ (cluster 16), where the absence of a hydrogen bond directly to the O" allowed the O" to relax onto the vacant oxygen site.

The most stable cluster at 351 μgH / gUO$_2$ is based on a I_2^x rather than a W$_{222}$ cluster and the most stable cluster, ${}^{L}I_2^x$ (cluster 15) has all hydrogen bonds pointing towards lattice oxygen.

Whereas the solution energies of clusters at 351 μgH / gUO$_2$ are lower compared with the clusters at 117 μgH / gUO$_2$, all clusters have either a favourable or a marginally unfavourable binding energy, with the exception of ${}^{D}I_2^x$ (cluster 17). This suggests that as the hydrogen concentration increases, the clustering of defects (H and O$_i$) becomes more favourable, and that reversible and irreversible hydrogen traps may also depend on the local hydrogen concentration.

Table 7.3: Final hydrogen oxygen defect cluster configurations, an arrow denotes where a change in the initial oxygen cluster geometry has occurred. ΔV is the change in calculated volume compared to stoichiometric UO$_2$, U^{5+} defect concentration, solution and binding energies per hydrogen and number of strong, medium and weak hydrogen bonds at 351 μgH / gUO$_2$.

Cluster	**Configuration**	**ΔV / H (Å^3)**	**[U^{5+}] (mgU^{5+} / gUO$_2$)**		**Energy / H (eV)**		**Hydrogen Bonds**		
			NN	**NNN**	**Solution**	**Binding**	**Strong**	**Medium**	**Weak**
15	${}^{L}I_2^x$	4.64	0	28	-0.97	0.36	0	3	7
16	${}^{L}\mathrm{W}_{222}^{2O',O''} \rightarrow {}^{L}I_2^x$	5.28	0	28	-0.86	0.25	0	1	12
17	${}^{D}I_2^x$	6.02	0	28	-0.42	-0.19	0	5	3
18	${}^{L}\mathrm{W}_{222}^{O',2O''}$	5.43	0	28	-0.78	0.17	0	2	10
19	${}^{D}\mathrm{W}_{222}^{O',2O''}$	5.76	0	28	-0.59	-0.02	2	1	5
20	${}^{D}\mathrm{W}_{222}^{2O',O''}$	6.02	0	28	-0.58	-0.03	3	0	4

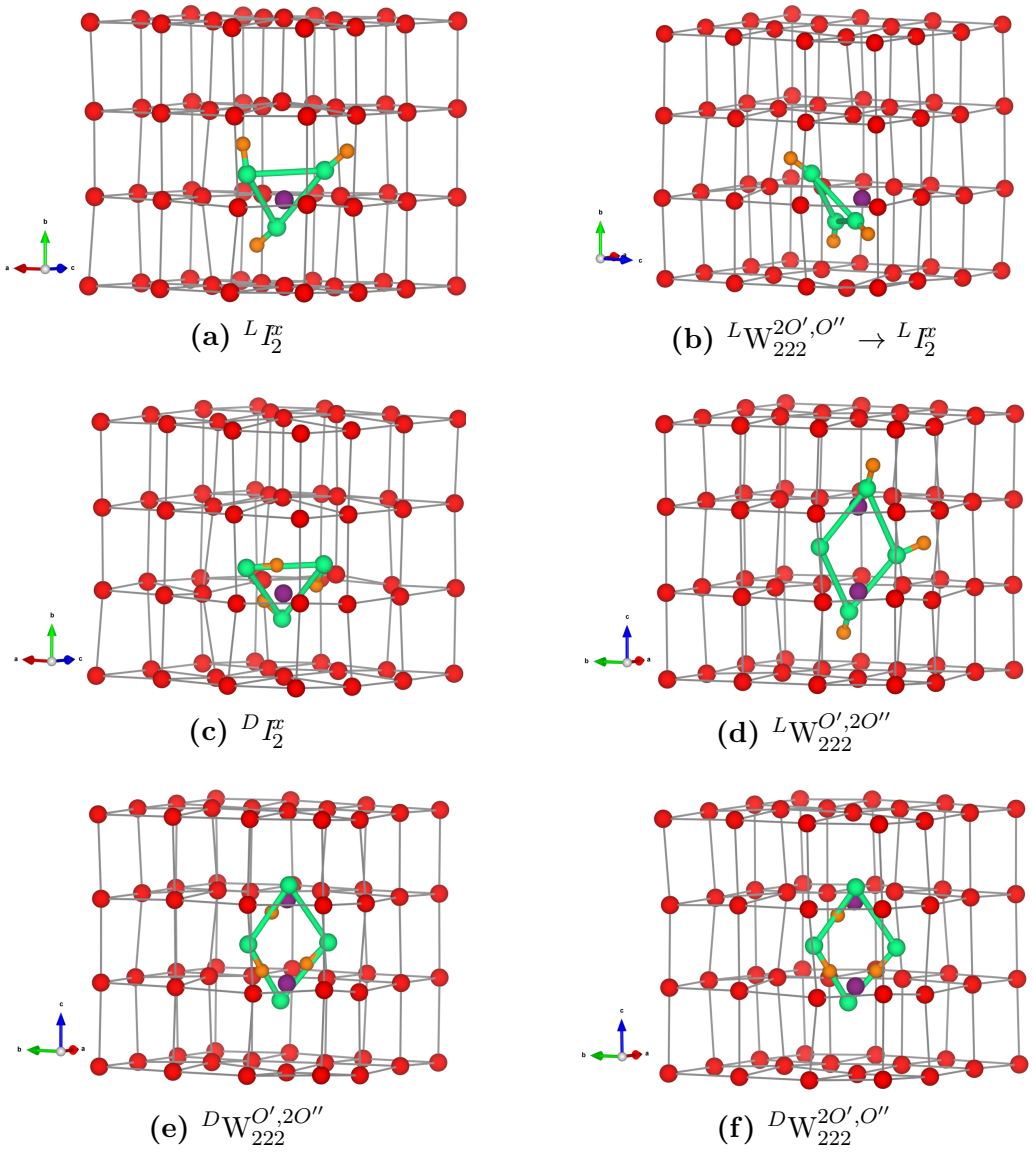

(a) ${}^{L}I_2^x$ (b) ${}^{L}\mathrm{W}_{222}^{2O',O''} \rightarrow {}^{L}I_2^x$

(c) ${}^{D}I_2^x$ (d) ${}^{L}\mathrm{W}_{222}^{O',2O''}$

(e) ${}^{D}\mathrm{W}_{222}^{O',2O''}$ (f) ${}^{D}\mathrm{W}_{222}^{2O',O''}$

Figure 7.5: Final configurations of clusters at 351 μgH / gUO_2. U^{4+}/U^{5+} not shown for clarity, lattice oxygen shown in red, O_i in green, V_O shown in purple and hydrogen shown in orange. Bonds have been drawn to highlight defect cluster geometries.

7.3.4 H-O clusters at 467 μgH / gUO$_2$

467 μgH / gUO$_2$ is the highest hydrogen concentration considered in this work. To achieve this concentration, we added four hydrogen species into the simulation cell, which allowed all the U^{5+} introduced by the excess oxygen to be reduced to U^{4+}. The most stable cluster is based on the W_{222} geometry as it was in the case of 234 μgH / gUO$_2$. There is a clear preference within the W_{222} clusters (Figure 7.6a, 7.6b), for the hydroxyl groups to point externally towards lattice oxygen ions rather than to other defect cluster O_i (cluster 22). The reason for this preference is due to a shortening of the O'-O" distances when hydrogen species are between the oxygen ions of the defect cluster. The more stable cluster, (cluster 21 - Figure 7.6a), has O'-O" distances of 2.34 Å, 2.36 Å, 2.50 Å and 2.62 Å, whereas cluster 22 (Figure 7.6b) has distances of 2.35 Å(x2), 2.43Å and 2.44 Å.

As stated in the UO_{2+x} model section, the I_2^x cluster only has three defect oxygen. For this reason, the fourth hydrogen was placed in close proximity to the V_O site of the defect cluster. In the case of cluster 24, the H-O cluster relaxed into 3 hydroxyl groups and 1 hydride species, and adopted a split tri-interstitial cluster geometry (I_3^x) as shown in Figure 7.1c. As a result of the formation of the hydride species, not all the U^{5+} were reduced to U^{4+}. This configuration is also the only one which has an unfavourable formation energy at this hydrogen concentration.

In the case of cluster 23, the I_2^x cluster geometry was retained, all U^{5+} introduced by the excess oxygen, were reduced to U^{4+}, and two hydroxyl and one water molecule were formed (Figure 7.6c).

At 467 μgH / gUO$_2$ all the clusters with favourable formation energies also had favourable binding energies, suggesting that once the concentration is high enough only irreversible trapping will occur.

Table 7.4: Final hydrogen oxygen defect cluster configurations, an arrow denotes where a change in the initial oxygen cluster geometry has occurred. ΔV is the change in volume calculated compared to stoichiometric UO_2, U^{5+} defect concentration, solution and binding energies per hydrogen and number of strong, medium and weak hydrogen bonds at 467 μgH / gUO$_2$.

Cluster	Configuration	ΔV / H (Å^3)	[U^{5+}] (mgU^{5+} / gUO$_2$)		Energy / H (eV)		Hydrogen Bonds		
			NN	NNN	Solution	Binding	Strong	Medium	Weak
21	${}^{L}W_{222}^{2O',O''}$	5.88	0	0	-0.79	0.39	0	2	14
22	${}^{D}W_{222}^{2O',O''}$	6.21	0	0	-0.50	0.10	4	0	6
23	${}^{L}I_2^x$	5.41	0	0	-0.60	0.20	0	6	6
24	${}^{D}I_2^x \rightarrow {}^{D}I_{(3)}^x$	3.35	28	28	0.09	-0.50	1	4	4

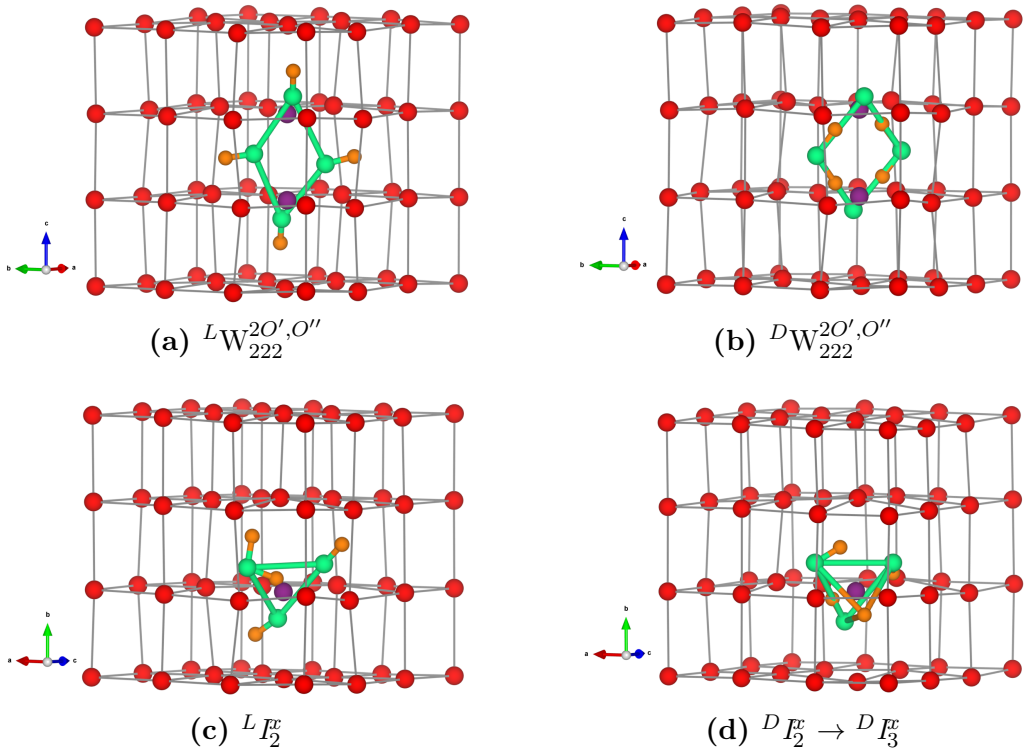

(a) ${}^{L}\mathrm{W}_{222}^{2O',O''}$ (b) ${}^{D}\mathrm{W}_{222}^{2O',O''}$

(c) ${}^{L}I_2^x$ (d) ${}^{D}I_2^x \rightarrow {}^{D}I_3^x$

Figure 7.6: Final configurations of clusters at 467 μgH / gUO_2. U^{4+}/U^{5+} not shown for clarity, lattice oxygen shown in red, O_i in green, V_O shown in purple and hydrogen shown in orange. Bonds have been drawn to highlight defect cluster geometries.

7.3.4.1 Effect of Hydrogen on Defect Cluster Energetics

Fig. 7.7 shows the solution and binding energies per hydrogen species as a function of hydrogen concentration for the most stable configurations of ${}^{L}I_2^x$, ${}^{D}I_2^x$, ${}^{L}W_{222}$ and ${}^{D}W_{222}$. For every system, with the exception of one, addition of hydrogen to the oxygen defect cluster resulted in favourable solution energies, although these become less favourable with increasing hydrogen concentration and the effect is more pronounced in ${}^{L}I_2^x$, ${}^{D}I_2^x$ and ${}^{L}W_{222}$ than ${}^{D}W_{222}$ (Fig. 7.7). Additionally, defect configurations with a hydrogen bonding network formed with lattice oxygen atoms (Fig. 7.7a and 7.7c) are always favoured compared to those with a hydrogen bonding network formed within the interstitial oxygen (*i.e.* that belonging to a defect cluster) (Fig. 7.7b and 7.7d). The preference for defect clusters over isolated point defects is expressed by the binding energy. This is generally unfavourable at low hydrogen concentrations (117-234 μgH / gUO_2) and becomes increasingly favourable at higher concentrations (351-467 μgH / gUO_2). At the highest concentration (467 μgH / gUO_2) all clusters with favourable solution energies also have favourable binding energies (Fig. 7.7). There is no straightforward correlation between stability of the clusters and the total number of hydrogen bonds (Fig. 7.7 and Tables 7.3 - 7.6). It appears that as the hydrogen concentration increases the number of hydrogen bonds per hydrogen decreases with the exception of ${}^{L}W_{222}$ clusters (Fig. 7.7c).

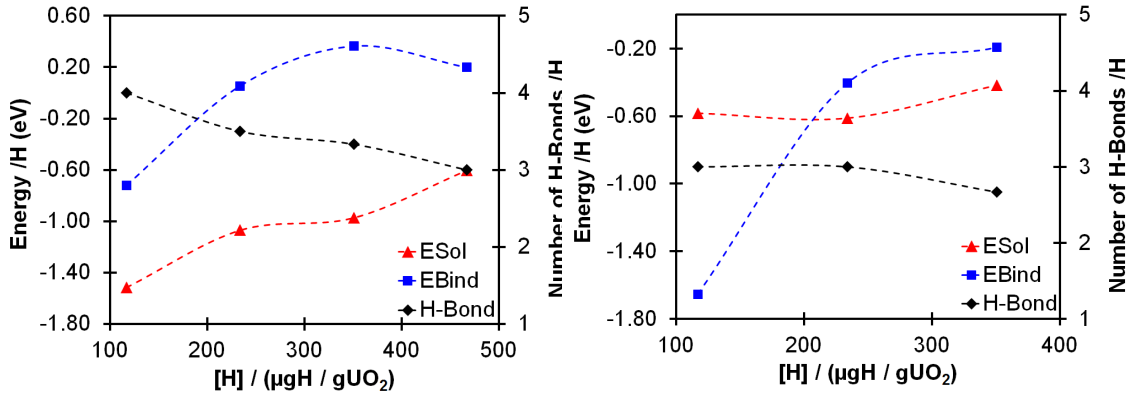

(a) ${}^{L}I_2^x$ (b) ${}^{D}I_2^x$

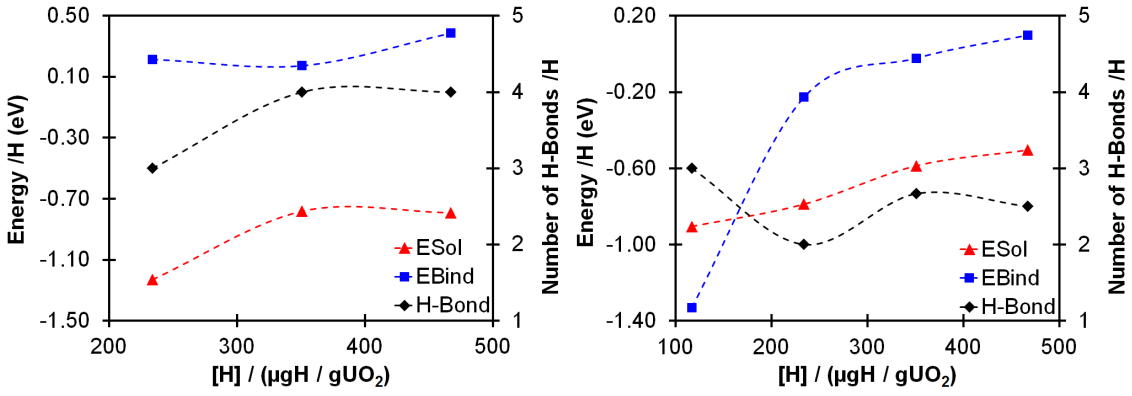

(c) ${}^{L}W_{222}$ (d) ${}^{D}W_{222}$

Figure 7.7: Solution energy per hydrogen (Red Triangles), binding energy per hydrogen (Blue Squares) and total number of hydrogen bonds per hydrogen (Black Diamonds) as a function of hydrogen concentration for the most stable configurations of ${}^{L}I_2^x$ (7.7a), ${}^{D}I_2^x$ (7.7b), ${}^{L}W_{222}$ (7.7c) and ${}^{D}W_{222}$ (7.7d) defect configurations.

7.3.4.2 Effect on Uranium Oxidation

It is widely accepted that the oxidation of UO_2 is accompanied by oxygen hyperstoichiometry and a contraction in volume due to the oxidation[22, 23, 51, 65, 84] of $U^{4+} \rightarrow U^{5+}$. The I_2^x, the only stable cluster at low partial pressure of oxygen, indeed shows a contraction (Fig. 7.8 - green triangle). Upon hydrogenation of oxygen defect clusters, our results show that the reduction of U^{5+} to U^{4+} is accompanied by an expansion of the lattice. This seems to take a relatively linear relationship as a function of hydrogen concentration (Fig. 7.8).

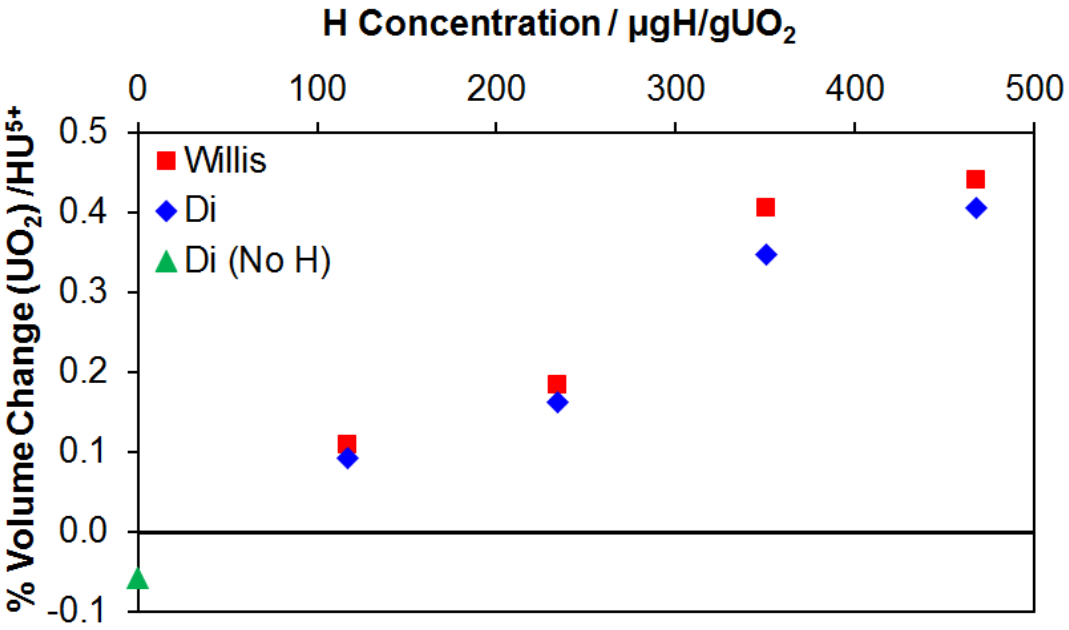

Figure 7.8: The Willis (Red Squares) and split di-interstitial (Blue Diamonds) configurations volume change compared to UO_2 for the range of hydrogen concentrations considered in this work. The volume of $UO_{2.06}$ was taken as that of the split di-interstitial with no hydrogen. The green triangle is the volume change compared to UO_2 for a split di-interstitial with no hydrogen present.

7.3.5 Thermodynamic Distribution of Defect Clusters

We suggest that these results can be used to infer which defect clusters maybe reversible and irreversible traps. Where reversible traps have a favourable solution energy and an unfavourable binding energy, whereas for an irreversible trap both energies are favourable. As the local concentration of hydrogen increases, there is a clear shift from reversible, which dominates at the lowest concentration 117 μgH / gUO_2, to irreversible trapping, independent of cluster type (Fig. 7.9).

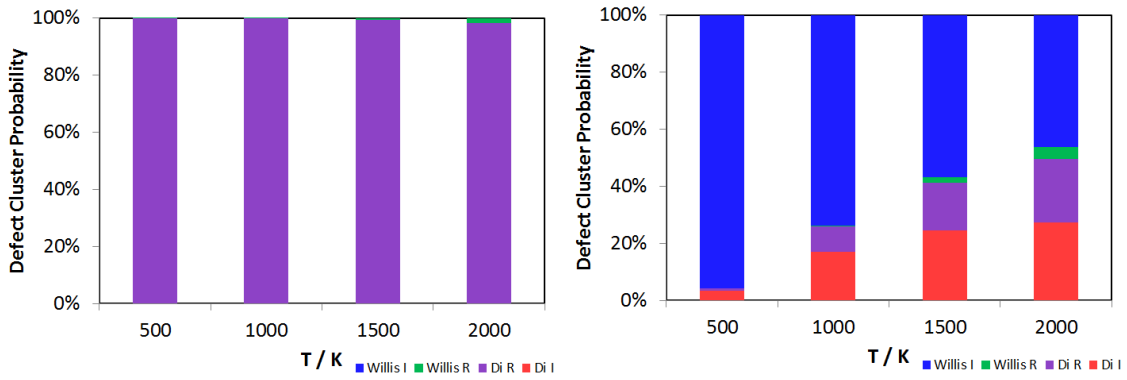

(a) 117 μgH / gUO_2

(b) 234 μgH / gUO_2

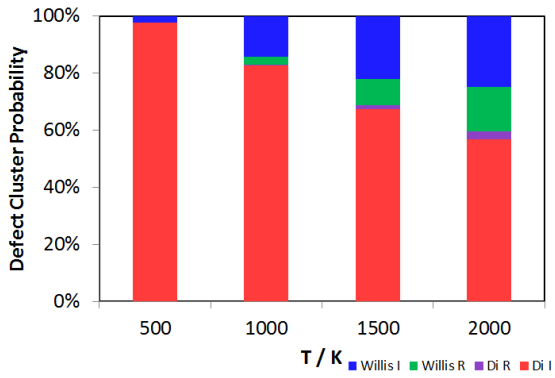

(c) 351 μgH / gUO_2

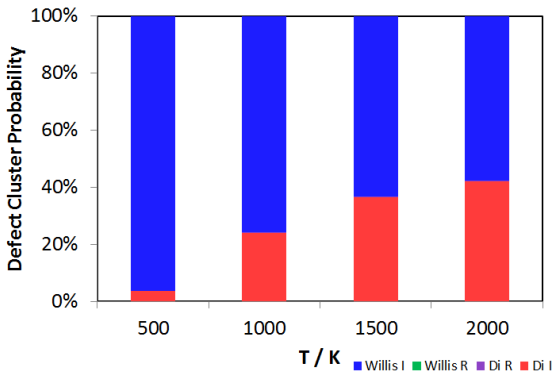

(d) 467 μgH / gUO_2

Figure 7.9: Defect Cluster Probability at varying concentrations. The probability of the different defect cluster configurations occurring at a range of temperatures, the probability has been calculated relative to the most stable cluster for each concentration. The defect configurations are considered in terms of the base oxygen cluster geometry (W_{222} or I_2^x) and if the reversibility of the cluster. Reversible W_{222} shown in green, irreversible W_{222} in blue, reversible I_2^x purple and irreversible I_2^x in red.

While we cannot compare our data directly with experimental detrapping data [42, 44], as this accounts for kinetic parameters, it is intriguing that the experimental models suggest that hydrogen dissolved in UO_2 is not released by a diffusion controlled process. The desorption curve for UO_2 single crystal shows a small peak at ≈1100 K and a large peak at ≈1700 K, associated with desorption energies of 80 and 210 kJmol^{-1} respectively [44]. This precludes hydrogen diffusion via interstitial sites in the UO_2 lattice and supports the idea that hydrogen is bound to discrete sites, as we see in our model structures. These hydrogen traps (although the ex-

perimental work cannot determine the nature of them) will be characterised by a binding energy and a rate constant of release.

Although we have calculated the binding energies for hydrogen to oxygen defect cluster in UO_2, we have no information on the rate constants for hydrogen release, which depend on temperature and the nature of the cluster. When considering a thermodynamic distribution that accounts for hydrogen traps at all hydrogen concentrations (Fig. 7.10), irreversible trapping (*i.e.* positive binding energy) appears at temperatures higher than 900 K and is slightly more likely to be based on the Willis geometry (1.3 % at 1000 K and 5 % at 2000 K) compared to the split di-interstitial (0.3 % at 1000 K and 3.5 % at 2000 K). Up to 10 % of irreversible hydrogen traps appear at 2000 K, whereas the majority (up to 90 %) of hydrogen traps will still be reversible and based on the I_2^x cluster (Fig. 7.10). As the irreversible traps are stabilised by a more complex hydrogen bonding network, they are more stable at higher hydrogen concentrations and thus their thermodynamic distribution increases with temperature, contrary to the reversible traps that are mainly oxygen-hydrogen clusters with low hydrogen concentration.

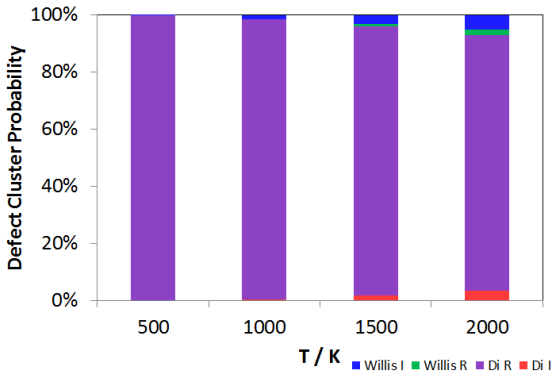

Figure 7.10: Defect Cluster Probability. The probability of the different defect cluster configurations occurring at a range of temperatures, the probability has been calculated relative to the most stable cluster for all concentrations. The defect configurations are considered in terms of the base oxygen cluster geometry (W_{222} or I_2^x) and if the reversibility of the cluster. Reversible W_{222} shown in green, irreversible W_{222} in blue, reversible I_2^x purple and irreversible I_2^x in red.

7.4 Conclusions

These calculations show that the presence of hydrogen greatly affects the oxygen defect chemistry of UO_2, altering the stability of oxygen defect clusters as a function of hydrogen content. The most crucial and significant finding is that hydrogen is found to stabilise the 2:2:2 Willis cluster, over the inherently more stable split di-interstitial cluster. The stabilisation of a W_{222} cluster in the presence of hydrogen, is of particular note, as this cluster has never been found to be stable, unless as a chain of Willis clusters at high partial pressure of O_2.

The calculations in this chapter show that hydrogen strongly affects the structure and energetics of oxygen defect clusters in hyperstoichiometric UO_2. The analysis used here defines a thermodynamic route to determine reversible and irreversible hydrogen traps. Reversible traps are identified by a favourable solution energy and

unfavourable binding energy, associated with the formation of the hydrogen-oxygen cluster; whereas irreversible traps are characterised by both energy contributions being favourable. Showing that there are stable local regions (*i.e.* oxygen defect clusters) that can trap and sustain high local hydrogen concentrations despite a low overall hydrogen concentration in the sample. The use of an *ab initio* approach allows for quantitative measurement of the population of hydrogen traps, which changes as a function of hydrogen concentration and temperature. This will enable the prediction of microscopic properties such as the dynamics of hydrogen-defect complexes and microstructural changes under non-equilibrium conditions that can arise in service due to the presence of extreme environments (*e.g.* radiation, temperature).

The stabilisation of I_2^x and W_{222} clusters is strongly dependent on local hydrogen concentration and that the presence of very small amounts of hydrogen within the oxygen cluster is sufficient to radically change the nature and structure of the cluster (as little as a single hydrogen interstitial per defect cluster). This is also likely to apply to the larger oxygen defect clusters, though a more compete survey is required before this can be confirmed.

The result of this study indicates that if safe and successful strategies for controlling the evolution of the nuclear fuels are to be devised, a greater advance in experimental and computational techniques has to be developed to gain insights into the structure and defect chemistry of the material. As most long term storage strategies consider the evolution of the fuel matrix based on the oxygen conditions and not how these are affected by the presence of other impurities.

8 Uranium Hydride (UH_3)

Uranium hydride (UH_3) is a pyrophoric [113] material which can form in the long term storage of waste nuclear material [376, 377], particularity uranium metal. As such it has received the attention of a number of experimental studies, but has been hampered by being very unstable in air and hence it is far less well characterised than the oxides of uranium. Thus the aim of the work in this chapter is to gain insight into the electronic structure, bonding and stability of this material, with the ultimate objective of investigating its reactivity with oxygen. However, in order to compare with the previous work in this thesis on hydride in UO_2 this chapter starts with the details of the convergence testing and how the calculated properties compare to experimental values. Although a study of reactivity is beyond the scope of this thesis, the effect of oxygen on the stability is assessed by evaluating the substitution of oxygen atoms onto the hydride sites. However, before the results are discussed and compared to experiment the available literature on UH_3 is reviewed.

8.1 UH_3 Literature Review

One of the major concerns of long term spent nuclear fuel storage is the integrity of the fuel matrix over extended time periods. This is especially important for the Magnox style reactors which use uranium metal rather than an oxide based fuel source. The formation of unwanted phases, such as uranium hydride (UH_3), in the fuel matrix can lead to stress on the fuel matrix due to the difference in lattice parameters between the oxide, hydride and metal [36, 278, 378]. Additionally, UH_3 is a pyrophoric [113] material, therefore understanding the process of hydride formation and how it can be prevented is of importance to the nuclear industry.

Uranium metal is typically covered by a passivating layer of UO_2. This passivating layer protects the underlying metal and reduces the rate at which the hydriding of the metal occurs. The protection provided is dependent on the oxide thickness and the presence of defects, *e.g.* grain boundaries, within the oxide layer [39, 40]. Despite the protection offered by the oxide layer hydriding of the underlying metal still occurs.

Unlike the uranium oxygen system where there are multiple different phases [19], only two different crystalline of UH_3 have been identified; α- and β-UH_3. Both of the reported uranium hydride phases are tri-hydrides. The uranium hydrogen system does not exhibit the multitude of phases seen in the uranium oxygen system despite the availability of multiple oxidation states. This is even in contrast with other actinide hydrides which exhibit multiple different hydride phases *e.g.* AmH_x (x = 1-3) [379], ThH_2 and Th_4H_{15} [380], PuH_2 and PuH_3 [381].

Structurally, α-UH_3 has two formula units per unit cell [382], where the uranium

ions occupy body centred cubic positions. Each uranium ion is surrounded by twelve equidistant hydride ions which form an icosahedron around the uranium ion (Figure 8.1a). β-UH_3 has eight formula units per unit cell [378], with two distinct uranium sites. Two uranium ions (U_I sites) occupy body centred cubic positions as in the α phase. The remaining six uranium ions (U_{II} sites) occupy face centred cubic positions. Figure 8.1b shows the two different uranium sites in β-UH_3. Uranium ions at both sites are surrounded by twelve hydride ions. For the U_I sites these are all equidistant, as is the case for α-UH_3, at 2.264 Å, whereas for the U_{II} sites the hydride ions are further away and have two sets of distances, four at 2.344 Å and eight at 2.310 Å.

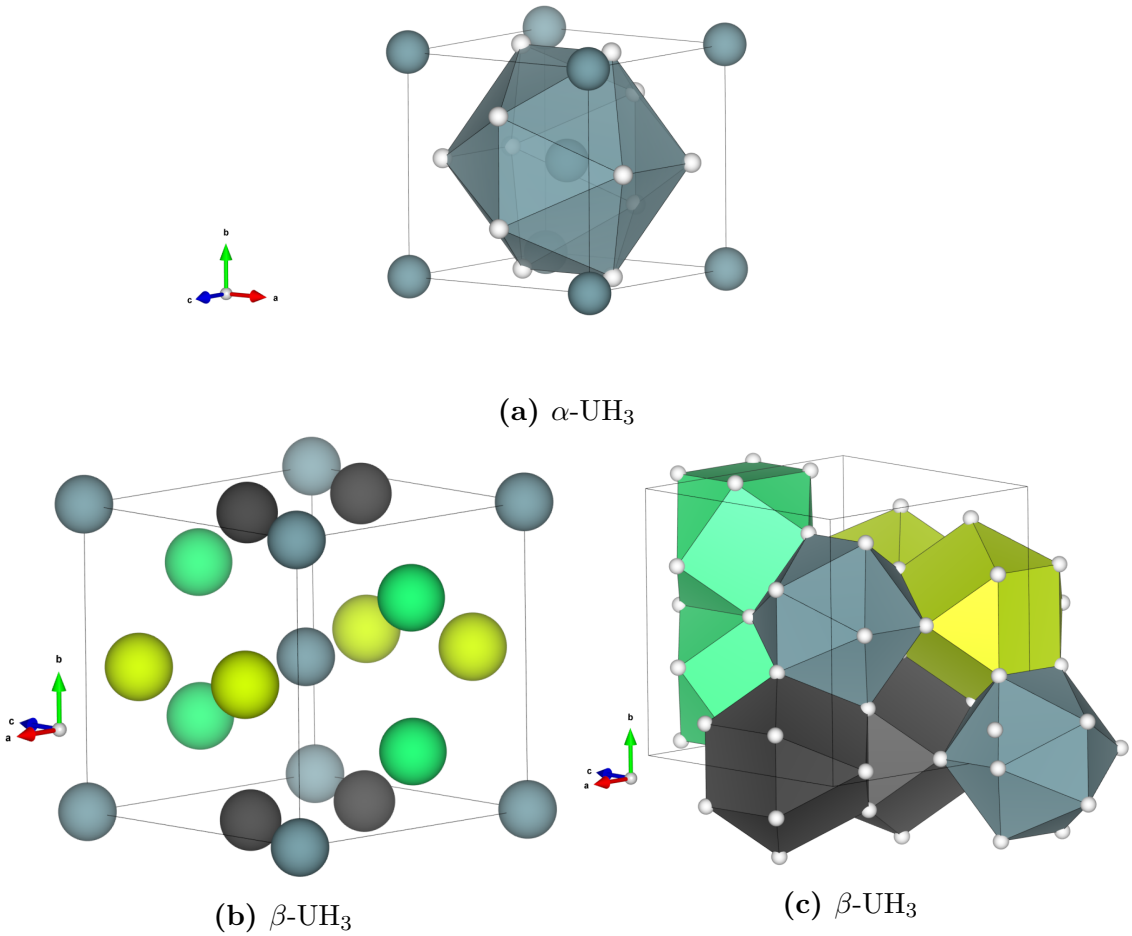

(a) α-UH_3

(b) β-UH_3

(c) β-UH_3

Figure 8.1: Crystal structures of α-UH_3 (8.1a) [382] and β-UH_3 [378]. For α-UH_3 uranium ions are shown in blue and hydrogen in white. For β-UH_3 the U_I sites shown in blue and the U_{II} sites shown in yellow, green and black. Only the uranium ions are shown in Figure 8.1b and the polyhedron of hydrogen around the uranium ions is shown in Figure 8.1c.

Recent work has suggested that under storage conditions α-UH_3 [376] is the dominate hydride phase. This is despite the α phase being unstable relative to the β phase, proposed on the basis of the irreversible transition occurring upon heating [382]. This poses a challenge in experimentally determining the properties of the relevant hydride as experimentally a pure α-UH_3 phase has never been synthesised.

The best reported sample of α-UH_3 is a 1:1 ratio of α-UH_3:β-UH_3. However, while it is not possible to prepare a pure binary hydride phase, addition of Zr results not only forming pure α phase but also the resulting material, $(UH_3)_{1-x}Zr_x$, is air stable [383].

The inability to synthesise pure α-UH_3 means there is still uncertainty in the nature of its electronic and magnetic properties. Experimental work to determine the magnetic moment of α-UH_3 has observed a magnetic ordering temperature ($\approx$170 K) that coincides with that of the β hydride [383, 384], and a magnetic moment of 0.9 μ_B. However, a later neutron study found that α-UH_3 was non-magnetic down to 15 K [385]. This was questioned by the work of Tkach *et al.* [383] who found for the Zr stabilised α-UH_3 the magnetic moment was 1 μ_B. Therefore, the magnetic nature of α-UH_3 is still to be fully resolved. However, there is some consistency in the limited literature to report magnetic values, where α-UH_3 is predicted to be magnetic the magnitude of the magnetic moment is $\approx$1 μ_B [383, 384]. The theoretical study of Taylor [386] showed that the magnetic moment predicted was sensitive to volume, where small changes in the volume could lead to significantly different predicted magnetic moments.

In contrast due to its relative stability and ability to be synthesised as a pure phase, β-UH_3 is much better characterised and studied. There have been several reports of the magnetism in β-UH_3 with the magnetic field measurements recording values between 0.86 - 1.18 μ_B [387–390]. These values are all lower than those that come from neutron or NMR measurements, where the measured values are in much closer agreement with each other at 1.45 $\pm$ 0.11 μ_B [378, 391, 392]. There are a number of reasons why the measured magnetic moments using magnetic fields are lower than those of the neutron measurement; firstly magnetic actinide compounds can exhibit large anisotropy, secondly the measured value comes from an extrapolation of experimental measurement and finally, Henry [388] also suggests that hydride exhibits a quasi-metallic behaviour which leads to a lower measured moment. Interestingly, despite the symmetrical inequivalence of the uranium sites in β-UH_3 they are reported to be magnetically equivalent [378].

Although the magnetism of β-UH_3 is characterised, the charge state of the uranium ions is less clear, which is likely due to the itinerant nature of the electrons in the hydride [390]. Formally, with a hydride carrying a charge of -1 the uranium ion would be expected to be in the +3 oxidation state. However, examining the literature, values of the oxidation state have been reported from the +2 to +5 [386, 393–395]. Allen even suggests that the oxidation state of the uranium ions is as low as +1.4 [395], with a high degree of covalancy present in the hydride. The reason for this uncertainty in the oxidation state of the uranium ions is likely due to the metallic nature of the hydride. This is seen in the experimental DOS spectrum, measured with XPS, where the DOS for the hydride is much closer to that of uranium metal than UO_2 [396]. Part of the reason for the wide ranging set of values for the oxidation state of uranium in the hydride could be due to the sensitivity of these properties to the volume. DFT calculations have shown that the electronic structure is sensitive to the volume, with small volume changes causing a large change in the predicted DOS spectrum [386].

Thus, the metallic nature of the hydride and the resulting itinerant electrons, along with the sensitivity to the volume, suggest that the oxidation state of the uranium ions is less clearly defined, than the oxide. This implies that the oxida-

tion state is potentially a non-integer value and somewhere between +2 and +3, depending on conditions.

In addition to the studies to determine the properties of pure uranium hydride phases, the hydriding of uranium metal is also an area of focused research effort, in order to determine the process by which the hydride phase forms. When clean uranium metal is exposed to a hydrogen atmosphere hydride formation occurs [395], however the hydride does not form evenly across the whole surface [397]. Instead regions of surface defects act as initiation sites for the formation of the hydride. The rate of hydride formation is also determined by the presence of an oxide over-layer, where the thicker the oxide over-layer the slower the rate of hydride formation [41]. In oxidising conditions uranium metal shows significant hydriding at grain boundaries [398], with an increase of three orders of magnitude in probability of hydriding occurring. This gives an explanation as to why the hydride occurs at the metal oxide interface. The oxide layer is stable with respect to reaction with hydrogen, so the hydrogen has to pass through the oxide layer and when it reaches a defective region (*i.e.* the metal oxide interface), the uranium metal is reactive enough for the hydride to form. This leads to the propagation of the hydride along the grain boundary.

The rate that the hydride forms controls how much of the α or β phase is formed. A slower rate of formation results in more of the β hydride forming [399]. There are a number of studies which suggest that the rate limiting step in hydride formation is the formation of the α hydride phase [386, 399]. Therefore, even though α-UH_3 is unstable and will convert to β-UH_3 it is likely to be present and hence its properties need to be considered. Additionally, there is work which shows under long term storage conditions [376] α-UH_3 is the most dominate hydride phase. Whilst the α-UH_3 may be the dominant phase under storage conditions, β-UH_3 will still be present and the rate of β-UH_3 with water has been shown to be increased by the presence of α-UH_3 [377]. This leads to a further imperative to understand the properties of both hydride phases.

8.2 Convergence Tests

As UH_3 is much closer in nature to uranium metal rather than the oxide, this requires a greater k-point density in order to accurately simulate its properties. This section will detail the k-point and convergence tests for both phases of UH_3. For both phases the energy cut-off was varied from 400 - 900 eV with k-point meshes from 4x4x4 - 18x18x18. Figure 8.2 shows the results for the convergence testing. In order to select parameters to use for the calculations the results will also be considered in relation to the other phase, to ensure results are easily comparable between the two phases.

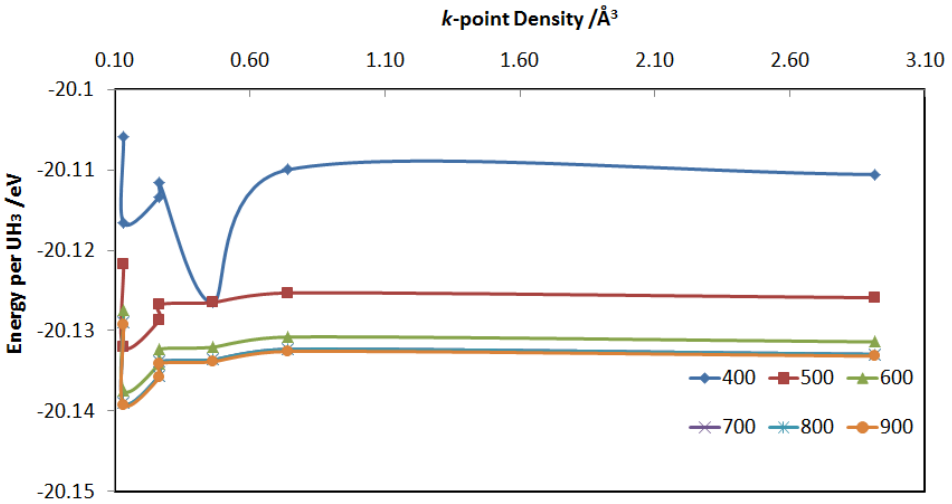

(a) α-UH_3

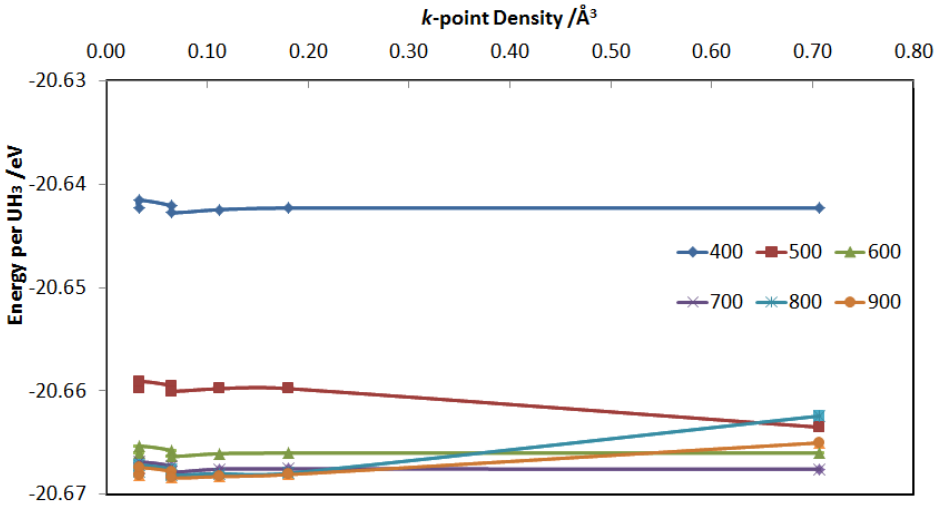

(b) β-UH_3

Figure 8.2: Results of convergence testing for α-UH_3 and β-UH_3.

The results show that while a cut-off of 500 eV is sufficient for the α phase convergence, it is not for the β phase. Therefore, for both phases a higher cut-off energy of 600 eV has been selected as very good convergence is achieved for both phases. The final consideration is the k-point mesh to use for each phase. In order to have similar k-point densities for both phases k-point meshes which give the closest densities have been chosen. For α-UH_3 this is a 5x5x5 k-mesh and a 8x8x8 k-point

mesh for β-UH_3. This give k-point densities of 0.13 k-point/Å^3 and 0.11 k-point/Å^3, respectively.

8.3 Methodology Assessment

Having established suitable cutoff parameters for UH_3, the suitability of the PBE+U methodology for determining the properties of UH_3 needs to be established. Due to the metallic nature of the hydride the presence of the Hubbard coefficient may result in incorrect properties being predicted. This will be assessed by consideration of predicted lattice parameters, DOS and hydrogen point defects with and without the inclusion of a Hubbard coefficient and SOC.

Table 8.1 compares the predicted lattice parameters and volume for both α- and β- UH_3, using the PBE functional, with and without inclusion of the Hubbard coefficient. As can be seen the PBE functional slightly underestimates the lattice parameter, while when the Hubbard coefficient is included there is a small expansion to the lattice predicted. α-UH_3 has a smaller volume per UH_3 compared with β-UH_3 and this is reproduced in the calculations for both PBE and PBE+U.

The energy per UH_3 is very similar for the PBE functional, with only a 0.02 eV difference in favour of the β hydride. This would suggest that both the α- and β-hydrides are of very similar stability, but, it does not explain why the transition from α-UH_3 to β-UH_3 is reported as irreversible [382]. When a Hubbard coefficient is included, in the calculation, the difference in energy increase to 0.43 eV, in favour of β-UH_3. This would suggest that there is more of an energetic driving force to convert from α-UH_3 to β-UH_3.

Both PBE and PBE+U give reasonable structural agreement with experiment for both α- and β- UH_3, however one of the other major effects of including a Hubbard coefficient is on the localisation of the electrons. UH_3 is metallic in nature and the DOS spectrum is much closer to that of U metal rather than the oxide [396]. Figure 8.3 shows the predicted partial DOS for both α- and β- UH_3, using the PBE functional with and without the inclusion of a Hubbard coefficient. All of the DOS predict metallic behaviour, though as would be expected the inclusion of the Hubbard coefficient results in suppression of these states. The pDOS also shows that the states present at the Fermi level are predominately from Uf states with some Ud states, while the hydrogen states are much lower in energy.

Overall the PBE+U functional reproduces the structural parameters of both hydride phases, with a small expansion as is typically seen for GGA+U approaches. Importantly the metallic nature of the hydride is retained with the inclusion of the Hubbard coefficient. Although the number of states are suppressed for the PBE+U when compared to the PBE calculation.

Table 8.1: Experimental and calculated properties for α- and β- UH_3 using the PBE functional with and without a Hubbard coefficient. The number in parenthesis is the percentage variation from the experimental value.

α-UH_3			
	Experiment [382]	**PBE**	**PBE+U**
Energy per UH_3 (eV)	-	-22.52	-20.13
***a* (Å)**	4.160	4.14 (-0.6)	4.22 (1.5)
***b* (Å)**	4.160	4.14 (-0.6)	4.22 (1.5)
***c* (Å)**	4.160	4.14 (-0.6)	4.22 (1.5)
Volume (Å^3)	71.99	70.81 (-1.6)	75.28 (4.6)
Volume per U (Å^3)	35.99	35.40 (-1.6)	37.64 (4.6)
β-UH_3			
	Experiment [378]	**PBE**	**PBE+U**
Energy per UH_3 (eV)	-	-22.54	-20.56
***a* (Å)**	6.643	6.60 (-0.6)	6.77 (1.9)
***b* (Å)**	6.643	6.60 (-0.6)	6.77 (1.9)
***c* (Å)**	6.643	6.60 (-0.6)	6.77 (1.9)
Volume (Å^3)	293.15	288.02 (-1.9)	310.17 (5.8)
Volume per U (Å^3)	36.64	36.00 (-1.9)	38.77 (5.8)

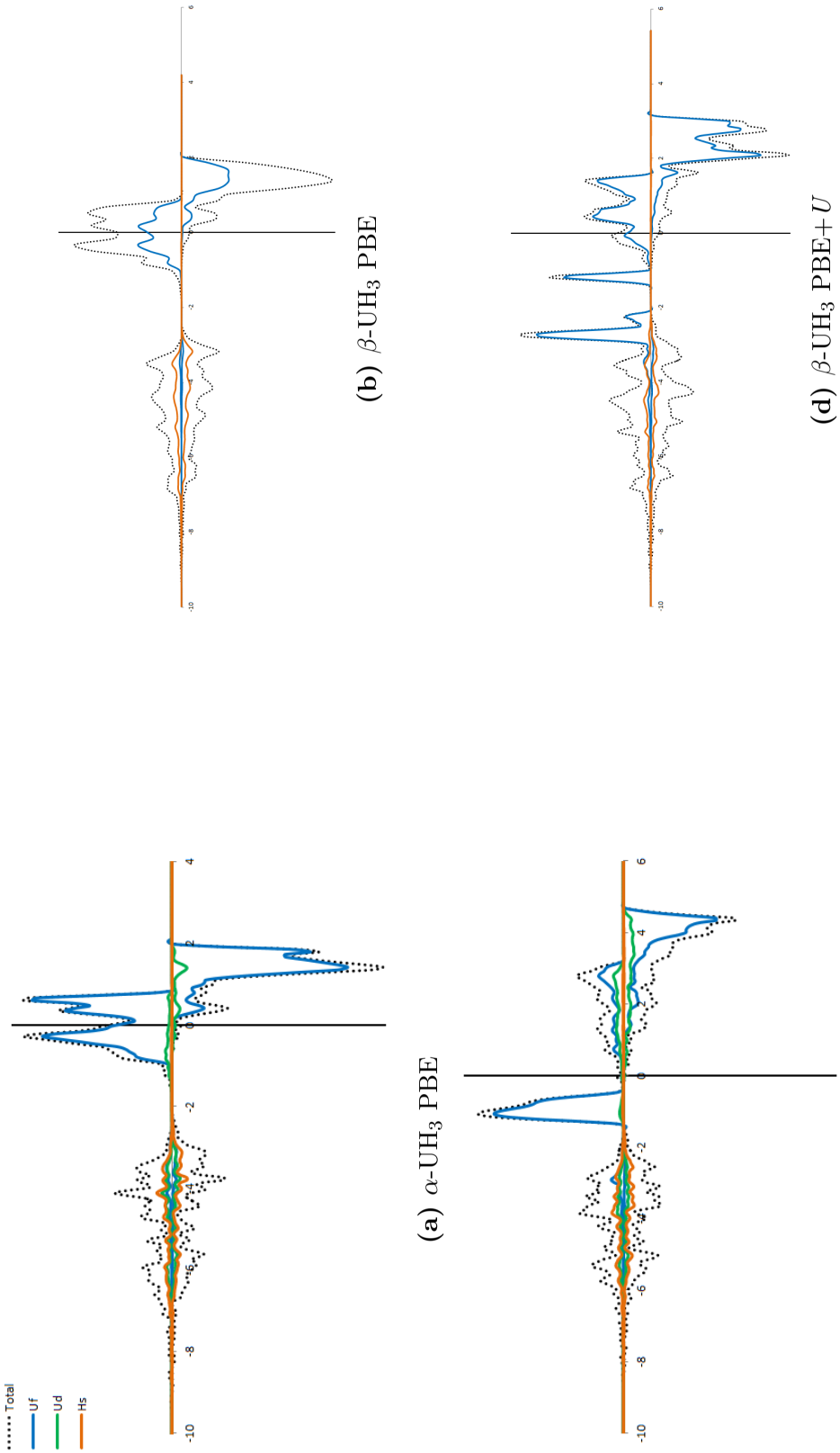

(a) α-UH_3 PBE **(b)** β-UH_3 PBE

(c) α-UH_3 PBE+U **(d)** β-UH_3 PBE+U

Figure 8.3: Partial density of states for α-UH_3 and β-UH_3 using the PBE functional with and without the inclusion of a Hubbard coefficient.

Having considered the effect of including a Hubbard coefficient on the structural and electronic properties of uranium hydrides, now the effect on the defect energetics will be considered. To investigate the effect on the defect energetics either a hydrogen vacancy (V_H) or hydrogen interstitial (H_I) were generated in a 2x2x2 expansion of the α-UH_3 unit cell or the β-UH_3 the cell, both defects are charge neutral. For β-UH_3 the cell was not expanded as this results in a simulation cell which is too expensive to calculate in a reasonable amount of time. While this results in a relatively large defect concentration as the aim is to compare between PBE and PBE+U the defect concentration will be the same for both systems. Uranium defects were not considered as this would result in a ± 0.2 change of stoichiometry in the largest simulation cell used for the hydride.

The formation energies of hypo- and hyper- stoichiometric UH_3 were calculated according to Equations 8.1 and 8.2 respectively.

$$E_F = (E_{UH_{3-x}} + \frac{x}{2}E_{H_2}) - E_{UH_3} \tag{8.1}$$

$$E_F = E_{UH_{3+x}} - (E_{UH_3} + \frac{x}{2}E_{H_2}) \tag{8.2}$$

Table 8.2 shows the results for charge neutral intrinsic hydrogen point defects placed in a 2x2x2 expansion of the α-UH_3 unit cell and a β-UH_3 unit cell. For α-UH_3 the PBE functional predicts that the hydrogen vacancy will cause a contraction of the lattice and a hydrogen interstitial will cause an expansion. Both defects have unfavourable formation energies, with the hydrogen vacancy being significantly larger than the hydrogen interstitial. Similar behaviour is seen when the Hubbard coefficient is included in the calculations, a contraction (albeit very minor) and an expansion are predicted for the vacancy and interstitial, respectively. Though this is much reduced compared to the PBE prediction, this can be ascribed to the stoichiometric hydride having a large predicted volume using PBE+U compared with PBE meaning that there is less of a contraction or expansion needed to accommodate the defect. The formation energies calculated using PBE+U similar to PBE are both large positive numbers, however, the order of the two defects has swapped. The hydrogen interstitial is now predicted to be less favourable that the hydrogen vacancy.

Examining the literature there is no available experimental values for the formation energy of H_I defects, but there is data for the hydrogen vacancy formation energy. This is reported to be 69 $\pm$ 1 kcal/mol [400, 401], which corresponds to a value of 3 eV. This is significantly larger than the predicted value of the V_H energy for α-UH_3. The stoichiometry of the hydride used in these calculations is at the limit that is reported experimentally, so this much lower energy cannot be readily attributed to a difference in vacancy concentration between experiment and theory. A potential explanation is that due to the elevated temperatures used in the experiment there was no α-UH_3 present and the calculated vacancy formation energy is for β-UH_3. It has been reported that at elevated temperatures (>250 °C) that α-UH_3 will irreversibly convert into β-UH_3 [382].

Table 8.2: Calculated formation energy (E_F), lattice parameter and change in volume (ΔV) for charge neutral intrinsic hydrogen point defects in a 2x2x2 expansion of the α-UH_3 unit cell and the β-UH_3 unit cell. Calculated using the PBE functional with and without a Hubbard coefficient. ΔV is calculated relative to the predicted volume for the stoichiometric hydride and is the total volume change.

PBE					
	α-UH_3		β-UH_3		
Defect	$\mathbf{V}_H$	$\mathbf{H}_I$	$\mathbf{2V}_H$	$\mathbf{V}_H$	$\mathbf{H}_I$
Stoichiometry	$UH_{2.94}$	$UH_{3.06}$	$UH_{2.75}$	$UH_{2.88}$	$UH_{3.12}$
$\boldsymbol{E_F}$ **/H (eV)**	0.90	0.60	0.91	0.91	1.35
a **(Å)**	8.22	8.24	6.56	6.60	6.63
b **(Å)**	8.27	8.33	6.58	6.58	6.67
c **(Å)**	8.27	8.24	6.60	6.61	6.66
ΔV (Å^3)	-1.56	1.60	-3.00	-1.15	6.61
PBE+*U*					
	α-UH_3		β-UH_3		
Defect	V_H	H_I	$2V_H$	V_H	H_I
Stoichiometry	$UH_{2.94}$	$UH_{3.06}$	$UH_{2.75}$	$UH_{2.88}$	$UH_{3.12}$
$\boldsymbol{E_F}$ **/H (eV)**	0.77	1.01	-0.52	-1.92	0.22
a **(Å)**	8.67	8.77	6.91	6.91	6.94
b **(Å)**	8.66	8.59	6.93	6.92	6.93
c **(Å)**	8.59	8.57	6.92	6.92	6.86
ΔV (Å^3)	-0.03	0.48	21.55	21.11	20.10

For β-UH_3, using the PBE functional, similar to the α-UH_3 calculations, both the vacancy and interstitial calculations have unfavourable formation energies and a predicted volume contraction and expansion respectively. The predicted expansion is much larger than for the α-UH_3 equivalent, this can be attribute to the larger defect concentration in the β-UH_3 calculation.

In contrast, for the PBE+U calculation the most striking result of the calculations is that a single hydrogen vacancy is predicted to be significantly more stable than the stoichiometric hydride. In order to determine if this was the most stable configuration a second vacancy was added to the system. The system with two hydrogen vacancies is less favourable than the single hydrogen vacancy system, however, it is still more favourable that the stoichiometric hydride, using the PBE+U functional. Calculating the properties of two vacancies using the PBE functional without the Hubbard coefficient predicts this to be more unfavourable than the mono-vacancy, with a volume contraction which is larger by a factor of 2.6.

One of the most significant differences between the PBE and PBE+U calculations is that a very large volume expansion predicted for single hydrogen vacancy and then this only increases by 0.44 Å^3 on the addition of a second vacancy. This volume expansion comes from the change in the uranium ions the presence of a va-

cancy causes. For the stoichiometric calculation the uranium ions have an average magnetic moment of 2.60 μ_B, suggesting a charge state that is some where between U^{3+} and U^{4+}. By comparison the average magnetic moment for the single vacancy calculation is 2.94 μ_B, which is indicative of a U^{3+}. Therefore, the large volume expansion that occurs from the introduction of a hydrogen vacancy is due to the uranium ions increasing in volume.

This leads to needing to consider the magnetism of the uranium ions. β-UH_3 is reported to have a magnetic moment of 1.45 $\pm$ 0.11 μ_B [378] which is the same for both of the two symmetrically inequivalent uranium sites. For α-UH_3 the magnetism is less well defined, with reports of α-UH_3 being non-magnetic down to 15 K [385] using neutron diffraction, though more recent study using Zr to stabilise α-UH_3 suggests that there is a magnetic moment of approximately 1 μ_B [383]. Thus there is still a debate as to whether both phases of the hydride have similar magnetic properties [383–385, 393].

Table 8.3 gives the predicted magnetic moments for both the α- and β- hydride calculations, using the PBE functional with and without a Hubbard coefficient. For both hydride phases using the PBE (without the Hubbard coefficient) the average magnetic moment per uranium ion is around 2.5 μ_B, this is also not significantly affected by the presence of hydrogen defects. Another key factor for β-UH_3 is there is a clear distinction between the two uranium sites, in contrast to experimental reports [378].

Table 8.3: Average predicted magnetic moments for the uranium ions in both α- and β- UH_3. For β-UH_3 the average for the U_I and U_{II} is also shown.

PBE								
	α-UH_3				**β-UH_3**			
Stoichiometry	$UH_{2.94}$	UH_3	$UH_{3.06}$		$UH_{2.75}$	$UH_{2.88}$	UH_3	$UH_{3.12}$
U_I (μ_B)	-	-	-		2.32	2.33	2.32	2.30
U_{II} (μ_B)	-	-	-		2.44	2.48	2.52	2.47
Average (μ_B)	2.48	2.51	2.48		2.41	2.44	2.47	2.43
PBE+U								
	α-UH_3				**β-UH_3**			
Stoichiometry	$UH_{2.94}$	UH_3	$UH_{3.06}$		$UH_{2.75}$	$UH_{2.88}$	UH_3	$UH_{3.12}$
U_I (μ_B)	-	-	-		2.91	2.85	2.85	2.81
U_{II} (μ_B)	-	-	-		3.02	2.97	2.51	2.69
Average (μ_B)	2.89	2.86	2.81		3.00	2.94	2.60	2.72

In contrast for the PBE+U calculation a larger magnetic moment per uranium ion is predicted, this is much close to a value of 3, which is what would be expected for an ion with three unpaired electrons using the spin only approximation. This value is much larger than experimental, however in these calculations the orbital component of the magnetism is not considered, inclusion would result in a reduction of the moment for each ion.

The most significant result of introducing a hydrogen vacancy on the magnetism

of the uranium ions is that there is now very good agreement between the predicted magnetic moments for both of the uranium sites. This, coupled to being the most stable β-hydride calculated, would suggest that there is some degree of hypostoichiometry for β-UH_3. It is unlikely to be as high as has been used here and it would be useful to use larger simulation cells to observe if a lower vacancy concentration would have a similar effect.

The hypostoichiometry of the β-hydride being predicted to be more favourable offers some insight into the work of Libowitz [400–402], who reported pressure-composition isotherms showing hypostoichiometric UH_3, at elevated temperatures. Due to the significant temperature differences (between theory and experiment), and both of the hydrogen vacancy concentrations used representing extreme H/U stoichiometry, it is difficult to compare directly with experiment. Therefore, it may be possible that β-UH_3 is intrinsically defective, though this may only occur at elevated temperatures. As the PBE+U calculations predicts that β-$UH_{2.88}$ is energetically more favourable than β-UH_3 it is important to check how this affects the DOS. Figure 8.4 shows the pDOS for β-$UH_{2.88}$, the presence of the V_H has not caused a loss of the metallic nature and there is a combination of f and d states above the Fermi level, while the main contribution below the Fermi level is from the f states. This is in contrast to the β-UH_3 pDOS (Figure 8.3d) which predicts the main contribution is from the f states above and below the Fermi level.

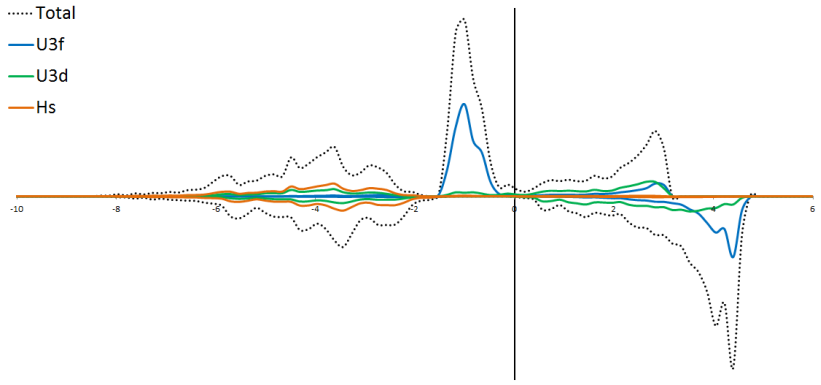

Figure 8.4: Partial DOS for β-$UH_{2.88}$. The Fermi energy has been set to 0 eV.

This presents an interesting direction for future research, exploring the effect of vacancy concentration on predicted properties, the effects and importance of including SOC and including varying values for the Hubbard coefficient.

Overall, for this research the inclusion of a Hubbard coefficient results in an expansion of the lattice parameters, quite significantly for the β-hydride vacancy calculation, however this is due to an increased localisation of the electron on the uranium ions resulting in all the uranium ions increasing in size. The other effect of the hydrogen vacancy is that there is now agreement between the two symmetrically distinct uranium sites in β-UH_3. This is only achieved with the inclusion of the Hubbard coefficient. Additionally, the inclusion of a Hubbard coefficient results in a suppression of the number of states in the DOS, when compared to the PBE calculation without the Hubbard coefficient as would be expected but crucially does not result in the loss of a metallic nature.

Thus, while the PBE+U approach used here may not be the most appropriate simulation criteria if the interest was purely in the hydride without considering any

other phase, it still results in a suitable enough model of the hydride to allow for comparison with the oxide calculations of this work. The next section will now use this simulation methodology to explore the oxidation of uranium hydride.

8.4 Oxidation of Uranium Hydride

The main focus of this work is to examine hydrogen defects in uranium dioxide, in order to build an understanding of the process of how uranium hydride forms at the uranium metal/oxide interface. As mentioned previously this is of concern due to the pyrophoric nature of UH_3, which leads to the formation of UO_2 under oxidising conditions. Therefore, in order to explore the formation of UO_2 from the oxidation of UH_3 we examine whether it forms via an oxy-hydride. This will allow for a model of UH_3 oxidation to be developed.

In order to achieve this goal, the Madelung energy of the hydride sites was calculated in the METADISE code and for each unique hydride site an oxygen atom replaced the hydride [371]. The most stable defect configuration was then determined using VASP and the process repeated, with the lowest energy system determined from the DFT calculations. The reason for this approach was to reduce the vast number of calculations for all possible configurations, for the oxidation of UH_3, to a reasonable number for which the properties could be calculated. In this chapter only the results of the most stable configuration, at each oxygen defect concentration, are reported, the complete results for all configurations are available in Appendix C. In order to make the calculated energies more easily comparable to experimental values water was chosen as product rather than hydrogen gas as the product of oxidation of UH_3 is UO_2 and water [113]. $UH_{2.88}$ (*i.e.* $1V_H$) was chosen as the starting hydride rather than UH_3 as the hypostoichiometric hydride was predicted to be more stable that the stoichiometric hydride. This gives the general reaction shown in Equation 8.3.

$$UH_{2.88} + \frac{y}{2}O_2 \rightarrow UH_{3-y}O_y + nH_2O \tag{8.3}$$

The defect formation energy was then calculated according to Equation 8.4.

$$E_F = ((nE_{H_2O} + E_{UH_{3-y}O_y}) - (E_{UH_{2.88}} + \frac{y}{2}E_{O_2})) \tag{8.4}$$

Table 8.4 summarises the calculated properties for uranium hydride at varying oxygen defect concentrations. One of the most notable results is the large and negative values of the formation energy for all the different oxygen concentrations. Given the pyrophoric nature of UH_3 this qualitatively agrees well with experiment and should perhaps not be that unexpected. The formation energy increases per O as the oxygen concentration increases, indicating that the reaction is more favourable at higher oxygen concentrations and there is no barrier to the oxidation of the hydride. There appears to be no discernible relationship between the volume and oxygen concentration. As the most favourable configuration for $UH_{2.75}O_{0.25}$ was the only calculation to predict a volume expansion and in the $UH_{2.63}O_{0.37}$ set of calculations there was an alternation of volume expansion and contractions which does not correlate to the relative energy ordering of the calculations (Appendix C).

Table 8.4: Calculated formation energies, volume change and number of U^{4+} defects in $UH_{3-x}O_x$ with varying oxygen concentrations. β-$UH_{2.88}$ has been include as a reference. The change in volume (ΔV) is calculated relative to β-$UH_{2.88}$.

	$\mathbf{UH_{2.88}}$	$\mathbf{UH_{2.88}O_{0.12}}$	$\mathbf{UH_{2.75}O_{0.25}}$	$\mathbf{UH_{2.63}O_{0.37}}$
$\boldsymbol{E_F}$ **/ O (eV)**	0.00	-4.34	-4.68	-4.94
a **(Å)**	6.91	6.92	6.95	6.92
b **(Å)**	6.92	6.90	6.91	6.92
c **(Å)**	6.92	6.91	6.92	6.90
ΔV / O (Å^3)	0.00	-1.17	0.40	-0.22
Number of U^{4+}	0	1	2	3

From these results, if the trend of uranium oxidation continues, then in order to achieve complete oxidation of the U^{3+} ions to U^{4+} only 8 oxygen atoms would be required, an O/U ratio of 1:1. This suggests that the U^{3+} oxidation state is particularly reactive and will easily be converted to a higher, more stable, oxidation state. This is further supported by the lack of any hypostoichiometric oxide phases (UO_{2-x}), which would require the presence of U^{3+} ions.

All of the configurations considered had significantly favourable formation energies, which is relatively unaffected by the configuration of the uranium ions that were oxidised. The largest difference in relative energy was 0.25 eV per defect oxygen (Table C.2).

Examining the data set above allows for some general trends to be extracted as to the nature of which uranium ions will be preferentially oxidised. For $UH_{2.75}O_{0.25}$ the most stable configuration was the only configuration to have a U_I oxidised. The remaining configurations had $2U_{II}$ sites oxidised. This suggests a small energetic preference for the U_I sites to be oxidised, although there is only a small energy range across all the configurations of 0.24 eV. The uranium ion which was oxidised was determined from the predicted magnetic moments of the uranium ions.

Increasing the oxygen defect concentration to $UH_{2.63}O_{0.37}$, resulted in the two most stable configurations with both U_I sites oxidised, the next most stable configurations (7 configurations) had $1U_I$ and U_{II} oxidised and the most unstable (3 configurations) had $2U_{II}$ oxidised. The configuration of uranium sites which were oxidised had a major role in determining the stability of the configuration, with an energy difference of 0.92 eV between the most stable and least stable configurations. It should be reiterated at this point whilst this is a large energy difference, nearly 1 eV, between the two configurations the overall solution energy is still a large negative value (≈-5 eV per O), this is far more significant than the relative energy difference.

This work is only the beginning of modelling the oxidation of UH_3 and needs to be taken to completion (including using the PBE functional) in order to build a more complete picture of oxidation. However, from these results here it would suggest that the oxidation of the U^{3+} to U^{4+}, is the first part of the oxidation process and this will occur when there is a 1:1 O/U ratio. There are also additional mechanisms that would require exploration before a more definitive answer to how the process occurs can be determined. An example of another potential reaction is

given in Equation 8.5, this is similar to the reaction in Equation 8.3 but for every oxygen atom added two hydrogen atoms are removed.

$$U_8H_{24} + O_2 \rightarrow U_8H_{22}O + H_2O \tag{8.5}$$

In addition to using these results to explore the effect of oxygen on the physical and energetic properties of UH_3, we can also explore how the presence of oxygen affects the electronic properties and how the conversion of UH_3 to UO_2 occurs.

8.4.1 Electronic Properties

The pDOS for β-$UH_{2.88}$, $UH_{2.88}O_{0.12}$, $UH_{2.75}O_{0.25}$ and $UH_{2.63}O_{0.37}$ is shown is Figure 8.5, a magnified area around the Fermi level for the different oxygen defect concentrations is shown in Figure 8.6.

On addition of a single oxygen defect ($UH_{2.88}O_{0.12}$) there are two major differences to the DOS spectrum (Figure 8.5b) when compared to β-$UH_{2.88}$. The first of these is presence of U^{4+} f-states in both the conduction and valence band regions of the DOS spectrum (Figure 8.5b). There is also clearly a loss of metallic nature, Figure 8.6a shows the pDOS magnified around the Fermi level, with only a very small number of states predicted to be at the Fermi level. Suggesting that the transition from metallic to insulating behaviour will only require a relatively low oxygen content. The oxygen p-states are predicted to exist between -2 eV and -6 eV below the Fermi level, which is very similar to the prediction for the oxygen p-states in UO_2 (Figure 8.7a).

However, the presence of a second oxygen defect ($UH_{2.75}O_{0.25}$) sees a very different predicted DOS (Figure 8.5c), compared to $UH_{2.88}O_{0.12}$. By contrast with the predicted DOS for $UH_{2.88}O_{0.12}$ there is a metallic nature predicted for the system, with this arising primarily from the U^{3+} f-states and a small contribution form the U^{4+} f-states.

The final DOS spectrum (Figure 8.5d) at the highest oxygen defect concentration ($UH_{2.63}O_{0.37}$), examined in this work, is remarkably different to the previous DOS for $UH_{2.75}O_{0.25}$. As with the predicted DOS for $UH_{2.88}O_{0.12}$ there is a reduction of states at the Fermi level (Figure 8.6c). Additionally, the predicted DOS bears some similarity to the pDOS predicted for a single hydroxyl defect in UO_2 (Figure 8.7b), where there is a gap of $\approx$2 eV between the U^{4+} f-states and the U^{3+} f-states occupy the gap in between. The oxygen p-states are again at lower energy values which are similar to that of UO_2 (Figure 8.7a).

The electronic properties of uranium hydride show an evolution towards a DOS which is similar to that of UO_2 as the oxygen content increases. The number of U^{4+} f-states predicted increases, with increasing oxygen content, and a corresponding decrease in the U^{3+} f-states is observed.

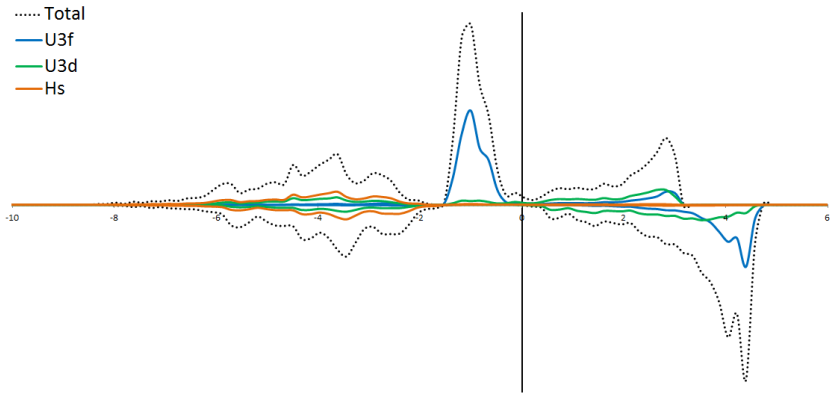

(a) β-$UH_{2.88}$

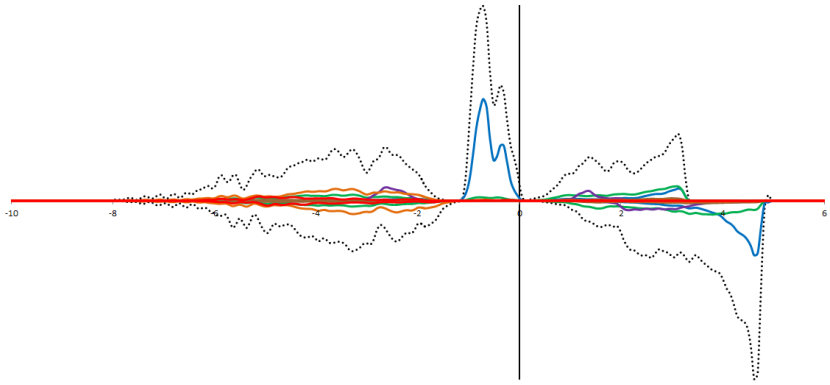

(b) $UH_{2.88}O_{0.12}$

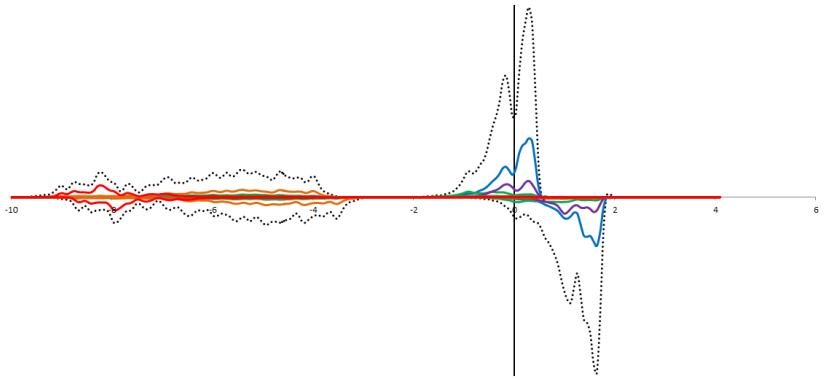

(c) $UH_{2.75}O_{0.25}$

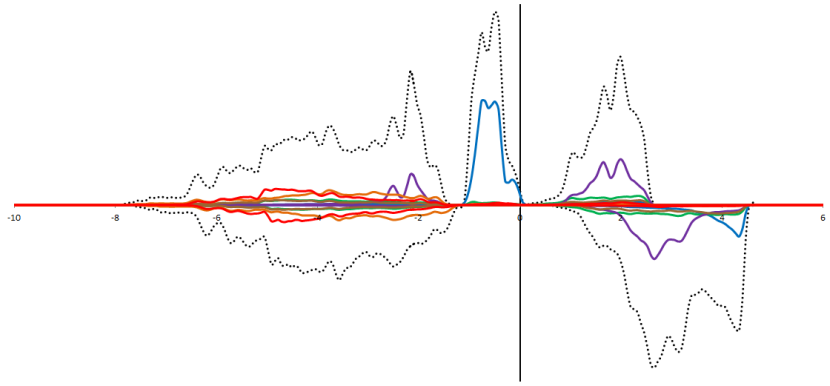

(d) $UH_{2.63}O_{0.37}$

Figure 8.5: Partial DOS for β-UH_3, $UH_{2.88}O_{0.12}$, $UH_{2.75}O_{0.25}$ and $UH_{2.63}O_{0.37}$. The Fermi energy has been set to 0 eV. The horizontal axis is E-E_f eV and the vertical axis is the number of state.

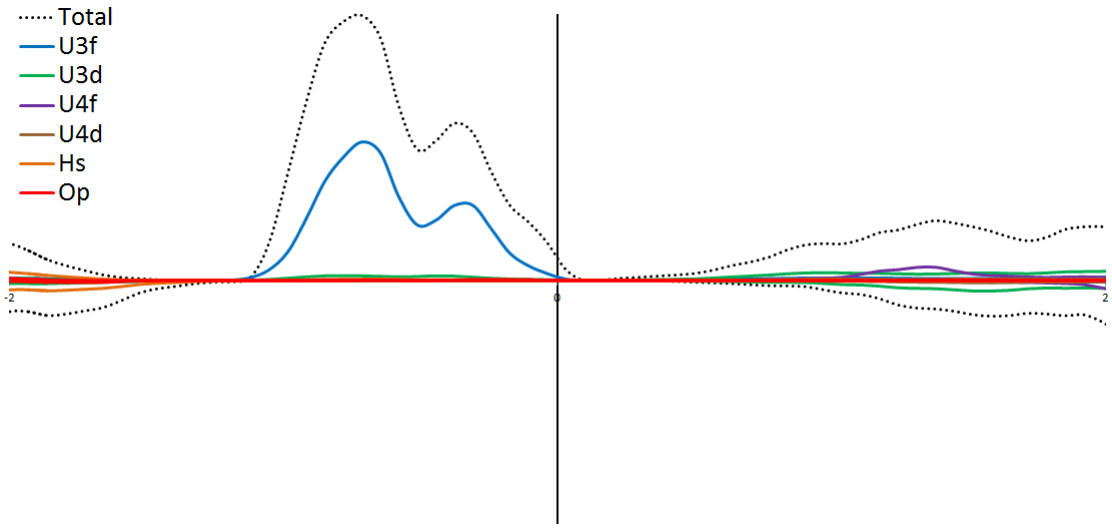

(a) $UH_{2.88}O_{0.12}$

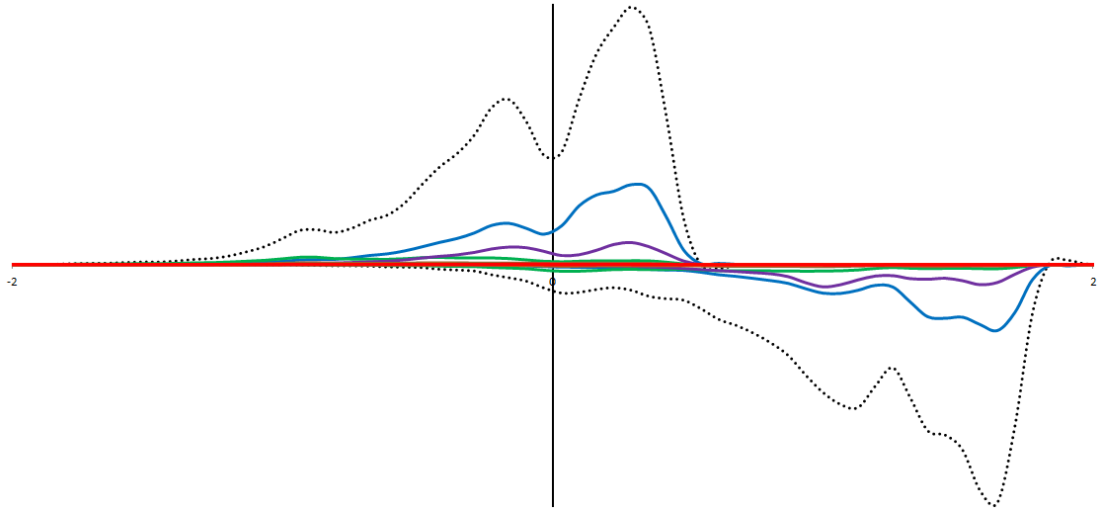

(b) $UH_{2.75}O_{0.25}$

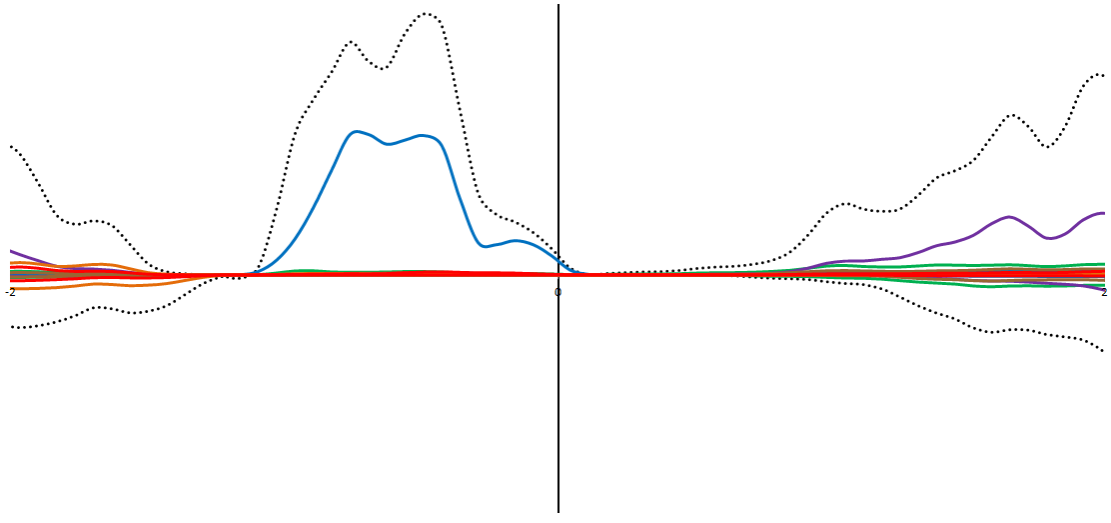

(c) $UH_{2.63}O_{0.37}$

Figure 8.6: Partial DOS for $UH_{2.88}O_{0.12}$, $UH_{2.75}O_{0.25}$ and $UH_{2.63}O_{0.37}$ the graphs have been scaled to highlight the region around the Fermi level. The Fermi energy has been set to 0 eV. The horizontal axis is E-E_f eV and the vertical axis is the number of state.

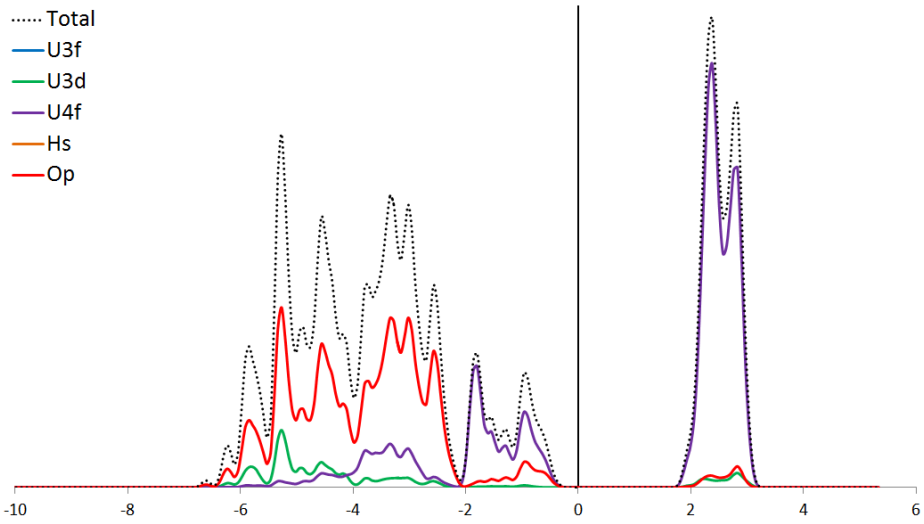

(a) UO_2

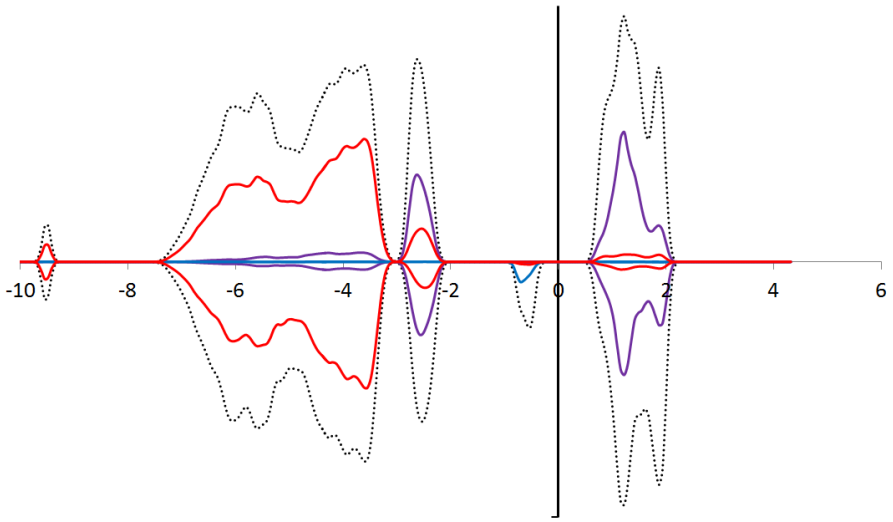

(b) $UO_2H_{0.03}$ (Hydroxyl Defect)

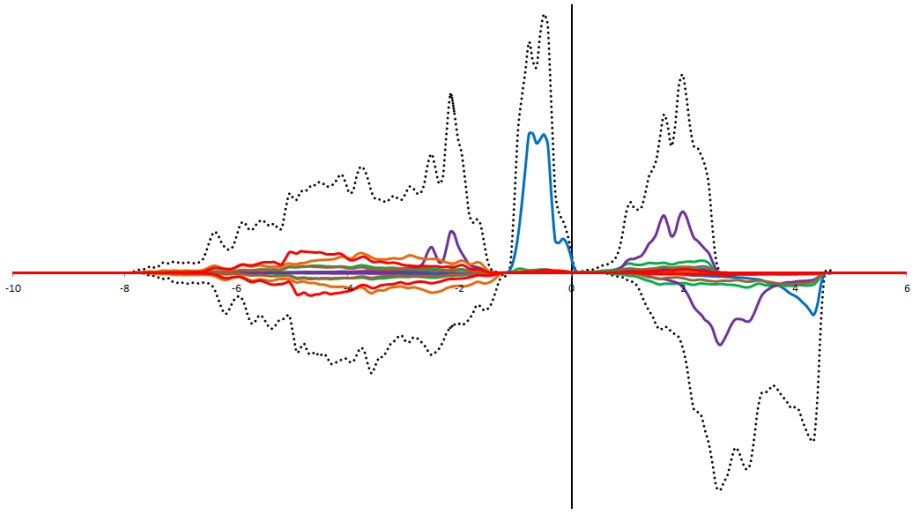

(c) $UH_{2.63}O_{0.37}$

Figure 8.7: Partial DOS for UO_2, a hydroxyl defect in UO_2 and $UH_{2.63}O_{0.37}$. The Fermi energy has been set to 0 eV. For UO_2 only the spin up channel is shown as the spin down is identical. The horizontal axis is E-E_f eV and the vertical axis is the number of state.

8.5 Conclusions

The formation of UH_3 is of considerable concern for the long term safe storage of uranium metal. This is due to the pyrophoric nature of UH_3. The work in this chapter has examined the suitability of the methodology developed for UO_2 in determining the properties of the hydride, in order to allow for a direct comparison between the oxide and hydride. Despite a Hubbard coefficient typically not being used in the simulation of metallic systems. However, whilst the inclusion of the Hubbard coefficient is not required it does not significantly alter predicted lattice parameters or atom positions. The electronic DOS is suppressed as would be expected from the inclusion of a Hubbard coefficient, but does not remove the metallic nature. Overall, the methodology developed for the simulation of UO_2 is suitable to simulate the hydride phases of uranium.

The simulation of hydrogen point defects in β-UH_3 showed that a single neutral hydrogen vacancy had a favourable formation energy and that potentially β-UH_3 is intrinsically defective. This is in contrast to experimental work [400–402] that shows the formation of a hydrogen vacancy is unfavourable and offers evidence that PBE+U may not be the best approach. This requires further research; the use of larger systems sizes and the inclusion of SOC to fully explore this behaviour. Another explanation for the significant difference between theory and experiment is the vastly different defect concentrations. Therefore, with the use of larger system sizes and defect concentrations closer to experimental values a more detailed study could be undertaken. If, hydrogen vacancies do have a favourable formation energy at the concentrations used in this work, then it suggests that once a certain vacancy concentration is reached β-UH_3 becomes unstable and either β-UH_{3-x} or β-UH_3 and U-metal would form.

In addition to exploring hydrogen point defects on the properties of β-UH_3 the effect of oxygen substitution on hydride sites was investigated, in order to build a model for the oxidation of UH_3 into UO_2. This showed very large and negative formation energies as would be expected for a pyrophoric material. The conversion of the U^{3+} present in the hydride to U^{4+} is predicted to only require an O/U ratio of 1:1, suggesting that the U^{3+} oxidation state is particularly unfavourable. The unfavourable nature of localised U^{3+} defects in UO_2 is well known.

The electronic DOS showed a conversion from the hydride DOS to a spectrum which resembled that of a hydroxyl defect in UO_2. The growth of the U f-states at the top of the valence and bottom of the conduction band was observed, with the U^{3+} f-states occupying the gap in between.

The work in this chapter and the previous chapters has explored a wide range of defects at varying oxygen and hydrogen concentrations, this makes it difficult to form a complete picture of what different defect states are the most significant and important to consider. Therefore the next chapter will use the data generated from this thesis to build a thermodynamic model which will facilitate an understanding of the most important defects and phases to consider with varying conditions. The data generated from this chapter can also be used to aid in the fitting of potentials to allow for simulation of larger systems and extended defect structures.

9 Representation of Thermodynamic Stability

The previous chapters in this thesis have examined a range of hydrogen defects with varying excess oxygen concentrations in order to determine how the structure, stability and electronic properties of UO_2 are affected by the presence of hydrogen. Whilst these calculations provide important insights at the atomic scale, it is difficult to draw macroscopic scale conclusions directly from these calculations. However, it is possible to use the data generated from these calculations to produce a thermodynamic model. This thermodynamic model will allow for an assessment of the most important phases, including defect phases, that need to be considered. Additionally, it will also allow for an exploration of which phases are important metastable states that also need to be considered, which is achieved by inhibiting the more thermodynamically stable states to determine which phases exist below them.

This chapter will first set out the methodology used to assess the thermodynamic stability. Following this will be the results of the thermodynamic stability assessment, which will also incorporate the data generated by Brincat for higher uranium oxides during his thesis [187] to encompass a more complete survey of the uranium/oxygen/hydrogen system.

9.1 Methodology

In order to assess the thermodynamic stability of different compositions of uranium, oxygen and hydrogen the free energy needs to be determined. The first stage to this is to determine an expression for the thermodynamic properties at equilibrium, once this has been established it is then possible to calculate the free energy which allows for the thermodynamic stability of the different compositions to be determined.

9.1.1 Calculating the Free Energy at Equilibrium ($\delta G_{T,p}$)

The first requirement to assess the thermodynamic stability is to define a generic reaction scheme, which can be used to form any of the phases considered in the model. This is achieved using Equation 9.1.

$$\mathrm{nUO_2} + \mathrm{xO_2} + \mathrm{yH_2} \rightarrow \mathrm{U}_n\mathrm{O}_m\mathrm{H}_z \tag{9.1}$$

When the system is at equilibrium the chemical potentials of the products and reactants will be equal. This also means than the change in free energy $\delta G_{T,p}$ is zero, such that:

$$\delta G_{T,p} = \mu_{U_nO_mH_z} - n\mu_{UO_2} - x\mu_{O_2} - y\mu_{H_2} = 0 \tag{9.2}$$

For the solid phases ($U_nO_mH_z$ and UO_2) the free energy is:

$$\mu_{Species} = \mu^0_{Species} \tag{9.3}$$

where $\mu^0_{Species}$ is the partial molar free energy of the species. For both H_2 and O_2 making the assumption that they behave as gases then the free energy is:

$$\mu_{Species} = \mu^0_{Species} + \delta\mu_{Species} \tag{9.4}$$

where the $\delta\mu_{Species}$ is the change in the chemical potential due to the change in partial pressure of the gas and can be calculated according to Equation 9.5, assuming ideal gas behaviour, where $p^{\ominus}$ is 1 bar in the standard state.

$$\delta\mu = RT\ln\left(\frac{p_x}{p^{\ominus}}\right) \tag{9.5}$$

Applying Equations 9.3 and 9.4 to Equation 9.2 gives Equation 9.6, which is the change in the free energy due to the change in number of a species. For this work this can be interpreted as a change of gas pressure.

$$\delta G_{T,p} = \mu^0_{U_nO_mH_z} - n\mu^0_{UO_2} - x(\mu^0_{O_2} + \delta\mu_{O_2}) - y(\mu^0_{H_2} + \delta\mu_{H_2}) = 0 \tag{9.6}$$

As $\mu^0_{Species}$ is the partial molar free energy of the individual species Equation 9.6 can be rewritten as:

$$\delta G_{T,p} = \Delta G^0 - x\delta\mu_{O_2} - y\delta\mu_{H_2} = 0 \tag{9.7}$$

where ΔG^0 is the free energy. As the system is at equilibrium Equation 9.7 can be rearranged to give:

$$\Delta G^0 = x\delta\mu_{O_2} + y\delta\mu_{H_2} \tag{9.8}$$

For an ideal gas Equation 9.8 can also be written as:

$$\Delta G^0 = RT\ln(p^x_{O_2} \cdot p^y_{H_2}) \tag{9.9}$$

It is now possible to determine $\delta\mu_{Species}$ for H_2 and O_2 when Equation 9.1 is at equilibrium. The method outlined can now be applied to all compositions of $U_nO_mH_z$ and this will identify the thermodynamically most stable composition, provided that ΔG^0 is known for each composition.

9.1.2 Calculating the Free Energy (ΔG^0)

The free energy of a system is calculated using Equation 9.10.

$$\Delta G^0 = \sum \Delta G^{0,\text{products}_\text{f}} - \sum \Delta G^{0,\text{reactants}_\text{f}} \tag{9.10}$$

For this work the free energy of each material is calculated using the DFT energy. Where there are three components to the free energy of each material (Equation 9.11), U_0 is the DFT calculated internal energy, U_{ZPE} is the zero point energy and A_{Vib} is the Helmholtz vibrational free energy.

$$\Delta G_f = U_0 + U_{\text{ZPE}} + A_{\text{Vib}} \tag{9.11}$$

This work currently only considers the internal energy component of the free energy, as to calculate the zero point energy and the Helmholtz vibrational free energy would require a large amount of computational resource and time. A clear expansion to the work here would be to calculate these properties for all of the phases considered and to determine how they affect the predicted thermodynamic stability. This would also show how necessary these contributions are to producing an accurate representation of thermodynamic stability.

9.2 Thermodynamically Stable Structures

This section will give the results of the thermodynamic assessment. Whilst the inclusion of kinetic effects is not possible, it is still possible to explore the stability of metastable phases. This is achieved by inhibiting the more stable phases, in practical terms this means that the phase is removed from the calculation. This will give insight into the first defect structures that are likely to form and need to be considered in long term waste storage plans. Additionally, a prediction of the likely pathway of UO_2 oxidation under varying conditions can be made, by predicting the thermodynamically stable phases from the least to the most stable phase.

In order to help interpret the results, three sets of reference conditions for $\Delta\mu$ of both H_2 and O_2 have been selected. These reference conditions are summarised in Table 9.1. The partial molar free energy ($\mu^0_{Species}$) excluding temperature effects (*i.e.* 0 K) has been set to zero and the change in free energy from 0 K to 298 K at 1 bar and atmospheric pressures of H_2 and O_2 has been calculated using data from the NIST database [403].

Table 9.1: Reference conditions chosen for the thermodynamic model.

Conditions			$\Delta\mu$ **(eV)**	
P_{H_2} **(bar)**	P_{O_2} **(bar)**	**Temperature (K)**	$\mathbf{H_2}$	$\mathbf{O_2}$
1	1	0	0.00	0.00
1	1	298	-0.54	-0.32
Atmospheric	Atmospheric	298	-0.58	-0.57

Listed in Table 9.2 are all of the lowest energy configurations for each stoichiometry. The number is an index to refer to the regions as they appear on the different thermodynamic model predictions, the stoichiometry represents the stoichiometry of the U-O-H system and the defect column identifies the corresponding defect.

Table 9.2: List of all of the lowest energy configurations for each stoichiometry. The index is a reference number for the regions in the thermodynamic model predictions, stoichiometry is the defect stoichiometry and the defect column identifies the defect corresponding to the given stoichiometry. All UO_2 systems are for a 96 atom simulation cell, all β-UH_3 is for a single unit cell and all α-UH_3 is a 2x2x2 supercell. All calculations used the PBE+U functional, with the same U_{eff} (3.96 eV).

Index	Stoichiometry	Defect
0	$UO_{1.97}$	V_O
1	$UO_{1.97}H_{0.03}$	V_O H_i
2	$UO_{1.97}H_{0.06}$	V_O $2H_i$
3	$UO_{2.00}$	-
4	$UO_{2.00}H_{0.03}$	H_i
5	$UO_{2.00}H_{0.06}$	H_{2i}
6	$UO_{2.03}$	O_i
7	$UO_{2.03}H_{0.03}$	O_iH_i
8	$UO_{2.03}H_{0.06}$	$2O_iH_i$
9	$UO_{2.06}$	I_2^x
10	$UO_{2.06}H_{0.03}$	I_2^x H_i
11	$UO_{2.06}H_{0.06}$	W_{222} $2H_i$
12	$UO_{2.06}H_{0.09}$	I_2^x $3H_i$
13	$UO_{2.06}H_{0.12}$	W_{222} $4H_i$
14	$UO_{2.09}$	I_3^x
15	$UO_{2.09}H_{0.03}$	I_3^x H_i
16	$UO_{2.09}H_{0.06}$	I_3^x $2H_i$
17	$UO_{2.09}H_{0.09}$	I_3^x $3H_i$
18	$UO_{2.09}H_{0.12}$	I_3^x $4H_i$
19	$UO_{2.13}$	I_4^x
20	$UO_{2.13}H_{0.03}$	I_4^x H_i
21	$UO_{2.13}H_{0.06}$	I_4^x $2H_i$
22	$UO_{2.13}H_{0.09}$	I_4^x $3H_i$
23	$UO_{2.13}H_{0.12}$	I_4^x $4H_i$
24	$UO_{2.16}$	*COT-13*
25	$UO_{2.16}H_{0.03}$	*COT-13* H_i
26	$UO_{2.16}H_{0.06}$	*COT-13* $2H_i$
27	α-U (metal)	-
28	β-$UH_{3.00}$	-
29	β-$UH_{2.88}O_{0.12}$	$1O_i$
30	β-$UH_{2.75}O_{0.25}$	$2O_i$
31	β-$UH_{2.63}O_{0.37}$	$3O_i$
32	U_3O_7	-
33	U_2O_5	-
34	β-U_3O_8	-
35	γ-UO_3	-
36	α-$UH_{3.06}$	H_i
37	α-$UH_{2.94}$	V_H
38	β-$UH_{2.75}$	$2V_H$
39	β-$UH_{2.88}$	V_H
40	β-$UH_{3.13}$	H_i

9.2.1 Full Thermodynamic Model

Figure 9.1 shows the predicted thermodynamically stable phases as a function of hydrogen and oxygen chemical potential. Extremely low pressures of oxygen and hydrogen are required in order for uranium metal (27) to be predicted as the most thermodynamically stable which agrees with uranium metal being passivated by a layer of UO_2 in atmospheric conditions. As the oxygen pressure is increased first UO_{2-x} (0) forms then UO_2 (3) before hyperstoichiometric UO_2 occurs in the form of O_i (6). Then the higher uranium oxides are predicted, with U_2O_5 (33), β-U_3O_8 (34) and finally γ-UO_3 (35). Here, it should be noted that the U_2O_5 structure used is based on that of Np_2O_5 which Brincat's calculations [404] have predicted to be more stable than the δ-U_2O_5 configuration. However, the Np_2O_5 structure was also predicted to be unstable at high pressures and temperatures, where U_2O_5 phases are synthesised. If the δ-U_2O_5 energy is used then the region of Np_2O_5 (33) disappears and is replaced by a combination of β-U_3O_8 (34) and O_i (6). This agrees well with the known oxidation behaviour of uranium metal into UO_2 and then eventually the higher uranium oxides.

A very important region to observe in the model is the presence of the Willis cluster with four hydrogen atoms (13). This predicts that it is possible for the Willis cluster to be stable as an isolated defect and does not require chains to stabilise the defect, which is the only previous theoretical report of stable Willis defects [21].

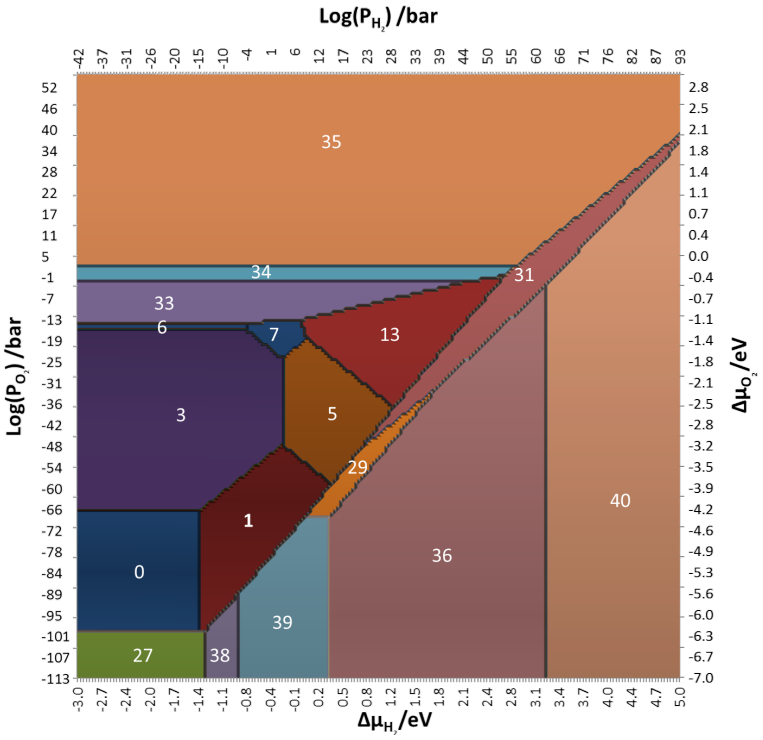

Figure 9.1: Thermodynamic model including all calculated systems, see Table 9.2 for a key of the structures shown.

If instead of increasing the oxygen pressure the hydrogen pressure is increased the model predicts that uranium metal will convert to different degrees of hyposto-ichiometric uranium hydride (38, 39) before becoming hyperstoichiometric uranium hydride (36 and 40). To simply use this model to say how uranium metal would

evolve under increasing pressures of hydrogen may not be accurate as this would suggest that a conversion from β-UH_3 (39) to α-UH_3 (36) occurs, which would contradict the experiments of Mulford [382] who reports that the conversion of α-UH_3 to β-UH_3 is irreversible. If the hypostoichiometric α-UH_3 (36) is removed from the calculation then the regions of hypo- (39) and hyper- (40) stoichiometric β-UH_3 expand to cover this region. There is no predicted region of stoichiometric UH_3, again suggesting that perhaps UH_3 is intrinsically defective. Though this could also be due to the PBE+U functional not being the most suitable for simulation of UH_3, resulting in stabilisation of the hydrogen vacancies. This is an area which will require further investigation.

Finally, if both hydrogen and oxygen pressures are increased together then as the pressures increase the most stable defects are those with the highest hydrogen and excess oxygen concentrations. There is a relatively small region where the oxygen defects in UH_3 (29 and 31) are predicted as stable, which seems unlikely given the reactivity of UH_3 towards oxygen. However, these regions are at extremes of either oxygen and/or hydrogen pressures.

The phases that exist at the set of reference conditions are given in Table 9.3. Under all three sets of conditions it is the higher uranium oxides which are predicted. For U_3O_8 and UO_3 this is understandable as U_3O_8 is the kinetic oxidation product and UO_3 is the thermodynamic oxidation product for uranium oxides. The unexpected result is under atmospheric conditions U_2O_5 is predicted. U_2O_5 is known to be one of the most unstable oxides of uranium [22, 50, 404], but as noted above, work by Brincat *et al.* [404] accounts for this by showing that Np_2O_5 based structure is unstable at the temperatures and pressure at which U_2O_5 is formed.

Table 9.3: Predicted most thermodynamically stable phase for the chosen set of reference conditions when all U-O-H compositions are included.

Conditions			$\Delta\mu$ **(eV)**		**Phase**
H_2 (bar)	**O_2 (bar)**	**Temperature (K)**	**H_2**	**O_2**	
Atmospheric	Atmospheric	298	-0.58	-0.57	U_2O_5
1	1	298	-0.54	-0.32	β-U_3O_8
1	1	0	0.00	0.00	γ-UO_3

The synthesis conditions for U_2O_5 are extreme and it is possible that these conditions are not suitable for the formation of a Np_2O_5 structured material. It is also possible that as this model only considers the thermodynamic stability that there are large kinetic barriers to the formation of U_2O_5. As mentioned previously if the δ-U_2O_5 structure is used then this region disappears and instead β-U_3O_8 is predicted to be the most stable oxide under atmospheric conditions. This shows that there is further research required into oxides of uranium around the O/U ratio of 2.5, which is the least studied region of the U/O system.

9.2.2 Inhibiting Higher Uranium Oxides

Another feature of this simple approach is that phases can be inhibited to explore the metastable phases which may potentially be pre-cursors to the most stable phases. Figure 9.2 shows the results of inhibiting the higher uranium oxides, in order to visualise the relative stabilities if the defective UO_2 structures.

As the higher uranium oxides are inhibited there is only a small change in the predicted phases. It is not until all the uranium oxides at an O/U ratio of 2.5 or greater have been inhibited that there is any real change to the predicted phases. Once the higher oxides are inhibited there are three new regions which appear, these are the split di-interstitial (9), the split tri-interstitial (14) and the split quad-interstitial with four hydrogen atoms (23). There is also a large expansion of the Willis cluster with 4 hydrogen defects (13). Showing that this is a very stable defect configuration and further supporting the earlier results showing that isolated Willis clusters are possible, in the presence of hydrogen.

The most stable phases at the chosen reference conditions changes to always be the highest uranium oxide included for all conditions, until UO_3, U_3O_8 and U_2O_5 are inhibited, Figure 9.2c. At the atmospheric reference conditions isolated O_i (9) are predicted to be the most stable phase, with U_3O_7 predicted for the other two reference conditions.

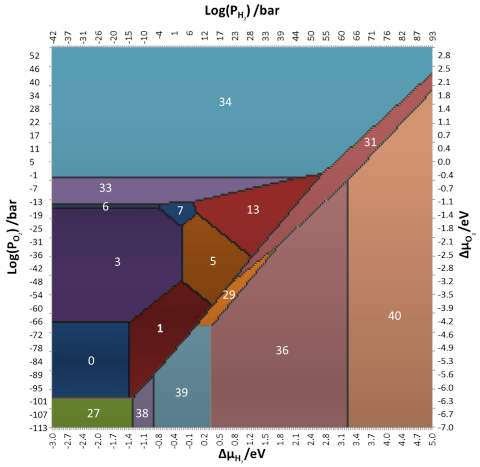

(a) Inhibiting UO_3

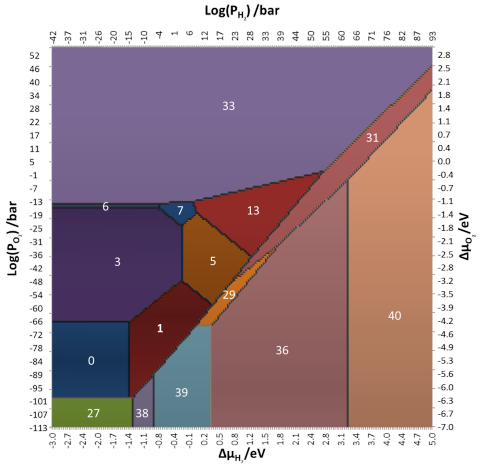

(b) Inhibiting UO_3 and U_3O_8

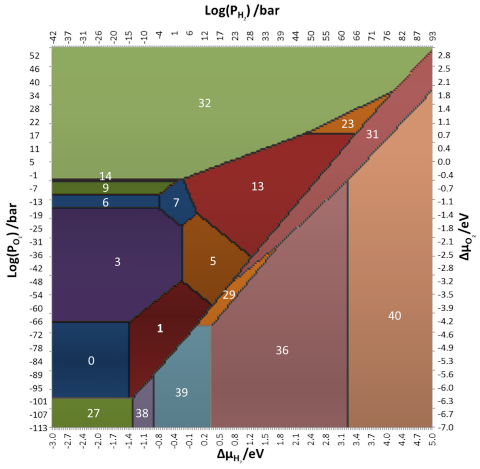

(c) Inhibiting UO_3, U_3O_8 and U_2O_5

Figure 9.2: Thermodynamic stability predictions when higher uranium oxides are inhibited. Showing the predicted most thermodynamically stable U-O-H configuration when all phases when UO_3 (9.2a), UO_3 and U_3O_8 (9.2b) and UO_3, U_3O_8 and U_2O_5 (9.2c) have been inhibited. See Table 9.2 for a key of the structures shown.

9.2.3 Complete Inhibition of Higher Uranium Oxides

This final section shows the predicted phases when all of the higher uranium oxides (O/U>2.33) have been inhibited. In this model a large number of new regions have appeared at higher oxygen pressures. The split tri-interstitial (14) region has expended slightly and then evolves into the cuboctahedron (*COT*-13) defect (24). The Willis defect with 4 hydrogen (13) is a larger region again and dominates the centre of the model. The split quad-interstitial with four hydrogen atoms (23) region is much larger. Finally, at high oxygen and hydrogen pressures a new region is predicted this is the *COT*-13 with 2 hydrogen defects (26). For the regions at the extreme high pressures of hydrogen and oxygen are likely to be subject to significant change as there are very few configurations included for this region. It is highly likely that as more of the larger oxygen defect clusters properties are explored with higher hydrogen concentration and even if higher uranium oxides are considered with hydrogen defects that they will dominate in this region of the model.

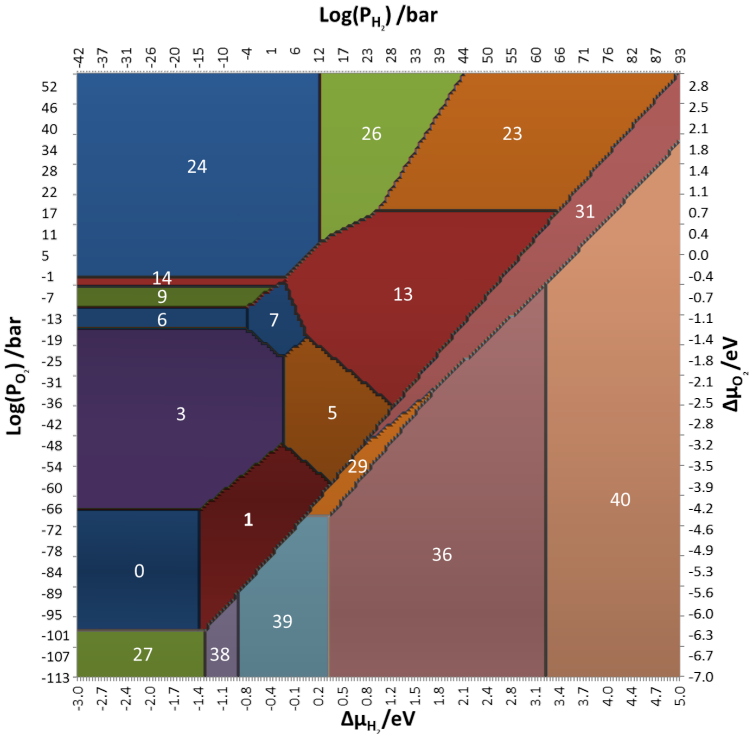

Figure 9.3: Thermodynamic model prediction inhibiting all higher uranium oxides. Showing the predicted most thermodynamically stable U-O-H configuration when all phases with an O/U>2.33 have been inhibited.

Table 9.4 shows the phases predicted at the set of reference conditions. Although not unexpected, it is worth noting that the split di-interstitial and cuboctahedron defects are commonly discussed in the literature, but less so is that the stability of these defects is heavily dependent on oxygen partial pressure. Additionally, the presence of hydrogen has been seen in this thesis to have a significant effect on the cluster stability. While the 1 bar H_2 and O_2 at 0 K predicts the *COT-13* this is on the border of stability with the Willis with four hydrogen atoms (13). This would only require a -0.1 shift in the chemical potential of oxygen, for the Willis to be the most stable defect under these conditions. This again highlights the need to extend

the range of defects and impurities when considering oxidation of UO_2, as these small concentrations of impurities significantly alter the chemistry and stability of these defects.

Table 9.4: Predicted most thermodynamically stable phase for the chosen set of reference conditions for the full thermodynamic model.

Conditions			$\Delta\mu$ **(eV)**		**Phase**
P_{H_2} **(bar)**	P_{O_2} **(bar)**	**Temperature (K)**	$\mathbf{H_2}$	$\mathbf{O_2}$	
Atmospheric	Atmospheric	298	-0.58	-0.57	$UO_{2.03}$ I_2^x
1	1	298	-0.54	-0.32	*COT-13*
1	1	0	0.00	0.00	*COT-13*

9.3 Conclusions

This chapter has built a simple thermodynamic model, to help visualise the relative stability of the different defects simulated in this thesis and included the higher uranium oxides previous simulated by Brincat [187] during his thesis, to construct a picture of the most important phases to consider for uranium oxidation.

The complete thermodynamic model, which includes the higher oxides, predicts the most stable phases to be U_3O_8 which is the kinetic oxidation product and UO_3 is the thermodynamic oxidation product for uranium oxides at 1 bar H_2 and O_2 at 298 K and 0 K, respectively. The model also predicts that under atmospheric conditions that U_2O_5 is the most stable phase. The structure of this phase is based on that of Np_2O_5 and is a newly predicted low energy U_2O_5 structure [404]. This strongly indicates that U_2O_5 has the potential to form stable structures, but have significant kinetic barriers to their formation. Which is why only the high energy structures have been observed, due to extreme synthesis conditions.

The model also allows for metastability to be explored, by the inhibition of phases. As the higher uranium oxides are inhibited, the model remains largely unchanged in its predictions. However, once all of the higher uranium oxides (O/U>2.33) have been removed a large range of different defect clusters with varying hydrogen concentrations are predicted. The most significant result from this calculation is that the hydrogen containing Willis cluster (with four hydrogen) only requires a shift of 0.1 eV in the chemical potential of oxygen from being predicted as the most stable configuration at 1 bar H_2 and O_2 at 0 K. This shows that this defect cluster has the potential to be stabilised under the appropriate environmental conditions.

While the work in this chapter has laid the foundations for a thermodynamic model which allows for an exploration of the stability of varying hydrogen and oxygen pressures it is currently limited by neglecting temperature. The most important progression of this work would be the calculations of the vibrational entropy of all the phases, as this would allow for the inclusion of temperature.

The thermodynamic model presented in this chapter acts as a method to combine all of the various calculations in this thesis and the thesis of Brincat in order to develop a visual representation of the relative stability of the U-O-H system. The

next chapter will collate the conclusions of the individual chapters and provide an overview of directions that future work could take in order to build on the work of this thesis and develop further understanding of the U-O-H system.

10 Conclusions and Future Work

The conclusions of the individual results chapter are summarised here, along with proposed routes for expanding and furthering this research.

10.1 DFT Model of Hydrogen in UO_2

Chapters 3 and 4 explored the suitability of a range of functionals to firstly model UO_2, due to the wide range of available experimental data to validate the model. Secondly these functionals were also used to explore hydrogen defects in UO_2. While there is not the same quantity of experimental evidence of hydrogen defects in UO_2, as there is for UO_2, by using the range of functionals this acted as a self validation to determine the sensitivity of the results to the functional chosen.

The necessity of SOC was also considered for both UO_2 and hydrogen defects. For the pure UO_2 system the inclusion of SOC gave a better representation of the magnetic moment of the uranium ions over the spin only formalism when compared to the experimental value. Additionally, the tetragonal distortion introduced by the simplified $1k$ AFM CL ordering used was removed. This distortion is a well documented and understood consequence of the simplified approach to simulating UO_2. Fortunately, the effect is minimal and does not affect the predicted properties or energies significantly, *i.e.* within 2 $kJmol^{-1}$.

Qualitatively, the functionals were all consistent with each other predicting the same order of stability and same type of hydrogen defects, with the occasional exception. The functionals also agreed well when SOC was included in the calculations, again showing qualitative agreement with each other. The agreement between the spin only and SOC formalisms agreed well and predicted the same order and type of defects to occur, however, while the relative energy of monatomic defects did not require the inclusion of SOC to make a comparison, for H_2 there was a large difference in the relative energy when compared to monatomic defects with the spin only and SOC formalisms. The exact reason for this is currently unknown, but appears to be related to the presence of a H-H bond. Further work is need to explore why this energy is so different and a potential route is to consider the weak van der Waals interactions. This can be achieved with a variety of correction functionals such as D3, opt-86 and opt-88.

Overall, the most efficient functional balancing reliability and CPU time, to simulate both UO_2 and hydrogen defects on UO_2 is currently PBE+U.

10.2 Hydrogen Defects in $UO_{2\pm x}$

The next investigation was to evaluate how the oxygen stoichiometry affected the structural stability of hydrogen defects. A range of hydrogen defects were explored in UO_2 containing a single oxygen vacancy or interstitial, generating three stoichiometries; hypo- ($UO_{1.97}$), hyper- $UO_{2.03}$ and stoichiometric UO_2. Hypostoichiometric UO_2 preferentially formed hydride defects occupying the vacancy site. Even H_2 when placed on the vacancy site dissociated into two hydride defects bridging the vacancy site. For hyperstoichiometric UO_2 protonic defects (hydroxyl) are the preferred species, again where the hydrogen interacts with the defect site, in this case the interstitial oxygen atom.

Stoichiometric UO_2 is the crossover between the hydride and protonic (hydroxyl) preference, in UO_2 both hydride and hydroxyl defects form with only a small energy difference between them (0.2 eV). This slightly favours the hydride due to the compensating uranium defect, U^{5+} versus the U^{3+} which forms with the hydroxyl. U^{3+} is known to be unfavourable in UO_2 matrices from oxygen defects. It is also possible that for stoichiometric UO_2, the H_2 molecule is overall the preferred hydrogen defect as this does not alter the uranium sub-lattice's oxidation state. This needs further work because as mentioned previously there was a discrepancy in the relative energy between spin only and SOC calculations, when comparing H_2 with a hydride or hydroxyl defect, which still needs resolving.

As UO_2 is also highly symmetric it was possible to build a simple model of hydrogen behaviour based on the O-H distance as this appears to be the major factor in determining the hydrogen defect state. When the O-H distance is less that $\approx$1.2 Å a hydroxyl defect forms, between $\approx$1.2 Å and $\approx$2.0 Å a radical defect forms and above $\approx$2.0 Å a hydride defect occurs. Further exploration of the hydrogen landscape in $UO_{1.97}$ and $UO_{2.03}$ would also allow for similar models to be built for the region around the defect.

10.3 Hydrogen Transport in UO_2

Another important property to be investigated was how hydrogen moves through the lattice and whether it moves as monatomic or molecular hydrogen. To simplify the problem only stoichiometric UO_2 was considered.

For monatomic hydrogen a range of different pathways were investigated. The lowest energy pathway, of those considered, was via the conversion of a hydride defect to a hydroxyl defect. This was accompanied by the corresponding conversion of a U^{5+} to U^{3+}. The barrier to this diffusion pathway was $\approx$1 eV.

In contrast, the nudged elastic band calculations for molecular hydrogen showed that there was a large energy barrier to diffusion $\approx$2.4 eV. Equally, while the H-H bond was predicted to elongate it did not break. The energy landscape for hydrogen transport appears to be relatively flat, until the H_2 approaches the edge of the oxygen sub-lattice. This is where the energy dramatically increases, the cause of this increase in the energy is due to the partial dissociation of the H-H bond and the two oxygen atoms on the corner of the oxygen sub-lattice being pushed away from their lattice positions. This gives rise to the possibility that molecular hydrogen defects could be a trapped defect species within UO_2 and it is monatomic species

which diffuse through UO_2.

The calculations to explore hydrogen transport in UO_2, whether minimisations or NEB calculations, neglect temperature. One extension to further this research would be to apply *ab initio* molecular dynamics (AIMD), though the major drawback of this approach is requiring electronic convergence at each time step. The resulting vast computational expense is the reason that it was not attempted here. A further expansion would be to consider *ab initio* path integral molecular dynamics to allow for the hydrogen nucleus to be treated as a quantum rather than classical particle and thus make an assessment of how significant tunnelling is for hydrogen diffusion in UO_2.

10.4 Uranium Hydride

In addition to exploring hydrogen defects in UO_2, uranium hydride was also considered as it is one of the key undesirable phases which can form in long term storage of spent nuclear fuel. The suitability of the PBE+U methodology, that was developed for UO_2, was assessed to determine how appropriate it was to simulate UH_3. The PBE+U was found to be suitable to simulate the properties of UH_3, while the inclusion of the Hubbard coefficient resulted in suppression of the states in the DOS, as would be expected, importantly the metallic nature of the hydride was retained. There was also a small expansion of the lattice parameters similar to that observed with UO_2.

Experimentally, both of the symmetrically inequivalent uranium sites in βUH_3 are magnetically equivalent. Stoichiometric β-UH_3 was predicted to have a magnetic difference between the two uranium sites, whereas hypo-stoichiometric UH_3 ($UH_{2.88}$) was found to have comparable magnetic values for all uranium sites. $UH_{2.88}$ was also found to be energetically favourable compared with UH_3 again further supporting the possibility of hydrogen vacancies being part of UH_3. This result does contrast with the available experimental data showing that there is an energy cost to form hydrogen vacancies in UH_3, this can potentially be explained by the significant difference in the stoichiometry of the experimental and simulated configurations. In order to fully explore this larger hydride systems containing hydrogen defects need to be explored, however, these larger systems are computationally very expensive to compute. For example a 2x2x2 expansion of the β-UH_3 unit cell contains more electrons from uranium atoms as the total number of electrons in a 2x2x2 expansion of the oxide unit cell. The PBE and PBE+U functionals did give different results, showing that there is a need to focus more attention on the functional and value of the Hubbard coefficient (if included at all) to accurately simulate UH_3. This will also become a balancing act with maintaining a functional which can accurately simulate the oxides of uranium if a comparison between phases or hydride/oxide interfaces are to be modelled.

In addition to the hydrogen defects the systematic conversion of the hydride into the oxide was investigated. In order to minimise the number of calculations required, the Madelung energies of all hydride sites was calculated and used to identify the unique hydride sites for substituting an oxygen atom. Each of these configurations was then minimised using DFT and the process repeated on the energetically most stable result from the DFT calculations.

These calculations showed that the oxidation of UH_3 is very favourable, with

large negative formation energies, in line with UH_3 being pyrophoric. The favourable energies is further evidence that the 3+ oxidation state is unfavourable. The electronic DOS also showed a rapid conversion from the metallic hydride DOS to a spectrum which resembled that of a hydroxyl defect in UO_2. The growth of the U f-states at the top of the valence and bottom of the conduction band was observed, with the U^{3+} f-states occupying the gap in between. The likely further evolution of the DOS spectrum would be a continued decrease in the U^{3+} f-states peak and continued growth of the U^{4+} f-states.

This work could provide the basis of exploring the oxidation of UH_3 in more detail and to complete oxidation. As this used a static approach and the oxidation is a violent exothermic reaction it would also be worth considering AIMD to investigate the structural changes into the oxide lattice.

10.5 Thermodynamic Model

Finally, the work presented in this thesis and the previous work of Brincat [187] was used to build a thermodynamic model of UO_2 under varying hydrogen and oxygen partial pressures. This allows for the most stable defect states to be identified and visualised as a function of excess hydrogen and oxygen concentrations. The inclusion of Brincat's work also allowed for the higher uranium oxides to be added into the model to give a more complete picture of the whole U-O-H system.

This model is only the basis or building a more complete picture of the U-O-H system. To improve this model there a several avenues available, firstly the completion of the exploration of hydrogen defects in oxygen defect clusters, particularly the larger clusters. Hydrogen defects could also be added to the higher uranium oxides and defects within the higher uranium oxides, though this is perhaps the least important avenue to explore as there is still much more that needs to be developed from understating the base oxide, *e.g.* U_2O_5, before another variable is added into the mix. Finally, vibrational analysis could be completed on all the structures included in the model, this would achieve three important outcomes; the stability of the defects and phases would be known, it would be possible to produce both IR and Raman spectra for the defects as a library to help interpret experimental results and most importantly for the thermodynamic model it would facilitate the inclusion of temperature.

Overall, the work in this thesis has shown that DFT can give valuable insights into the nature of hydrogen defects in uranium matrices. However, what is also abundantly clear is this is an area of research which still has many unanswered questions. For example, it is clear that there is a strong concentration dependence. In our case the largest super cell available to us was considered for this work, clearly considering larger supercells or QM/MM approaches would represent valuable future directions. This means that research into UO_2 and other actinides will remain an interesting and active field for many years.

References

[1] O. Hahn and F. Strassmann, "Proof of the Formation of Active Isotopes of Barium from Uranium and Thorium Irradiated with Neutrons; Proof of the Existence of More Active Fragments Produced by Uranium Fission," *Journal of Chemical Education*, vol. 66, pp. 362–363, 1989.

[2] World Nuclear Association, "Outline History of Nuclear Energy," 2014. http://www.world-nuclear.org/information-library/current-and-future-generation/outline-history-of-nuclear-energy.aspx, Accessed on 16/05/2016.

[3] J. R. Matthews, "Technological Problems and the Future of Research on the Basic Properties of Actinide Oxides," *Journal of the Chemical Society - Faraday Transactions II*, vol. 83, pp. 1273–1285, 1987.

[4] R. W. Grimes and W. J. Nuttall, "Generating the Option of a Two-Stage Nuclear Renaissance," *Science*, vol. 329, pp. 799–803, 2010.

[5] BBC News, "Germany stages anti-nuclear marches after Fukushima," 2011. http://www.bbc.co.uk/news/world-europe-12872339, Accessed on 16/05/2016.

[6] BBC News, "Germany: Nuclear power plants to close by 2022," 2011. http://www.bbc.co.uk/news/world-europe-13592208, Accessed on 16/05/2016.

[7] World Nuclear Association, "Nuclear Power in the World Today," 2016. http://www.world-nuclear.org/information-library/current-and-future-generation/nuclear-power-in-the-world-today.aspx, Accessed on 17/05/2016.

[8] H. Hernandez, "Nuclear Reactor Power Characterization and Simulation Tools," 2016. http://www.nuclear.utah.edu/wp-content/themes/nuclear-express-theme/uploads/INPO_AdditonalInfo.pdf, Accessed on 17/05/2016.

[9] World Nuclear Association, "Generation IV Nuclear Reactors," 2015. http://www.world-nuclear.org/information-library/nuclear-fuel-cycle/nuclear-power-reactors/generation-iv-nuclear-reactors.aspx, Accessed on 17/05/2016.

[10] World Nuclear Association, "Nuclear Power Reactors," 2016. http://www.world-nuclear.org/information-library/nuclear-fuel-cycle/nuclear-power-reactors/nuclear-power-reactors.aspx, Accessed on 17/05/2016.

[11] World Nuclear Association, "Physics of Uranium and Nuclear Energy," 2016. http://www.world-nuclear.org/information-library/nuclear-fuel-cycle/introduction/physics-of-nuclear-energy.aspx, Accessed on 01/08/2017.

[12] World Nuclear Association, "Fast Neutron Reactors," 2016. http://www.world-nuclear.org/information-library/current-and-future-generation/fast-neutron-reactors.aspx, Accessed on 19/05/2016.

[13] World Nuclear Association, "Uranium Enrichment," 2016. http://www.world-nuclear.org/information-library/nuclear-fuel-cycle/conversion-enrichment-and-fabrication/uranium-enrichment.aspx, Accessed on 19/05/2016.

[14] World Nuclear Association, "Fast Neutron Reactors," 2016. http://www.world-nuclear.org/information-library/current-and-future-generation/fast-neutron-reactors.aspx, Accessed on 23/05/2016.

[15] World Nuclear Association, "The Nuclear Fuel Cycle," 2016. http://www.world-nuclear.org/information-library/nuclear-fuel-cycle/introduction/nuclear-fuel-cycle-overview.aspx, Accessed on 20/03/2016.

[16] World Nuclear Association, "Nuclear Fuel Fabrication," 2016. http://www.world-nuclear.org/information-library/nuclear-fuel-cycle/conversion-enrichment-and-fabrication/fuel-fabrication.aspx, Accessed on 23/05/2016.

[17] I. Kapshukov, N. Lyalyshkin, L. Sudakov, A. Bevz, and O. Skiba, "Preparation of Hypostoichiometric UO_{2-x} at Low Temperatures and Study of some Properties," *Journal of Radioanalytical and Nuclear Chemistry*, vol. 143, pp. 213–220, 1990.

[18] N. Brincat, S. C. Parker, M. Molinari, G. C. Allen, and M. Storr, "*Ab initio* Investigation of the UO_3 Polymorphs: Structural Properties and Thermodynamic Stability," *Inorganic Chemistry*, vol. 53, pp. 12253–12264, 2014.

[19] H. Hoekstra, S. Siegel, and F. Gallagher, "The Uranium-Oxygen System at High Pressure," *Journal of Inorganic & Nuclear Chemistry*, vol. 32, pp. 3237–3248, 1970.

[20] G. C. Allen and N. Holmes, "A Mechanism for the UO_2 to Alpha-U_3O_8 Phase Transition," *Journal of Nuclear Materials*, vol. 223, pp. 231–237, 1995.

[21] N. Brincat, M. Molinari, S. C. Parker, G. C. Allen, and M. Storr, "Computer Simulation of Defect Clusters in UO_2 and their Dependence on Composition," *Journal of Nuclear Materials*, vol. 456, pp. 329–333, 2015.

[22] N. Brincat, S. C. Parker, M. Molinari, G. C. Allen, and M. Storr, "Density Functional Theory Investigation of the Layered Uranium Oxides U_3O_8 and U_2O_5," *Dalton Transactions*, vol. 44, pp. 2613–2622, 2015.

[23] N. Brincat, M. Molinari, G. C. Allen, M. Storr, and S. C. Parker, "Density Functional Theory Calculations of Defective UO_2 at U_3O_7 Stoichiometry," *Journal of Nuclear Materials*, vol. 467, pp. 724–729, 2015.

[24] D. A. Andersson, T. Watanabe, C. Deo, and B. P. Uberuaga, "Role of Di-interstitial Clusters in Oxygen Transport in UO_{2+x} from First Principles," *Physical Review B*, vol. 80, p. 060101(R), 2009.

[25] D. A. Andersson, J. Lezama, B. P. Uberuaga, C. Deo, and S. D. Conradson, "Cooperativity Among Defect Sites in AO_{2+x} and A_4O_9 (A=U,Np,Pu): Density Functional Calculations," *Physical Review B*, vol. 79, pp. 024110–1, 2009.

[26] D. A. Andersson, F. Espinosa-Faller, B. P. Uberuaga, and S. D. Conradson, "Stability and Migration of Large Oxygen Clusters in UO_{2+x}: Density Functional Theory Calculations," *The Journal of Chemical Physics*, vol. 136, p. 234702, 2012.

[27] B. Dorado, M. Freyss, and G. Martin, "GGA+U Study of the Incorporation of Iodine in Uranium Dioxide," *European Physical Journal B*, vol. 69, pp. 209–209, 2009.

[28] B. Dorado, B. Amadon, M. Freyss, and M. Bertolus, "DFT+U Calculations of the Ground State and Metastable States of Uranium Dioxide," *Physical Review B*, vol. 69, p. 235125, 2009.

[29] B. Dorado, G. Jomard, M. Freyss, and M. Bertolus, "Stability of Oxygen Point Defects in UO_2 by First-principles DFT+U Calculations: Occupation Matrix Control and Jahn-Teller Distortion," *Physical Review B*, vol. 82, pp. 035114–1, 2010.

[30] B. Dorado and P. Garcia, "First-principles DFT plus U Modelling of Actinide-based Alloys: Application to Paramagnetic Phases of UO_2 and (U,Pu) Mixed Oxides," *Physical Review B*, vol. 87, 2013.

[31] G. Allen and P. Tempest, "Linear Ordering of Oxygen Clusters in Hyperstoichiometric Uranium Dioxide," *Journal of the Chemical Society - Dalton Transactions*, p. 2169, 1982.

[32] U. Benedict, G. D. Andreetti, J. M. Fournier, and A. Waintal, "X-ray Powder Diffraction Study of the High Pressure Behaviour of Uranium Dioxide," *Journal de Physique - Letters*, vol. 43, pp. L–171, 1982.

[33] D. J. M. Bevan, O. Greis, and J. Strähle, "A New Structural Principle in Anion-excess Fluorite-related Superlattices," *Acta Crystallographica Section A*, vol. 36, pp. 889–890, 1980.

[34] D. J. M. Bevan, I. E. Grey, and B. T. M. Willis, "The Crystal-Structure of Beta-U_4O_{9-y}," *Journal of Solid State Chemistry*, vol. 61, pp. 1–7, 1986.

[35] O. G. Brandt and C. T. Walker, "Temperature Dependence of Elastic Constants and Thermal Expansion for UO_2," *Physical Review Letters*, vol. 18, pp. 11–13, 1967.

[36] L. Desgranges, G. Baldinozzi, G. Rousseau, J. C. Niepce, and G. Calvarin, "Neutron Diffraction Study of the in Situ Oxidation of UO_2," *Inorganic Chemistry*, vol. 48, pp. 7585–7592, 2009.

[37] L. Desgranges, Y. Ma, P. Garcia, G. Baldinozzi, D. Simeone, and H. E. Fischer, "What Is the Actual Local Crystalline Structure of Uranium Dioxide, UO_2? A New Perspective for the Most Used Nuclear Fuel," *Inorganic Chemistry*, vol. 56, pp. 321–326, 2016.

[38] A. Banos and T. Scott, "Statistical Analysis of UH_3 Initiation Using Electron Back-scattered Diffraction (EBSD)," *Solid State Ionics*, vol. 296, pp. 137–145, 2016.

[39] J. Glascott, "A Model for the Initiation of Reaction Sites During the Uranium-Hydrogen Reaction Assuming Enhanced Hydrogen Transport Through Thin Areas of Surface Oxide," *Philosophical Magazine*, vol. 94, pp. 221–241, 2014.

[40] J. Glascott, "A Model for the Initiation of Reaction Sites During the Uranium-Hydrogen Reaction Assuming Enhanced Hydrogen Transport Through Linear Oxide Discontinuities," *Philosophical Magazine*, vol. 94, pp. 1393 – 1413, 2014.

[41] R. M. Harker, "The Influence of Oxide Thickness on the Early Stages of the Massive Uranium–Hydrogen Reaction," *Journal of Alloys and Compounds*, vol. 426, pp. 106–117, 2006.

[42] V. Wheeler, "The Diffusion and Solubility of Hydrogen in Uranium Dioxide Single Crystals," *Journal of Nuclear Materials*, vol. 40, pp. 189 – 194, 1971.

[43] D. Olander, D. Sherman, and M. Balooch, "Retention and Release of Water by Sintered Uranium Dioxide," *Journal of Nuclear Materials*, vol. 107, pp. 31–45, 1982.

[44] D. Sherman and D. Olander, "Hydrogen Dissolution in and Release from Non-metals I. Uranium Dioxide," *Journal of Nuclear Materials*, vol. 166, pp. 307–320, 1989.

[45] B. T. M. Willis, "Positions of the Oxygen Atoms in $UO_{2.13}$," *Nature*, vol. 197, pp. 755–756, 1963.

[46] B. T. M. Willis, "Structures of UO_2, UO_{2+x} and U_4O_9 by Neutron Diffraction," *Journal De Physique*, vol. 25, pp. 431–441, 1964.

[47] B. T. M. Willis, "Defect Structure of Hyper-Stoichiometric Uranium-Dioxide," *Acta Crystallographica Section A*, vol. 34, pp. 88–90, 1978.

[48] K. Govers, S. Lemehov, M. Hou, and M. Verwerft, "Comparison of Interatomic Potentials for UO_2. Part I: Static Calculations," *Journal of Nuclear Materials*, vol. 366, pp. 161–177, 2007.

[49] H. Y. Geng, Y. Chen, and Y. Kaneta, "*Ab initio* Investigation on Oxygen Defect Clusters in UO_{2+x}," *Applied Physics Letters*, vol. 93, p. 201903, 2008.

[50] D. A. Andersson, G. Baldinozzi, L. Desgranges, D. Conradson, and S. D. Conradson, "Density Functional Theory Calculations of UO_2 Oxidation: Evolution of UO_{2+x}, U_4O_{9-y}, U_3O_7, and U_3O_8," *Inorganic Chemistry*, vol. 52, pp. 2769–2778, 2013.

[51] G. Rousseau, L. Desgranges, F. Charlot, N. Millot, J. Niepce, M. Pijolat, F. Valdivieso, G. Baldinozzi, and J. Berar, "A Detailed Study of UO_2 to U_3O_8 Oxidation Phases and the Associated Rate-limiting Steps," *Journal of Nuclear Materials*, vol. 355, pp. 10–20, 2006.

[52] Y. A. Teterin, "The Structure of the X-ray Photoelectron Spectra of Light Actinide Compounds," *Russian Chemical Reviews*, vol. 73, pp. 541–580, 2004.

[53] W. R. Cornman, "Preparation and Characterisation of the Polymorphs of UO_3," tech. rep., Savannah River National Laboratory, 1962. TID-4500.

[54] B. S. Girgis and N. H. Rofail, "Reactivity of Various UO_3 Modifications in the Fluorination to UF_4 by FREON-12," *Journal of Nuclear Materials*, vol. 195, pp. 126–133, 1992.

[55] J. A. Johnson, *Studies of Reaction Processes for Voloxidation Methods*. PhD thesis, University of Tennessee, 2013.

[56] L. Kovba, N. I. Komarevtseva, and E. Kuz'mitcheva, "On the Crystal Structures of $U_{13}O_{34}$ and delta-U_2O_5," *Radiokhimiya*, vol. 21, pp. 754–757, 1979.

[57] B. O. Loopstra, "Neutron Diffraction Investigation of U_3O_8," *Acta Crystallographica*, vol. 17, p. 651, 1964.

[58] A. Andresen, "The Structure of U_3O_8 Determined by Neutron Diffraction," *Acta Crystallography and Crystal Chemistry*, vol. 11, pp. 621–614, 1958.

[59] B. O. Loopstra, "Structure of beta-U_3O_8," *Acta Crystallographica Section B-Structural Crystallography and Crystal Chemistry*, vol. B 26, p. 656, 1970.

[60] B. Chodura and J. Maly, "A Contribution to the Solution of the Structure of U_3O_8," *Journal of Inorganic & Nuclear Chemistry*, vol. 7, pp. 177–178, 1958.

[61] W. H. Zacharisen, "Crystal Chemical Studies of the 5F-Series of Elements 1. New Structure Types," *Acta Crystallographica*, vol. 1, pp. 265–269, 1948.

[62] B. O. Loopstra and E. Cordfunk, "On Structure of Alpha-UO_3," *Recueil Des Travaux Chimiques Des Pays-Bas*, vol. 85, p. 135, 1966.

[63] C. Greaves and B. E. F. Fender, "Structure of Alpha-UO_3 by Neutron and Electron-Diffraction," *Acta Crystallographica Section B-Structural Science*, vol. 28, pp. 3609–3614, 1972.

[64] P. C. Debets, "Structure of Beta-UO_3," *Acta Crystallographica*, vol. 21, p. 589, 1966.

[65] B. O. Loopstra, J. Taylor, and A. B. Waugh, "Neutron powder diffraction studies gamma-uranium trioxide phases," *Journal of Solid State Chemistry*, vol. 20, pp. 9–19, 1977.

[66] M. T. Weller, P. G. Dickens, and D. J. Penny, "The Structure of Delta-UO_3," *Polyhedron*, vol. 7, pp. 243–244, 1988.

[67] S. Siegel, H. Hoekstra, and E. Sherry, "Crystal Structure of High-Pressure UO_3," *Acta Crystallographica*, vol. 20, p. 292, 1966.

[68] L. Kovba, L. M. Vidavskii, and E. G. Lavut, "Study of ϵ-UO_3," *Zhumal Strukturnoi Khimii*, vol. 2, p. 4, 1963.

[69] H. R. Hoekstra, S. Siegel, L. H. Fuchs, and J. J. Katz, "The Uranium-Oxygen System: $UO_{2.5}$ to U_3O_8," *Journal of Physical Chemistry*, vol. 59, pp. 136–138, 1955.

[70] J. Pireaux, J. Riga, E. Thibaut, C. Tenret-Noël, R. Caudano, and J. Verbist, "Shake-up Satellites in the X-ray Photoelectron Spectra of Uranium Oxides and Fluorides. A Band Structure Scheme for Uranium Dioxide, UO_2," *Chemical Physics*, vol. 22, pp. 113–120, 1977.

[71] X.-D. Wen, R. L. Martin, G. E. Scuseria, S. P. Rudin, E. R. Batista, and A. K. Burrell, "Screened Hybrid and DFT+U Studies of the Structural, Electronic and Optical Properties of U_3O_8," *Journal of Physics: Condensed Matter*, vol. 25, p. 025501, 2013.

[72] G. Leinders, R. Delville, J. Pakarinen, T. Cardinaels, K. Binnemans, and M. Verwerft, "Assessment of the U_3O_7 Crystal Structure by X-ray and Electron Diffraction," *Inorganic Chemistry*, vol. 55, pp. 9923–9936, 2016.

[73] H. R. Hoekstra and S. Siegel, "The Uranium-Oxygen System - U_3O_8-UO_3," *Journal of Inorganic & Nuclear Chemistry*, vol. 18, pp. 154–165, 1961.

[74] E. H. P. Cordfunke and P. Aling, "System UO_3 + U_3O_8: Dissociation Pressure of gamma-UO_3," *Transactions of the Faraday Society*, vol. 61, pp. 50–53, 1965.

[75] B. O. Loopstra, "Phase Transition in Alpha-U_3O_8 at 210 Degrees C," *Journal of Applied Crystallography*, vol. 3, pp. 94-&, 1970.

[76] G. C. Allen, J. A. Crofts, M. T. Curtis, P. M. Tucker, D. Chadwick, and P. J. Hampson, "X-Ray Photoelectron Spectroscopy of Some Uranium Oxide Phases," *Journal of the Chemical Society: Dalton Transactions*, vol. 12, pp. 1296–1301, 1974.

[77] B. O. Loopstra, "Crystal Structure of Alpha-U_3O_8," *Journal of Inorganic & Nuclear Chemistry*, vol. 39, pp. 1713–1714, 1977.

[78] G. Allen and A. J. Griffiths, "Electron Spin Resonance Spectra of Mixed Oxides Containing Uranium and Alkaline Earth Metals," *Chemical Physics Letters*, vol. 53, p. 309, 1977.

[79] A. Caneiro and J. Abriata, "Equilibrium Oxygen Partial Pressure and Phase Diagram of the Uranium-Oxygen System in the Composition Range 2.61 <O/U< 2.67 Between 844 and 1371 K," *Journal of Nuclear Materials*, vol. 126, pp. 255–267, 1984.

[80] G. C. Allen, I. S. Butler, and N. A. Tuan, "Characterisation of Uranium Oxides by Micro-Raman Spectroscopy," *Journal of Nuclear Materials*, vol. 144, pp. 17–19, 1987.

[81] C. Pallai, A. Dua, and P.Raj, "Thermal Conductivity of U_3O_8 from 300 to 1100 K," *Journal of Nuclear Materials*, vol. 288, pp. 87–91, 2001.

[82] T. Vitova, K. O. Kvashnina, G. Nocton, G. Sukharina, M. A. Denecke, S. M. Butorin, M. Mazzanti, R. Caciuffo, A. Soldatov, T. Behrends, and H. Geckeis, "High Energy Resolution X-ray Absorption Spectroscopy Study of Uranium in Varying Valence States," *Physical Review B*, vol. 82, p. 235118, 2010.

[83] A. Y. Teterin, M. V. Ryzhkov, Y. A. Teterin, K. I. Maslakov, T. Reich, and S. L. Molodtsov, "Resonant Emission of UO_2, U_3O_8 and UO_{2+x} Valence Electrons Under Sr Excitation Near the $O_{4,5}$(U) Absorption Edge," *Journal of Structural Chemistry*, vol. 52, pp. 295–303, 2011.

[84] K. Kvashnina, S. Butorin, P. Martin, and P. Glatzel, "Chemical State of Complex Uranium Oxides," *Physical Review Letters*, vol. 111, pp. 253002–1, 2013.

[85] H. He, D. A. Andersson, D. D. Allred, and K. D. Rector, "Determination of the Insulation Gap of Uranium Oxides by Spectroscopic Ellipsometry and Density Functional Theory," *The Journal of Physical Chemistry C*, vol. 117, pp. 16540–16551, 2013.

[86] R. G. J. Ball and R. W. Grimes, "Diffusion of xe in uo2," *Journal of the Chemical Society-Faraday Transactions*, vol. 86, no. 8, pp. 1257–1261, 1990. Times Cited: 24.

[87] R. G. J. Ball and P. G. Dickens, "Calculation of Structural and Defect Properties of alpha-U_3O_8," *Journal of Materials Chemistry*, vol. 1, pp. 105–112, 1991.

[88] H. Y. Geng, H. X. Song, K. Jin, S. K. Xiang, and Q. Wu, "First-Principles Study on Oxidation Effects in Uranium Oxides and High-Pressure High-Temperature Behaviour of Point Defects in Uranium Dioxide," *Physical Review B*, vol. 84, p. 174115, 2011.

[89] Y. Yun, J. Rusz, M. T. Suzuki, and P. M. Oppeneer, "First-principles Investigation of Higher Oxides of Uranium and Neptunium: U_3O_8 and Np_2O_5," *Physical Review B*, vol. 83, 2011.

[90] G. C. Allen and N. R. Holmes, "Mixed-Valency Behaviour in some Uranium-Oxides Studies by X-ray Photoelectron-Spectroscopy," *Canadian Journal of Applied Spectroscopy*, vol. 38, pp. 124–130, 1993.

[91] R. G. J. Ball and P. G. Dickens, "Computer-Simulation Study of Alkali-Metal Insertion into Alpha-U_3O_8," *Journal of Materials Chemistry*, vol. 1, pp. 415–421, 1991.

[92] B. L. Scott, J. J. Joycea, T. D. Durakiewicz, R. L. Martin, T. M. McCleskey, E. Bauer, H. Luo, and Q. Jia, "High Quality Epitaxial Thin Films of Actinide Oxides, Carbides and Nitrides: Advancing Understanding of Electronic Structure of f-element Materials," *Coordination Chemistry Reviews*, vol. 266-267, pp. 137–154, 2014.

[93] L. E. Sweet, T. A. Blake, J. Henager, Charles H., S. Hu, T. J. Johnson, D. E. Meier, S. M. Peper, and J. M. Schwantes, "Investigation of the Polymorphs and Hydrolysis of Uranium Trioxide," *Journal of Radioanalytical and Nuclear Chemistry*, vol. 296, pp. 105–110, 2013.

[94] V. Wheeler, R. Dell, and E. Wait, "Uranium Trioxide and the UO_3 Hydrates," *Journal of Inorganic & Nuclear Chemistry*, vol. 26, pp. 1829 – 1845, 1964.

[95] E. H. P. Cordfunke and P. C. Debets, "Preparation and Properties of a New Uranium Trioxide Epsilon-$UO_3.H_2O$," *Journal of Inorganic & Nuclear Chemistry*, vol. 26, p. 1671, 1964.

[96] C. Colmeares, "The Oxidation of Thorium, Uranium and Plutonium," *Progress in Solid State Chemistry*, vol. 9, p. 317, 1975.

[97] P. Bagus and E. Ilton, "Theory for the XPS of Actinides," *Topics in Catalysis*, vol. 56, pp. 1121–1128, 2013.

[98] P. Bagus, C. Nelin, and E. Ilton, "Theoretical Modelling of the Uranium $4f$ XPS for U(VI) and U(IV) Oxides," *Journal of Chemical Physics*, vol. 139, p. 244704, 2013.

[99] R. Guillaumont, T. Fanghael, J. Fuger, I. Grenthe, V. Neck, D. Palmer, and M. Rand, *Update on the Chemical Thermodynamics of Uranium, Neptunium, Plutonium, Americium and Technetium.* Amsterdam: Elsevier, 2003.

[100] H. Chen and M. S. Islam, "Lithium Extraction Mechanism in Li-Rich Li_2MnO_3 Involving Oxygen Hole Formation and Dimerization," *Chemistry of Materials*, vol. 28, pp. 6656–6663, 2016.

[101] M. Molinari, S. C. Parker, D. C. Sayle, and M. S. Islam, "Water Adsorption and Its Effect on the Stability of Low Index Stoichiometric and Reduced Surfaces of Ceria," *Journal of Physical Chemistry C*, vol. 116, no. 12, pp. 7073–7082, 2012.

[102] J. K. Cooper, S. B. Scott, Y. Ling, J. Yang, S. Hao, Y. Li, F. M. Toma, M. Stutzmann, K. V. Lakshmi, and I. D. Sharp, "Role of Hydrogen in Defining the n-Type Character of $BiVO_4$ Photoanodes," *Chemistry of Materials*, vol. 28, pp. 5761–5771, 2016.

[103] D. A. Tompsett, S. C. Parker, and M. S. Islam, "Rutile (β-)MnO_2 Surfaces and Vacancy Formation for High Electrochemical and Catalytic Performance," *Journal of the American Chemical Society*, vol. 136, pp. 1418–1426, 2014.

[104] M. Lahmer, "Hydrogen Sensing Properties of the ZnO(0 0 0 $\bar{1}$) Surface Enhanced by Be Doping: A First Principles Study," *Sensors and Actuators B: Chemical*, vol. 221, pp. 906–913, 2015.

[105] M.E. Ivanova, S. Escolástico, M. Balaguer, J. Palisaitis, Y. Sohn, W.A. Meulenberg, O. Guillon, J. Mayer, and J.M. Serra, "Hydrogen Separation Through Tailored Dual Phase Membranes with Nominal Composition $BaCe_{0.8}Eu_{0.2}O_{3-\delta}$:$Ce_{0.8}Y_{0.2}O_{2-\delta}$ at Intermediate Temperatures," *Scientific Reports*, vol. 6, p. 34773, 2016.

[106] S. Escolastico, S. Somacescu, and J. Serra, "Solid State Transport and Hydrogen Permeation in the System $Nd_{5.5}W_{1-x}Re_xO_{11.25-\delta}$," *Chemistry of Materials*, vol. 26, pp. 982–992, 2013.

[107] F. Jun, D. Min, J. Fanya, C. Meiyan, S. Liru, T. Honghui, and Z. Guikai, "Preparation and Properties of Alumina Coatings as Tritium Permeation Barrier by Plasma Electrolytic Oxidation," *Rare Metal Materials and Engineering*, vol. 45, pp. 315–320, 2016.

[108] B. Singh, S. Ghosh, S. Aich, and B. Roy, "Low Temperature Solid Oxide Electrolytes (LT-SOE): A Review," *Journal of Power Sources*, vol. 339, pp. 103–135, 2017.

[109] T. M. Nenoff, B. W. Jacobs, D. B. Robinson, P. P. Provencio, J. Huang, S. Ferreira, and D. J. Hanson, "Synthesis and Low Temperature In Situ Sintering of Uranium Oxide Nanoparticles," *Chemistry of Materials*, vol. 23, pp. 5185–5190, 2011.

[110] T. Norby, M. Wideroe, R. Glockner, and Y. Larring, "Hydrogen in Oxides," *Dalton Transactions*, pp. 3012–3018, 2004.

[111] E. Serra, G. Benamati, and O. Ogorodnikova, "Hydrogen Isotopes Transport Parameters in Fusion Reactor Materials," *Journal of Nuclear Materials*, vol. 255, pp. 105–115, 1998.

[112] Y. Nissan-Cohen and T. Gorczyca, "The Effect of Hydrogen on Trap Generation, Positive Charge Trapping, and Time-Dependent Dielectric Breakdown of Gate Oxides," *IEEE ELECTRON DEVICE LETTERS*, vol. 9, p. 287, 1988.

[113] F. L. Guyadec, X. Génin, J. Bayle, O. Dugne, A. Duhart-Barone, and C. Ablitzer, "Pyrophoric Behaviour of Uranium Hydride and Uranium Powders," *Journal of Nuclear Materials*, vol. 396, pp. 294–302, 2010.

[114] C. Stitt, N. Harker, K. Hallam, C. Paraskevoulakpos, A. Banos, S. Rennie, J. Jowset, and T. Scott, "An Investigation of the Persistance of Uranium Hydride During Storage of Simulant Nuclear Waste Packages," *PLOS ONE*, vol. 10, pp. 1–13, 2015.

[115] M. Garcia-Melchor and N. Lopez, "Homolytic Products from Heterolytic Paths in H Dissociation on Metal Oxides: The Example of CeO_2," *Journal of Physical Chemistry C*, vol. 118, pp. 10921–10926, 2014.

[116] E. Gribov, S. Bertarione, D. Scarano, C. Lamberti, G. Spoto, and A. Zecchina, "Vibrational and Thermodynamic Properties of H_2 Adsorbed on MgO in the 300-20 K Interval," *Journal of Physical Chemistry B*, vol. 108, pp. 16174–16186, 2004.

[117] H.-Y. T. Chen, L. Giordano, and G. Pacchioni, "From Heterolytic to Homolytic H_2 Dissociation on Nanostructured MgO(001) Films As a Function of the Metal Support," *Journal of Physical Chemistry C*, vol. 117, pp. 10623–10629, 2013.

[118] J. Joubert, A. Salmeh, V. Krakoviack, F. Delbecq, P. Sautet, C. Coperet, and J. Basset, "Heterolytic Splitting of H_2 and CH_4 on γ-Alumina as a Structural Probe for Defect Sites," *Journal of Physical chemistry B*, vol. 110, pp. 23944–23950, 2006.

[119] M. Menetrey, A. Markovits, and C. Minot, "Reactivity of a Reduced Metal Oxide Surface: Hydrogen, Water and Carbon Monoxide Adsorption on Oxygen Defective Rutile TiO_2(110)," *Surface Science*, vol. 524, pp. 49–62, 2003.

[120] C. Binet, M. Daturi, and J.-C. Lavalley, "IR Study of Polycrystalline Ceria Properties in Oxidised and Reduced States," *Catalysis Today*, vol. 50, pp. 207–225, 1999.

[121] H.-T. Chen, Y. M. Choi, M. Liu, and M. C. Lin, "A Theoretical Study of Surface Reduction Mechanisms of CeO_2 (111) and (110) by H_2," *ChemPhysChem*, vol. 8, no. 6, pp. 849–855, 2007.

[122] W. G. Reimers, M. A. Baltanas, and M. M. Branda, "CO, CO_2 and H_2 adsorption on ZnO, CeO_2 and ZnO/CeO_2 surfaces: DFT simulations," *Journal of Molecular Modelling*, vol. 20, 2014.

[123] J. Vecchietti, S. Collins, W. Xu, L. Barrio, D. Stacchiola, M. Calatayud, F. Tielens, J. J. Delgado, and A. Bonivardi, "Surface Reduction Mechanism of Cerium-Gallium Mixed Oxides with Enhanced Redox Properties," *The Journal of Physical Chemistry C*, vol. 117, pp. 8822–8831, 2013.

[124] M. Lahmer, "The Effect of Hydrogen Adsorption on the Properties of Undoped and Cu-Doped ZnO($10\bar{1}0$) Surfaces: A First-principles Study," *Journal of Physics and Chemistry of Solids*, vol. 89, pp. 89–96, 2016.

[125] S. H. Chung and I. Sohn, "Hydrogen Dissolution and Structural Analysis in High Temperature TiO_x-MnO-SiO_2 Oxide Melts," *International Journal of Hydrogen Energy*, vol. 40, pp. 15893–15900, 2015.

[126] B. Szost, R. Vegter, and P. R.-D. del Castillo, "Hydrogen-Trapping Mechanisms in Nanostructured Steels," *Metallurgical and Materials Transactions A*, vol. 44A, pp. 4542–4550, 2013.

[127] C. González, M. Panizo-Laiz, N. Gordillo, C.L. Guerrero, E. Tejado, F. Munnik, P. Piaggi, E. Bringa, R. Iglesias, J.M. Perlado and R. González-Arrabal, "H Trapping and Mobility in Nanostructured Tungsten Grain Boundaries: A Combined Experimental and Theoretical Approach," *Nuclear Fusion*, vol. 55, p. 113009, 2015.

[128] W. Mao, T. Chikada, K. Shimura, A. Suzuki, and T. Terai, "Energetics and Diffusion of Hydrogen in α-Al_2O_3 and Er_2O_3," *Fusion Engineering and Design*, vol. 88, pp. 2646–2649, 2013.

[129] Q. Yu, L. Hao, S. Li, D. He, X. Liu, L. Jiang, and S. Wang, "Microstructure and Deuterium Permeation Resistance of the Oxide Scale Prepared by Initial Oxidation Method on Vacuum Solar Receiver," *Solid State Ionics*, vol. 231, pp. 5–10, 2013.

[130] W. Mao, T. Chikada, A. Suzuki, T. Terai, and H. Matsuzaki, "Hydrogen Isotope Dissolution, Diffusion and Permeation in Er_2O_3," *Journal of Power Sources*, vol. 303, pp. 168–174, 2016.

[131] T. Chikadaa, T. Tanaka, K. Yuyama, Y. Uemura, S. Sakurada, H. Fujita, X.-C. Li, K. Isobe, T. Hayashi, and Y. Oyaa, "Crystallization and Deuterium Permeation Behaviours of Yttrium Oxide Coating Prepared by Metal Organic Decomposition," *Nuclear Materials and Energy*, vol. 9, pp. 526–534, 2016.

[132] Y. Hatano, K. Zhang, and K. Hashizume, "Fabrication of ZrO_2 Coatings on Ferritic Steel by Wet-Chemical Methods as a Tritium Permeation Barrier," *Physica Scripta*, vol. T145, p. 4044, 2011.

[133] Y. Wu, S. Wang, S. Li, D. He, X. Liu, L. Jiang, and H. Huang, "Deuterium Permeation Properties of Er_2O_3/Cr_2O_3 Composite Coating Prepared by MOCVD on 316L Stainless Steel," *Fusion Engineering and Design*, vol. 113, pp. 205–210, 2016.

[134] Y. Wu, D. He, H. Zhang, S. Li, X. Liu, S. Wang, and L. Jiang, "Preparation of Yttrium Oxide Coating by MOCVD as Tritium Permeation Barrier," *Fusion Engineering and Design*, vol. 90, pp. 05–109, 2015.

[135] A. Zielinski and S. Sobieszczyk, "Hydrogen-Enhanced Degradation and Oxide Effects in Zirconium Alloys for Nuclear Applications," *International Journal of Hydrogen Energy*, vol. 36, pp. 8619–8629, 2011.

[136] G. Sundell, M. Thuvander, A. Yatim, H. Nordin, and H.-O. Andrén, "Direct Observation of Hydrogen and Deuterium in Oxide Grain Boundaries in Corroded Zirconium Alloys," *Corrosion Science*, vol. 90, pp. 1–4, 2015.

[137] G. Sundell, M. Thuvander, and H.-O. Andrén, "Barrier Oxide Chemistry and Hydrogen Pick-up Mechanisms in Zirconium Alloys," *Corrosion Science*, vol. 102, pp. 490–502, 2016.

[138] Y. Nigara, K. Kawamura, T. Kawada, J. Mizusaki, , and M. Ishigame, "Hydrogen Permeability in Sintered CeO_2 at High Temperatures," *Journal of The Electrochemical Society*, vol. 146, pp. 2948–2953, 1999.

[139] K. Sohlberg, S. T. Pantelides, and S. J. Pennycook, "Interactions of Hydrogen with CeO_2," *Journal of the American Chemical Society*, vol. 123, pp. 6609–6611, 2001.

[140] B. Ao, R. Qui, H. Lu, and P. Chen, "Differences in the Existence States of Hydrogen in UO_2 and PuO_2 from DFT Calculations," *The Journal Physical Chemistry C*, vol. 120, pp. 18445–18451, 2016.

[141] J. Flitcroft, N. Brincat, M. Molinari, S. C. Parker, and M. Storr, "Hydride Ion Formation in Stoichiometric UO_2," *Chemical Communications*, vol. 51, p. 16209, 2015.

[142] H. Yu, G. Li, H. Li, R. Qiu, H. Huang, and D. Meng, "Adsorption and Dissociation of H_2 on PuO_2 (110) Surface: A Density Functional Theory Study," *Journal of Alloys and Compounds*, vol. 654, pp. 567–576, 2016.

[143] H. Yu, T. Tang, S. Zheng, Y. Shi, R. Qiu, W. Luo, and D. Meng, "A Theoretical Study of Hydrogen Atoms Adsorption and Diffusion on PuO_2 (110) Surface," *Journal of Alloys and Compounds*, vol. 666, pp. 287–291, 2016.

[144] T. Gouder, A. Shick, and F. Huber, "Surface Interaction of PuO_2,UO_{2+x} and UO_3 with Water Ice," *Topics in Catalysis*, vol. 56, pp. 1112–1120, 2013.

[145] T. Bo, J.-H. Lan, C.-Z. Wang, Y.-L. Zhao, C.-H. He, Y.-J. Zhang, Z.-F. Chai, and W.-Q. Shi, "First-Principles Study of Water Reaction and H_2 Formation on UO_2 (111) and (110) Single Crystal Surfaces," *Journal of Physical Chemistry*, vol. 118, pp. 21935–21944, 2014.

[146] T. Bo, J.-H. Lan, Y.-L. Zhao, C.-H. He, Z.-F. Chai, and W.-Q. Shi, "First-principles Study of Water Adsorption and Dissociation on the UO_2 (111), (110) and (100) Surfaces," *Journal of Nuclear Materials*, vol. 454, pp. 446–454, 2014.

[147] X.-F. Tian, H. Wang, H.-X. Xiao, and T. Gao, "Adsorption of Water on UO_2 (1 1 1) Surface: Density Functional Theory Calculations," *Computational Materials Science*, vol. 91, pp. 364–371, 2014.

[148] B. Tegner, M. Molinari, A. Kerridge, S. Parker, and N. Kaltsoyannis, "Water Adsorption on AnO_2 111,110 and 100 Surfaces (An= U, Pu); A DFT+ U Study," *The Journal of Physical Chemistry C*, vol. 121, pp. 1675–1682, 2016.

[149] V. Alexandrov, T. Y. Shvareva, S. Hayun, M. Asta, and A. Navrotsky, "Actinide Dioxides in Water: Interactions at the Interface," *Journal of Physical Chemistry Letters*, vol. 2, pp. 3130–3134, 2011.

[150] J. P. Wellington, A. Kerridge, J. Austin, and N. Kaltsoyannis, "Electronic Structure of Bulk AnO_2 (An = U, Np, Pu) and Water Adsorption on the (111) and (110) Surfaces of UO_2 and PuO_2 from Hybrid Density Functional Theory Within the Periodic Electrostatic Embedded Cluster Method," *Journal of Nuclear Materials*, vol. 482, pp. 124–134, 2016.

[151] M. Hedhili, B. Yakshinsky, and T. Madey, "Interaction of Water Vapor with UO_2 (001)," *Surface Science*, vol. 445, pp. 512–525, 2000.

[152] J. Stultz, M. Paffett, and S. Joyce, "Thermal Evolution of Hydrogen Following Water Adsorption on Defective UO_2 (100)," *Journal of physical chemistry B*, vol. 108, pp. 2362–2364, 2004.

[153] S. D. Senanayake and H. Idriss, "Water Reactions Over Stoichiometric and Reduced UO_2(1 1 1) Single Crystal Surfaces," *Surface Science*, pp. 135–144, 2004.

[154] S. D. Senanayake, R. Rousseua, D. Colegrave, and H. Idriss, "The Reaction of Water on Polycrystalline UO_2: Pathways to Surface and Bulk Oxidation," *Journal of Nuclear Materials*, vol. 342, pp. 179–187, 2005.

[155] S. D. Senanayake, W. G.I.N., A. Chan, T. Madey, D. R. Mullins, and H. Idriss, "The Reactions of Water Vapour on the Surfaces of Stoichiometric and Reduced Uranium Dioxide: A High Resolution XPS Study," *Catalysis Today*, vol. 120, pp. 151–157, 2007.

[156] H. He, M. Broczkowski, K. O'Neil, D. Ofori, O. Semenikhin, and D. Shoesmith, "Corrosion of Nuclear Fuel (UO_2) Inside a Failed Nuclear Waste Container," tech. rep., Western University, 2012. NWMO TR-2012-09.

[157] N. M. Trotsenko, I. A. Belov, and F. S. Bochagin, "Thermodynamic Investigation of the Possibility of Using Uranium Dioxide to Obtain Hydrogen and Oxygen from Water," *Atomic Energy*, vol. 106, pp. 94–99, 2009.

[158] A. Espriu-Gascon, J. Llorca, M. Domínguez, J. Gimenez, I. Casas, and J. de Pablo, "UO_2 Surface Oxidation by Mixtures of Water Vapor and Hydrogen as a Function of Temperature," *Journal of Nuclear Materials*, vol. 467, pp. 240–243, 2015.

[159] E. Ekeroth and M. Jonsson, "Oxidation of UO_2 by Radiolytic Oxidants," *Journal of Nuclear Materials*, vol. 322, pp. 242–248, 2003.

[160] S. Sunder, N. H. Miller, and D. W. Shoesmith, "Corrosion of Uranium Dioxide in Hydrogen Peroxide Solutions," *Corrosion Science*, vol. 46, pp. 1095–1111, 2004.

[161] J. Wren, D. W. Shoesmith, and S. Sunder, "Corrosion Behaviour of Uranium Dioxide in Alpha Radiolytically Decomposed Water," *Journal of the Electrochemical Society*, vol. 152, no. 11, pp. B470–481, 2005.

[162] M. M. Hossain, E. Ekeroth, and M. Jonsson, "Effects of HCO_3^- on the Kinetics of UO_2 Oxidation by H_2O_2," *Journal of Nuclear Materials*, vol. 358, pp. 202–208, 2006.

[163] P. Keech, J. Noel, and D. W. Shoesmith, "The Electrochemical Reduction of Hydrogen Peroxide on Uranium Dioxide Under Intermediate pH to Acidic Conditions," *Electrochimica Acta*, vol. 53, pp. 5675–5683, 2008.

[164] S. Sundin, B. Dahlgren, O. Roth, and M. Jonsson, "H_2O_2 and Radiation Induced Dissolution of UO_2 and SIMFUEL in HCO_3^- Deficient Aqueous Solution," *Journal of Nuclear Materials*, vol. 443, pp. 291–297, 2013.

[165] E. Ekeroth, O. Roth, and M. Jonsson, "The Relative Impact of Radiolysis Products in Radiation Induced Oxidative Dissolution of UO_2," *Journal of Nuclear Materials*, vol. 355, pp. 38–46, 2006.

[166] M. E. Broczkowski, P. G. Keech, J. J. Noël, and D. W. Shoesmith, "Corrosion of Uranium Dioxide Containing Simulated Fission Products in Dilute Hydrogen Peroxide and Dissolved Hydrogen," *Journal of The Electrochemical Society*, vol. 157, pp. C275–C281, 2010.

[167] M. Trummer, S. Nilsson, and M. Jonsson, "On the Effects of Fission Product Noble Metal Inclusions on the Kinetics of Radiation Induced Dissolution of Spent Nuclear Fuel," *Journal of Nuclear Materials*, vol. 378, pp. 55–59, 2008.

[168] L. Wu, J. S. Goldik, and D. W. Shoesmith, "The Anodic Reactions on Simulated Spent Fuel (SIMFUEL) in H_2O_2 Solutions: Effect of Carbonate/Bicarbonate," *Journal of the Electrochemical Society*, vol. 161, no. 6, pp. C363–C371, 2014.

[169] E. Ekeroth, M. Jonsson, T. E. Eriksen, K. L. S. Kovacs, and I. Puigdomenech, "Reduction of UO_2^{2+} by H_2," *Journal of Nuclear Materials*, vol. 334, pp. 35–39, 2004.

[170] S. Nilsson and M. Jonsson, "On the Catalytic Effects of $UO_{2(s)}$ and $Pd_{(s)}$ on the Reaction Between H_2O_2 and H_2 in Aqueous Solution," *Journal of Nuclear Materials*, vol. 372, pp. 160–163, 2008.

[171] P. Carbol, P. Fors, T. Gouder, and K. Spahiu, "Hydrogen Suppresses UO_2 Corrosion," *Geochimica et Cosmochimica Acta*, vol. 73, pp. 4366–4375, 2009.

[172] M. Trummer, O. Roth, and M. Jonsson, "H_2 Inhibition of Radiation Induced Dissolution of Spent Nuclear Fuel," *Journal of Nuclear Materials*, vol. 383, pp. 226–230, 2009.

[173] R. Pehrman, M. Trummer, C. M. Lousada, and M. Jonsson, "On the Redox Reactivity of Doped UO_2 Pellets – Influence of Dopants on the H_2O_2 Decomposition Mechanism," *Journal of Nuclear Materials*, vol. 430, no. 6-11, 2012.

[174] C. M. Lousada, M. Trummer, and M. Jonsson, "Reactivity of H_2O_2 Towards Different UO_2-Based Materials: The Relative Impact of Radiolysis Products Revisited," *Journal of Nuclear Materials*, vol. 434, pp. 434–439, 2013.

[175] L. Wu, N. Liu, Z. Qin, and D. W. Shoesmith, "Modelling the Radiolytic Corrosion of Fractured Nuclear Fuel under Permanent Disposal Conditions," *Journal of the Electrochemical Society*, vol. 161, no. 8, pp. E3259–3266, 2014.

[176] M. Born and J. Oppenheimer, "On the Quantum Theory of Molecules," *Annalen der Physik*, vol. 84, p. 458, 1927.

[177] A. R. Leach, *Molecular Modelling*. Pearson Education Limited, Second ed.

[178] L. H. Thomas, "The Calculation of Atomic Fields," *Mathematical Proceedings of the Cambridge Philosophical Society*, vol. 23, pp. 542–548, 1927.

[179] E. Fermi, "Statistical Method to Determine Some Properties of Atoms," *Atti della Accademia Nazionale dei Lincei, Classe di Scienze Fisiche, Matematiche e Naturali, Rendiconti*, vol. 6, pp. 602–607, 1927.

[180] P. A. M. Dirac, "Note on Exchange Phenomena in the Thomas Atom," *Mathematical Proceedings of the Cambridge Philosophical Society*, vol. 26, pp. 376–385, 1930.

[181] P. Hohenberg and W. Kohn, "Inhomogeneous Eletron Gas," *Physical Review B*, vol. 136(3B), p. B864, 1964.

[182] W. Kohn and L. Sham, "Self-Consistent Equations Including Exchange and Correlations Effects," *Physical Review*, vol. 140(4A), p. 1133, 1965.

[183] A. D. Becke, "Density-Functional Exchange-Energy Approximation with Correct Asymptotic-Behaviour," *Physical Review A*, vol. 38, pp. 3098–3100, 1988.

[184] J. P. Perdew, K. Burke, and M. Ernzerhof, "Generalized Gradient Approximation Made Simple," *Physical Review Letters*, vol. 77, pp. 3865–3868, 1996.

[185] J. Perdew, A. Ruzsinszky, G. Csonka, O. Vydrov, G. Scuseria, L. Constantin, X. Zhou, and K. Burke, "Restoring the Density-Gradient Expansion for Exchange in Solids and Surfaces," *Physical Review Letters*, vol. 100, p. 136406, 2008.

[186] J. P. Perdew and K. Schmidt, "Jacob's Ladder of Density Functional Approximations for the Exchange-Correlation Energy," *AIP Conference Proceedings*, vol. 577, p. 1, 2016.

[187] N. Brincat, *Density Functional Theory Investigation of the Uranium Oxides*. PhD thesis, 2015.

[188] M. Filatov and W. Thiel, "Exchange-Correlation Density Functional Beyond the Gradient Approximation," *Physical Review A*, vol. 57, p. 189, 1998.

[189] J. Sun, M. Marsman, G. I. Csonka, A. Ruzsinszky, P. Hao, Y.-S. Kim, G. Kresse, and J. P. Perdew, "Self-Consistent Meta-Generalized Gradient Approximation within the Projector-Augmented-Wave Method," *Physical Review B*, vol. 84, p. 035117, 2011.

[190] T. V. Voorhis and G. E. Scuseria, "A Novel Form for the Exchange-Correlation Energy Functional," *Journal of Chemical Physics*, vol. 109, p. 400, 1998.

[191] J. Tao, J. P. Perdew, V. N. Staroverov, and G. E. Scuseria, "Climbing the Density Functional Ladder: Nonempirical Meta–Generalized Gradient Approximation Designed for Molecules and Solids," *Physical Review Letters*, vol. 91, pp. 1469401–1, 2003.

[192] Y. Zhao and D. G. Truhlar, "Construction of a Generalized Gradient Approximation by Restoring the Density-Gradient Expansion and Enforcing a Tight Lieb–Oxford Bound," *Journal of Chemical Physics*, vol. 128, p. 184109, 2008.

[193] J. P. Perdew, A. Ruzsinszky, G. I. Csonka, L. A. Constantin, and J. Sun, "Workhorse Semilocal Density Functional for Condensed Matter Physics and Quantum Chemistry," *Physical Review Letters*, vol. 103, p. 026403, 2009.

[194] J. P. Perdew, A. Ruzsinszky, G. I. Csonka, L. A. Constantin, and J. Sun, "Erratum: Workhorse Semilocal Density Functional for Condensed Matter Physics and Quantum Chemistry," *Physical Review Letters*, vol. 106, p. 179902, 2011.

[195] A. D. Becke, "Correlation energy of an inhomogeneous electron gas: A coordinate-space model," *Journal of Chemical Physics*, vol. 88, p. 1053, 1988.

[196] A. D. Becke and M. R. Roussel, "Exchange Holes in Inhomogeneous Systems: A Coordinate-Space Model," *Physical Review A*, vol. 39, p. 3761, 1989.

[197] A. D. Becke and E. R. Johnson, "A Simple Effective Potential for Exchange," *The Journal of Chemical Physics*, vol. 124, p. 221101, 2006.

[198] Y. Zhao and D. G. Truhlar, "A New Local Density Functional for Main-Group Thermochemistry, Transition Metal Bonding, Thermochemical Kinetics and Noncovalent Interactions," *The Journal of Chemical Physics*, vol. 125, p. 194101, 2006.

[199] A. Ruzsinszky, J. Sun, B. Xiao, and G. I. Csonka, "A meta-GGA Made Free of the Order of Limits Anomaly," *Journal of Chemical Theory and Computation*, vol. 8, pp. 2078–2087, 2012.

[200] J. M. del Campo, J. L. Gázquez, S. Trickey, and A. Vela, "A New meta-GGA Exchange Functional Based on an Improved Constraint-Based GGA," *Chemical Physics Letters*, vol. 543, pp. 179–183, 2012.

[201] L. Sun, D. Marrocchelli, and B. Yildiz, "Edge Dislocation Slows Down Oxide Ion Diffusion in Doped CeO_2 by Segregation of Charged Defects," *Nature Communications*, vol. 6, p. 6294, 2015.

[202] N. Mardirossian and M. Head-Gordon, "ωB97M-V: A Combinatorially Optimized, Range-Separated Hybrid, meta-GGA Density Functional with VV10 Nonlocal Correlation," *The Journal of Chemical Physics*, vol. 144, p. 214110, 2016.

[203] V. N. Staroverov, G. E. Scuseria, J. Tao, and J. P. Perdew, "Tests of a Ladder of Density Functionals for Bulk Solids and Surfaces," *Physical Review B*, vol. 69, p. 075102, 2004.

[204] J. P. Perdew, J. Sun, R. M. Martin, and B. Delley, "Semilocal Density Functionals and Constraint Satisfaction," *International Journal of Quantum Chemistry*, vol. 116, pp. 847–851, 2016.

[205] F. D. Sala, E. Fabiano, and L. A. Constantin, "Kinetic-Energy-Density Dependent Semilocal Exchange-Correlation Functionals," *International Journal of Quantum Chemistry*, vol. 116, pp. 1641–1694, 2016.

[206] J. Sun, R. C. Remsing, Y. Zhang, Z. Sun, A. Ruzsinszky, H. Peng, Z. Yang, A. Paul, U. Waghmare, X. Wu, M. L. Klein, and J. P. Perdew, "Accurate First-Principles Structures and Energies of Diversely Bonded Systems from an Efficient Density Functional," *Nature Chemistry*, vol. 8, p. 831, 2016.

[207] C. T. Lee, W. T. Wang, and R. G. Parr, "Development of the Colle-salvetti Correlation-Energy Formula into a Functional of the Electron Density," *Physical Review B*, vol. 37, pp. 785–789, 1988.

[208] A. D. Becke, "Density-Functional Thermochemistry .3. The Role of Exact Exchange and Correlation Effects," *Physical Review*, vol. 98, pp. 5648–5652, 1993.

[209] C. Adamo and V. Barone, "Towards Reliable Density Functional Methods Without Adjustable Parameters: The PBE0 Model," *Journal of Chemical Physics*, vol. 110, pp. 6158–6170, 1999.

[210] J. Heyd, G. E. Scuseria, and M. Ernzerhof, "Hybrid Functionals Based on a Screened Coulomb Potential," *Journal of Chemical Physics*, vol. 118, no. 18, pp. 8207–8215, 2003.

[211] Y. Zhao and D. G. Truhlar, "The M06 Suite of Density Functionals for Main Group Thermochemistry, Thermochemical Kinetics, Noncovalent Interactions,

Excited States and Transition Elements: Two New Functionals and Systematic Testing of Four M06-Class Functionals and 12 Other functionals," *Theoretical Chemistry Accounts*, vol. 120, pp. 215–241, 2008.

[212] W. Kohn, Y. Meir, and D. E. Makarov, "van der Waals Energies in Density Functional Theory," *Physical Review Letters*, vol. 80, p. 4153, 1998.

[213] E. Hult, H. Rydberg, and B. I. Lundqvist, "Unified Treatment of Asymptotic van der Waals Forces," *Physical Review B*, vol. 59, p. 4708, 1999.

[214] M. Lein, J. F. Dobson, and E. K. U. Gross, "Toward the Description of van der Waals Interactions within Density Functional Theory," *Journal of Computational Chemistry*, vol. 20, pp. 12–22, 1999.

[215] M. Lein, E. K. U. Gross, and J. P. Perdew, "Electron Correlation Energies from Scaled Exchange-Correlation Kernels: Importance of Spatial versus Temporal Nonlocality," *Physical Review B*, vol. 61, p. 431, 2000.

[216] J. F. Dobson and J. Wang, "Energy-Optimized Local Exchange-Correlation Kernel for the Electron Gas: Application to van der Waals Forces," *Physical Review B*, vol. 62, p. 38, 2000.

[217] S. Grimme, "Semiempirical GGA-type Density Functional Constructed with a Long-Range Dispersion Correction," *Journal of Computational Chemistry*, vol. 27, no. 15, pp. 1787–1799, 2006.

[218] S. Grimme, J. Antony, S. Ehrlich, and S. Krieg, "A Consistent and Accurate *Ab initio* Parametrization of Density Functional Dispersion Correction (DFT-D) for the 94 Elements H-Pu," *The Journal of Chemical Physics*, vol. 132, p. 154104, 2010.

[219] S. Grimme, S. Ehrlich, and L. Goerigk, "Effect of the Damping Function in Dispersion Corrected Density Functional Theory," *Journal of Computational Chemistry*, vol. 32, p. 1456, 2011.

[220] M. Dion, H. Rydberg, E. Schroder, D. C. Langreth, and B. I. Lundqvist, "van der Waals Density Functional for General Geometries," *Physical Review Letters*, vol. 92, p. 246401, 2004.

[221] E. D. Murray, K. Lee, and D. C. Langreth, "Investigation of Exchange Energy Density Functional Accuracy for Interacting Molecules," *Journal of Chemical theory and Computation*, vol. 5, pp. 2754–2762, 2009.

[222] K. Lee, E. D. Murray, L. Kong, B. I. Lundqvist, and D. C. Langreth, "Higher-Accuracy van der Waals Density Functional," *Physical Review B*, vol. 82, p. 081101, 2010.

[223] J. Klimes, D. R. Bowler, and A. Michaelides, "Chemical Accuracy for the van der Waals Density Functional," *Journal of Physics: Condensed Matter*, vol. 22, p. 022201, 2010.

[224] D. M. Ceperley and B. J. Alder, "Ground State of the Electron Gas by a Stochastic Method," *Physical Review Letters*, vol. 45, p. 566, 1980.

[225] S. H. Vosko, L. Wilk, and M. Nussair, "Accurate Spin-Dependent Electron Liquid Correlation Energies for Local Spin Density Calculations: A Critical Analysis," *Canadian Journal of Physics*, vol. 58, pp. 1200–1211, 1980.

[226] J. P. Perdew and A. Zunger, "Self-Interaction Correction to Density-Functional Approximations for Many-Electron Systems," *Physical Review B*, vol. 23, p. 5048, 1981.

[227] J. P. Perdew and Y. Wang, "Accurate and Simple Analytic Representation of the Electron-Gas Correlation Energy," *Physical Review B*, vol. 45, p. 13244, 1992.

[228] U. V. Barth and L. Hedin, "Local Exchange-Correlation Potential for Spin Polarised Case .1.," *Journal of Physics Part C Solid State Physics*, vol. 5, p. 1629, 1972.

[229] R. M. Martin, *Electronic Structure: Basic Theroy and Practical Methods*. Cambridge University Press, 2004.

[230] J. P. Perdew, J. A. Chevary, S. H. Vosko, K. A. Jackson, M. R. Pederson, D. J. Singh, and C. Fiolhais, "Atoms, Molecules, Solids, and Surfaces - Applications of the Generalized Gradient Approximation for Exchange and Correlation," *Physical Review B*, vol. 46, no. 11, pp. 6671–6687, 1992.

[231] A. D. Becke, "Density Functional Calculations of Molecular Bond Energies," *The Journal of Chemical Physics*, vol. 84, p. 4524, 1986.

[232] B. J. Morgan, D. O. Scanlon, and G. W. Watson, "The Use of the "$+U$" Correction in Describing Defect States at Metal Oxide Surfaces: Oxygen Vacancies on CeO_2 and TiO_2, and Li-doping of MgO," *Journal of Surface Science and Nanotechnology*, vol. 7, pp. 389–394, 2009.

[233] M. Cococcioni and S. de Gironcoli, "Linear response approach to the calculation of the effective interaction parameters in the lda + u method," *Physical review B*, vol. 71, p. 035105, 2005.

[234] V. I. Anisimov, F. Aryasetiawan, and A. I. Lichtenstein, "First-Principles Calculations of the Electronic Structure and Spectra of Strongly Correlated Systems: The LDA+U Method," *Journal of Physics - Condensed Matter*, vol. 9, pp. 767–808, 1997.

[235] S. L. Dudarev, G. A. Botton, S. Y. Savrasov, Z. Szotek, W. M. Temmerman, and A. P. Sutton, "Electronic Structure and Elastic Properties of Strongly Correlated Metal Oxides from First Principles: LSDA + U, SIC-LSDA and EELS Study of UO_2 and NiO," *phys. stat. sol.*, vol. 166, p. 429, 1998.

[236] M. R. Castell, S. L. Dudarev, C. Muggelberg, A. P. Sutton, G. A. D. Briggs, and D. T. Goddard, "Surface Structure and Bonding in the Strongly Correlated Metal Oxides NiO and UO_2," *Journal of Vacuum Science & Technology A: Vacuum, Surfaces, and Films*, vol. 16, p. 1055, 1998.

[237] J. Hubbard, "Electron Correlations in Narrow Energy Bands .4. Atomic Representation," *Proceedings if the Royal Society of London Series A - Mathematical and Physical Sciences*, vol. 285, pp. 542–560, 1965.

[238] A. I. Lichtenstein, V. I. Anisimov, and J. Zaaen, "Density Functional Theory and Strong Interactions - Orbital Ordering in Mott-Hubbard Insulators," *Physical Review B*, vol. 52, pp. R5467–R5470, 1995.

[239] S. L. Dudarev, G. A. Botton, S. Y. Savrasov, C. J. Humphreys, and A. P. Sutton, "Electron-Energy-Loss Spectra and the Structural Stability of Nickel Oxide: An LSDA+U Study," *Physical Review B*, vol. 57, pp. 1505–1509, 1998.

[240] H. J. Kulik, M. Cococcioni, D. A. Scherlis, and N. Marzari, "Density functional theory in transition-metal chemistry: A self-consistent hubbard u approach," *Physical Review Letters*, vol. 97, p. 103001, 2006.

[241] F. Zhou, M. Cococcioni, C. A. Marianetti, D. Morgan, and G. Ceder, "First-principles prediction of redox potentials in transition-metal compounds with lda+u," *Physical Review B*, vol. 70, p. 235121, 2004.

[242] T. Yamazaki and A. Kotani, "Systematic Analysis of 4*f* Core Photoemission Spectra in Actinide Oxides," *Journal of the Physical Society of Japan*, vol. 60, pp. 49–52, 1991.

[243] A. Kotani and T. Yamazaki, "Systematic Analysis of Core Photoemission Spectra for Actinide Dioxides and Rare Earth Sesquioxides," *Progress of Theoretical Physics Supplement*, vol. 108, pp. 117–131, 1992.

[244] G. W. Watson, E. T. Kelsey, N. H. deLeeuw, D. J. Harris, and S. C. Parker, "Atomistic Simulation of Dislocations, Surfaces and Interfaces in MgO," *Journal of the Chemical Society-Faraday Transactions*, vol. 92, pp. 433–438, 1996.

[245] G. Kresse and J. Hafner, "*Ab initio* Molecular-Dynamics for Liquid Metals," *Physical Review B*, vol. 47, pp. 558–561, 1993.

[246] G. Kresse and J. Hafner, "*Ab initio* Molecular-Dynamics Simulation of the Liquid-Metal Amorphous-Semiconductor Transition in Germanium," *Physical Review B*, vol. 49, pp. 14251–14269, 1994.

[247] G. Kresse and J. Furthmüller, "Efficient iterative schemes for *Ab initio* total-energy calculations using a plane-wave basis set," *Physical Review B*, vol. 54, no. 16, pp. 11169–11186, 1996. Times Cited: 14679.

[248] G. Kresse and J. Furthmuller, "Efficiency of *Ab initio* Total Energy Calculations for Metals and Semiconductors Using a Plane Wave Basis Set," *Computational Materials Science*, vol. 6, pp. 15–50, 1996.

[249] R. Fletcher and M. J. D. Powell, "A Rapidly Convergent Descent Method for Minimisation," *The Computer Journal*, vol. 6, no. 2, p. 163, 1963.

[250] R. Fletcher and C. M. Reeves, "Function Minimization by Conjugate Gradients," *The Computer Journal*, vol. 7, no. 2, pp. 149–154, 1964.

[251] M. J. Norgett and R. Fletcher, "Fast Matrix Methods for Calculating relaxation About Defects in Crystals," *Journal of Physics Part C Solid State Physics*, vol. 3, p. L190, 1970.

[252] C. G. Broyden, "Convergence of Single-Rank Quasi-Newton Methods," *Mathematics of Computation*, vol. 365, p. 24, 1970.

[253] R. Fletcher, "A New Approach to Variable Metric Algorithms," *Computer Journal*, vol. 317, p. 13, 1970.

[254] D. Goldfarb, "A Family of Variable-Metric Methods Derived by Variational Means," *Mathematics of Computation*, vol. 23, p. 24, 1970.

[255] D. F. Shanno, "Conditioning of Quasi-Newton Methods for Function Minimisation," *Mathematics of Computation*, vol. 111, p. 24, 1970.

[256] P. Pulay, "Convergence Acceleration of Iterative Sequences - the Case of SCF Iteration," *Chemical Physics Letters*, vol. 393-398, p. 73, 1980.

[257] L. Wang, *Molecular Dynamics - Studies of Synthetic and Biological Macromolecules*, p. 444.

[258] P. Weaver, *Computational Studies of Interstitial-type Oxide Ion Conductors for Applications in Solid Oxide Fuel Cells*. PhD thesis, 2011.

[259] M. C. Payne, M. P. Teter, D. C. Allan, T. A. Arais, and J. D. Jannopoulos, "Iterative Minimisation Techniques for *Ab initio* Total-Energy Calculations - Molecular Dynamics and Conjugate Gradients," *Reviews of Modern Physics*, vol. 64, pp. 1045–1097, 1992.

[260] H. J. Monkhorst and J. D. Pack, "Special points for Brillouin-Zone Integrations," *Physical Review B*, vol. 13, no. 12, pp. 5188–5192, 1976.

[261] V. Heine, "The Pseudopotential Concept," *Solid State Physical*, vol. 24, pp. 1–36, 1970.

[262] D. J. Singh and L. Nordstrom, *Planewaves, Pseudopotentials and the LAPW Method*.

[263] P. E. Bloch, "Projector Augmented-Wave Method," *Physical Review B*, vol. 50, pp. 17953–17979, 1994.

[264] P. Kupier, G. K. J. Ghijsen, G. A. Sawatzky, and H. Verweij, "Character of Holes in $Li_xNi_{1-x}O$ and Their Magnetic Behaviour," *Physical Review Letters*, vol. 62, p. 221, 1989.

[265] S. L. Dudarev, D. N. Mahn, and A. P. Sutton, "Effect of Mott-Hubbard Correlations on the Electronic Structure and Structural Stability of Uranium Dioxide," *Philosophical Magazine B - Physics of Condensed Matter Statistical Mechanics Electronic Optical and Magnetic Properties*, vol. 75, pp. 613–628, 1997.

[266] F. Birch, "Finite Elastic Strain of Cubic Crystal," *Physical Review*, vol. 71, pp. 809–824, 1947.

[267] M. Hebbache and M. Zemzemi, "*Ab initio* Study of High-Pressure Behaviour of a Low Compressibility Metal and a Hard Material: Osmium and Diamond," *Physical Review B*, vol. 70, 2004.

[268] C. Kittel, *Introduction to Solid State Physics*. New York: John Wiley & Sons, 8^{th} edition ed.

[269] Y. LePage and P. Saxe, "Symmetry-General Least-Squares Extraction of Elastic Data for Strained Materials from *Ab initio* Calculations of Stress," *Physical Review B*, vol. 65, 2002.

[270] A. J. Devey, "First Principles Calculation of the Elastic Constants and Phonon Modes of UO_2 using GGA plus U with Orbital Occupancy Control," *Journal of Nuclear Materials*, vol. 412, no. 3, pp. 301–307, 2011.

[271] L. Fast, J. M. Willis, B. Johansson, and O. Eriksson, "Elastic-Constants of Hexagonal Transition Metals Theory," *Physical Review B*, vol. 51, pp. 17431–17438, 1995.

[272] P. Ravindran, L. Fast, P. A. Korzhavyi, B. Johansson, J. Willis, and O. Eriksson, "Density Functional Theory for Calculation of Elastic Properties of Orthorhombic Crystals: Applications to $TiSi_2$," *Journal of Applied Physics*, vol. 84, 1998.

[273] S. Baroni, P. Giannozzi, and A. Testa, "Greens Function Approach to Linear Response in Solids," *Physical Review Letters*, vol. 58, pp. 1861–1864, 1987.

[274] X. Gonze, "Perturbation Expansion of Variational-Principles at Arbitrary Order," *Physical Review A*, vol. 52, pp. 1086–1095, 1995.

[275] K. P. Huber and G. Herzberg, *Molecular Spectra and Molecular Structure*.

[276] H. C. Chang and M. Ogawa, "Rotational Analysis of a High-Resolution Absorption Band of O_2 at 1161 Å," *Journal of Molecular Spectroscopy*, vol. 44, pp. 405–406, 1972.

[277] G. Herzberg, "Forbidden Transitions in Diatomic Molecules: II. The $^3\Sigma_u^+ \leftarrow ^3\Sigma_g^-$ Absorption Bands of the Oxygen Molecule," *Canadian Journal of Physics*, vol. 30, pp. 185–210, 1952.

[278] G. H. Lander and m. H. Mueller, "Neutron Diffraction Study of α-Uranium at Low Temperatures," *Acta Crystallographica B*, vol. 26, pp. 129–136, 1970.

[279] C. W. Tucker and P. Senio, "An Improved Determination of the Crystal Structure of β-uranium," *Acta Crystallographica*, vol. 6, pp. 753–760, 1953.

[280] J. Thewlis, "Structures of Uranium," *Nature*, vol. 168, pp. 198–199, 1951.

[281] J.-W. Yang, T. Gao, B.-Q. Liu, G.-A. Sun, and B. Chen, "*Ab initio* Calculations of the Ideal Tensile and Shear Strengths of Uranium Metal," *Journal of Nuclear Materials*, vol. 458, pp. 122–128, 2015.

[282] J. Nie, H. Xiao, F. Gao, and X. Zu, "Electronic and Magnetic Properties of Al Adsorption on α-Uranium (0 0 1) Surface: *Ab initio* Calculations," *Journal of Alloys and Compounds*, vol. 476, pp. 675–682, 2009.

[283] C. D. Taylor, "Evaluation of First-Principles Techniques for Obtaining Materials Parameters of α-Uranium and the (001) α-Uranium Surface," *Physical Review B*, vol. 77, p. 094119, 2008.

[284] P. Söderlind, "First-Principles Elastic and Structural Properties of Uranium Metal," *Physical Review B*, vol. 66, p. 085113, 2002.

[285] J. P. Crocombette, F. Jollet, L. T. Nga, and T. Petit, "Plane-Wave Pseudopotential Study of Point Defects in Uranium Dioxide," *Physical Review B*, vol. 64, p. 104107, 2001.

[286] A. N. Chantis, R. C. Albers, M. D. Jones, M. van Schilfgaarde, and T. Kotani, "Many-Body Electronic Structure of Metallic α-Uranium," *Physical Review B*, vol. 78, p. 081101, 2008.

[287] S. G. Popov, J. J. Carbajo, V. K. Ivanov, and G. L. Yoder, "Thermophysical Properties of MO_X and UO_2 Fuels Including the Effects of Irradiation," tech. rep., Oak Ridge National Laboratory, 11 2000.

[288] M. Idiri, T. L. Bihan, S. Heathman, and J. Rebizant, "Behaviour of Actinide Dioxides Under Pressure: UO_2 and ThO_2," *Physical Review B*, vol. 70, p. 014113, 2004.

[289] J. Wang, R. C. Ewing, and U. Becker, "Electronic Structure and Stability of Hyperstoichiometric UO_{2+x} Under Pressure," *Physical Review B*, vol. 88, p. 024109, 2013.

[290] J. C. Crowhurst, J. R. Jeffries, D. Åberg, J. M. Zaug, Z. R. Dai, W. J. Siekhaus, N. E. Teslich, K. S. Holliday, K. B. Knight, A. J. Nelson, and I. D. Hutcheon, "A Combined Theoretical and Experimental Investigation of Uranium Dioxide Under High Static Pressure," *Journal of Physics: Condensed Matter*, vol. 27, p. 265401, 2015.

[291] S. Gréaux, L. Gautron, D. Andrault, N. Bolfan-Casanova, N. Guignot, and J. Haines, "Structural Characterization of Natural UO_2 at Pressures up to 82 GPa and Temperatures up to 2200 K," *American Mineralogist*, vol. 93, pp. 1090–1098, 2008.

[292] O. G. Brandt and C. T. Walker, "Ultrasonic Attenuation and Elastic Constants of Uranium Dioxide," *Physical Review*, vol. 170, p. 528, 1968.

[293] J. J. B. Watchman, M. L. Wheat, H. J. Anderson, and J. L. Bates, "Elastic Constants of Single Crystal UO_2 at 25 ^{O}C," *Journal of Nuclear Materials*, vol. 16, pp. 39–41, 1965.

[294] I. J. Fritz, "Elastic Properties of UO_2 at High Pressure," *Journal of Applied Physics*, vol. 47, p. 4353, 1976.

[295] M. Sanati, R. C. Albers, T. Lookman, and A. Saxena, "Elastic Constants, Phonon Density of States and Thermal Properties of UO_2," *Physical Review B*, vol. 84, p. 014116, 2011.

[296] Z.-G. Mei, M. Stan, and J. Yang, "First-Principles Study of Thermophysical Properties of Uranium Dioxide," *Journal of Alloys and Compounds*, vol. 603, pp. 282–286, 2014.

[297] W. Huang and H. Chen, "Investigation of the Elastic, Hardness and Thermodynamic Properties of Actinide Oxides," *Physica B*, vol. 446, pp. 133–137, 2014.

[298] B. C. Frazer, G. Shirane, D. E. Cox, and C. E. Olsen, "Neutron-Diffraction Study of Antiferromagnetism in UO_2," *Physical Review*, vol. 140, pp. A1448–A1452, 1965.

[299] S. J. Allen, "Spin-Lattice Interaction in UO_2. I. Ground-State and Spin-Wave Excitations," *Physical Review*, vol. 166, pp. A1448–A1452, 1965.

[300] J. J. Faber, G. H. Lander, and B. H. Cooper, "Neutron-Diffraction Study of UO_2: Observation of an Internal Distortion," *Physical Review Letters*, vol. 35, pp. 1770–1773, 1975.

[301] J. J. Faber, G. H. Lander, and B. H. Cooper, "Neutron-Diffraction Study of UO_2: Antiferromagnetic state," *Physical Review B*, vol. 14, pp. 1151–1164, 1976.

[302] K. Schwarz, Magnetism (FM, AFM, FSM), 2011, Wien, Austria. http://susi.theochem.tuwien.ac.at/reg_user/textbooks/WIEN2k_lecture-notes_2013/magnetism.pdf.

[303] K. Ikushima, S. Tsutsui, Y. Haga, H. Yasuoka, R. E. Walstedt, N. M. Masaki, A. Nakamura, S. Nasu, and Y. Onuki, "First-Order Phase Transition in UO_2: ^{235}U and ^{17}O NMR Study," *Physical Review B*, vol. 63, p. 104404, 2001.

[304] E. Blackburn, R. Caciuffo, N. Magnani, P. Santini, P. J. Brown, M. Enderle, , and G. H. Lander, "Spherical Neutron Spin Polarimetry of Anisotropic Magnetic Fluctuations in UO_2," *Physical Review B*, vol. 72, p. 184411, 2005.

[305] R. Laskowski, G. K. H. Madsen, P. Blaha, and K. Schwarz, "Magnetic Structure and Electric-Field Gradients of Uranium Dioxide: An *Ab initio* Study," *Physical Review B*, vol. 69, pp. 140408–1, 2004.

[306] D. Gryaznov, E. Heifets, and D. Sedmidubsky, "Density Functional Theory Calculations on Magnetic Properties of Actinide Compounds," *Phys. Chem. Chem. Phys.*, vol. 12, pp. 12273–12278, 2010.

[307] F. Zhou and V. Ozoliņš, "Crystal Field and Magnetic Structure of UO_2," *Physical Review B*, vol. 83, p. 085106, 2011.

[308] J. Schoenes, "Optical Properties and Electronic Structure of UO_2," *Journal of Applied Physics*, vol. 49, p. 1463, 1978.

[309] Y. Baer and J. Schoenes, "Electronic Structure and Coulomb Correlation Energy in UO_2 Single Crystals," *Solid State Communications*, vol. 33, pp. 885–888, 1980.

[310] S. W. Yu, J. G. Tobin, J. C. Crowhurst, S. Sharma, J. K. Dewhurst, P. Olalde-Velasco, W. L. Yang, and W. J. Siekhaus, "f-f origin of the insulating state in uranium dioxide: X-ray adsorption experiments and first-calculations," *Physical Review B*, vol. 83, p. 165102, 2011.

[311] B. Szpunar, "Investigation of Urania within LDA+U Method," *Journal of Physics and Chemistry of Solids*, vol. 73, pp. 1003–1009, 2012.

[312] M. T. Suzuki, N. Magnani, and P. M. Oppeneer, "Microscopic Theory of the Insulating Electronic Ground States of the Actinide Dioxides AnO_2 (An = U, Np, Pu, Am, and Cm)," *Physical Review B*, vol. 88, p. 195146, 2013.

[313] D. Gryaznov, E. Heifets, and E. Kotomin, "*Ab initio* DFT+U study of He Atom Incorporation into UO_2 Crystals," *Physical Chemistry Chemical Physics*, vol. 11, pp. 7241–7247, 2009.

[314] K. N. Kudin, G. E. Scuseria, and R. L. Martin, "Hybrid Density-Functional Theory and the Insulating Gap of UO_2," *Physical Review Letters*, vol. 89, pp. 266402–1, 2002.

[315] L. M. R. Atta-Fynn and A. K. Ray, "Elemental and Mixed Actinide Dioxides: An *Ab initio* Study," *Journal of Theoretical and Computational Chemistry*, vol. 11, p. 611, 2012.

[316] G. Allen, J. Crofts, and A. Griffiths, "Infrared Spectroscopy of the Uranium/Oxygen System," *Journal of Nuclear Materials*, vol. 62, pp. 273–281, 1976.

[317] J.-G. Kim, Y.-S. Park, Y.-K. Ha, and K. Song, "Infrared Spectra of Uranium Oxides Measured by ATR-FTIR," *Journal of Nuclear Science and Technology*, vol. 12, pp. 1188–1192, 2009.

[318] M. L. Palacios and S. H. Taylor, "Characterization of Uranium Oxides Using in-situ Micro-Raman Spectroscopy," *Applied Spectroscopy*, vol. 54, no. 9, pp. 1372–1378, 2000.

[319] D. Manara and B. Renker, "Raman Spectra of Stoichiometric and Hyperstoichiometric Uranium Dioxide," *Journal of Nuclear Materials*, vol. 321, no. 2–3, pp. 233–237, 2003.

[320] L. Desgranges, G. Baldinozzi, P. Simon, G. Guimbretière, and A. Canizares, "Raman Spectrum of U_4O_9: A New Interpretation of Damage Lines in UO_2," *Journal of Raman Spectroscopy*, vol. 43, pp. 455–458, 2012.

[321] J. M. Elorrieta, L. J. Bonales, N. Rodrıguez-Villagra, V. G. Baonza, and J. Cobos, "A Detailed Raman and X-ray Study of UO_{2+x} Oxides and Related Structure Transitions," *Physical Chemistry Chemical Physics*, vol. 18, pp. 28209–28216, 2016.

[322] T. D. Chikalla, C. E. McNeilly, and R. E. Skavdahl, "The Plutonium-Oxygen System," *Journal of Nuclear Materials*, vol. 12, pp. 131–141, 1964.

[323] M. Wulff and G. H. Lander, "Magnetic Structure and Pu Ground State in Beta-Pu_2O_3," *Journal of Chemical Physics*, vol. 89, pp. 3295–3299, 1988.

[324] L. R. Morss, J. Fuger, J. Goffart, and R. G. Haire, "Enthalpy of Formation and Magnetic Susceptibility of Curium Sesquioxide, Cm_20_3," *Inorganic Chemistry*, vol. 22, p. 1993, 1983.

[325] L. R. Morss and D. C. Sonneberger, "Enthalpy of Formation of American Sesquioxide; Systematics of Actinide Sesquioxide Thermochemistry," *Journal of Nuclear Materials*, vol. 130, pp. 266–272, 1985.

[326] H. Geng, Y. Chen, Y. Kaneta, M. Iwasawa, T. Ohnuma, and M. Kinoshita, "Point Defects and Clustering in Uranium Dioxide by LSDA+U Calculations," *Physical Review B*, vol. 77, p. 104120, 2008.

[327] B. Dorado, P. Garcia, G. Carlot, C. Davoisne, M. Fraczkiewicz, B. Pasquet, M. Freyss, C. Valot, G. Baldinozzi, D. Simeone, and M. Bertolus, "First-principles Calculation and Experimental Study of Oxygen Diffusion in Uranium Dioxide," *Physical Review B*, vol. 83, 2011.

[328] T. Petit, C. Lemaignan, F. Jollet, B. Bigot, and A. Pasturel, "Point Defects in Uranium Dioxide," *Philosophical Magazine*, vol. 77, pp. 779–786, 1998.

[329] M. Freyss, T. Petit, and J.-P. Crocombette, "Point Defects in Uranium Dioxide: *Ab initio* Pseudopotential Approach in the Generalized Gradient Approximation," *Journal of Nuclear Materials*, vol. 347, pp. 44–51, 2005.

[330] J.-P. Crocombette, D. Torumba, and A. Chattier, "Charge States of Point Defects in Uranium Oxide Calculated with a Local Hybrid Functional for Correlated Electrons," *Physical Review B*, vol. 83, p. 184107, 2011.

[331] J. P. Crocombette, "Influence of Charge States on Energies of Point Defects and Clusters in Uranium Dioxide," *Physical Review B*, vol. 85, p. 144101, 2012.

[332] F. Gupta, G. Brillant, and A. Pasturel, "Correlation Effects and Energetics of Point Defects in Uranium Dioxide: A First Principle Investigation," *Philosophical Magazine*, vol. 87, pp. 2561–2569, 2007.

[333] P. Nerikar, T. Watanabe, J. S. Tulenko, S. R. Phillpot, and S. B. Sinnott, "Energetics of Intrinsic Point Defects in Uranium dioxide from Electronic-Structure Calculations," *Journal of Nuclear Materials*, vol. 384, pp. 61–69, 2009.

[334] K. Clausen, W. Hayes, M. T. Hutchings, J. E. Macdonald, R. Osborn, and P. Schnabel, "Investigation of Oxygen Disorder, Thermal Parameters, Lattice-Vibrations and elastic-Constants of UO_2 and ThO_2 at Temperatures up to 2930 K," *Revue De Physique Appliquee*, vol. 19, pp. 719–722, 1984.

[335] M. T. Hutchings, "High-Temperature Studies of UO_2 and ThO_2 Using Neutron-Scattering Techniques," *Journal of the Chemical Society-Faraday Transactions II*, vol. 83, pp. 1083–1103, 1987.

[336] H. Matzke, "Atomic Transport-Properties in UO_2 and Mixed Oxides (U, Pu)O_2," *Journal of the Chemical Society-Faraday Transactions II*, vol. 83, p. 1121, 1987.

[337] M. S. D. Read and R. A. Jackson, "Derivation of Enhanced Potentials for Uranium Dioxide and the Calculation of Lattice and Intrinsic Defect Properties," *Journal of Nuclear Materials*, vol. 406, pp. 293–303, 2010.

[338] H. Y. Geng, H. X. Song, and Q. Wu, "Theoretical Assessment on the Possibility of Constraining Point-Defect Energetics by Pseudo Phase Transition Pressures," *Physical Review B*, vol. 87, p. 174107, 2013.

[339] J. Yu, R. Devanathan, and W. J. Weber, "First-principles Study of Defects and Phase Transition in UO_2," *Journal of Physics: Condensed Matter*, vol. 21, p. 435401, 2009.

[340] M. Iwasawa, Y. Chen, Y. Kaneta, T. Ohnuma, H.-Y. Geng, and M. Kinoshita, "First-Principles Calculation of Point Defects in Uranium Dioxide," *Materials Transactions*, vol. 47, pp. 2651–2657, 2006.

[341] C. R. A. Catlow, "Point Defect and Electronic Properties of Uranium Dioxide," *Proceedings of the Royal Society A: Mathematical, Physical and Engineering Sciences*, vol. 353, pp. 533–561, 1977.

[342] R. A. Jackson, A. D. Murray, and C. R. A. Catlow, "The Calculation of Basic Defect Energies of UO_2," *Physica B & C*, vol. 131, pp. 136–138, 1985.

[343] R. A. Jackson, C. R. A. Catlow, and A. D. Murry, "Point-Defect Calculations on UO_2," *Journal of the Chemical Society: Faraday Transactions*, vol. 83, pp. 1171–1176, 1987.

[344] R. W. Grimes and C. R. A. Catlow, "The Stability of Fission-Products in Uranium-Dioxide," *Philosophical Transactions of the Royal Society a-Mathematical Physical and Engineering Sciences*, vol. 335, pp. 609–634, 1991.

[345] N. D. Morelon, D. Ghaleb, J. M. Delaye, and L. Van Brutzel, "A New Empirical Potential for Simulating the Formation of Defects and their Mobility in Uranium Dioxide," *Philosophical Magazine*, vol. 83, pp. 1533–1550, 2003.

[346] T. Arima, S. Yamasaki, Y. Inagaki, and K. Idemitsu, "Evaluation of Thermal Properties of UO_2 and PuO_2 by Equilibrium Molecular Dynamics Simulations from 300 to 2000 K," *Journal of Alloys and Compounds*, vol. 400, pp. 43–50, 2005.

[347] G. Sattonay and R. Tetot, "Bulk, Surface and Point Defect Properties in UO_2 from a Tight-Binding Variable-Charge Model," *Journal of Physics: Condensed Matter*, vol. 25, p. 125403, 2013.

[348] N. R. Williams, *Atomistic Simulation of Uranium Dioxide Interfaces*. PhD thesis, 2014.

[349] Y. Zhang and W. Yang, "Comment on "Generalized gradient approximation made simple "," *Physical Review Letters*, vol. 80, pp. 890–890, 1998.

[350] R. Armiento and A. E. Mattsson, "Functional Designed to Include Surface Effects in Self-Consistent Density Functional Theory," *Physical Review B*, vol. 72, p. 085108, 2005.

[351] A. E. Mattsson and R. Armiento, "Implementing and Testing the AM05 Spin Density Functional," *Physical Review B*, vol. 79, p. 155101, 2009.

[352] I. D. Prodan, G. E. Scuseria, and R. L. Martin, "Assessment of Metageneralized Gradient Approximation and Screened Coulomb Hybrid Density Functionals on Bulk Actinide Oxides," *Physical Review B*, vol. 73, p. 045104, 2006.

[353] X.-D. Wen, R. L. Martin, L. E. Roy, G. E. Scuseria, S. P. Rudin, E. R. Batista, T. M. McCleskey, B. L. Scott, E. Bauer, J. J. Joyce, and T. Durakiewicz, "Effect of Spin-Orbit Coupling on the Actinide Dioxides AnO_2 (An=Th, Pa, U, Np, Pu, and Am): A Screened Hybrid Density Functional Study," *The Journal of Chemical Physics*, vol. 137, p. 154707, 2012.

[354] J. Axe and G. Pettit, "Infrared Dielectric Dispersion and Lattice Dynamics of Uranium Dioxide and Thorium Dioxide," *Physical Review*, vol. 151, p. 676, 1966.

[355] J. Schoenes, "Electronic Transitions, Crystal Field Effects and Phonons in UO_2," *Physics Reports Review Section of Physics Letters*, vol. 63, pp. 301–336, 1980.

[356] D. F. Sherman, *Hydrogen Retention and Release from Uranium Dioxide*. PhD thesis, 1987.

[357] D. R. Mullins, P. M. Albrecht, T.-L. Chen, F. C. Calaza, M. D. Biegalski, H. M. Christen, and S. H. Overbury, "Water Dissociation on $CeO_2(100)$ and $CeO_2(111)$ Thin Films," *Journal of physical chemistry C*, vol. 116, pp. 19419–19428, 2012.

[358] L. Xin-Zheng, B. Walker, and A. Michaelides, "Quantum Nature of the Hydrogen Bond," *Proceedings of the National Academy of the united States of America*, vol. 108, no. 16, p. 6369, 2011.

[359] M. Ceriotti, J. More, and D. E. Manolopoulos, "i-PI: A Python Interface for *Ab initio* Path Integral Molecular Dynamics Simulations," *Computer Physics Communications*, vol. 185, p. 1019, 2014.

[360] G. A. Jeffrey, *An Introduction to Hydrogen Bonding*. Oxford University Press, 1997.

[361] C. Ganguly and U. Basak, "Fabrication of High Density UO_2 Fuel Pellets Involving Sol-Gel Microsphere Pelletisation and Low Temperature Sintering," *Journal of Nuclear Materials*, vol. 178, pp. 179–183, 1991.

[362] N. Harker, T. Scott, C. Jones, J. Petherbridge, and J. Glascott, "Altering the Hydriding Behaviour of Uranium Metal by Induced Oxide Penetration Around Carbo-Nitride Inclusions," *Solid State Ionics*, vol. 241, pp. 46–52, 2013.

[363] T. B. Scott, G. C. Allen, I. Findlay, and J. Glascott, "UD_3 Formation on Uranium: Evidence for Grain Boundary Precipitation," *Philosophical Magazine*, vol. 87, pp. 117–187, 2007.

[364] S. T. Murphy, E. E. Jay, and R. W. Grimes, "Pipe Diffusion at Dislocations in UO_2," *Journal of Nuclear Materials*, vol. 447, no. 1–3, pp. 143–149, 2014.

[365] N. R. Williams, M. Molinari, S. C. Parker, and M. T. Storr, "Atomistic Investigation of the Structure and Transport Properties of Tilt Grain Boundaries of UO_2," *Journal of Nuclear Materials*, vol. 458, pp. 44–55, 2015.

[366] Y. Chen, H. Y. Geng, Y. Kaneta, M. Kinoshita, and S. Iwata, "First Principles Modelling of Stability Mechanism of Nonstoichiometric Uranium Dioxide," *Computational Materials Science*, vol. 49, pp. S364–S368, 2010.

[367] H. Y. Geng, Y. Chen, and Y. Kaneta, "Stability Mechanism of Cuboctahedral Clusters in UO_{2+x}: First-Principles Calculations," *Physical Review B*, vol. 77, 2008.

[368] G. J. Snyder and E. S. Toberer, "Complex Thermoelectric Materials," *Nature Materials*, vol. 7, pp. 105–114, 2008.

[369] M. Molinari, D. Tompsett, S. Parker, F. Azough, and R. Freer, "Structural, Electronic and Thermoelectric Behaviour of $CaMnO_3$ and $CaMnO_{(3-\delta)}$," *Journal of Materials Chemistry A*, vol. 2, pp. 14109–14117, 2014.

[370] S. R. Yeandel, M. Molinari, and S. Parker, "Nanostructuring Perovskite Oxides: The Impact of $SrTiO_3$ Nanocube 3D Self-Assembly on Thermal Conductivity," *RSC Advances*, vol. 6, pp. 114069–114077, 2016.

[371] T. X. T. Sayle, M. Cantoni, U. M. Bhatta, S. C. Parker, S. R. Hall, G. Möbus, M. Molinari, D. Reid, S. Seal, and D. C. Sayle, "Strain and Architecture-Tuned Reactivity in Ceria Nanostructures; Enhanced Catalytic Oxidation of CO to CO_2," *Chemistry of Materials*, vol. 24, pp. 1811–1821, 2012.

[372] T. X. T. Sayle, M. Molinari, S. Das, U. M. Bhatta, G. Mobus, S. C. Parker, S. Seal, and D. C. Sayle, "Environment-Mediated Structure, Surface Redox Activity and Reactivity of Ceria Nanoparticles," *Nanoscale*, vol. 5, pp. 6063–73, 2013.

[373] F. Wang, W. Lai, R. Li, B. He, and S. Li, "Fast Hydrogen Diffusion Along the $\Sigma 7$ Grain Boundary of α-Al_2O_3: A First-Principles Study," *International Journal of Hydrogen Energy*, vol. 41, pp. 22214–22220, 2016.

[374] W. Xing, X.-Q. Chen, P. Liu, X. Wang, P. Zhang, D. Li, and Y. Li, "First-Principles Studies of Hydrogen Behaviour Interacting with Oxygen-Enriched Nanostructured Particles in the ODS Steels," *International Journal of Hydrogen Energy*, vol. 39, pp. 18506–18519, 2014.

[375] D. Andersson, P. Garcia, X.-Y. Liu, G. Pastore, M. Tonks, P. Millett, B. Dorado, D. Gaston, D. Andrs, R. Williamson, R. Martineau, B. Uberuaga, and C. Stanek, "Atomistic Modeling of Intrinsic and Radiation-enhanced Fission gas (Xe) Diffusion in $UO_{2\pm x}$: Implications for Nuclear Fuel Performance Modelling," *Journal of Nuclear Materials*, vol. 451, pp. 225–242, 2014.

[376] R. Orr, H. Godfrey, C. Broan, D. Goddard, G. Woodhouse, P. Durham, A. Diggle, and J. Bradshaw, "Formation and Physical Properties of Uranium Hydride Under Conditions Relevant to Metallic Fuel and Nuclear Waste Storage," *Journal of Nuclear Materials*, vol. 477, pp. 236–245, 2016.

[377] R. Orr, H. Godfrey, C. Broan, D. Goddard, G. Woodhouse, P. Durham, A. Diggle, and J. Bradshaw, "Kinetics of the Reaction Between Water and Uranium Hydride Prepared Under Conditions Relevant to Uranium Storage," *Journal of Alloys and Compounds*, vol. 695, pp. 3727–3735, 2017.

[378] W. Bartscher, A.Boeuf, R. Caciuffo, J. Fournier, W. Kuhs, J. Rebizant, and F. Rustichelli, "Neutron Diffraction Study of β-UD_3 and β-UH_3," *Solid State Communications*, vol. 53, pp. 423–426, 1985.

[379] J. W. Roddy, "The Actinide Hydrides: The Americium-Hydrogen System," *Journal of Nuclear Inorganic Chemistry*, vol. 35, pp. 4141–4148, 1973.

[380] J. H. Weaver, J. A. Knapp, D. E. Eastman, D. T. Peterson, and C. B. Satterthwaite, "Electronic Structure of the Thorium Hydrides ThH_2 and $Th4H_{15}$," *Physical Review Letters*, vol. 39, p. 639, 1977.

[381] R. N. R. Mulford and G. E. Sturdy, "The Plutonium-Hydrogen System. II. Solid Solution of Hydrogen in Plutonium Dihydride," *Journal of the American Chemical Society*, vol. 78, pp. 3897–3901, 1956.

[382] R. Mulford, F. H. Ellinger, and W. H. Zacariasen, "A New Form of Uranium Hydride," *Journal of the American Chemical Society*, vol. 76, pp. 297–298, 1954.

[383] I. Tkach, M. Paukov, D. Drozdenko, M. Cieslar, B. Vondrackova, Z. Matej, D. Kriegner, A. Andreev, N.-T. H. Kim-Ngan, I. Turek, M. Divis, Z. Mat, and L. Havela, "Electronic properties of α-UH_3 stabilized by Zr," *Physical Review B*, vol. 91, p. 115116, 2015.

[384] A. Sliwa and W. Trzebiatowski, "Magnetic Properties of α-Uranium Hydride," *Bulletin de l'Academie polonaise des sciences. Serie des sciences chimiques*, vol. X, p. 217, 1962.

[385] A. C. Lawson, J. A. Goldstone, J. G. Huber, A. L. Giorgi, J. W. Conant, A. Severing, B. Cort, and R. A. Robinson, "Magnetic Structure of Actinide Materials by Pulsed Neutron Diffraction (invited)," *Journal of Applied Physics*, vol. 69, p. 5112, 1991.

[386] C. D. Taylor, "Characterizing Electronic Structure Motifs in β-UH_3," *Physical Review B*, vol. 82, p. 224408, 2010.

[387] D. M. Gruen, "Magnetic Properties of Uranium Hydride," *The Journal of Chemical Physics*, vol. 23, p. 1708, 1955.

[388] W. E. Henry, "Low-Temperature Magnetic Studies of Uranium Hydride, Uranium Deuteride, and Uranium Dioxide," *Physical Review*, vol. 109, p. 1976, 1958.

[389] H. Drulis, F. G. Vagizov, M. Drulis, and T. Mydlarz, "Magnetic and Mossbauer-Effect Studies of U_6Fe Hydride," *Physical Review B*, vol. 52, p. 9500, 1995.

[390] A. V. Andreev, "Magnetic and Magnetoelastic Properties of β-UH_3," *Journal of Alloys and Compounds*, vol. 1998, pp. 32–36, 1998.

[391] J. B. Y. B. Barash and M. H. Mintz, "NMR Study of Hydrogen in Ferromagnetic β-UH3," *Physical Review B*, vol. 29, p. 6096, 1984.

[392] C. Zhang, H. Jiang, H.-L. Shi, G.-H. Zhong, and Y.-H. Su, "Mechanical and Thermodynamic Properties of α-UH_3 Under Pressure," *Journal of Alloys and Compounds*, vol. 604, pp. 171–174, 2014.

[393] J. Grunzweig-Genossar, M. Kunznietz, and B. Meerovici, "Nuclear Magnetic Resonance in Uranium Hydride and Deuteride," *Physical Review B*, vol. 1, p. 1958, 1970.

[394] M. Peretz, D. Zamir, G. Cinader, and Z. Hadari, "NMR Study of Hydrogen Diffusion in Uranium Hydride," *Journal of Physical Chemistry Solids*, vol. 37, pp. 105–111, 1976.

[395] G. C. Allen and J. C. H. Stevens, "The Behaviour of Uranium Metal in Hydrogen Atmospheres," *Journal of the Chemical Society-Faraday Transactions I*, vol. 84, pp. 165–174, 1988.

[396] T. Gouder, R. Eloirdi, F. Wastin, E. Colineau, J. Rebizant, D. Kolberg, and F. Huber, "Electronic Structure of UH_3 Thin Films Prepared by Sputter Deposition," *Physical Review B*, vol. 70, p. 235108, 2004.

[397] J. Bloch, F. Simca, M. Kroup, A. Stern, D. Shmariahu, and M. H. Mintz, "The Initial Kinetics of Uranium Hydride Formation Studies by a Hot-Stage Microscope Technique," *Journal of the Less Common Metals*, vol. 103, pp. 163–171, 1984.

[398] M. Balooch and A. Hamza, "Hydrogen and Water Vapor Adsorption on and Reaction with Uranium," *Journal of Nuclear Materials*, vol. 230, pp. 259–270, 1996.

[399] G. L. Powell, W. L. Harper, and J. R. Kirkpatrick, "The kinetics of the hydriding of uranium metal," *Journal of the Less -Common Metals*, vol. 172, pp. 116–123, 1991.

[400] G. G. Libowitz, "Nonstoichiometry and Lattice Defects in Uranium Hydride," *The Journal of Chemical Physics*, vol. 27, pp. 514–518, 1957.

[401] F. A. Krouger, D. Turnbull, and G. G. Libowitz, "Equilibrium Properties of Dilute Solid Solutions Nonstoichiometry and Lattice Defects in Transition Metal Hydrides," *Journal of Applied Physics*, vol. 33, pp. 399–405, 1962.

[402] G. G. Libowitz and T. R. Gibb, "High Pressure Dissociation of the Uranium Hydrogen System," *Journal of Physical Chemistry*, vol. 61, pp. 793–795, 1957.

[403] M. W. Chase, N. I. of Standards, and T. (U.S.), *NIST-JANAF Thermochemical Tables*. Journal of physical and chemical reference data Monograph, Washington, D.C. Woodbury, N.Y.: American Chemical Society ; American Institute of Physics for the National Institute of Standards and Technology, 4th ed., 1998. 98086732 Malcolm W. Chase, Jr. 29 cm. Rev. ed. of: JANAF thermochemical tables. 2nd ed. 1971. Includes bibliographies. pt. 1. Al-Co – pt. 2. Cr-Zn. JANAF thermochemical tables.

[404] M. Molinari, N. Brincat, G. Allen, and S. Parker, "Structure and Properties of Some Layered U_2O_5 Phases: A Density Functional Theory Study," *Inorganic Chemistry*, vol. 56, pp. 1036–1044, 2017.

A pDOS of Hydrogen Defects in UO_2

Complete set of DOS graphs for 36 and 96 atom unit cells for pure, hydride and hydroxyl defects. Using a range of functionals and including the effects of SOC for the 36 atom system.

A.1 96 atom Cell DOS

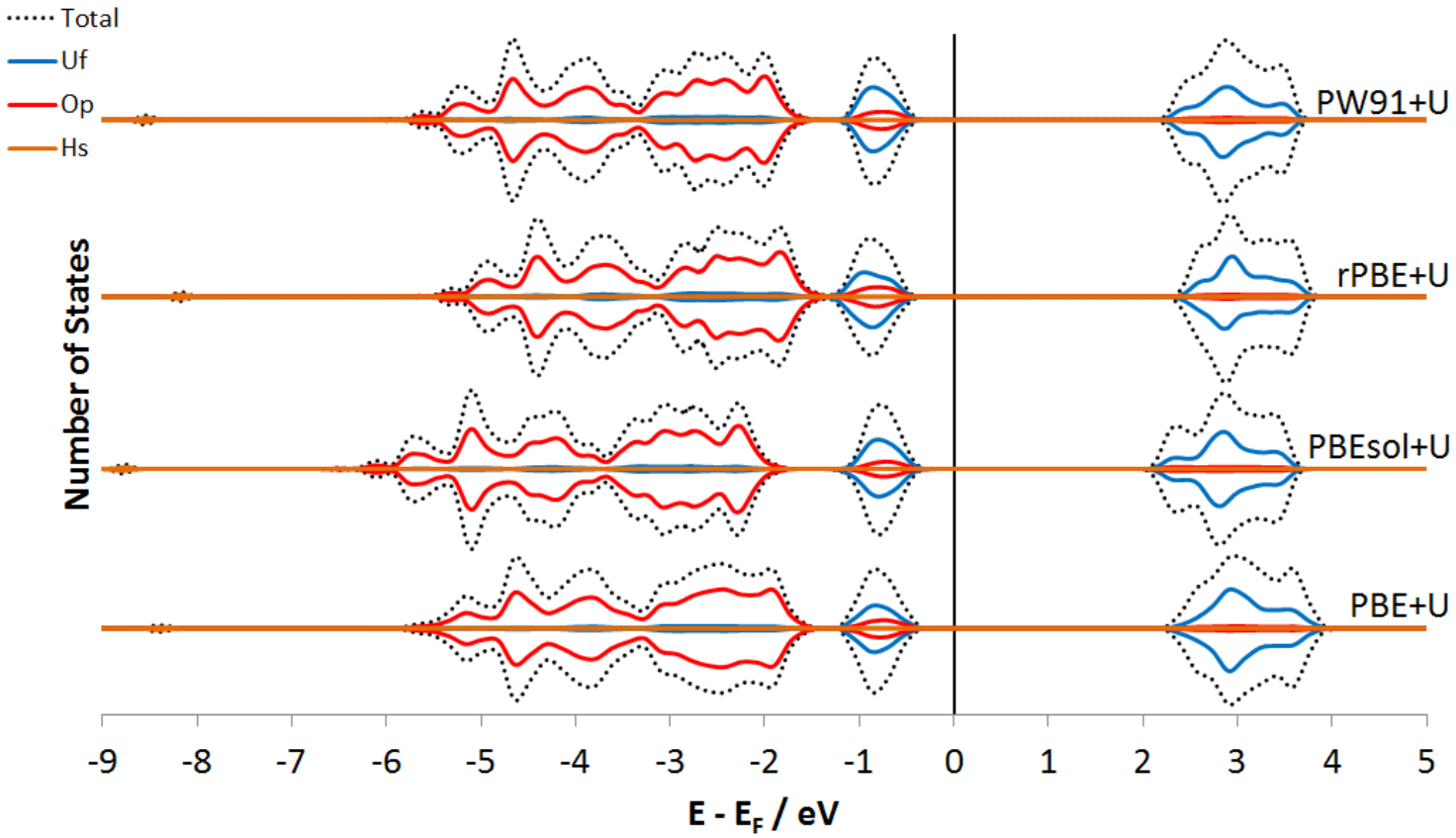

Figure A.1: Partial DOS for a Hydrogen defect in a 96 atom UO_2 cell calculated with a range of functionals. The Fermi energy has been set to 0 eV.

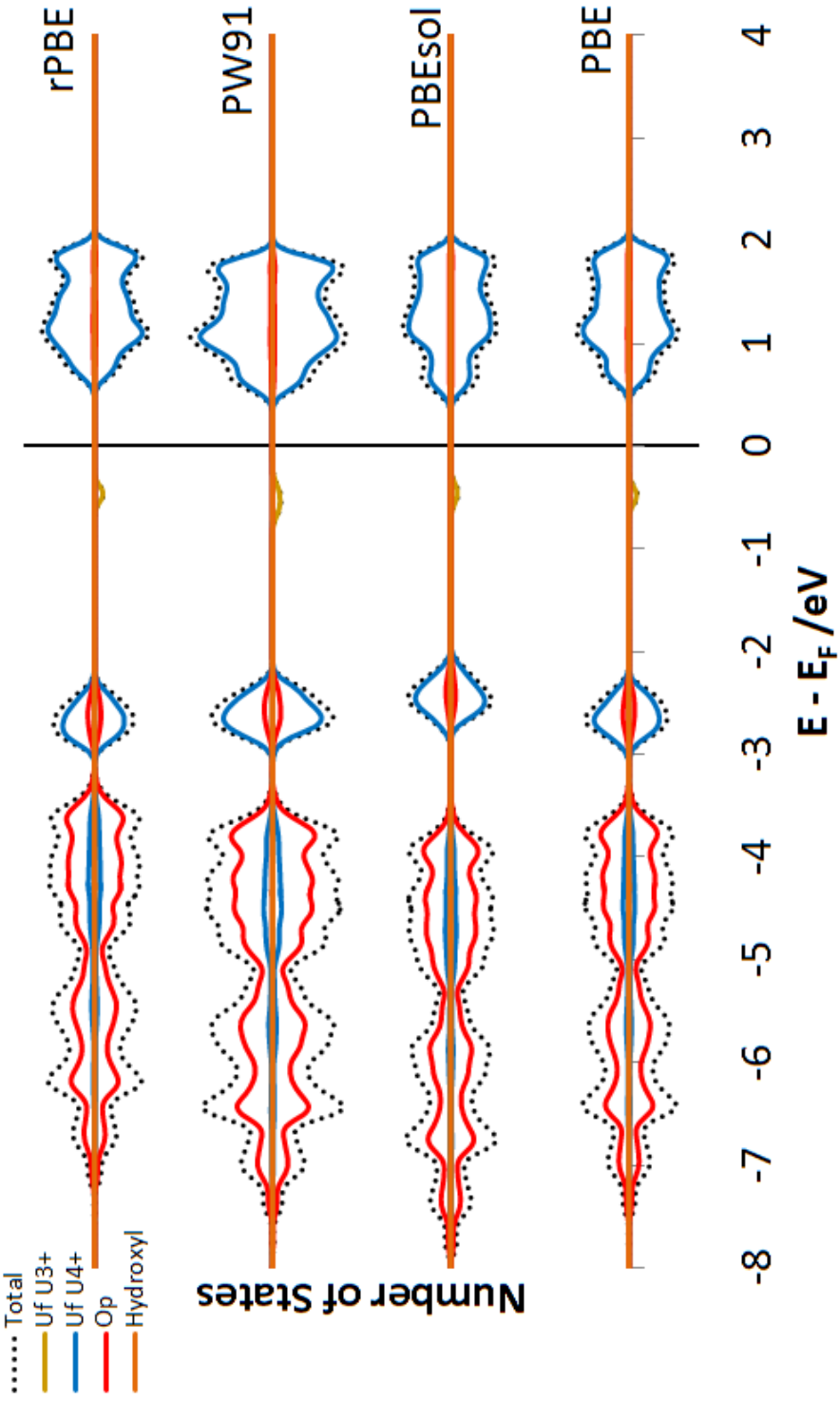

Figure A.2: Partial DOS for a Hydroxyl defect in a 96 atom UO_2 cell calculated with a range of functionals. The Fermi energy has been set to 0 eV.

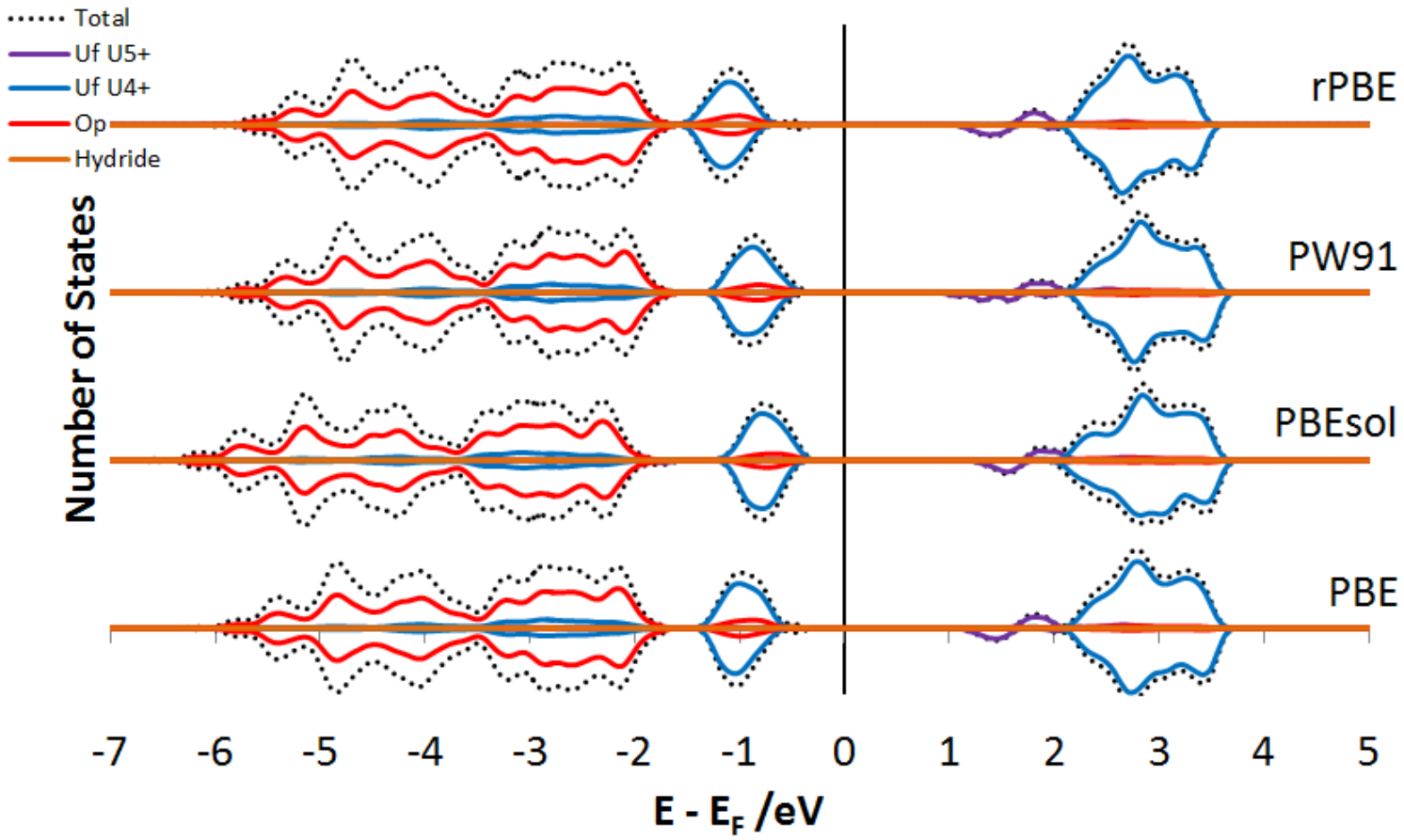

Figure A.3: Partial DOS for a Hydride defect in a 96 atom UO_2 cell calculated with a range of functionals. The Fermi energy has been set to 0 eV.

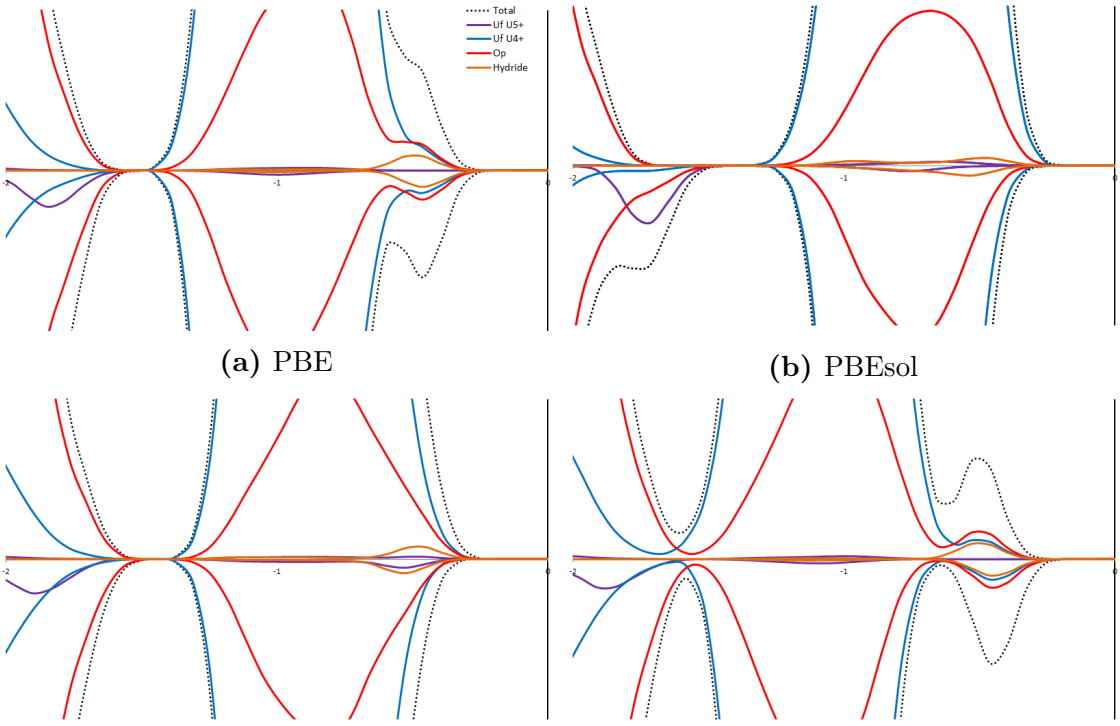

(a) PBE **(b)** PBEsol

(c) PW91 **(d)** rPBE

Figure A.4: Partial DOS for a Hydride defect in a 96 atom UO_2 cell calculated with a range of functionals. The Fermi energy has been set to 0 eV. The graph has been scaled to show the Hydride states at the top of the valence band.

A.2 36 atom Cell Spin DOS

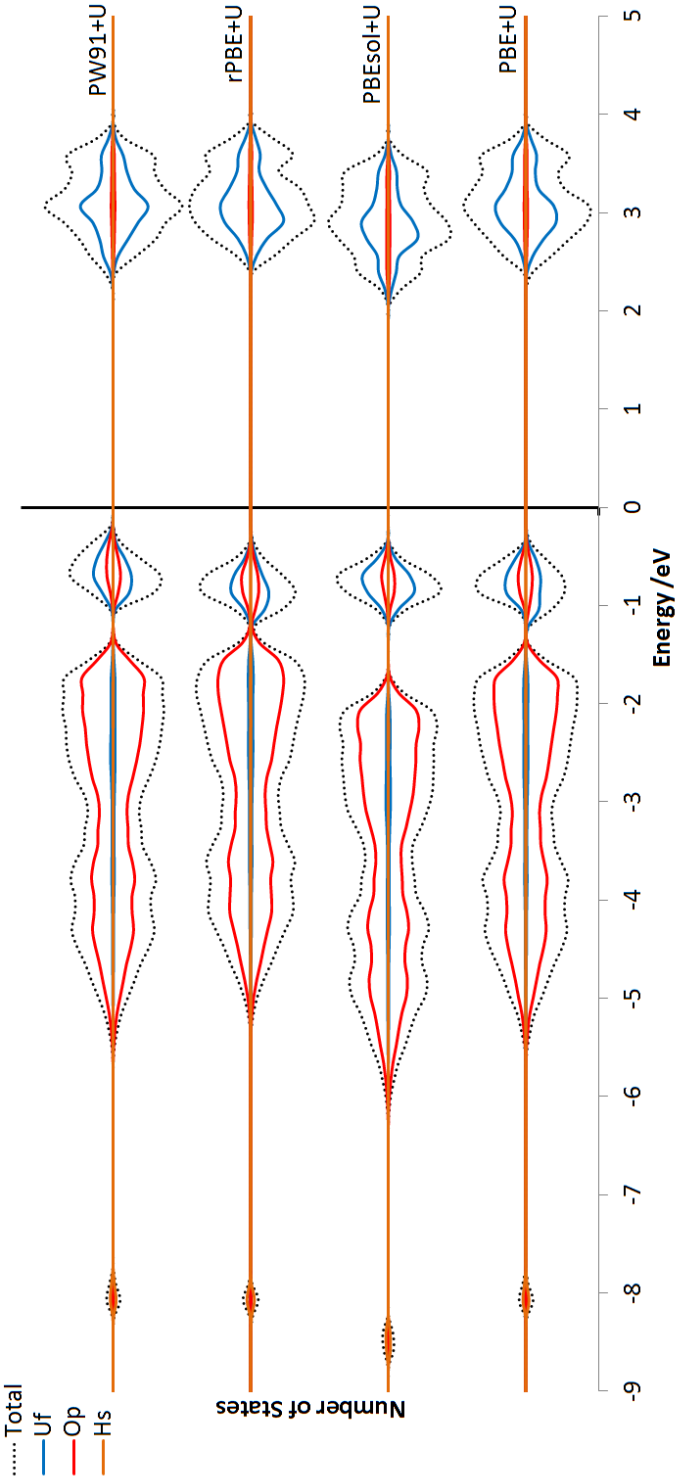

Figure A.5: Partial DOS for a Hydrogen defect in a 36 atom UO_2 cell calculated with a range of functionals. The Fermi energy has been set to 0 eV.

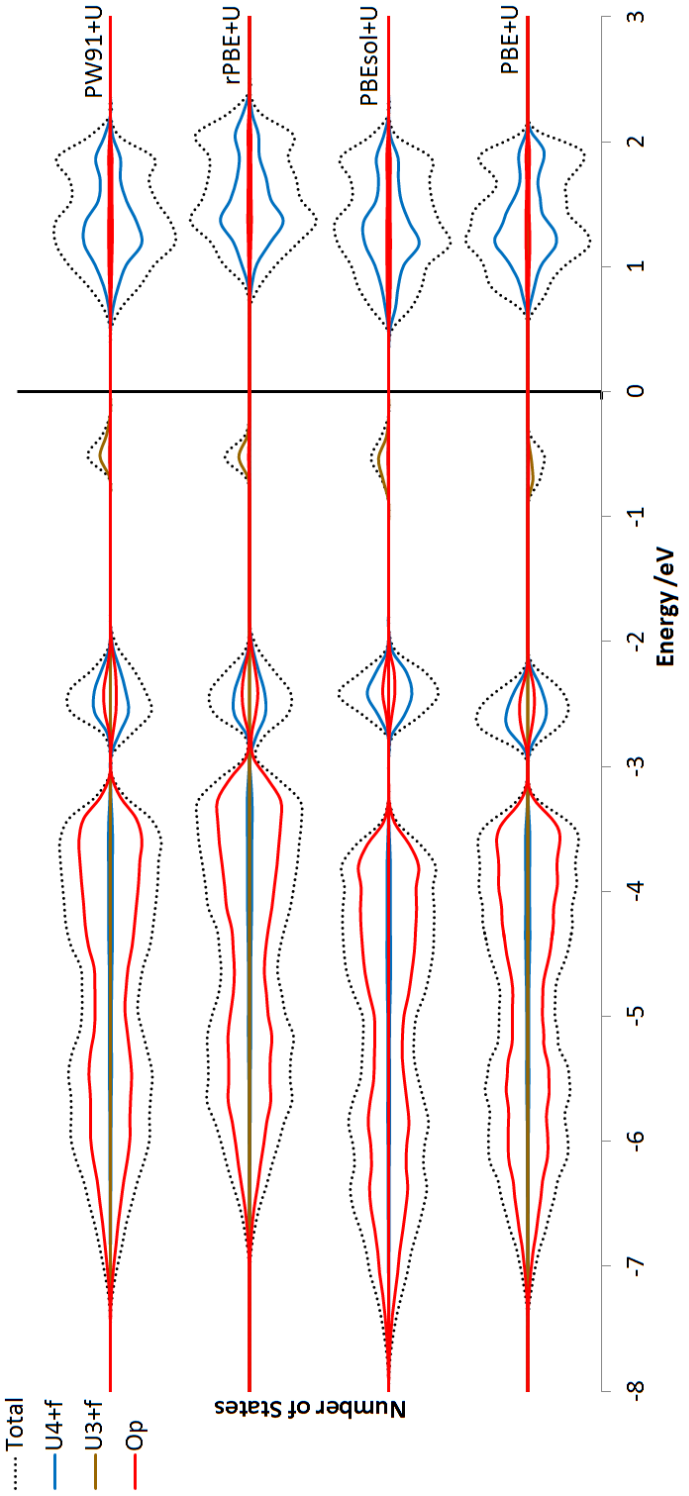

Figure A.6: Partial DOS for a Hydroxyl defect in a 36 atom UO_2 cell calculated with a range of functionals. The Fermi energy has been set to 0 eV.

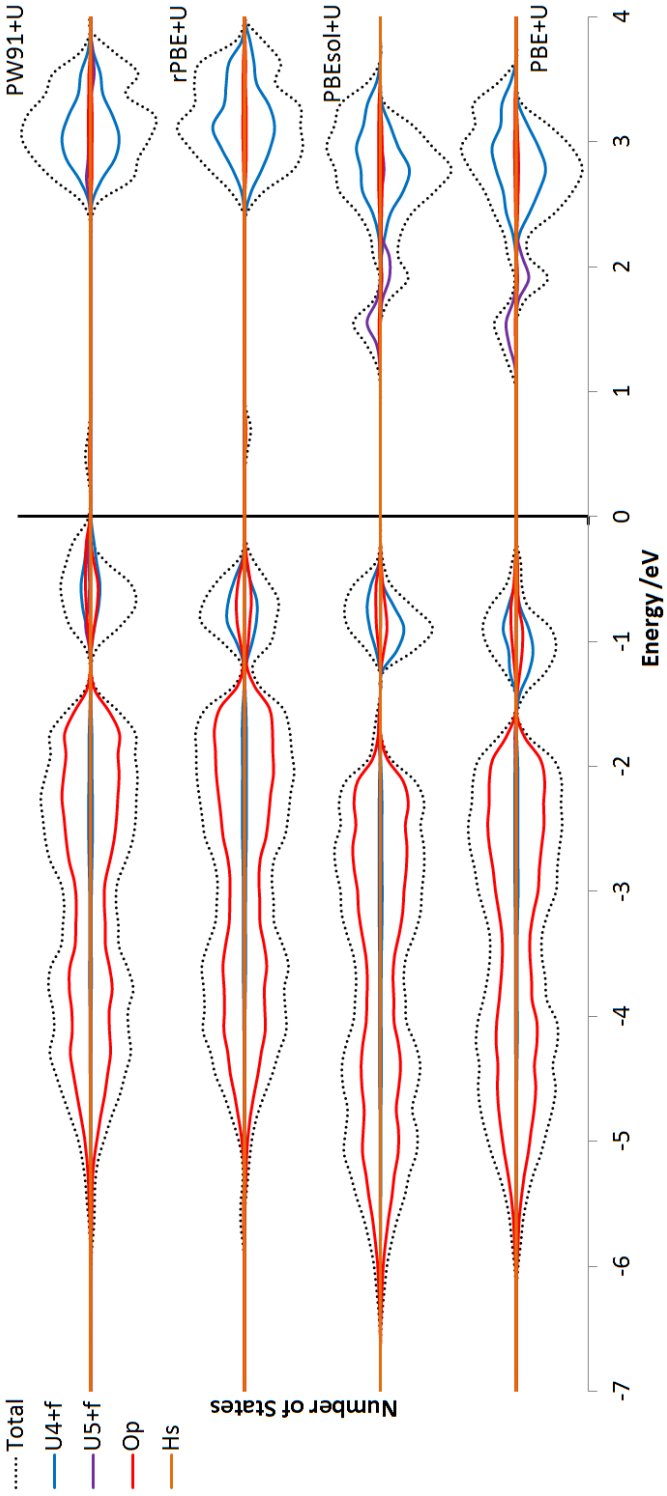

Figure A.7: Partial DOS for a Hydride defect in a 36 atom UO_2 cell calculated with a range of functionals. The Fermi energy has been set to 0 eV.

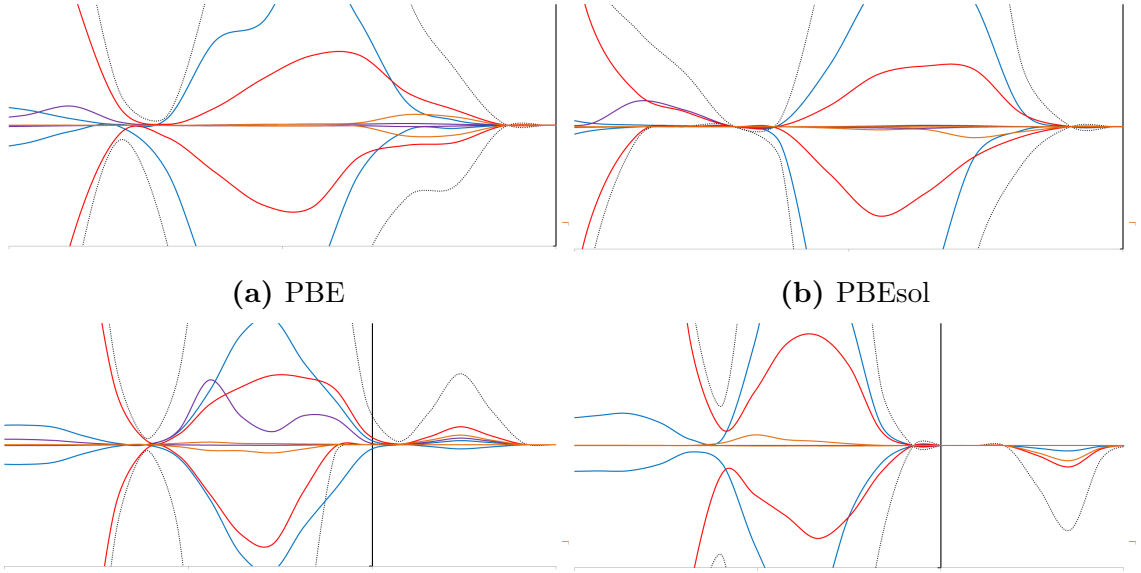

(a) PBE **(b)** PBEsol

(c) PW91 **(d)** rPBE

Figure A.8: Partial DOS for a Hydride defect in a 36 atom UO_2 cell calculated with a range of functionals. The Fermi energy has been set to 0 eV. The graph has been scaled to show the Hydride states at the top of the valence band.

A.3 36 atom Cell SOC DOS

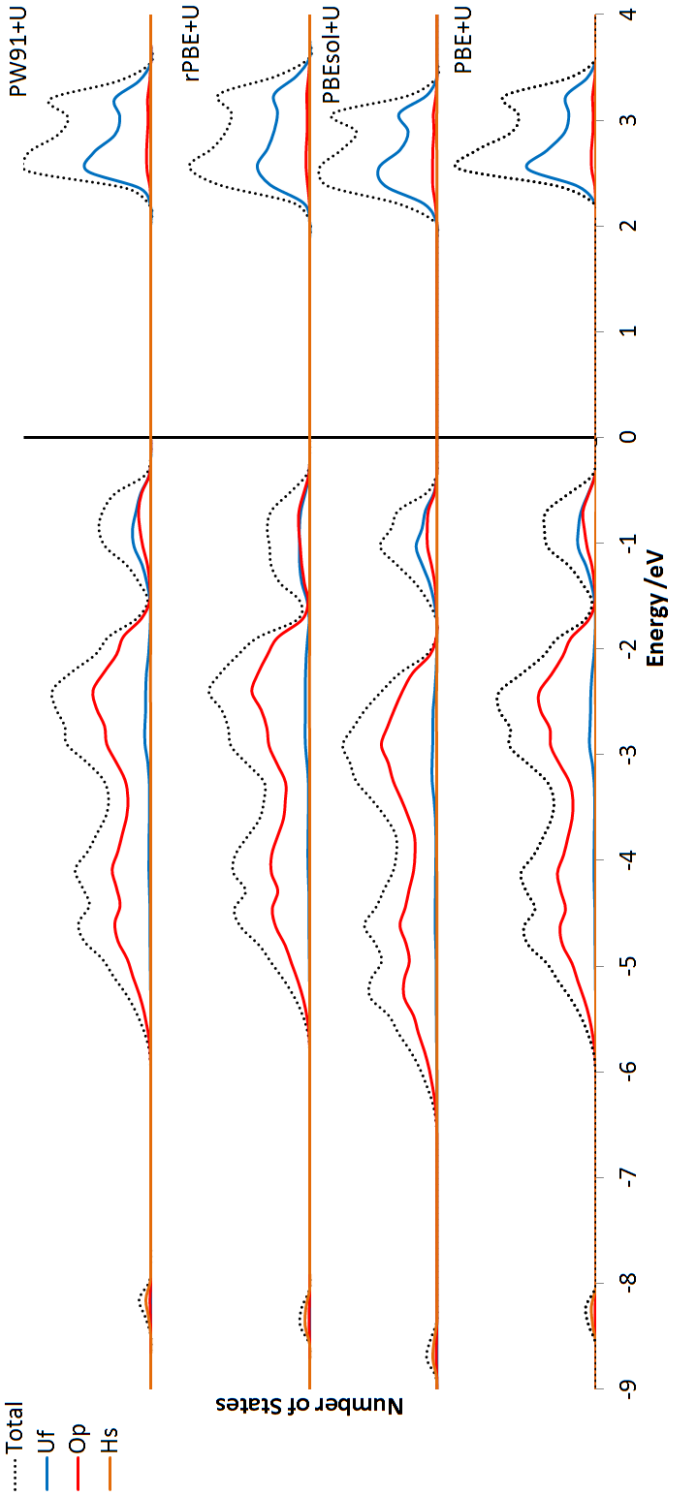

Figure A.9: Partial DOS for a Hydrogen defect in a 36 atom UO_2 cell calculated with a range of functionals. The Fermi energy has been set to 0 eV.

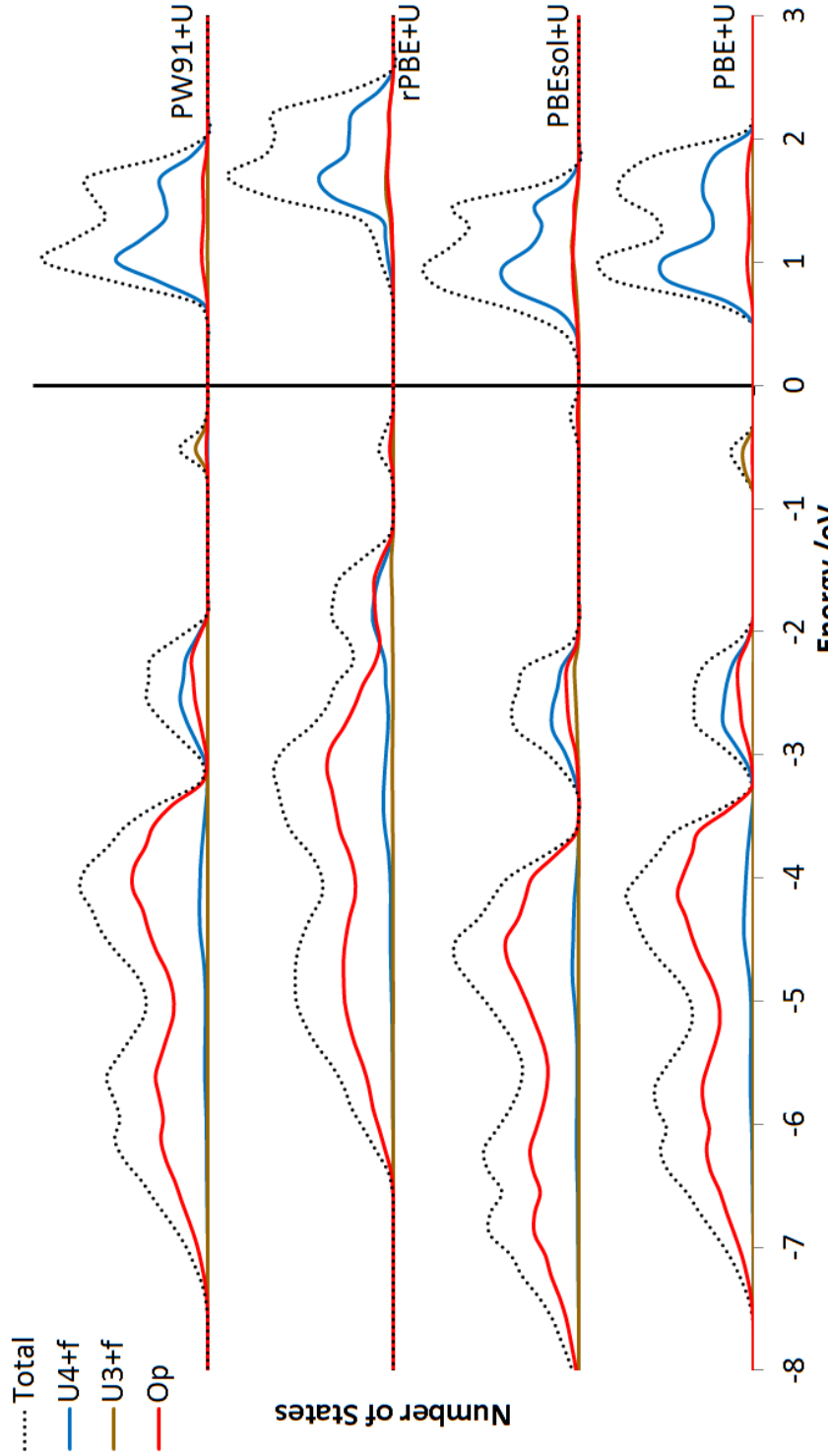

Figure A.10: Partial DOS for a Hydroxyl defect in a 36 atom UO_2 cell calculated with a range of functionals. The Fermi energy has been set to 0 eV.

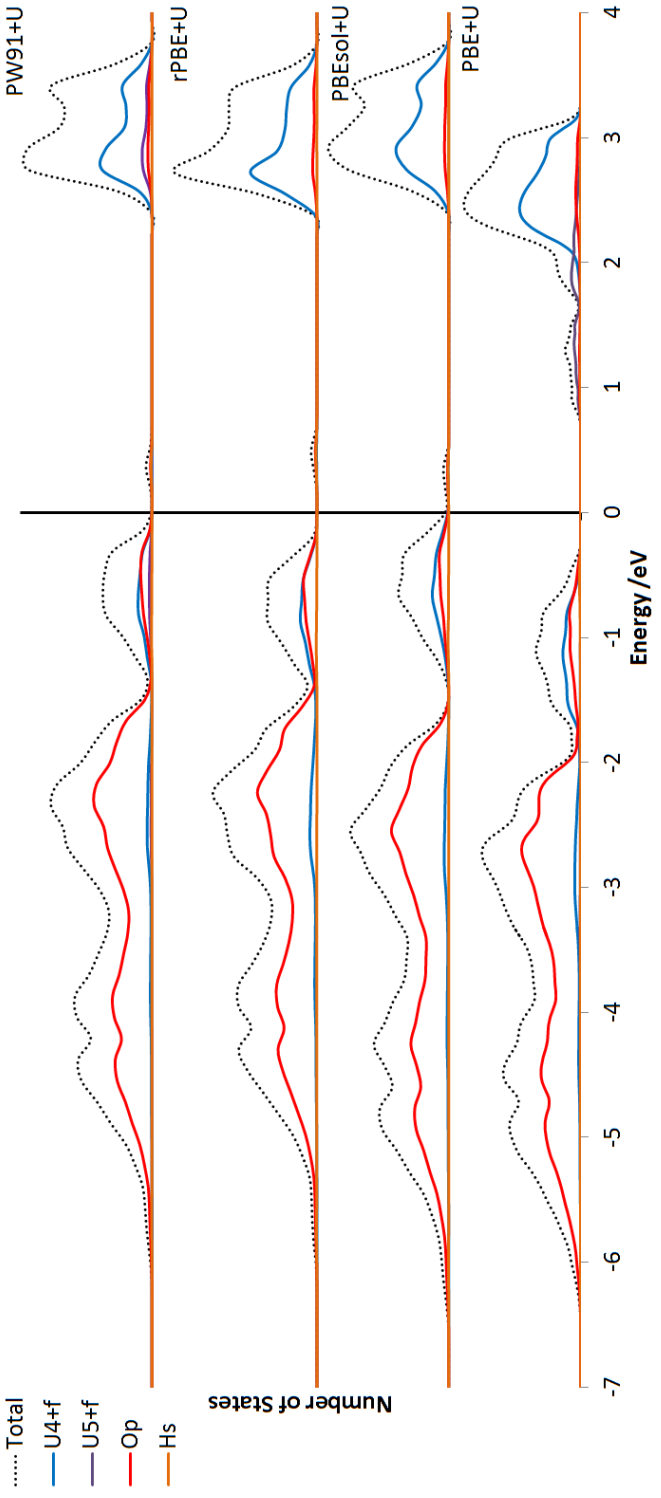

Figure A.11: Partial DOS for a Hydride defect in a 36 atom UO_2 cell calculated with a range of functionals. The Fermi energy has been set to 0 eV.

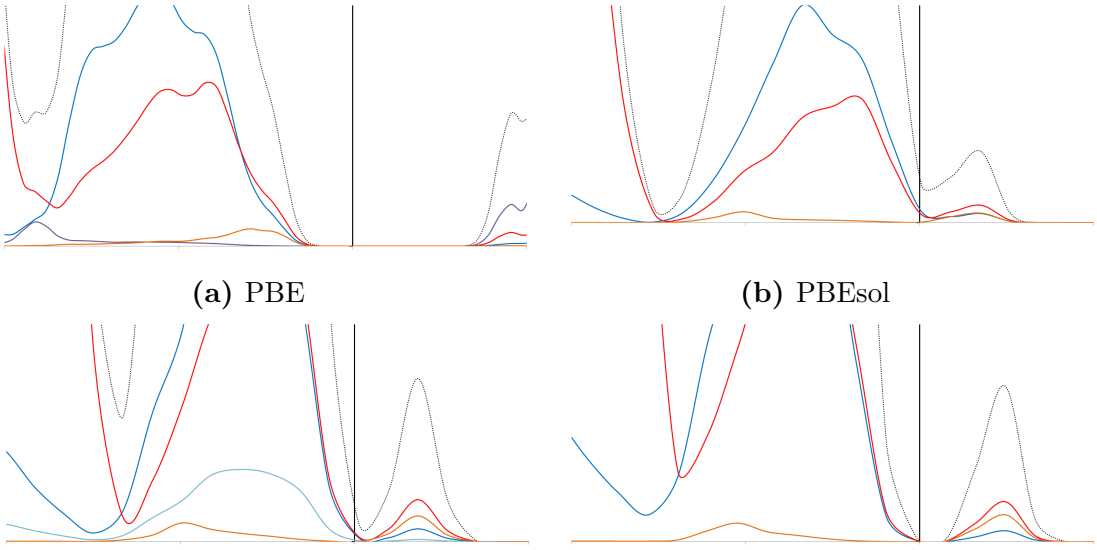

(a) PBE **(b)** PBEsol

(c) PW91 **(d)** rPBE

Figure A.12: Partial DOS for a Hydride defect in a 36 atom UO_2 cell calculated with a range of functionals and including the effect of SOC. The Fermi energy has been set to 0 eV. The graph has been scaled to show the Hydride states at the top of the valence band.

B Hydrogen Defects in Larger Oxygen Defect Clusters

B.1 Hydrogen in Larger Oxygen Defect Clusters

Chapter 7 has only focused on the smallest reported oxygen clusters, the I_2^r and W_{222}, however there are a number of larger reported cluster models. In order to survey how these clusters respond to varying hydrogen concentrations as has been done in this chapter for the I_2^r and W_{222} would require a significant number of calculations, especially if hydrogen is added until all U^{5+} has been reduced. This would require the addition of 10 hydrogen atoms for the COT-13 cluster. Despite this a small number of configurations have been trialled for these larger clusters to make an assessment of how they respond to addition of hydrogen.

Table B.1 summarises the results for the hydrogen configurations trialled on the larger oxygen defect clusters. The behaviour is similar to that seen for the smaller oxygen clusters. Addition of hydrogen results in the reduction of U^{5+}, proportional to the hydrogen concentration added. The hydrogen species convert into hydroxyl or water groups, depending on if the multiple hydrogen are placed near the same defect oxygen. The formation energy shows the same trend as the hydrogen concentration, increasing with hydrogen concentration, while the binding energy shows the reverse becoming more favourable. Though without a full range of configurations tested it is not possible to say for certain if this trend will hold true to the complete reduction of the U^{5+} concentration. There is also the preference for hydrogen to point towards lattice, rather then defect oxygen, as shown by clusters 28, 32 and 33 where the O-H groups have rotated to point away from defect oxygen.

It would be interesting to do a full study of hydrogen on the *COT* clusters, as these are the defects that exists before the phase change into U_4O_9. As the *COT* cluster has a large amount of empty space it could contain large quantities of hydrogen with relative ease and therefore act as a trap site, or indeed a possibly reservoir of hydrogen if reversible trapping occurs. Though this would mean that there are potentially very large local hydrogen concentrations. Additionally, it would be interesting to compare between the *COT-12* and *COT-13* clusters, as the void in the centre of the *COT-12* could very easily accommodate a hydride or even H_2 defect.

Table B.1: Final hydrogen oxygen defect cluster configurations for the I_3^x, I_4^x and *COT-13* clusters, an arrow denotes where a change in the initial oxygen cluster geometry has occurred. ΔV is the change in volume calculated compared to stoichiometric UO_2, U^{5+} defect concentration, solution and binding energies per hydrogen and number of strong, medium and weak hydrogen bonds for hydrogen concentrations of 117 - 467 μgH / gUO_2. Where the final configuration contains hydrogen pointing towards both lattice and defect oxygen is denoted by a having both the D and L superscript, the accompanying number denotes how many hydrogen point to defect/lattice oxygen.

Cluster	Configuration	ΔV / H (Å^3)	[H] (μgH / gUO_2)	[U^{5+}] (mgU^{5+} / gUO_2)		Energy / H (eV)		Hydrogen Bonds		
				NN	NNN	Solution	Binding	Strong	Medium	Weak
25	${}^{D}I_3^x$	-0.25	117	110	28	-0.69	-2.77	0	3	0
26	${}^{D}I_3^x$	4.09	234	28	83	-0.49	-1.38	0	4	2
27	${}^{D}I_3^x$	5.00	351	0	83	-0.49	-0.85	0	6	2
28	${}^{D}I_3^x \rightarrow {}^{D^2L^2}I_3^x$	5.63	467	28	28	-0.57	-0.57	0	5	9
29	${}^{D}I_4^x$	-0.86	117	165	28	-0.86	-3.82	1	2	0
30	${}^{D}I_4^x$	2.23	234	138	28	-0.47	-2.00	1	0	2
31	${}^{D}I_4^x$	4.45	351	83	55	-0.35	-1.31	3	7	1
32	${}^{D}I_4^x \rightarrow {}^{D^3L}I_4^x$	5.19	467	55	55	-0.40	-0.92	3	4	7
33	${}^{D}I_4^x \rightarrow {}^{D^2L^2}I_4^x$	4.74	467	55	55	-0.43	-0.91	2	3	8
34	^{D}*COT-13*	-8.66	117	165	83	-3.11	-2.79	0	0	5
35	^{D}*COT-13*	-0.01	234	165	55	-1.49	-2.10	0	3	5

C Complete UH_3 Oxygen Defects Data

Full set of results for oxygen defects in UH_3.

Table C.1: Calculated formation energies, relative energy, volume change and number of U^{4+} defects in $UH_{3-x}O_x$ with varying oxygen concentrations. The relative energy is given with the most stable defect at any oxygen concentration set to zero.

	$\mathbf{UH_{2.88}O_{0.12}}$	$\mathbf{UH_{2.75}O_{0.25}}$					
Configuration Number	1	1	2	3	4	5	6
$\boldsymbol{E_F}$**/O (eV)**	-4.34	-4.65	-4.57	-4.64	-4.58	-4.68	-4.63
Relative Energy (eV)	-	0.03	0.12	0.04	0.11	0.00	0.05
a **(Å)**	6.92	6.90	6.88	6.92	6.90	6.95	6.92
b **(Å)**	9.60	6.90	6.90	6.9	6.92	6.91	6.93
c **(Å)**	6.91	6.90	6.90	6.87	6.90	6.92	6.88
ΔV / O (Å^3)	-1.17	-1.21	-1.56	-1.22	-0.61	0.40	-0.62
Number of U^{4+}	1	2	2	2	2	2	2

Table C.2: Calculated formation energies, relative energy, volume change and number of U^{4+} defects in $UH_{2.63}O_{0.37}$. The relative energy is given with the most stable defect set to zero.

$UH_{2.63}O_{0.37}$												
Configuration Number	1	2	3	4	5	6	7	8	9	10	11	12
E_F/O (eV)	-4.83	-4.85	-4.82	-4.88	-4.73	-4.80	-4.84	-4.70	-4.76	-4.64	-4.94	-4.80
Relative Energy (eV)	0.12	0.10	0.12	0.06	0.22	0.14	0.10	0.25	0.19	0.31	0.00	0.15
***a* (Å)**	6.96	6.98	6.95	6.96	6.94	6.95	6.90	6.91	6.98	6.91	6.92	6.95
***b* (Å)**	6.91	6.92	6.91	6.93	6.94	6.90	6.93	6.92	6.95	6.91	6.92	6.96
***c* (Å)**	6.89	6.89	6.89	6.88	6.88	6.91	6.91	6.88	6.87	6.90	6.90	6.84
ΔV / O (Å^3)	0.18	0.67	0.04	0.31	0.12	0.10	-0.52	-0.77	0.77	-0.50	-0.22	0.07
Number of U^{4+}	3	3	3	3	3	3	3	3	3	3	3	3